Université de Montréal

Étudier les fonctions des protéines avec des nanoantennes fluorescentes

Par

Scott G. Harroun

Département de chimie, Faculté des arts et des sciences

Thèse présentée en vue de l’obtention du grade de doctorat (Ph.D.) en chimie

Septembre 2021

Université de Montréal

Département de chimie, Faculté des arts et des sciences

Cette thèse intitulée

Étudier les fonctions des protéines avec des nanoantennes fluorescentes

Présentée par

Scott G. Harroun

A été évaluée par un jury composé des personnes suivantes

Joelle N. Pelletier
Président-rapporteur

Alexis Vallée-Bélisle
Directeur de recherche

William D. Lubell
Membre du jury

Anthony Mittermaier
Examinateur externe

Résumé

Caractériser la fonction des protéines est crucial pour notre compréhension des mécanismes moléculaires de la vie, des maladies, et aussi pour inspirer de nouvelles applications en bionanotechnologie. Pour y arriver, il est nécessaire de caractériser la structure et la dynamique de chaque état occupé par la protéine durant sa fonction. La caractérisation expérimentale des états transitoires des protéines représente encore un défi majeur parce que les techniques à haute résolution structurelle, telles que la spectroscopie RMN et la cristallographie aux rayons X, peuvent difficilement être appliquées à l'étude des états de courte durée. De plus, les techniques à haute résolution temporelle, telles que la spectroscopie de fluorescence, nécessitent généralement une chimie complexe pour introduire des fluorophores à des endroits spécifiques dans la protéine.

Dans cette thèse nous introduisons l'utilisation des nanoantennes fluorescentes en tant que nouvelle stratégie pour détecter et signaler les changements de conformation des protéines via des interactions non covalentes entre des fluorophores spécifiques et la surface de la protéine. En utilisant des expériences et des simulations moléculaires, nous démontrons que des fluorophores chimiquement divers peuvent se lier et être utilisés pour sonder différentes régions d'une enzyme modèle, la phosphatase alcaline (PA). Ces nanoantennes peuvent être fixées directement aux protéines ou utilisées à l'aide du système de fixation simple et modulaire, le complexe biotine-streptavidine (SA), qui permet un criblage rapide et efficace de la nanoantenne optimale tant dans sa composition que sa longueur. Dans le cas de la PA, nous montrons que nos nanoantennes permettent la détection et la caractérisation des conformations distinctes incluant les changements conformationnels nanoscopiques produisant durant la catalyse du substrat. Nous démontrons également que les signaux fluorescents émis par la nanoantenne peuvent également permettre de caractériser la cinétique enzymatique d'une protéine en une seule expérience tout en incluant la détermination des paramètres « Michaelis-Menten » de ses substrats et inhibiteurs.

Nous avons également exploré l'universalité de la stratégie ces nanoantennes fluorescentes en utilisant une autre protéine modèle, la Protéine G et son interaction avec les anticorps, et avons démontré son utilité pour mettre au point un essai permettant de détecter les anticorps. Ces nanoantennes simples et faciles à utiliser peuvent être appliquées pour détecter et analyser les changements conformationnels de toutes tailles et nos résultats suggèrent qu'elles pourraient être utilisées pour caractériser n’importe quel type de fonction.

Mots-clés : fonction des protéines, cinétique des enzymes, interaction protéine-protéine, nanotechnologie de l’ADN, nanoantenne, spectroscopie fluorescence, phosphatase alcaline, biotine-streptavidine, Protéine G, inhibiteur enzymatique, biosenseur

Abstract

The characterisation of protein function is crucial to understanding the molecular mechanisms of life and disease, and inspires new applications in bionanotechnology. To do so, it is necessary to characterise the structure and dynamics of each state that proteins adopt during their function. Experimental study of protein transient states, however, remains a major challenge because high-structural-resolution techniques, including NMR spectroscopy and X-ray crystallography, can often not be directly applied to study short-lived protein states. On the other hand, high-temporal-resolution techniques, such as fluorescence spectroscopy, typically require complicated site-specific labelling chemistry.

This thesis introduces the use of fluorescent nanoantennas as a new strategy for sensing and reporting on protein conformational changes through noncovalent dye-protein interactions driven by a high local concentration. Using experiments and molecular simulations, we first demonstrate that chemically diverse dyes can bind and be used to probe different regions of a model enzyme, intestinal alkaline phosphatase (AP). These nanoantennas can be attached directly to proteins or employed using the simple and modular biotin-streptavidin (SA) attachment system, which enables rapid and efficient screening for high sensitivity by tuning their length and composition. We show that these nanoantennas enable the detection and characterisation of distinct conformational changes of AP, including nanoscale conformational changes that occur during substrate catalysis. We also show that the fluorescent signal emitted by the nanoantenna enables complete characterisation of enzyme kinetics in one experiment, including determination of Michaelis-Menten parameters of substrates and inhibitors of AP.

We then explored the universality of the nanoantenna strategy by using a different model protein system. Protein G was shown to interact with antibodies, using a rapid screening strategy for antibody detection. These effective and easy-to-use nanoantennas could potentially be employed to monitor various conformational changes, and our results offer potential for characterising various protein functions.

Keywords: protein function, enzyme kinetics, protein-protein interaction, DNA nanotechnology, nanoantenna, fluorescence spectroscopy, alkaline phosphatase, biotin-streptavidin, Protein G, enzyme inhibitor, biosensor

Table of contents

Résumé i

Abstract iii

Table of contents v

List of tables ix

List of figures x

List of important acronyms and abbreviations xiii

Article xvii

Acknowledgments xviii

Chapter 1 – Introduction 1

- 1.1 Proteins 1
- 1.2 Enzymes 3
- 1.3 Characterising proteins 10
  - 1.3.1 Ultraviolet-visible spectroscopy 11
  - 1.3.2 Fluorescence spectroscopy 13
  - 1.3.3 Nuclear magnetic resonance spectroscopy 17
  - 1.3.4 Electron paramagnetic resonance spectroscopy 18
  - 1.3.5 Circular dichroism spectroscopy 19
  - 1.3.6 Infrared and Raman spectroscopies 20
  - 1.3.7 Electrochemistry 21
  - 1.3.8 Isothermal titration calorimetry 22
  - 1.3.9 What is missing? 24
  - 1.3.10 Introducing “fluorescent nanoantennas” 27

1.4 Alkaline phosphatase 29

1.4.1 Catalytic mechanism of alkaline phosphatase 29

1.4.2 Biological function of alkaline phosphatase..30

1.4.3 Biological substrates of alkaline phosphatase 32

1.4.4 Relation to disease 33

1.4.5 Detection of alkaline phosphatase function – synthetic substrates............................35

1.4.6 Detection of alkaline phosphatase function – biomolecular substrates 37

1.5 Tools employed in this project 40

1.5.1 DNA Nanotechnology 40

1.5.2 Biotin-streptavidin interaction 45

1.5.3 Fluorescent dyes..47

1.5.4 Molecular docking simulations 51

1.5.5 Molecular dynamics simulations...54

Chapter 2 – Fluorescent nanoantennas and their mechanism 56

2.1 Introduction...56

2.2 Tuning the linker...57

2.3 Origin of transient fluorescence spike 67

2.4 Nanoantennas are sensitive to small chemical modifications 70

2.5 FAM binding site on SA and AP 74

2.6 Nanoantennas with different dyes...78

2.7 Discussion 89

2.8 Supplementary figures for Chapter 2 92

Chapter 3 – Characterising conformational states of alkaline phosphatase with fluorescent nanoantennas...102

3.1 Introduction 102

3.2 Fluorescence spike correlates with enzyme-substrate concentration 103

3.3 Extraction of parameters: kinetics and inhibition 107

3.4 Characterising any substrate 111

3.5 "One shot" kinetic fitting saves time and material 117

3.6 Characterising inhibitors 120

3.7 Transition state analogue inhibitors 123

3.8 Unfolded state 127

3.9 Discussion 130

3.10 Supplementary Figures for Chapter 3 138

Chapter 4 – Rapid screening of nanoantennas to monitor other protein functions 149

4.1 Introduction 149

4.2 Screening Protein G and immunoglobulin binding 150

4.3 Discussion 155

Chapter 5 – Overall discussion and conclusions 157

Chapter 6 – Materials and methods 160

6.1 Methods 160

6.1.1 Oligonucleotide synthesis 160

6.1.2 Fluorescence 160

6.1.3 Buffer conditions 161

6.1.4 Software 162

6.1.5 Molecular docking simulations 162

6.1.6 Molecular dynamics simulations 163

6.1.7 Kinetic fitting (K_M, k_{cat}, K_i) 164

6.1.8 Density functional theory computations 166

6.1.11 Presentation of data 167

6.2 List of reagents 167

6.2.1 Enzymes and proteins 167

6.2.2 Substrates and inhibitors 168

6.2.3 Oligonucleotide synthesis reagents 169

6.2.4 Miscellaneous reagents 169

6.3 List of oligonucleotides sequences 170

6.4 Phosphoramidite synthesis of DNA 172

6.5 Script for fitting kinetic data in MATLAB 179

References 181

List of tables

Table 1.1 – Summary of reported properties for fluorescent dyes used in this project………..... 49

Table 3.1 – Michaelis–Menten kinetic parameters of AP with pNPP substrate…………………… 108

Table 3.2 – Determined K_i values for competitive inhibitor P_i……………………………………….. 109

Table 3.3 – Determined K_M and k_{cat} values for various substrates…………………………………... 113

Table 3.4 – Kinetic parameters for amifostine with various effectors……………………………….. 123

List of figures

Figure 1.1. – Protein Structure……2

Figure 1.2. – Enzymatic reactions……5

Figure 1.3. – The effect of substate concentration [S] on initial reaction rate (V_0)……8

Figure 1.4. – Extraction of Michaelis-Menten parameters……8

Figure 1.5. – Jablonski diagram……12

Figure 1.6. – Progress of a typical enzymatic reaction……26

Figure 1.7. – Example of the nanoantenna strategy to sense protein function……28

Figure 1.8. – The catalytic mechanism of AP……30

Figure 1.9. – Programmable DNA nanothermometers……42

Figure 1.10. – Swing arm concept……43

Figure 1.11. – Crystal structure of streptavidin……46

Figure 1.12. – Popularity of fluorescent dyes……48

Figure 1.13. – Overview of molecular docking……53

Figure 2.1. – Relative signal change for different linkers……58

Figure 2.2. – PEG Linker Length……59

Figure 2.3. – PEG nanoantennas are less sensitive to pH variation……60

Figure 2.4. – Tuning the nanoantenna linker for optimal signalling……61

Figure 2.5. – Molecular dynamics (MD) simulation of nanoantenna-SA-bAP complex……62

Figure 2.6. – Optimal nanoantenna length, composition, and ratio……65

Figure 2.7. – Saturating streptavidin with nanoantennas prevents bAP binding……66

Figure 2.8. – The fluorescence spikes only when […]……68

Figure 2.9. – Alternative attachment strategies of nanoantenna to protein also work……69

Figure 2.10. – Effect of various chemical modifiers……72

Figure 2.11. – Effect of FAM connections and isomer……73

Figure 2.12. – Addition of excess biotin……75

Figure 2.13. – Docking of dyes and substrates with proteins……77

Figure 2.14. – Probing different regions of the AP surface with FAM, CAL and Cy3……80

Figure 2.15. – Kinetics of pNPP hydrolysis as monitored by different dyes……………………………….81
Figure 2.16. – Kinetics of bAP attachment onto SA as monitored by FAM nanoantennas…………82
Figure 2.17. – Kinetics of bAP attachment on SA as monitored by different nanoantennas……….83
Figure 2.18. – Molecular dynamics (MD) trajectories of dyes and/or substrate on AP………………85
Figure 2.19. – Excitation and emission spectra of dual-dye dsDNA nanoantenna……………………88
Figure 2.20. – Double-dye competition kinetic signatures………………………………………………………89
Figure S2.1. – Optimal nanoantenna signalling spectra…………………………………………………………92
Figure S2.2. – Tryptophan fluorescence does not detect enzyme catalytic activity……………………93
Figure S2.3. – ANS probe does not detect enzyme catalytic activity……………………………………….94
Figure S2.4. – Versatility of nanoantenna in different buffer conditions…………………………………95
Figure S2.5. – Nanoantenna-protein complex maintains functionality after 100 days………………96
Figure S2.6. – Effect of pH on dye hydrophobicity………………………………………………………………….97
Figure S2.7. – Probing different regions of the protein surface with other dyes……………………….98
Figure S2.8. – Spike above initial fluorescence baseline…………………………………………………………99
Figure S2.9. – Dual-dye controls………………………………………………………………………………………100
Figure 3.1. – Effect of pNPP concentration of fluorescence spike intensity and time…………….104
Figure 3.2. – Nanoantenna fluorescence correlates with the rate of reaction……………………….105
Figure 3.3. – Nanoantenna spike intensity corresponds to reaction rate……………………………….106
Figure 3.4. – Multiple injections of pNPP……………………………………………………………………………107
Figure 3.5. – Fitting data to extract the kinetic parameters…………………………………………………108
Figure 3.6. – Multiple iterations of data fitting result in their convergence……………………………110
Figure 3.7. – Real-time monitoring of any substrate hydrolysed by AP………………………………….112
Figure 3.8. – Real-time monitoring of AP function using LPS substrate…………………………………116
Figure 3.9. – Comparison of methods and error………………………………………………………………….118
Figure 3.10. – Kinetic parameters can be obtained with various dyes……………………………………119
Figure 3.11. – Theoretical nanoantenna kinetic signatures for inhibitors……………………………….121
Figure 3.12. – Screening inhibitors……………………………………………………………………………………..121
Figure 3.13. – States of AP during enzymatic reaction and denaturation……………………………….125
Figure 3.14. – Vanadate and tungstate binding…………………………………………………………………….126

Figure 3.15. – Monitoring protein unfolding with fluorescent nanoantennas……128
Figure 3.16. – Determination of the apparent Gibbs free energy (ΔG) of bAP……129
Figure S3.1. – Area under spike increases linearly with pNPP concentration……138
Figure S3.2. – Saturation binding plot……139
Figure S3.3. – Comparison of classic assay and nanoantenna……140
Figure S3.4. – Streptavidin and nanoantennas do not affect the kinetic parameters……141
Figure S3.5. – Fitting of the fluorescent spikes to extract kinetic parameters of bAP……142
Figure S3.6. – Kinetic parameters determined using different concentrations of substrate……142
Figure S3.7. – The spike intensity decreases with increasing inhibitor concentration……143
Figure S3.8. – bAP batch-to-batch variation accounts for differences in kinetic parameters……144
Figure S3.9. – Variation in baseline after substrate hydrolysis……145
Figure S3.10. – Increase in baseline after the reaction is linked to phosphate……146
Figure S3.11. – Addition of oxyanions does not affect the fluorescence……147
Figure S3.12. – Monitoring unfolding transition of proteins……148
Figure S3.13. – Different FAM connections……148
Figure 4.1. – Rapid screening strategy for identification of functional nanoantennas……151
Figure 4.2. – Cuvette validation of nanoantennas……153
Figure 4.3. – Detection of Antibodies……154
Figure 4.4. – Effect of dilution in control experiments……154
Figure 6.1. – Solid support and detritylation step……174
Figure 6.2. – Composition of a phosphoramidite……175
Figure 6.3. – Coupling step……176
Figure 6.4. – Oxidation step……176
Figure 6.5. – Capping step……177
Figure 6.6. – Cleavage step……178
Figure 6.7. – Deprotection step (#1)……178
Figure 6.8. – Deprotection step (#2)……179

List of important acronyms and abbreviations

λ_{abs}: maximum absorbance wavelength
λ_{em}: maximum emission wavelength
λ_{ex}: maximum excitation wavelength
4-MU: 4-methylumbelliferone
4-MUP: 4-methylumbelliferyl phosphate
5-FAM: 5-carboxyfluorescein (or 5-carboxyfluorescein amidite)
6-FAM: 6-carboxyfluorescein (or 6-carboxyfluorescein amidite)
ADP: adenosine diphosphate
AMP: adenosine monophosphate
ANS: 8-anilinonaphthalene-1-sulfonic acid
ATP: adenosine triphosphate
AP: alkaline phosphatase
bAP: biotinylated alkaline phosphatase
BGP: β-glycerophosphate
bPA: biotinylated Protein A
bPG: biotinylated Protein G
BSA: bovine serum albumin
Cal: Cal Fluor Orange 560
CIAP: calf intestinal alkaline phosphatase
CD: circular dichroism spectroscopy
CoV Ab: SARS-CoV-2 antibodies
Cryo-EM: cryogenic electron microscopy
Ctrl: control
Cy3: Cyanine 3
Cy5: Cyanine 5
Docking: molecular docking
dsDNA: double-stranded DNA
E: enzyme
E_t: total amount of enzyme
E. coli.: *Escherichia coli*
ECAP: *Escherichia coli* alkaline phosphatase
EI: enzyme-inhibitor complex
EP: enzyme-product intermediate
EPR: electron paramagnetic resonance spectroscopy

ES: enzyme-substrate intermediate
ESI: enzyme-substrate-inhibitor complex
$\mathrm{ES}^{\ddagger}$: enzyme-substrate transition state
F6P: fructose-6-phosphate
FAM: carboxyfluorescein (or carboxyfluorescein amidite)
FRET: Förster resonance energy transfer
G6P: glucose-6-phosphate
GCAP: germ cell alkaline phosphatase
GOx: glucose oxidase
GTP: guanosine triphosphate
HRP: horseradish peroxidase
IAP: intestinal alkaline phosphatase
IgG: immunoglobulin G
IR: infrared spectroscopy
ITC: isothermal titration calorimetry
k_{cat}: catalytic rate constant (also called turnover number)
$k_{\mathrm{cat}}/K_{\mathrm{M}}$: catalytic efficiency (also called the specificity constant)
K_{d}: dissociation constant
K_{i}: inhibition constant
K_{M}: Michaelis constant
LPS: lipopolysaccharides
MB: methylene blue
MD: molecular dynamics
NA: nanoantenna
NMR: nuclear paramagnetic resonance
P650: Pulsar 650
PCr: phosphocreatine
PDB: Protein Data Bank
PEG: polyethylene glycol
PEP: phosphoenolpyruvate
PET: photoinduced electron transfer
P: product
$\mathrm{P_i}$: inorganic phosphate
PIFE: protein-induced fluorescence enhancement
PLAP: placental alkaline phosphatase
PLP: pyridoxal 5'-phosphate
pNP: *p*-nitrophenol

pNPP: *p*-nitrophenyl phosphate
PolyT: poly-thymine
PP_i: pyrophosphate
PSer: phosphoserine
Q570: Quasar 570
Q670: Quasar 670
ROX: carboxyrhodamine
S: substrate
SA: streptavidin
SA-AP: streptavidin-alkaline phosphatase conjugate
ssDNA: single-stranded DNA
TAMRA: carboxytetramethylrhodamine
T_M: melting temperature
TNAP: tissue-nonspecific alkaline phosphatase
Trp: tryptophan
TSA: transition state analogue
UV-Vis: ultraviolet-visible spectroscopy
V_i: inorganic vanadate
V_0: initial rate
V_{max}: maximum rate
WT: wildtype
XRC: X-ray crystallography

This thesis is dedicated to my cat, Callie, because she watched me write it.

Article

Harroun, S. G.; Lauzon, D.; Ebert, M. C. C. J. C.; Desrosiers, A.; Wang, X.; Vallée-Bélisle, A.
Monitoring protein conformational changes using fluorescent nanoantennas
Nature Methods **19**, 71-80 (2022)

Acknowledgments

I appreciate and thank Prof. Alexis Vallée-Bélisle for being a great mentor during my doctoral studies here at Université de Montréal. I have learned much from him on the topics of bionanotechnology, characterisation of proteins, and DNA nanotechnology. We have had many fruitful deliberations about presentation of data and how to best draft a paper, plus countless other insightful scientific and non-scientific discussions. He has provided excellent advice about life inside and outside of the laboratory. I am grateful for everything that I have learned from him.

I thank the committee members, Prof. Joelle N. Pelletier and Prof. William D. Lubell, for their time and their questions that have helped refine this work. Likewise, I appreciate that the external examiner, Prof. Anthony Mittermaier from McGill University, was willing to be involved.

Past and present members of the lab are acknowledged for contributions to the project: Dominic Lauzon (script to fit kinetics), Arnaud Desrosiers (some ideas), and Xiaomeng Wang (synthesis). Others are acknowledged for helpful discussions, particularly Carl Prévost-Tremblay and Dr. Guichi Zhu. Liliana Pedro helped in many ways, such as processing chemical orders. Dr. Maximilian Ebert from the Chemical Computing Group helped with the MD simulations.

Support and encouragement from my parents, Peter and Cindy, has been very much appreciated. Carolyne was also supportive during the latter phases of this project.

Funding for my doctoral studies from these organisations via scholarships and/or funding of the project is acknowledged: Alexander Graham Bell Canada Graduate Scholarships-Doctoral (CGS-D) from the Natural Sciences and Engineering Research Council of Canada (NSERC); Bourse de doctorat en recherche from the Fonds de recherche du Québec - Nature et technologies (FRQNT); Bourse alma mater; Bourse de recrutement du Groupe de Recherche Universitaire sur le Médicament (GRUM); Bourse du Fonds Wilrose Desrosiers et Pauline Dunn; Bourses du Département de chimie et Faculté des études supérieures et postdoctorales de l’Université de Montréal; and Le regroupement québécois de recherche sur la fonction l’ingénierie et les applications des protéines (PROTEO).

Chapter 1 – Introduction

1.1 Proteins

Proteins play central roles in life and disease. They are mostly made from amino acids. These consist of a carbon atom bonded to an amino group, a carboxyl group, a proton, and the part that distinguishes one amino acid from another, a side chain (or R group). There are 20 encoded amino acids, typically grouped as those with nonpolar aliphatic R groups (alanine, valine, leucine, isoleucine, glycine, methionine and proline), aromatic R groups (phenylalanine, tryptophan and tyrosine), polar uncharged R groups (serine, threonine, cysteine, asparagine and glutamine), positively charged R groups (lysine, arginine and histidine), and negatively charged R groups (aspartic acid and glutamic acid).[1] Others can be added during protein synthesis, such as selenocysteine,[2] as well as by other post-translational modifications. Two or more covalently attached amino acids is called a peptide.[1] In addition to their biological role in the formation of proteins, some small synthetic peptides display medicinal properties, such as reduction of inflammation.[3, 4] A chain composed of many amino acids attached together is called a polypeptide, and the threshold between a polypeptide and a heavier protein is around ~10,000 g/mol (10 kDa).[1] Proteins can also contain other components, such as lipids, sugars, and metals, which are found in lipoproteins, glycoproteins, and metalloproteins, respectively.[1]

The different functions of proteins are not only derived from their amino acid sequence and other components, but also from their three-dimensional structure.[1] By convention, this structure is defined in a hierarchy of four levels. The primary structure of a protein is the order of covalent bonds therein, mostly the peptide bonds but also disulfide bonds (**Figure 1.1a**).[1] Recurring patterns of the peptide chain that form stable structures within proteins are the secondary structure. These include α-helices, β-sheets, β-turns, and others (**Figure 1.1b**).[1] Next is the tertiary structure, which describes the three-dimensional (3D) folding of the protein (**Figure 1.1c**).[1] Finally, there is quaternary structure, which is applicable when the protein has multiple subunits, such as a dimer with two subunits, trimer with three subunits, and so on (**Figure 1.1d**).[1]

Two identical subunits form a homodimeric structure, whereas two different subunits form a heterodimeric structure.

a

MKQSTIALALLPLLFTPVTKARTPEMPVLENRAAQGDI
TAPGGARRLTGDQTAALRDSLSDKPAKNIILLIGDGMG
DSEITAARNYAEGAGGFFKGIDALPLTGQYTHYALNKK
TGKPDYVTDSAASATAWSTGVKTYNGALGVDIHEKDH
PTILEMAKAAGLATGNVSTAELQDATPAALVAHVTSRK
CYGPSATSEKCPGNALEKGGKGSITEQLLNARADVTL
GGGAKTFAETATAGEWQGKTLREQAQARGYQLVSD
AASLNSVTEANQQKPLLGLFADGNMPVRWLGPKATY
HGNIDKPAVTCTPNPQRNDSVPTLAQMTDKAIELLSKN
EKGFFLQVEGASIDKQDHAANPCGQIGETVDLDEAVQ
RALEFAKKEGNTLVIVTADHAHASQIVAPDTKAPGLTQ
ALNTKDGAVMVMSYGNSEEDSQEHTGSQLRIAAYGP
HAANVVGLTDQTDLFYTMKAALGLK

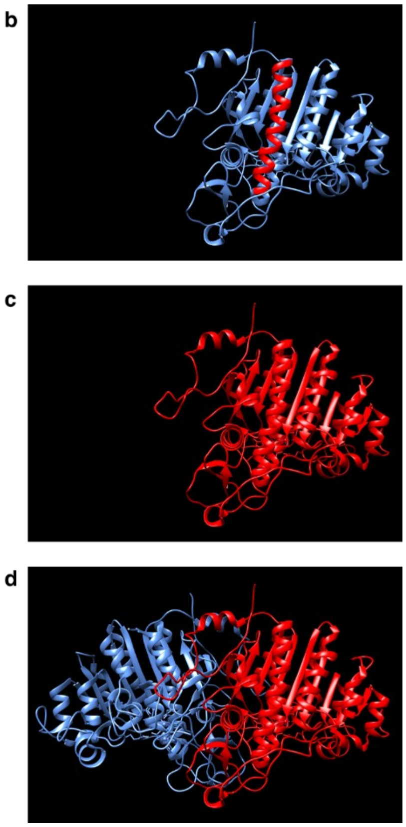

Figure 1.1. – Protein Structure. The crystal structure of bacterial alkaline phosphatase from *Escherichia coli* is shown as an example (PDB: 1ALK)[5]. a) The primary structure is the amino acid sequence (UniProtKB: P00634). b) As an example of the secondary structure, an α-helix is shown in red with the rest of the monomer in blue. c) The tertiary structure is the entire 3D structure of the monomer. d) The quaternary structure is the AP homodimer, with each unit shown in red and blue. The images were generated from the PDB ID listed above.

There are many types of proteins exhibiting a plethora of distinct functions. Some common examples include the strong and flexible fibrous proteins (*e.g.,* α-keratins in horns and collagen in muscle),[1] as well as the more compact globular proteins, such as transport proteins (*e.g.,* Na^+/K^+-ATPase that acts as a sodium-potassium pump across membranes; it is also an enzyme),[6] motor proteins (*e.g.,* myosin involved in muscle contraction),[7] regulatory proteins (*e.g.,* ubiquitin that can alter another protein's function),[8] antibodies or immunoglobulins that bind to a specific antigen (*e.g.,* targeting a virus),[9] and enzymes that catalyse a chemical reaction (*e.g.,* alkaline phosphatase that catalyses the removal of phosphates from various molecules).[10] Many proteins are involved in reversible interactions at a specific binding site with another molecule, called a ligand. Importantly, proteins do not consist of static 3D structures, as proposed in the initial lock and key model (more on this below), but instead can experience different conformations that do not require the breaking of covalent bonds.[1] There has been debate about these conformational changes, whereby two general models have been proposed. In the induced fit model, the ligand first binds to the protein, and subsequently the protein undergoes a conformational change. In the conformational selection model, however, the protein is in an equilibrium of various conformations, one of which can bind the ligand.[11] Overall, it is the conformational changes of proteins enable their function to occur.[1]

1.2 Enzymes

Catalysis – or the speeding up – of a chemical reaction is crucial to life. Many reactions are thermodynamically favourable, but they are very slow. Enzymes are proteins that catalyse specific reactions to enable the functioning of a living organism.[1] Note that while enzymes do speed up a reaction, meaning that equilibrium is reached more quickly, they do not affect the equilibrium of the reactants and products. The study of enzymes, enzymology, is not only crucial to understanding the underlying mechanisms of life,[12] but also to study diseases,[13] to develop new forms of biotechnology,[14] and to make molecular nanomachines.[15] The binding of a substrate (or substrates), *i.e.*, the ligand for an enzyme, at an enzyme's active site enables its (their) transformation to a product (products). This chemical transformation can involve the enzyme's amino acid residues, as well as additional components such as metallic or organic cofactors.[1] Some enzymes display group specificity, such as alkaline phosphatase (AP), which can remove the phosphate group from various substrates. Other enzymes display high specificity, such as glucose oxidase with its substrate, β-D-glucose.[16]

How does an enzyme function? Under biological conditions, crucial reactions often do not readily occur in a reasonable amount of time. This is because the required molecules are not present as unstable charged intermediates and they do not frequently collide in the correct orientation to mediate a reaction. As biological catalysts, enzymes make these reactions happen faster. It was first proposed by Fisher in 1894 that a substrate with a correct size and shape fits into a static active site in an analogous manner to a key fitting into a keyhole. However, it was later determined that enzymes are flexible molecules, which led to Koshland asserting the induced-fit model in 1958, whereby an enzyme changes its shape to mediate substrate binding and stabilisation of the transition state.[1, 16] Recently, it has been proposed that both forms coexist to help enable catalysis, whereby the flexible form as proposed by Koshland has weak affinity for the substrate while the stiff form as proposed by Fisher has a strong affinity for the transition state to prevent irreversible binding of the substrate.[17] Generally, upon binding at the active site, the amino acid side chains and/or cofactors, as stabilised by the rest of the enzyme, provide a chemical environment that is more amenable to the reaction. In other words, binding at the active site drastically lowers the activation energy required for the substrate to form a transition state, whereupon it has an equally likely chance of decaying back to the enzyme-bound substrate or forward to the enzyme-bound product.[1, 16]

Recent work has further added to the understanding of enzyme catalysis. AP, for example, has structurally similar ground states (*i.e.*, substrate- and product-bound states) and transition state. Despite this, AP provides enormous transition state stability to facilitate the reaction, whereas the ground state stability is much weaker (10^{22}-fold). By removing the anionic active site by substitution of a crucial serine residue with glycine or alanine, it was shown that ground state stability increased but no structural rearrangement occurred. Thus, the results revealed that the serine residue enables ground state electrostatic destabilisation that hinders substrate saturation and product inhibition while also partially contributing to the enhancement of the catalytic reaction. Similar effects were observed with a tyrosine phosphatase, suggesting that ground state destabilisation could be a general phosphatase strategy.[18]

The steps of an enzymatic reaction are as follows: the enzyme and unbound substrate (E + S), the enzyme-substrate intermediate (ES), the unstable transition state ($ES^{\ddagger}$), the enzyme-product intermediate (EP), and finally, the enzyme and released product (E + P). This process is visualised in **Figure 1.2**.[1, 19] Each type of enzyme catalyses a specific reaction for a molecule or a category of molecules.

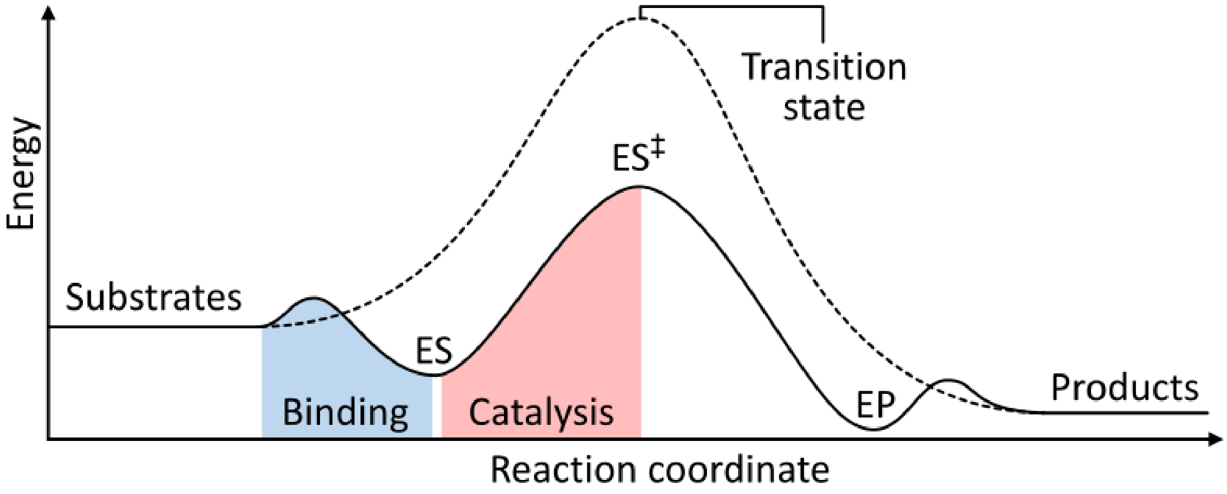

Figure 1.2. – Enzymatic reactions. For an uncatalysed reaction (dashed line), the activation energy to reach the transition state is high. In contrast, binding of a substrate to an enzyme lowers the activation energy for the reaction to proceed. Figure made by Thomas Shafee and reproduced in accordance with the Creative Commons Attribution 4.0 International license.

Michaelis-Menten kinetics provides a mathematical description of the activity of most enzymes and is described below.[20, 21] Increasing concentrations of substrate ([S]) will typically increase the initial rate of the reaction (V_0; units of M s^{-1}).[1] At low [S], the V_0 will increase almost linearly. At increasingly higher [S], however, the increase will be less pronounced until eventually reaching a plateau, which is the maximum rate (V_{max}; also units of M s^{-1}).[1]

An enzymatic reaction can be described by a model with a two-step process. The binding of the substrate is a reversible process (E + S to ES), with rate constants for binding (k_1) and unbinding (k_{-1}). Similarly, the catalysis of the enzyme-substrate complex to the enzyme and products (ES to E + P) is a reversible process (k_2 and k_{-2}):

$$\mathrm{E} + \mathrm{S} \underset{k_{-1}}{\overset{k_1}{\rightleftharpoons}} \mathrm{ES} \underset{k_{-2}}{\overset{k_2}{\rightleftharpoons}} \mathrm{E} + \mathrm{P}$$ **Eqn 1.1**

The product concentration ([P]) is low early in the reaction, so the reverse reaction is ignored:

$$\mathrm{E} + \mathrm{S} \underset{k_{-1}}{\overset{k_1}{\rightleftharpoons}} \mathrm{ES} \xrightarrow{k_2} \mathrm{E} + \mathrm{P}$$ **Eqn 1.2**

Since the rate-limiting step is the breakdown of the ES complex, the V_0 can be described as:

$$V_0 = k_2[\mathrm{ES}]$$ **Eqn 1.3**

In most cases it is difficult to measure [ES], so the rates of formation and breakdown of ES are expressed via the total enzyme concentration ($[\mathrm{E_t}]$):

$$rate\ of\ ES\ formation = k_1([\mathrm{E_t}] - [\mathrm{ES}])[\mathrm{S}]$$ **Eqn 1.4**

$$rate\ of\ ES\ breakdown = k_{-1}[\mathrm{ES}] + k_2[\mathrm{ES}]$$ **Eqn 1.5**

Next, there is the steady-state assumption, whereby it is assumed that the initial rate reflects a constant [ES]. In other words, the rates of formation and breakdown are equal:

$$k_1([\mathrm{E_t}] - [\mathrm{ES}])[\mathrm{S}] = k_{-1}[\mathrm{ES}] + k_2[\mathrm{ES}]$$ **Eqn 1.6**

Rearranging the equation and solving for [ES] results in:

$$[\mathrm{ES}] = \frac{[\mathrm{E_t}][\mathrm{S}]}{[\mathrm{S}] + (k_{-1} + k_2)/k_1} \qquad \textbf{Eqn 1.7}$$

Next, the rate constants are defined simply as the Michaelis constant (K_M; units of M). Also, the V_0 is expressed in terms of [ES], from Eqn 1.3:

$$V_0 = \frac{k_2[\mathrm{E_t}][\mathrm{S}]}{K_\mathrm{M} + [\mathrm{S}]} \qquad \textbf{Eqn 1.8}$$

Finally, since the V_max occurs when [ES] = [$\mathrm{E_t}$], the equation is as follows:

$$V_0 = \frac{V_\mathrm{max}[\mathrm{S}]}{K_\mathrm{M} + [\mathrm{S}]} \qquad \textbf{Eqn 1.9}$$

This is the Michaelis–Menten equation (Eqn 1.9). It describes the kinetics of a one-substrate enzymatic reaction. An important consideration is the significance of K_M. If V_0 in the above equation is at $V_\mathrm{max}/2$, then solving for the Michaelis constant will result in K_M = [S]. In other words, the K_M is the substrate concentration when V_0 is equal to half of the V_max. This is visualised in **Figure 1.3**. To extract the K_M and V_max values, one can employ the classic Lineweaver-Burk double reciprocal plot of $1/V_0$ versus 1/[S], wherein the y-intercept is equal to $1/V_\mathrm{max}$ and the x-intercept equals $-1/K_\mathrm{M}$ (**Figure 1.4a**). It is also possible to use graphing software with non-linear curve fitting, which extracts the Michaelis-Menten kinetic parameters (**Figure 1.4b**).[1]

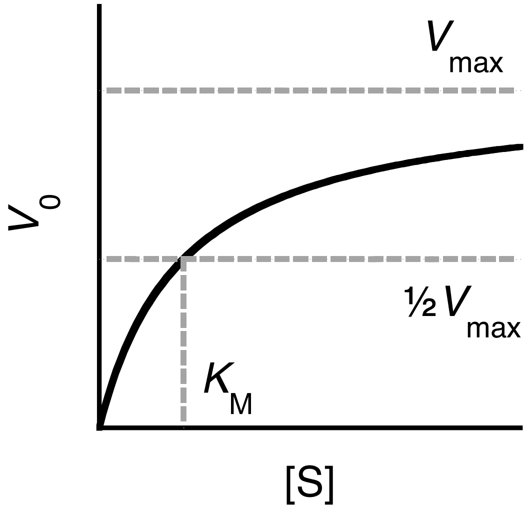

Figure 1.3. – The effect of substate concentration [S] on initial reaction rate (V_0). In a typical enzymatic reaction, the V_0 increases as the [S] increases. At low [S] the increase is almost linear, but much less at high [S]. One typically does not reach the V_{max} in an experiment, but instead a value approaching it.

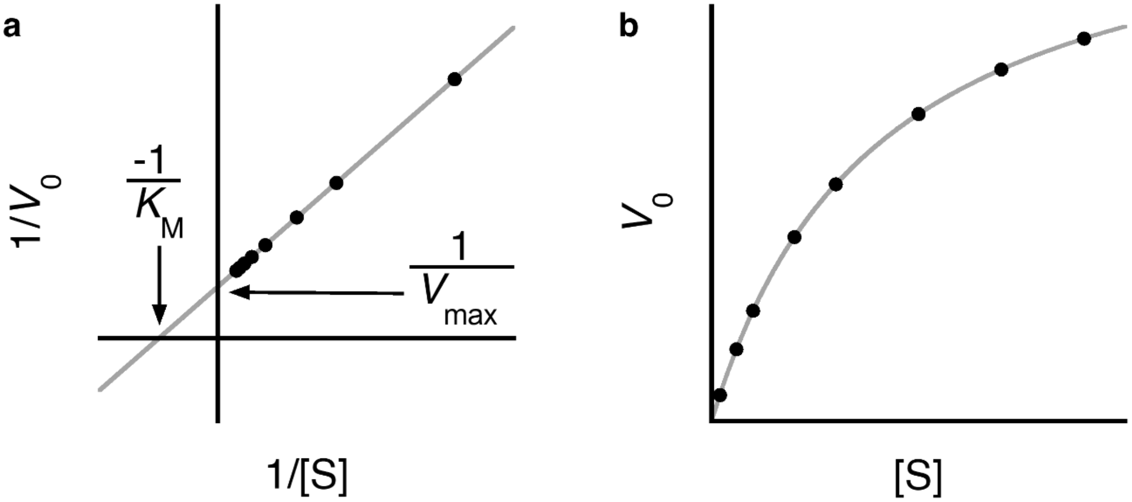

Figure 1.4. – Extraction of Michaelis-Menten parameters. Two common strategies to extract the K_M and V_{max} are (a) the Lineweaver–Burk double reciprocal plot and (b) non-linear curve fitting software.

While the K_M will remain constant, the V_{max} will vary at different concentrations of enzyme (*i.e.*, having more enzyme present will catalyse the reaction more quickly), which makes comparisons difficult. When k_2 is rate-limiting, the V_{max} would thus be:

$$V_{\max} = k_2[\mathrm{E_t}]$$ **Eqn 1.10**

However, while this is true for a two-step reaction, it could differ for a reaction with more steps, wherein another step is rate-limiting. Thus, the turnover number, also called the catalytic rate constant (k_{cat}; units of s^{-1}) is for the rate-limiting step of the reaction at saturation. It indicates the number of substrate molecules converted to product molecules for a given unit of time by a single enzyme molecule that is saturated with substrate. From $[E_t]$ and V_{max}, one can find the k_{cat}:

$$V_{\max} = k_{\mathrm{cat}}[\mathrm{E_t}]$$ **Eqn 1.11**

With the K_M and k_{cat} values, one can further examine the enzyme's catalytic efficiency, also called the specificity constant, which is simply k_{cat}/K_M (units of $M^{-1}\ s^{-1}$). When $[S] \ll K_M$, this is the rate constant for the conversion of E + S to E + P, although when $[S] \gg K_M$ the reaction becomes independent of [S] and approaches the V_{max}. Note that although different combinations of k_{cat} and K_M can give the same k_{cat}/K_M, it has a diffusion-controlled upper limit of 10^8 to $10^9\ M^{-1}\ s^{-1}$.[1]

Lastly, a brief review of the types of enzyme inhibition and how they affect the kinetic parameters of the reaction. Of the three types, competitive inhibition is most relevant to this project. The inhibitor binds to the enzyme, typically the active site, to form an enzyme-inhibitor (EI) complex. This will increase the apparent K_M, since it shifts the equilibrium to the left (*i.e.*, Le Chatelier's principle), but will not affect the V_{max}, whereby increased [S] ought to reach the same value. There is also uncompetitive inhibition, whereby the inhibitor binds to the ES complex, and the K_M and the V_{max} will both decrease. The decrease of the apparent K_M, indicative of a higher affinity for the substrate, is counterintuitive. However, it is because the formation of the enzyme-substrate-inhibitor (ESI) complex reduces the concentration of the ES complex and shifts the equilibrium to the right. In non-competitive inhibition, the inhibitor binds to the enzyme, which reduces its activity but not the ability of the substrate to bind. Thus, the $V_{\max}$ decreases, but the K_M is unaffected.[1] By studying an enzyme-substrate system with and without the inhibitor, and therefore its effect on the kinetic mechanism via the Michaelis-Menten parameters, one can determine the mode of inhibition.

1.3 Characterising proteins

Characterising the structure and function of proteins facilitates their study. Knowing the sequence of a protein, its primary structure, is among the first steps. This involves determining the amino acid composition and their order. This can be done via sequencing the corresponding coding DNA to deduce the protein sequence that would be created during translation,[22] or by chemical and enzymatic degradation steps to create smaller fragments followed by mass spectrometry (MS) to piece together the sequence via points of overlap.[23, 24] Knowing a protein's 3D structure, including its secondary, tertiary and quaternary structure, is also important.[1] This 3D structure can be determined by various methods, including X-ray diffraction (XRC)[25] and nuclear magnetic resonance (NMR) spectroscopy.[26] Overall, XRC faces fewer challenges in determination of the structure of larger proteins, whereas NMR spectroscopy enables structural determination in solution and can monitor the various states of the protein.[1] More recently, technical and computational advances have brought cryogenic electron microscopy (cryo-EM) to prominence, and this technique continues to undergo development.[27]

Once a protein's 3D structure is known, the functions of its various components can be examined by different methods, including computational simulations. For example, molecular docking may predict protein-ligand interactions,[28] and molecular dynamics may examine the movements of a protein.[29] It is also possible to study the interactions of proteins with other molecules, such as protein-protein interactions.[30] Among the many interesting aspects of proteins that are worthy of study, this thesis focusses on the experimental detection of conformational change during protein-ligand interaction, particularly in the contexts of enzyme-substrate and enzyme-inhibitor complexes. Protein-protein interaction is another topic explored herein. In this section, various methods to characterise protein function are reviewed, with an emphasis on the short-lived transient states that are pertinent to enzyme-substrate complexes.

The purpose of this section is to provide an *overview* of various protein characterisation methods. In accordance with that, there may be exceptions to the points raised below. Also important is that, depending on the relevance of various techniques to this thesis, different amounts of detail are provided for each technique's theoretical background. Most examples discussed below focus on alkaline phosphatase (AP) because it is the main enzyme studied herein.

1.3.1 Ultraviolet-visible spectroscopy

Ultraviolet-visible (UV-Vis) spectroscopy is based on molecular absorption of energy in the form of light, which causes the molecule to pass from its lowest energy electronic ground state (S_0) to a higher energy excited state (S_1, …, S_n) (**Figure 1.5**).[31] Typically, this process involves a transition from the highest occupied molecular orbital (HOMO) to the lowest unoccupied molecular orbital (LUMO). This process is quantised, meaning that the amount of energy absorbed is exactly equal to the energy difference of the ground and excited states. Furthermore, for a given molecular species, the sample will contain a collection of its various vibrational and rotational states, which can also be excited to higher states (v_1, v_2, v_3, and so on). However, because each state differs only slightly in energy, the UV-Vis spectrophotometer cannot resolve each one. It is for this reason that a UV-Vis spectrum typically appears as a broad band that is centred near the main transition. The position of this band, *i.e.*, the maximum absorbance wavelength (λ_{abs}), will differ from one molecule to another, thus making UV-Vis spectroscopy useful to determine concentration and to follow chemical reactions.

One can quantify a sample by using a molecule's molar absorptivity (a constant for each chemical species), the known length of the sample cell, and the measured absorbance value. This is achieved by the Beer-Lambert Law, given by the equation:

$$A = \log\left(\frac{I_0}{I}\right) = \varepsilon c \ell \qquad \textbf{Eqn 1.12}$$

Where, A = the absorbance, I_0 = the intensity of light incident on the sample cell, I = the intensity of light leaving the sample cell, ε = molar absorptivity, c = molar concentration of the sample, and ℓ = the length of the sample cell.

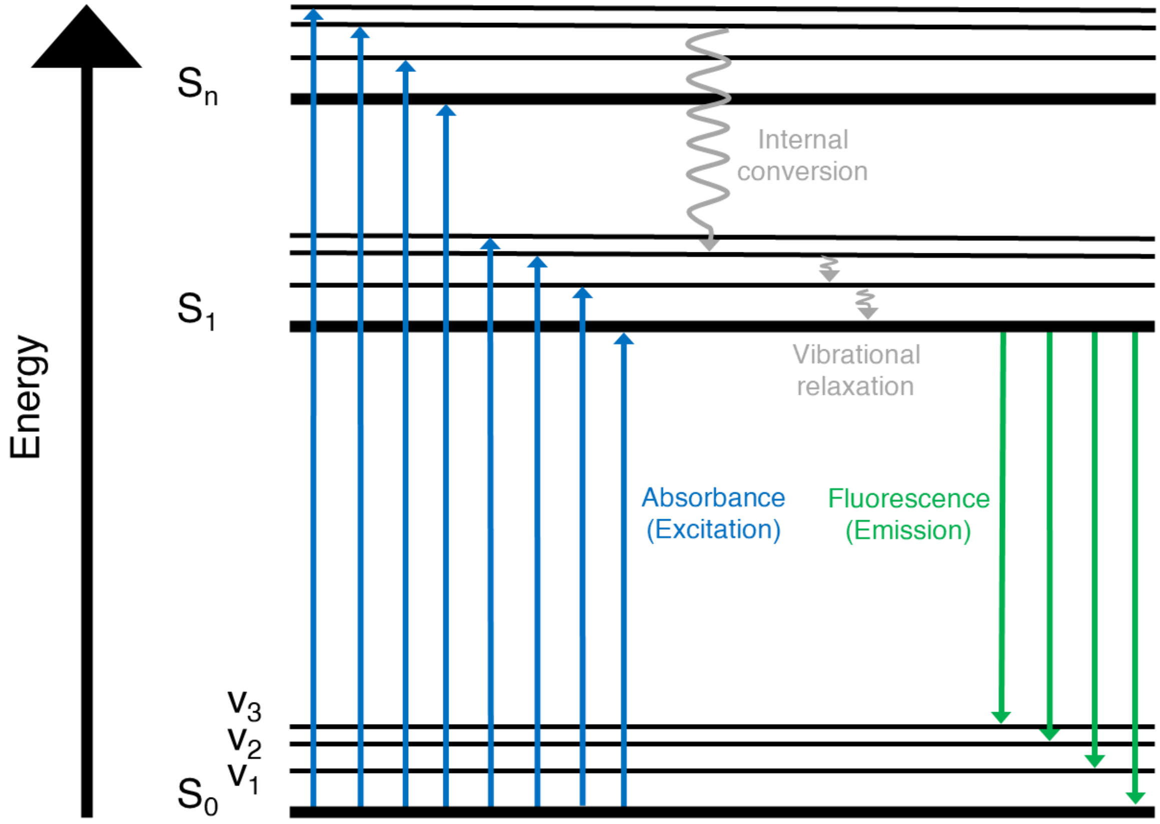

Figure 1.5. – Jablonski diagram. Representation of the absorbance and fluorescence processes, as well as non-radiative internal conversion and vibrational relaxation. Figure based on a similar figures in refs [23, 32].

UV-Vis spectroscopy is used for a wide variety of applications in protein science. One typical application is for the enzyme-linked immunosorbent assay (ELISA).[23] The basic format of a sandwich ELISA assay is as follows: the surface is coated with an antibody that recognises a target antigen. Any remaining exposed areas on the surface are then blocked, such as by bovine serum albumin (BSA). Next, the sample is introduced. If present, the target antigen will bind to the surface-bound antibody. Then, a secondary antibody is introduced, and it will only bind if the antigen is present. This secondary antibody contains an enzyme label, such as AP. The role of the enzyme is to covert a substrate with no UV-Vis signal to a colorimetric product that is detectable by UV-Vis spectroscopy (or another method). For example, *p*-nitrophenylphosphate (pNPP) is hydrolysed by AP to yellow *p*-nitrophenol (pNP; $\lambda_{abs} = 405$ nm) and inorganic phosphate (P_i).[33] This indicates the presence (or not) of the second antibody conjugated with AP. Thus, UV-Vis spectroscopy and ELISA are a powerful combination for practical analytical applications, sample quantification, and to characterise antibody-antigen interaction. However, it is less useful for characterisation of transient states. In the context of AP kinetics, real-time analysis by UV-Vis spectroscopy is widely used but limited to synthetic substrates that can provide a colorimetric signal change upon generation of their product, as is the case with pNPP.[34] Thus, despite its widespread availability and straightforward procedures, UV-Vis faces the limitation of requiring a non-native substrate for the characterisation of protein function in real-time.

In this project, UV-Vis spectroscopy was employed to quantify nucleic acids after their synthesis and purification. This involved determining the molar absorptivity for a given DNA sequence ($\lambda_{abs} = 260$ nm), plus consideration of the molar absorptivity for various functional moieties. It was also used to monitor AP-mediated hydrolysis of pNPP to pNP.[34]

1.3.2 Fluorescence spectroscopy

This section begins with the principles of fluorescence spectroscopy.[23, 32, 35] Luminescence is the process whereby a chemical or material emits light. Several types of luminescence exist, such as chemiluminescence and photoluminescence. The latter includes phosphorescence and fluorescence, the second of which is the focus here. Fluorescence is illustrated in the Jablonski diagram (**Figure 1.5**). Firstly, by absorption of a photon, a molecule or other chemical species is excited from its electronic ground state (S_0) to its first excited state (S_1) or to a higher state (S_n). Next, the molecule will lose its excess energy, either by non-radiative transitions or by fluorescence emission. Non-radiative transitions include internal conversion (IC), which is a transition from the lower vibrational energy levels of an excited state to the higher vibrational energy levels of the lower state, as well as by vibrational relaxation (VR), whereby the excited molecule relaxes to the lowest vibrational energy levels of the excited state by collision with the solvent molecules. These do not result in the emission of a photon. On the contrary, fluorescence provides a signal via the emission of a photon upon relaxation from of S_1 to S_0. It is typically from the lowest vibrational energy level of S_1 because the internal conversion and vibrational relaxation processes are much faster than that of fluorescence. Furthermore, a fluorescence spectrum typically has one band with many closely spaced lines for the transition from the lowest level of S_1 to different vibrational levels of S_0. It is important to note that the excitation energy is greater than the emitted energy, *i.e.*, the excitation wavelength is shorter than the emission wavelength. For example, the maximum excitation wavelength (λ_{ex}) of fluorescein is ~498 nm, and its maximum emission wavelength (λ_{em}) is ~520 nm. This difference is called the Stokes shift. Since some energy is lost due to the non-radiative transitions, fluorescence emission shifts toward the red relative to the excitation wavelength.

A fluorophore is a molecule that can emit fluorescence. All molecules can absorb light, but the reason that not all fluoresce is because that for many their structure enables a greater rate of non-radiative emission pathways compared to the rate of fluorescence emission. From this, we derive the quantum yield (QY), which is the ratio of the molecules that fluoresce to the total number of excited molecules; *i.e.*, the ratio of emitted photons to absorbed photons.[23, 32] In most applications, a higher QY is desirable. The most common structural feature of fluorophores is an aromatic ring. Some other aliphatic molecules and those with highly conjugated double-bond structures can emit fluorescence too, but they are less common. While some heterocyclic compounds do not fluorescence, those with multiple fused rings often do emit fluorescence. The fluorescence can be tuned, that is, shifting of the λ_{ex} and the λ_{em}, as well as the intensity of fluorescence, by chemical substitutions on the aromatic rings.[36] Moreover, rigid molecules also tend to exhibit greater fluorescence, as evidenced by their greater QY.[32] Various natural and synthetic fluorophores are discussed in greater detail in section 1.5.3.

Just as one can study enzyme kinetics in real-time by monitoring product generation with UV-Vis spectroscopy, a similar strategy is also possible with fluorescence spectroscopy. In a typical experiment, the substrate does not provide a fluorescence signal, but its product molecule does. With AP, for example, this can be achieved via non-fluorescent 4-methylumbelliferylphosphate

(4-MUP), which generates fluorescent 4-methylumbelliferone (4-MU) and P_i.[37] A fluorescent leaving group can also be adapted for use with another enzyme. For example, with *Escherichia coli* (*E. coli*) β-glucuronidase, the substrate 4-methylumbelliferyl-β-D-glucuronide generates 4MU and D-glucuronic acid.[38] It is possible as well to label a substrate with a fluorophore and quencher pair. For instance, when collagenase cleaves a specific peptide sequence labelled with fluorescein and dabcyl, their separation provides a fluorescence signal increase.[39] Overall, the procedures for fluorescence spectroscopy are roughly the same as for UV-Vis spectroscopy. Fluorescence instrumentation is widely available, although typically more expensive than UV-Vis instruments, but has the benefit of a lower limit of detection. However, there is also the analogous problem concerning the necessity of synthetic substrates to provide a fluorescent signal change. This often precludes the study of biomolecular substrates.

The emission signal obtained from a fluorescent dye is often sensitive to the dye's chemical environment. Thus, covalently attaching a fluorophore is another way to monitor a protein's function via its conformational change, ligand binding, catalysis, and other events. For example, the Wiskott Aldrich Syndrome Protein (WASP) binds to a GTPase (Cdc42) when it has guanosine triphosphate (GTP) bound but not with guanosine diphosphate (GDP) bound. By attaching an environmentally-sensitive cyanine dye to an introduced cysteamine residue on a fragment of WASP, it was possible to monitor its binding to the GTP-activated Cdc42 protein as evidenced by a substantial increase in fluorescence.[40] Fluorescent moieties can also be designed for specific recognition. For instance, WW domain is a protein domain (*i.e.*, a self-stabilising region of the polypeptide chain) that can selectively bind phosphorylated proline-rich sequences. A fluorophore-containing (stilbazole) phosphate-binding motif based on a zinc complex of 2,2′-dipicolylamine was attached to WW domain. This system could detect a specific bisphosphorylated peptide even in the presence of a monophosphorylated peptide or molecules such as adenosine triphosphate (ATP) and adenosine diphosphate (ADP). It was then applied to further detect cyclin-dependent protein kinase 9 (CDK9) phosphorylation of a monophosphorylated peptide, which generates a bisphosphorylated peptide.[41] Another strategy employed both covalent and non-covalent interactions. Conjugates were prepared that contained a quencher dye and a Tris-based histidine tag (his-tag) binding moiety. Type I interferon receptor ectodomains were covalently labelled with a fluorophore, followed by the site-specific binding of the quencher-containing conjugate via a his-tag. Upon ligand binding, a change in fluorescence signal was observed.[42]

Despite the advantages provided by labelling proteins with fluorophores, they can disturb protein function. One study examined the S-peptide, which has been employed as a model system for intrinsically disordered peptides. It was labelled with a fluorophore (Atto655) at the N-terminus and an additional tryptophan (Trp) residue as a quencher at the C-terminus. Experimental observations and molecular dynamics (MD) simulations indicated that the Atto655 and Trp experience π-stacking interactions, thereby shifting the conformational and dynamical properties of the peptide. More specifically, the disordered conformational state shifted to a semi-stable fold with β-sheet structures.[43] Fluorescent labelling can also affect enzyme function. For example, fluorescein was covalently attached near the active site of a mutant β-lactamase to enable detection of the conformational changes upon binding of β-lactam antibiotics. Although its purpose was to serve as a biosensor for antibiotic detection, and not for kinetic characterisation, it should be noted that this modification decreased the $k_{\mathrm{cat}}/K_{\mathrm{M}}$ of the enzyme.[44]

Another specialised fluorescence method to monitor protein function via conformational change is Förster resonance energy transfer (FRET).[45, 46] In this method, a protein is labelled with two fluorophores, called the donor and acceptor, such as TAMRA and Cy5, respectively.[47] Both have distinct excitation and emission maxima, but crucially, the emission spectrum of the donor dye must substantially overlap with the excitation spectrum of the acceptor dye to enable energy transfer. Thus, when the fluorophores are in proximity, applying light at the donor's excitation wavelength will result in emission at the acceptor's emission wavelength. However, if the fluorophores are spatially separated, this effect will not be observed. FRET typically enables distance measurements over the 3-9 nm range.[45] Therefore, FRET has been employed to study many enzymes that undergo large conformational changes, such as G-protein-coupled receptors (GPCR),[12] DNA helicase II (UvrD),[48] ATP synthase,[49] dihydrofolate reductase (DHFR),[50, 51] and lysozyme.[52] However, FRET is not applicable to proteins that do not experience a large conformational change, such as AP, and when it is applicable, it requires the knowledge of where to label the protein (*i.e.*, which two amino acids).

To avoid the use of an external light source due to the possibility of photobleaching and high background noise, there is also bioluminescence resonance energy transfer (BRET). Instead of a light source, the bioluminescent enzyme luciferase generates the photons. BRET has been employed, for example, to monitor protein conformational changes inside cells. In one study, a biosensor was based on a GPCR with *Renilla* luciferase (RlucII) as a donor and a fluorophore inserted at different sites as an acceptor. The strategy could detect the binding of various types of ligands and provided mechanistic information about the protein.[53] The BRET-based biosensor strategy could also be employed to study the distinct conformational changes of various receptors inside cells.[54]

Instead of covalent labelling with fluorescent dyes, one can also monitor protein conformational changes by intrinsic tryptophan fluorescence. While this is an excellent method for large conformational changes, such as protein folding-unfolding,[55] it is not usually applicable to study enzyme kinetics. Some dyes, such as 8-anilinonaphthalene-1-sulfonic acid (ANS), display a fluorescence signal increase upon non-covalent interaction with proteins. However, while ANS is also used to monitor protein folding-unfolding, it is not typically used for enzyme kinetics.[56] In a recent example, ANS was employed to screen inhibitors of the SARS-CoV-2 main protease (3C-like protease). Binding of a natural product inhibitor (*e.g.*, baicalein and rutin) displaces ANS, and in turn, decreases the fluorescence signal.[57]

1.3.3 Nuclear magnetic resonance spectroscopy

NMR spectroscopy can be employed as a high-structural-resolution technique to characterise protein structure, or as a high-temporal-resolution technique to characterise the function of proteins and their transient states. This method provides information about the number of magnetically distinct atoms and their environment when exposed to a magnetic field. It is used to detect nuclei displaying a spin, most commonly ^{1}H or ^{13}C, but ^{15}N, ^{31}P, and others are also possible.[31] Solution NMR has enabled the study of motion in enzymes under physiologically relevant aqueous conditions.[58, 59] Moreover, although NMR had previously faced challenges to study proteins larger than ~50 kDa, various strategies have been developed to overcome this limitation.[59, 60] NMR can study a variety of timescales, including those for protein folding and the function of enzymes that occur on the order of µs to ms, as well as faster events like sidechain rotation on the ns timescale.[59] NMR characterisation of enzymatic conformational change has been demonstrated with human cyclophilin A (CypA), for example. This enzyme catalyses the *trans*-to-*cis* isomerisation of peptide bonds containing a proline residue and another amino acid. Using NMR, it was possible to study the reaction kinetics and the residues involved in peptide binding and isomerisation.[61] Other studies have used NMR spectroscopy to follow substrate or product concentration.[62, 63] Benefits of NMR spectroscopy relative to other techniques include that it can characterise protein conformational change with atomic resolution,[64] and that it can obtain structural, kinetic and thermodynamic properties simultaneously.[65] Detriments, however, are that it is a specialist technique requiring complicated data analysis, and it is hardly amenable to high-throughput screening,[66, 67] although there have been advances in this domain.[68]

In the context of AP, NMR spectroscopy was employed in the early days to study the enzyme's metal ion-binding sites.[69] However, there have not been recent studies of AP function with atom-specific resolution. Despite this, NMR has also been used to study rates of reaction. In one paper, a phosphate-containing substrate was designed that contained both fluorescein and perfluorinated dendrimers attached to a silica nanoparticle. This environment quenched the fluorescence of fluorescein, and also the ^{19}F NMR signal of the perfluorinated dendrimers via restriction of molecular rotation. Hydrolysis of the substrate releases both components, which are detectable by fluorescence and NMR spectroscopies. Both detection strategies displayed the same kinetics.[70]

1.3.4 Electron paramagnetic resonance spectroscopy

Electron paramagnetic resonance (EPR) spectroscopy is similar to NMR spectroscopy, but it differs whereby instead of exciting the spins of atomic nuclei, it excites the spins of electrons. The signal arises from unpaired electrons. EPR can detect paramagnetic species, such as Fe^{3+}, Cu^{2+}, and proteins with semiquinones or tyrosyl radicals. In the absence of these, however, it is necessary to label a protein with spin labels; this process is called site-directed spin labelling (SDSL). In a manner analogous to labelling with fluorescent dyes, these spin labels, typically containing nitroxide, can be attached by various coupling chemistries, often to cysteine side chains. They can also be designed to display sensitivity to various conditions (*e.g.*, pH).[71]

EPR spectroscopy has been employed to study the structural dynamics of AP from marine bacteria, *Vibrio* sp. This study found that the mobility of a helical region near the active site of AP is related to its catalysis and efficiency.[72] Recently, it was also demonstrated for the first time that it is possible to monitor AP activity in real-time by EPR with a paramagnetic substrate.[73]

1.3.5 Circular dichroism spectroscopy

Circular dichroism (CD) spectroscopy can be employed to study the electronic transitions of molecules. Electronic CD is the focus here, although there are also more specialist techniques, such as vibrational CD and fluorescence-detection CD.[74] Plane-polarised light consists of two components of equal magnitude; one rotates counter-clockwise and is called left-handed (L), and the other rotates clockwise and is called right-handed (R). If they are absorbed differently in a sample, this is known as elliptical polarisation.[74, 75] Chromophores within chiral structures and asymmetric environments may absorb light in this manner.[74, 75] The most commonly used method involves continuously switching between L and R light.[74] With CD, it is possible to detect various chromophores in proteins, such as peptide bonds, aromatic amino acid side chains, disulfide bonds, and various cofactors.[74, 75] Moreover, the CD spectral features enable one to have a quantitative estimate of a protein's secondary structure, such as α-helix, β-sheet, and random coil structures, for example.[74, 75] Thus, one can monitor how their relative proportions differ during conformational change. While CD lacks the high resolution structural information provided by XRC or NMR, it is a good technique to rapidly monitor changes under physiologically relevant conditions.[74]

In an example relevant to this project, wildtype (WT) and two mutants of *Escherichia coli* (*E. coli*) AP were studied. The WT and one mutant maintained the homodimeric structure, while the other mutant was instead present as a monomer. By CD spectroscopy, the study observed that the WT and mutants all had similar CD spectra, indicating that the mutation affected the quaternary structure (*i.e.*, dimer or monomer) but not the secondary structure. Furthermore, CD spectroscopy enabled determination of their different melting temperatures (T_M).[76]

1.3.6 Infrared and Raman spectroscopies

Vibrational spectroscopic methods, such as infrared (IR) spectroscopy and Raman spectroscopy, enable one to study molecular vibrations. As complementary techniques, they detect different vibrational symmetries, whereby some vibrations will be IR-active and Raman-inactive, or *vice versa.* In both cases, they provide a rich vibrational fingerprint of the analyte, rather than the single peak observed in fluorescence or absorbance spectroscopies, but they do not provide the same level of detail of protein secondary structure as XRC and NMR.[77]

IR spectroscopy can estimate the relative content of α-helix *versus* β-sheet structures, for example, via changes of the "amide I" band that arises mainly due to C=O stretching.[78] IR spectroscopy can also identify amino acids and functional groups, although obtaining local information is typically only possible for relatively uncommon components (*e.g.,* S–H stretching of cysteine) or those that are sensitive to their microenvironment (*e.g.,* tyrosine).[79] It is also possible to incorporate environmentally sensitive probe moieties with distinct bands, which is analogous to attaching a fluorophore to a protein.[80] Thus, IR spectroscopy is not an ideal method for overall structural characterisation, although it can be useful to rapidly monitor individual marker bands of a conformation or to monitor an amino acid upon subjecting a protein to different environments, such as temperature or pH, as well as time-dependent changes induced by an effector. Typically, the difference spectrum of a sample before and after a change of conditions is used to avoid introducing an artifact, since experimental error between samples could be larger than spectral changes upon a change of conditions in a single sample.[79] Thus, in the difference spectrum, all non-changing bands will become a baseline, while increases or decreases of band intensity can easily be distinguished.

In one example relevant to this project, IR spectroscopy was employed to study the thermal unfolding of AP with and without (apoAP) bound metal ions. With an increase of temperature, there was an increase in β-sheet bands, a decrease in an α-helical band, and a higher T_M for AP with metal ions compared to apoAP.[78] It is also possible to monitor the effects of enzymatic reactions by IR spectroscopy. This is typically achieved by employing "caged" substrates, such as adenosine triphosphate (ATP) with a photo-cleavable component that prevents the reaction from occurring until the desired time. Instead of adding the substrate, which could introduce artifacts to the difference spectrum, this method enables recording of the before and after spectra for the same sample.[79, 81] In a study of AP with caged ATP, there were minimal changes to the enzyme's backbone bands before and after the reaction, suggesting that binding of the product/inhibitor phosphate did not induce significant conformational changes.[82]

Many of the principles of characterising protein function with IR spectroscopy also apply to Raman spectroscopy. On a practical level, the main difference is that while Raman spectroscopy provides an overall weaker signal intensity than IR spectroscopy and there is sometimes a strong fluorescence background, an important advantage is that the intense H–O–H bending vibration of water that plagues IR spectra is not a problem in Raman spectra.[83]

In addition to monitoring changes to the enzyme itself, it is also possible to monitor the conversion of a substrate to products via their vibrational fingerprints. With the AP enzyme, this has been achieved with the substrate fosfosal, which has a much weaker Raman spectrum than the enzymatic reaction's product molecule, salicylic acid.[84] Other studies have employed surface-enhanced Raman spectroscopy (SERS), which relies on the enormous enhancement of the Raman spectra of molecules adsorbed on gold or silver nanoparticles. For example, the substrate 5-bromo-4-chloro-3-indolyl phosphate (BCIP) does not undergo a significant signal enhancement, but the product molecule after hydrolysis by AP displays an intense SERS spectrum.[85, 86] One detriment to these techniques, however, is that while they could work for detection of AP and its kinetic characterisation with these substrates, such characterisation is limited to substrates that display these differential spectral properties and which may not be of biological interest.

1.3.7 Electrochemistry

The most well-known electrochemical sensing platform of protein function is the glucose meter. Although various designs exist, the principle involves oxidation of glucose to gluconic acid by the enzyme glucose oxidase (GOx), which is coupled with a cyclic redox reaction that can be detected by an electrode.[87] Using electrochemistry, there have been some studies involving protein conformational change, but these have typically been for molecules that undergo large conformational changes, such as lysozyme.[88] Other proteins have been studied too, whereupon denaturation exposes their redox-active residues (*e.g.,* cysteine, tryptophan, tyrosine, methionine, histidine, and disulfide bonds).[89, 90] Generally speaking, electrochemical assays are often limited to detection of the presence of proteins or their substrates, rather than characterisation studies. This is illustrated below for the case of AP.

Some electrochemical methods can monitor enzymatic function directly. For example, amperometric sensing of AP catalytic function on a graphite screen printed electrode. AP hydrolyses ascorbic acid 2-phosphate to ascorbic acid,[91] or alternatively, catechol monophosphate to catechol.[92] In both cases, the enzymatic products are electroactive, and the detection strategy is based on their oxidation. A more recent work developed a more sensitive strategy with a substrate that contains ferrocene and phosphate moieties. Removal of the phosphate by AP causes a breakdown of the hydrolysed product molecule, and in turn, release of the electroactive ferrocene component.[93] Other methods have relied on indirect detection of AP activity, such as hydrolysis of *p*-hydroxyphenyl phosphate to hydroquinone, which is oxidised to quinone but reduced back to hydroquinone via GOx in the presence of glucose, thereby amplifying the signal.[94] Another indirect amplification strategy is based on hydrolysis of phenyl phosphate to phenol, which is then oxidised by immobilised tyrosinase to quinone, and in turn, is oxidised to catechol on the surface and cycled back to quinone by the tyrosinase.[95] These electrochemical methods have the advantage of low cost instrumentation and low sample volume (*i.e.*, several µL), but they all suffer from the same detriment as fluorogenic substrates in that they rely on the specific electroactive properties of the substrates or their products. Therefore, while these methods are suitable for the detection of AP, they are typically unsuitable for the characterisation of this enzyme's kinetics with its natural substrates.

1.3.8 Isothermal titration calorimetry

Isothermal titration calorimetry (ITC) is a technique to study the binding interactions of two components, often called the host and the guest. In an environment at a constant temperature, the released (exothermic) or absorbed (endothermic) heat upon binding is measured. The heat change is converted to units of power, based on the amount needed to maintain a constant temperature, and is plotted against time for each injection, thereby providing quantitative information about the reaction's thermodynamics.[96]

An emerging application of ITC is to study enzyme kinetics. This is because most enzymatic reactions release or absorb heat, and consequently, employing ITC avoids the necessities of signal-generating substrates needed for various methods, clear solutions for spectroscopy, coupled reactions for electrochemistry, and post-reaction processing of the sample.[97] Two general strategies to characterise enzyme reaction kinetics by ITC include multiple injection and single injection. The former involves multiple injections of varying concentrations of substrate, while the latter involves a single injection of a large concentration of substrate.[97, 98] The multiple injection method can determine Michaelis-Menten kinetic parameters in manner analogous to increasing concentrations of substrate detected by UV-Vis or fluorescence spectroscopies, while the single injection method involves mathematically modelling the signal from one addition. Thus, while it requires the use of less enzyme, the method does require more data manipulation and the requisite skills to implement appropriate fitting scripts.[97, 99]

One of the main limitations in deriving enzymatic reaction kinetic parameters from ITC peaks has been, traditionally, that for short reactions taking place on the scale of seconds to tens of seconds, it is difficult to deconvolute the kinetics of the reaction from the kinetics of the instrument response. Thus, the experimental and calculated peaks for a single ITC reaction will differ, hindering accurate extraction of kinetic information. Recent works, however, have addressed this problem. One approach, based on the multiple injection strategy, employed a calibration method for the given instrument and found that the initial rate of the ITC data corresponds to the reaction velocity upon injection. With this approach, it is necessary to determine the enthalpy (ΔH) of the reaction, which is analogous to one having to determine the molar extinction coefficient (ε) for kinetic characterisation by UV-Vis.[100, 101] A more recent study based on the single injection strategy incorporated the post-reaction heat transfer and the electronic response of the instrument into the mathematical model.[102] In both cases, the methods could obtain kinetic parameters of enzymatic reactions that agreed with standard spectroscopic approaches.[100, 102] The latter method was subsequently adapted to characterise inhibitors by having substrate and inhibitor in the syringe, which are injected to the calorimeter containing the enzyme. Thus, consecutive injections result in each reaction having the same amount of substrate but increasing amounts of built-up inhibitor. By modelling each reaction by the single injection method, one can derive the inhibitory properties of the inhibitor (K_i). A major benefit of this method is that an inhibitor can be screened much more rapidly than by multiple experiments with the necessary steps of cleaning and equilibrating the ITC instrument between each concentration of inhibitor.[103] It has also been adapted for the kinetics of inhibitor binding.[104]

1.3.9 What is missing?

Anecdotally, I have observed that many scientific papers in the fields of analytical chemistry, detecting protein function, biosensors, and so on, will say that the method developed therein for a specific task is superior to every other available method. Sometimes the claims might be correct; other times they seem like an obligatory dogma chanted in the introduction of every paper coming from that research community ("Our method is more convenient than [insert rival method here]"). The claim might even be supported by an out-of-date citation that no longer represents the forefront – or never even did – of that putatively inferior rival technique! I am probably guilty of this style of writing somewhere in this thesis. The purpose of this section, therefore, is not to expound why the method developed herein is better in every way compared to every other option. Instead, this section categorises the abovementioned methods, takes note of what is missing, and then considers how this project partially fills that gap.

The first category includes strategies to monitor the substrate or product. With these, one typically monitors an enzymatic reaction in real-time by detecting the rate of product generation by UV-Vis[34] or fluorescence spectroscopy.[37] Note that more examples of substrates for these techniques for AP are discussed later in section 1.4.5. Electrochemistry,[92-95] as well as NMR,[70] EPR,[73] and Raman[84-86] spectroscopic strategies have also been demonstrated. Their commonality, however, is that these strategies all typically rely on the specific properties of certain substrates, which precludes general methods for real-time characterisation of biomolecules. This has necessitated the development of substrate-specific assays[105] or labourious time-point assays,[106] which are not amenable to the screening of diverse substrates and rapid screening, respectively.

The second category includes strategies to monitor the enzyme, either by its intrinsic properties or with labels attached thereon. NMR spectroscopy can characterise protein function with atomic resolution,[61] but it requires complicated data analysis and is not conveniently amenable to rapid screening of fast reactions.[66, 67] Other spectroscopic methods, such as CD,[76] tryptophan fluorescence,[78] and ANS fluorescence,[56] as well as electrochemistry,[89] can rapidly monitor structural changes, but these typically provide an overall picture rather than site-specific information. Moreover, they are often better suited to monitor folding-unfolding rather than enzyme kinetics. IR spectroscopy represents a compromise, because although it cannot provide atomic resolution, it can probe structural features in moderate detail. However, the requirement of a difference spectrum to avoid the introduction of artifacts demands highly sensitive procedures, such as caged substrates.[82] Alternatively, one can label a protein to obtain site-specific information via tryptophan fluorescence[55] FRET,[52] EPR[72] and IR spectroscopies.[80] However, these require complicated and time-consuming mutation and/or labelling procedures. Moreover, FRET requires a substantial conformational change of ~3-9 nm,[45] which can preclude many enzymes that undergo only miniscule conformational changes. In contrast, ITC is label-free and can, in principle, detect any reaction.[97]

So, what is missing? While there are surely many unmet needs for the characterisation of protein function, one such unmet need is a method that can rapidly characterise an enzyme itself in real-time even if it does not undergo significant conformational change. Alkaline phosphatase (AP) is an ideal model enzyme to explore this concept, since it undergoes minimal conformational changes.[82, 107] Consider the various steps of an enzymatic reaction: the E + S, the ES complex, the $ES^{\ddagger}$ transition state, the EP complex, and then E + P (**Figure 1.6a**). Which of these reaction steps have been characterised for AP? Crystal structures are available for AP itself,[5, 108-113] which represents E + S (well, just E). Likewise, the crystal structure of AP with bound phosphate represents EP,[108] as do its inhibitory effects.[100] It is not possible to obtain a stable transition state, but crystal structures are also available for AP with bound transition state analogue (TSA) inhibitors.[107, 114] These stabilise a geometry that is similar to the transition state, and represent $ES^{\ddagger}$. For biomolecular substrates, it is often necessary to characterise their AP-mediated hydrolysis via quantification of released phosphate, which represents E + P.[106, 115] One step of the reaction is missing, ES. Of course, it is possible to characterise the rate of substrate consumption or product generation (**Figure 1.6b**).[34, 37] However, among the methods discussed above and others, none can detect the ES intermediate of AP and its associated small conformational changes. Some studies have reported the detection of protein intermediate states, such as photoactive yellow protein with time-resolved XRC,[116] as well as the enzymes cyclophilin A with NMR spectroscopy,[61] chymotrypsin with fluorescence spectroscopy via radiationless energy transfer (RET) between Trp residues and a fluorescent substrate,[117] and fluorophore-labelled β-lactamase with fluorescence spectroscopy.[44] However, despite much research focussing on AP, these strategies have not been applied to study its transient intermediate states.

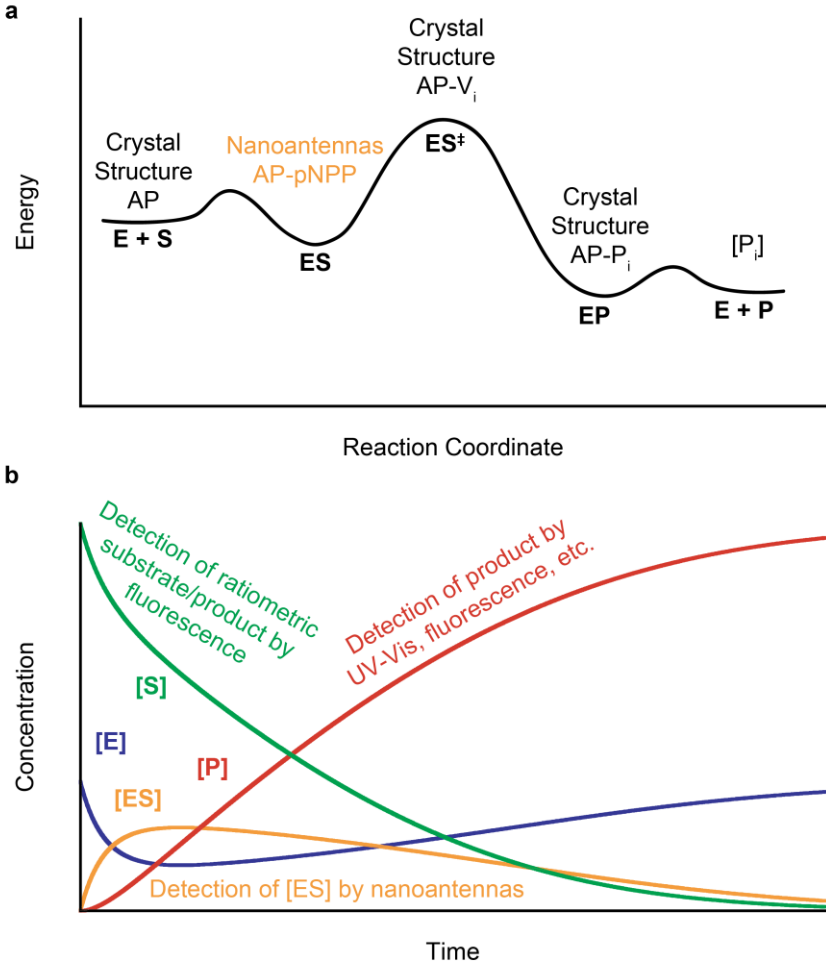

Figure 1.6. – Progress of a typical enzymatic reaction. (a) The states present during the enzymatic reaction: the enzyme and substrate(s) (E + S) are introduced, followed by formation of the enzyme-substrate complex intermediate (ES). Next is the transition state (ES‡), followed by the enzyme-product complex intermediate (EP), and finally the enzyme and released product(s) (E + P). (b) Representative changes with time in concentration of the substrate(s) ([S]), product(s) ([P]), enzyme ([E]) and enzyme-substrate complex ([ES]) are shown.

1.3.10 Introducing "fluorescent nanoantennas"

With the above in mind, this thesis introduces fluorescent nanoantennas as a new method to characterise protein function, with an emphasis on detecting the conformational changes of the ES intermediate.[61] The principles discussed here are illustrated in **Figure 1.7**. Many fluorescent dyes will undergo a fluorescence signal change upon binding to a protein. However, the dissociation constant (K_d) of dyes is often in the micromolar range, such as 1-10 μM for various cyanines and 100 μM for fluorescein with serum albumins (*n.b.,* from reported K_a values).[118, 119] Thus, to study enzymes with a concentration of 10 nM, for example, one would require a dye-to-protein ratio of 100:1 to 10000:1. Such a ratio should make it impossible to obtain a signal change for structural perturbations on the dye-protein complexes. Furthermore, even if it were possible, micromolar concentrations of these dyes would saturate the detector. Fluorescent nanoantennas instead drive dye-protein interaction at a more reasonable ratio via a high local concentration.

A nanoantenna has a fluorescent dye at one end, and a chemical moiety at the other end to enable its attachment to the protein of interest. In this work, we typically leveraged the convenience of biotin-streptavidin interaction to facilitate attachment, although other attachment strategies are also possible. The linker between the dye and the attachment moiety can be made from a flexible component, such as single-stranded DNA (ssDNA) or polyethylene glycol (PEG). As shown in **Figure 1.7**, the experiment *Starts* with the nanoantenna in solution. For *Step 1*, streptavidin (SA) is introduced to the cuvette. This tetrameric protein has four biotin-binding sites that can capture the biotinylated nanoantennas with high affinity. Concurrently, signal quenching is observed due to dye-SA interaction.[120-122] Together, we call these the nanoantenna-SA platform. Next, for *Step 2*, biotinylated AP (bAP) is introduced to the cuvette. Although the binding is slower, typically several minutes, a stable nanoantenna-protein complex will eventually form, which is also indicated by a fluorescent signal change due to dye-AP interaction. Finally, we observe that the fluorescent dye can sense events happening at the enzyme, including its catalytic function, the binding of effectors, and unfolding. This project demonstrates how these signal responses arise due to conformational change on the enzyme that perturb the dye-protein interaction.

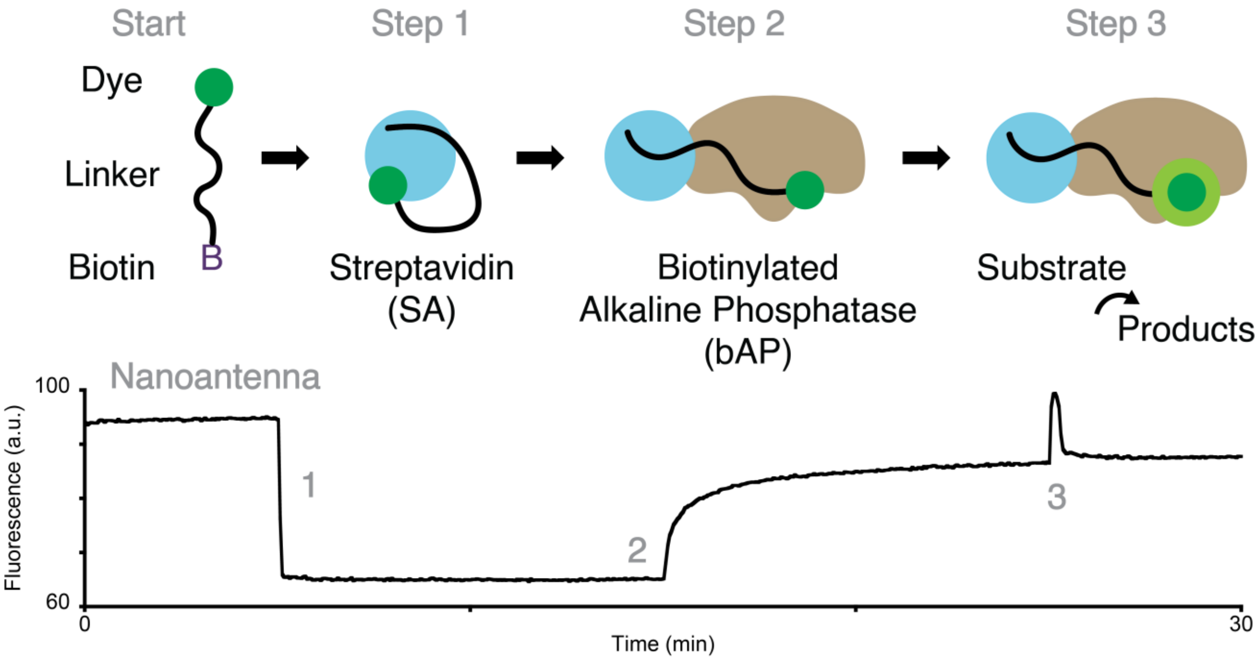

Figure 1.7. – Example of the nanoantenna strategy to sense protein function. (*Start*) The nanoantenna has a fluorescent dye (green circle) at one end and biotin (B) at the other. The experiment starts with monitoring the nanoantenna fluorescence in the cuvette. (*Step 1*) The protein streptavidin (SA) has four biotin-binding sites. After addition of SA, binding of the nanoantenna to it is evidenced by a rapid quenching of fluorescence. Note that the biotin is no longer shown because it will be located within the biotin-binding site of streptavidin. Also, for simplicity, only one nanoantenna is shown on SA, although there will be a diverse population of complexes formed that have multiple nanoantennas. (*Step 2*) Subsequent addition of biotinylated AP (bAP) to the cuvette and its binding to the remaining unoccupied biotin-binding sites of the nanoantenna-SA platform results in a fluorescence signal increase, indicative of dye-bAP interaction. (*Step 3*) Binding of a substrate induces conformational change, perturbing the dye and displaying a transient fluorescence spike. Note: We typically employed a ratio of 2-3 nanoantennas per SA and 2 bAP per SA, as discussed later herein, but since a diverse population of complexes will be formed in solution,[123] which we did not characterise or separate them, so for simplicity, just one of each component is shown in the cartoon.

1.4 Alkaline phosphatase

Besides being a model enzyme for us to explore the nanoantenna concept, there are also many reasons for which one might want to study AP. For instance, AP is likely the most frequently assayed enzyme in all of medicine[124] and it has been the subject of recent studies exploring controversial questions of biophysics.[125] This section reviews its catalytic function, role in biology, relation to disease, and methods to study it.

1.4.1 Catalytic mechanism of alkaline phosphatase

APs are homodimeric metalloenzymes with two active sites. Each active site contains one Mg^{2+} ion and two Zn^{2+} ions, denoted hereafter as $Zn^{2+}{}_1$ and $Zn^{2+}{}_2$. While most of the amino acids of mammalian and *E. coli* APs (ECAP) are poorly conserved, the three metal ions and a serine residue (Ser102) necessary for catalysis are highly conserved across all species.[126, 127] Building on earlier work,[5, 69] a mechanism of AP catalytic function at the active site has been proposed via the crystal structure of ECAP (**Figure 1.8**).[108] Firstly, water molecules are present in the active site of the free enzyme. The hydroxyl group of Ser102 has a hydrogen bond to a hydroxide ion coordinated to the Mg^{2+}. The phosphate monoester substrate (ROP) binds to form the enzyme-substrate complex (E·ROP), whereby the substrate's ester oxygen coordinates to $Zn^{2+}{}_1$ as well as the other oxygens to $Zn^{2+}{}_2$ and the guanidinium group of Arg166. Then, the hydroxide ion coordinated to Mg^{2+} acts as a base, and it accepts a proton from Ser102. The deprotonated oxygen of Ser102 is then stabilised by $Zn^{2+}{}_2$. Next, the activated hydroxyl group of Ser102 enables nucleophilic attack of the phosphorous atom of the substrate, thereby forming a covalent serine-phosphate intermediate (E−P). Also, $Zn^{2+}{}_1$ coordinates the "bridging" oxygen of the substrate and helps the departure of the RO^- leaving group. Then, a nucleophilic hydroxide ion coordinated to $Zn^{2+}{}_1$ attacks the phosphorous atom, thereby hydrolysing the covalent serine-phosphate intermediate and forming a non-covalent enzyme-product complex ($E{\cdot}P_i$). The Mg^{2+} and a coordinated water molecule may then re-protonate the serine residue, which might help with departure of the product.[108]

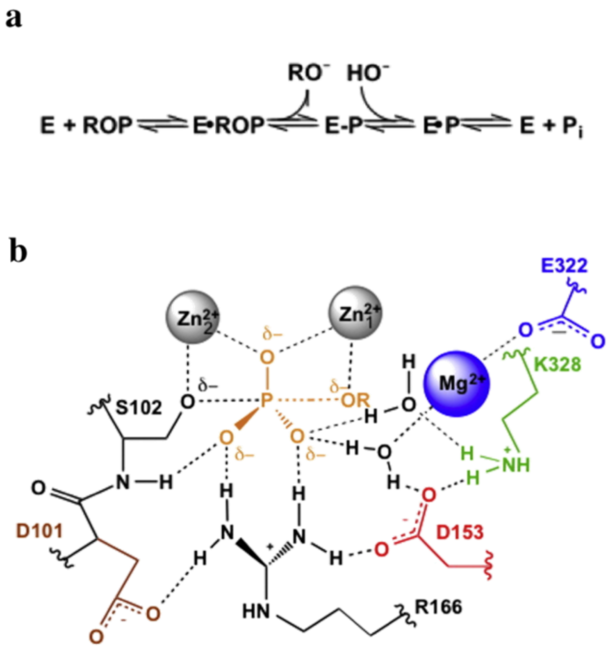

Figure 1.8. – The catalytic mechanism of AP. (a) Summary of the reaction for phosphate monoester hydrolysis with alkaline phosphatase. (b) Scheme of the presumed transition state at the alkaline phosphatase active site. The figure was modified from ref [114] with permission.

1.4.2 Biological function of alkaline phosphatase

Four isoforms of AP are expressed in humans, and there are various isoforms in other mammals too. Throughout most of this thesis it is redundant to indicate the isoform and species of AP, since calf intestinal AP was always used. In this section about the biological function of AP, however, it is pertinent to indicate specific names for the species and/or isoform to avoid confusion. As its name implies, intestinal AP (IAP) is expressed in the intestine, wherein it is secreted by intestinal epithelial cells. It is active within the mucosal membrane and the intestinal lumen. Its expression is highest in the duodenum, the first section of the small intestine.[126, 128, 129] The other two tissue-specific isoforms of AP are placental AP (PLAP), expressed in the syncytiotrophoblasts of the placenta, and germ cell or placental-like AP (GCAP), expressed in germ cells, embryonal tissues, and testis.[126, 128, 129] The fourth isoform is found throughout the body, but mainly in the liver, kidney and bones. It is called tissue-nonspecific AP (TNAP; or sometimes

L/B/K AP).[126, 128, 129] TNAPs expressed in different tissues display slight differences in post-translational modifications.[129] Human IAP, PLAP and GCAP have ~90% sequence identity, but TNAP displays only ~50% sequence identity to them.[130]

While the catalytic mechanisms of various the APs may be similar, or even identical, the complete picture of their biological roles remains unclear. As one review article recently put it, “This begs the question: how is it, after 90+ years, we still know relatively little about the overall functions of APs?”[131] While APs can hydrolyse various substrates, we do not wholly know which are of biological relevance. Indeed, we also do not currently know the roles of PLAP and GCAP in healthy individuals.[126, 128, 129] TNAP is important for bone mineralisation,[132, 133] but its role in the other tissues wherein it is expressed remains uncertain.[126, 128, 129] Recent years, however, have witnessed important advances concerning the biological role of IAP.

All vertebrates, including humans, have coevolved bacteria in their intestines. This microbiota plays important roles in digestion, synthesis of vitamins, and protection against other harmful microbes. However, excess release of lipopolysaccharide (LPS) from the outer membrane of Gram-negative bacteria is toxic and can trigger an inflammatory response. LPS molecules bind to a receptor, Toll-like receptor 4 (TLR4), thereby triggering a signalling cascade that results in proinflammatory cytokine expression and other problems. Thus, high concentrations of LPS are toxic and can result in septic shock.[134, 135] One proposed role of intestinal AP is to reduce the toxicity of LPS by dephosphorylating its Lipid A moiety.[134-138] IAP has also recently been determined to be a regulator of tight junction proteins, plus it prevents LPS-induced gut mucosal permeability and inflammation.[139] IAP has been further shown to prevent the inflammatory effects of LPS by inducing autophagy.[140] Moreover, IAP may prevent intestinal inflammation by hydrolysis of uridine diphosphate (UDP).[141]

Bicarbonate secretion increases IAP activity by increasing the local pH at its active sites. This aids its hydrolysis of luminal phosphates (*e.g.*, ATP), thereby increasing bicarbonate secretion via the activation of P2Y receptors.[142] A subsequent study reported that ATP is indeed a biological substrate of IAP, and that this enzyme regulates the surface pH of the duodenum.[143, 144] Another proposed role of IAP is the maintenance of normal gut microbial homeostasis. IAP-knockout mice were found to have less diverse microbiota compared to wildtype (WT) mice. Moreover, this could be reversed by treatment with supplementary IAP. Thus, IAP has a role in determining which types of bacteria inhabit the gut.[145] In a later study from the same group, it was reported that IAP-knockout mice have more luminal ATP. The study concluded that IAP promotes the growth of intestinal commensal bacteria by reducing the ATP concentration.[146, 147]

1.4.3 Biological substrates of alkaline phosphatase

APs can hydrolyse a wide variety of substrates. The occurrence of APs in many species in nature, and in various tissues, suggests its involvement in many biochemical processes. In most cases, however, its role and natural substrates remain unknown.[148] Nevertheless, there have been some important advances in recent years. As noted above, LPS and ATP are now known to be natural substrates of IAP. It has been proposed that phosphorylated proteins (phosphoproteins) could be a substrate of human PLAP[109] and of rat liver AP.[149] Proposed natural substrates of human TNAP and PLAP are pyrophosphate (PP_i), phosphoethanolamine (PEA), and pyridoxal 5'-phosphate (PLP; Vitamin B_6).[150-153] The phosphorylated protein osteopontin (OPN) has also been proposed as a substrate of TNAP.[154, 155] In another study employing the substrate β-glycerophosphate (BGP), TNAP was associated with mineralisation in other tissues besides bones. Interestingly, this process might not involve its catalytic activity.[156] In addition, human PLAP and IAP can hydrolyse phosphatidates with long fatty acyl chains, but liver AP (presumably TNAP) cannot. While this observation does not prove that these molecules are natural substrates of PLAP and IAP, it does support a difference in biological function for these isoforms relative to TNAP.[157]

The function of AP with various substrates has similarly been studied in non-mammalian species. For the fungus *Glomus etunicatum*, it was observed that AP hydrolyses BGP, glucose-6-phosphate (G6P), glucose-1-phosphate (G1P), and trehalose-6-phosphate (T6P), but not the pyrophosphate-containing molecules, PP_i and ATP. These differences of substrate specificity suggested that this AP may be involved in the fungal sugar metabolism.[158] On the contrary, for the yeast *Candida utilis*, it displayed the most activity with polyphosphate (polyP; 25 chain length), but reduced or no activity with other substrates. Thus, it was proposed that the biological role of this AP is to hydrolyse polyP stored in yeast vacuoles.[159] PolyP was also proposed as a substrate for AP from the yeast *Saccharomyces cerevisiae,*[160] while an earlier study had suggested phosphoproteins.[161] G6P has been suggested a substrate for various species of marine algae AP,[162, 163] but ruled out for another.[164] Finally, a recent study of the cyanobacterium *Microcystis aeruginosa* examined the effects of various phosphate sources on bacterial growth and AP activity. This study checked 59 substrates and other phosphate molecules![165] Total AP activity for each substrate was reported, rather than full characterisation of Michaelis-Menten kinetic parameters – this feat would have been unrealistic, albeit possible, with the currently available time-consuming methods. Clearly, there is more to learn about the substrates of APs.

1.4.4 Relation to disease

Intestinal AP and other isoforms of AP have been linked to inflammatory gastrointestinal diseases, cancers, and other conditions.[128, 129, 131, 166, 167] Some diseases involve AP deficiency. Recently, it was reported that repeated non-lethal *Salmonella enterica* serovar typhimurium infections in mice, as a model of reoccurring food poisoning, induced intestinal AP deficiency in the colon. This led to increased levels of LPS, and consequently, inflammation. Thus, the study proposed an environmental and pathogenic origin of chronic intestinal inflammation.[168] Inflammatory bowel disease (IBD) has also been linked to deficiency of the gene for IAP[169] and other factors.[170] In this case, IAP can serve as a biomarker via its absence in stool samples.[169] Moreover, intestinal AP deficiency has been linked to faster weight gain,[171] metabolic syndrome in mice,[172] and type 2 diabetes mellitus in humans.[173] In another study, humans with type 1 diabetes mellitus were observed to have intestinal inflammation and low levels of IAP.[174]

Higher levels of APs have been implicated in various cancers. For example, the TNAP and IAP isoforms are expressed in human breast cancer MCF-7 cells.[175-177] APs have also been associated with renal[178] and oral[179, 180] cancer cells. Tumour-derived AP was recently associated with metastatic prostate cancer. There was also a significant decrease in survival for patients with high AP expression.[181] Moreover, several clinical studies have reported that patients with high levels of serum AP had worse prognosis or survival rates for colon,[182, 183] rectal,[182] gastric,[184] breast,[185] and non-small cell lung cancer (NSCLC).[186] Aside from cancers, higher serum AP levels have been linked to spontaneous intestinal perforation,[187] various cardiovascular diseases, such as myocardial infarction, coronary heart disease, and stroke,[188, 189] chronic kidney disease (CKD),[190, 191] and even severe cases of COVID-19.[192] It is important to note that while IAP contributes about 70-80% of AP activity in stool samples and can serve as a biomarker, IAP accounts for only about 6-7% of AP activity in the serum samples of healthy individuals.[167, 169, 193] Nevertheless, many of the aforementioned studies apparently did not determine which isoforms were contributing to the higher levels of serum AP activity. Speculatively, serum IAP could increase in absolute and relative terms for some diseases, especially for those related to the gastrointestinal tract. Thus, there is still much for us to learn about the role of IAP in human health and disease.

APs can treat a variety of conditions, either as a medicine or under natural circumstances. In animal studies, IAP displayed therapeutic effects against metabolic syndrome that leads to type 2 diabetes.[172] It was also found to be effective for treatment of lethal *E. coli* infection,[194] *E. coli*-induced peritonitis,[195] alcohol-induced hepatosteatosis,[196] and necrotizing enterocolitis (NEC).[197] The last of these, NEC, is an intestinal inflammation disease that mainly affects premature infants. In a human study, it was recently proposed that risk factors for NEC are preterm birth and a lack of breast milk feeding, as evidenced by, respectively, the higher IAP activity in the full-term neonatal intestine and the high AP activity of breast milk that aids in detoxification of LPS in the first few days after birth.[198] Similarly, it has been proposed elsewhere that consumption of dairy products containing TNAP can lead to it functioning alongside IAP, thereby lowering the incidence of cardiovascular diseases.[199] In other human studies, IAP was effective for treatment of ulcerative colitis[200] and renal inflammation in the context of septic acute kidney injury.[201-203] Another emerging possibility is to employ IAP as a food additive in pig farming to replace antimicrobial growth promoters, which is important in the context of drug-resistant bacteria.[204] Note that several of these medical studies,[172, 194, 197, 200] and presumably another,[195] employed calf IAP – the main enzyme studied in this thesis.

IAP also has a role in converting various prodrugs to their active metabolite form. For example, amifostine (Ethyol) is employed to protect normal tissues against the toxicities of radiation treatment and chemotherapy. It is used to reduce xerostomia (dry mouth) in patients receiving postoperative radiation treatment for head and neck cancer that affects the parotid glands as well to reduce renal toxicity in relation to repeated administration of cisplatin.[10, 205-207] Dephosphorylation by IAP generates its active form, WR-1065, which can diffuse into cells.[206-208] Another such prodrug is fosamprenavir, which is dephosphorylated by IAP to amprenavir, a protease inhibitor used to treat human immunodeficiency virus (HIV) infection.[209-211]

Overall, there are a myriad of reasons to study intestinal AP, including its biological function in the dephosphorylation of substrates like ATP and LPS, examination of biomolecules that are potentially natural substrates of the enzyme, its relation to various diseases ranging from bacterial infection to cancer, its use as a medicine, and its role in converting drugs to active metabolites. Simple tools to monitor AP function in real time could be useful for these purposes.

1.4.5 Detection of alkaline phosphatase function – synthetic substrates

Chromogenic or fluorogenic substrates of AP are the easiest to detect, via UV-Vis and fluorescence spectroscopy, respectively. Other techniques employ resonance-based spectroscopies or electrochemistry. In most cases, however, the principle of detection remains the same: the phosphate monoester substrate itself does not provide a signal, but after removal of its phosphate (P_i), the leaving group product displays a strong signal intensity. This enables real-time monitoring of enzyme kinetics.

The quintessential substrate to study AP catalytic activity is pNPP.[34] Upon hydrolysis, its product molecules are pNP and P_i. The former is detected by UV-Vis spectroscopy (λ_{abs} = 405 nm) via the high molar absorptivity in alkaline solution of its phenolate form (~18000 L mol^{-1} cm^{-1}) relative to pNPP (~50 L mol^{-1} cm^{-1}).[212] Owing to its convenience, pNPP has been widely used to study how various factors can affect AP, such as temperature,[213, 214] pH,[213-216] ions,[216, 217] inhibitors,[112, 215, 216, 218, 219] and mutations.[72, 219, 220] Other classic applications of pNPP are verification of milk pasteurisation[221, 222] and soil phosphatase activity.[223] This substrate can also be employed to study other phosphatases, such as tyrosine phosphatase.[224]

Another popular substrate to study AP catalytic activity is 4MUP.[37] Its product molecule, 4MU, can be detected by fluorescence spectroscopy via its λ_{ex} and λ_{em} of 360 nm and 440 nm, respectively. One advantage of 4MUP and fluorescence spectroscopy is the higher sensitivity.

However, a disadvantage of 4MUP is that it requires alkaline conditions (pK_a ≈ 8), although this limitation can be avoided by employing its variant, 6,8-difluoro-4-methylumbelliferyl phosphate (DiFMUP).[225] Both pNPP and 4MUP are widely available from various commercial suppliers. It remains in active use, such as to discriminate isoforms of AP based on their differing kinetics.[226]

Designing new AP substrates detectable by fluorescence spectroscopy is a popular field of research.[227, 228] These follow the same detection scheme as 4MUP, whereby upon release of P_i after substrate hydrolysis, the other product is detectable by fluorescence spectroscopy.[229, 230] These alternative substrates are purported to have various advantages over the classic 4MUP. For example, unlike fluorophores with ultraviolet or visible emission, those with near infrared (NIR) emission are ideally suited for *in vivo* analysis since their spectral window does not overlap with biomolecules. They have enabled the study of AP in biological samples, including cells and mice.[231-233] Another class of substrates for *in vivo* analysis are those with water-insoluble fluorescent products that do not diffuse from the inside of cells.[234-237] Some substrates leverage aggregation-induced emission (AIE) of the products to prevent fluorescence quenching at high concentrations and to improve the signal-to-noise ratio by ~3-fold relative to 4MUP.[238] Other substrates avoid sample autofluorescence via their large Stokes shift, such as commercially available AttoPhos and ELF-97.[239] Some studies have reported ratiometric probes. These involve monitoring two distinct emission wavelengths corresponding to substrate consumption and product generation. This mitigates the effects of experimental conditions on fluorescent products and improves the signal-to-noise ratio.[237, 240-245] It is worth noting that while all of these substrates ought to be hydrolysed by all non-specific phosphatases, one has been engineered for specific recognition *in vivo* by AP.[246] Finally, another substrate enables the monitoring of substrate consumption rather than product generation, but the principle remains the same.[247]

Alternative substrates for UV-Vis,[248] plus others for Raman,[84] EPR,[73] NMR,[70] and chemical exchange saturation transfer magnetic resonance imaging (CEST MRI)[249] have been reported. Some studies have employed nanomaterials, such as detecting the interaction of product molecules with gold nanoparticles (Au NPs) by SERS[85, 86] and UV-Vis.[250] Others have integrated the substrate with CdSe/ZnS quantum dots (QDs).[251] Non-spectroscopic techniques have employed electrochemistry.[91-95, 252] Like their fluorescence spectroscopy counterparts, however, these techniques require the properties of specific molecules to generate a signal. Thus, although pNPP, 4MUP, and all the other strategies noted above can detect the presence of AP and many can characterise its activity, they are not biologically relevant enzyme-substrate systems.

1.4.6 Detection of alkaline phosphatase function – biomolecular substrates

Bimolecular substrates of AP and their products are not as easy to detect. Instead of being cleaved to form P_i and a colorimetric or fluorescent molecule, they instead form P_i and a spectroscopically silent molecule. Consequently, their hydrolysis by AP is typically characterised by quantification of P_i.[106, 115, 253] A popular assay[106] involves first preparing a solution of concentrated H_2SO_4 and malachite green. This solution is stable, but one must wait until the day of analysis to add ammonium molybdate and Tween 20. Then, one equivalent of this solution is mixed with four equivalents of the analyte solution containing P_i. After 10 min, absorbance of the phosphomolybdate-malachite green complex can be measured by its λ_{max} of 630 nm. The details of this technique are listed here to demonstrate its obvious disadvantages. One is that using concentrated H_2SO_4 to improve the solubility of malachite green can be dangerous. Moreover, although detection of malachite green is ~6-fold more sensitive than detection of pNP, UV-Vis is less sensitive than fluorescence. Most consequential, the assay cannot be performed as a continuous assay to obtain kinetic data in real time.

Some strategies can monitor continuous P_i release. For example, a coupled assay employs the enzyme purine-nucleoside phosphorylase to convert 2-amino-6-mercapto-7-methylpurine ribonucleoside and P_i to 2-amino-6-mercapto-7-methylpurine and ribose-1-phosphate. The absorbance difference allows monitoring of the reaction by UV-Vis, and thus, indirect monitoring of phosphatase activity in real-time.[254] While this strategy may work for specific enzymes like ATPases, it is unsuitable for promiscuous APs, which would simply hydrolyse the ribose-1-phosphate and alter the observed kinetics. Another prominent assay involves attaching a coumarin-based fluorophore to a phosphate-binding protein. While able to monitor P_i release in real time, this assay has some disadvantages. Specific labelling of proteins is time-consuming, it apparently has a narrow pH range of 7-8, and monitoring release of high concentrations of substrate could become prohibitively expensive.[255]

Perhaps with these limitations in mind, substrate-specific continuous assays have been developed. These works have overwhelmingly focused on PP_i and ATP. In one strategy, a fluorescent poly(phenylene ethynylene) polymer ($PPECO_2$) is first quenched by Cu^{2+}, but addition of PP_i increases fluorescence by complexation with Cu^{2+}. The assay begins when AP is added, whereupon it hydrolyses PP_i to $2P_i$, and one monitors the enzyme's activity via fluorescence quenching.[256] Other fluorescent assays for AP activity with PP_i have also been reported. For example, a recent work synthesised a benzimidazole-based zinc complex, which was selective for PP_i and enhanced the fluorescence signal. AP activity toward PP_i could then be monitored via a decrease in fluorescence.[257] Other assays involving PP_i based on DNA and nanomaterials could detect the presence of AP, but were not used for the characterisation of enzyme kinetics.[258-261]

AP assays for ATP are available too. This important biomolecule was reported to have no significant effect on gold nanoparticles (Au NPs) and silver nanoparticles (Ag NPs), but its adenosine product causes their aggregation. The resulting colour change, red to blue for Au NPs or yellow to brown for Ag NPs, can be monitored by UV-Vis.[262, 263] Although kinetic parameters were not reported, the colour change was time-dependent.[262] One potential pitfall of this style of assay, however, is that non-specific aggregation of NPs could occur in complex media.[262] Thus, later studies have employed specific recognition of ATP relative to its products, such as with a fluorescent perylene probe. This fluorescent sensor is quenched upon binding of ATP, but the fluorescence recovers after its hydrolysis.[105] This assay was also sensitive to AMP and ADP, but PP_i had no effect on the signal. Elsewhere, a fluorescently labelled structure-switching DNA aptamer used with AP was able to monitor AMP hydrolysis to adenosine and P_i.[264]

An interesting design for specific recognition is that of supramolecular tandem assays. These leverage the difference in affinity of the "host" molecule for different "guest" molecules (*e.g.*, fluorescent dye, substrate, product).[265] For example, calixpyridinium has a higher affinity to bind ATP than a pyrene dye, but after the enzymatic reaction, calixpyridinium has a higher affinity for the dye than for the product adenosine. Thus, this strategy can monitor ATP hydrolysis via quenching of fluorescence upon binding of the dye to calixpyridinium.[266] Conceptually similar assays employing different hosts and guests can monitor AP activity with the substrates PLP,[267] phosphotyrosine (PTyr),[268] and phosphorylated peptides.[269]

There are also specific assays for other molecules. For example, one study leveraged DNA nanotechnology with the substrate ascorbic acid-2-phosphate (AAP). Silver(I) ions prevent formation of a G-quadruplex secondary structure, but upon conversion of AAP to ascorbic acid (AA), the AA reduces Ag^+ to Ag^0, thereby enabling formation of the G-quadruplex, which binds the dye Thioflavin T and increases its fluorescence.[270] Although interesting and potentially useful for the detection of the presence of AP, AAP is not known to be a natural substrate of this enzyme.

One study has reported detection of more than one substrate. This method employs histidine-protected gold nanoclusters, which oxidise the molecule 3,3′,5,5′-tetramethylbenzidine (TMB) in the presence of H_2O_2 to generate a colorimetric blue product. This peroxidase-like reaction of the nanomaterial is blocked by substrates containing a pyrophosphate moiety, such as PP_i, ADP and ATP. Thus, their hydrolysis by AP enables one to detect AP via its enzymatic activity with UV-Vis spectroscopy. This assay, however, does not work with AMP, and presumably other substrates without a pyrophosphate moiety.[271] It was also not used to derive kinetic parameters. Overall, while chemically quite impressive in many cases, a drawback common to these methods is that they only work for one substrate[105, 256-264, 266-268, 270, 272, 273] or a class of substrates.[269, 271]

Some assays of AP enzymatic function enable real-time analysis *and* are not substrate-specific. In several studies, Ce^{3+} ions first quench the fluorescence of carbon quantum dots (CQDs),[274] boron-doped graphene quantum dots (BGQDs),[275] or the dye calcein.[276] Subsequent AP-mediated hydrolysis of ATP releases P_i, which then forms $CePO_4$ and increases the fluorescence. However, despite these methods being able to theoretically monitor any AP substrate, a potential problem is the Ce^{3+}-mediated sequestration P_i, which is not only a product but also an inhibitor. Therefore, these assays ought to be suitable for detection of AP,[272, 274-276] as is the intended purpose, but not for characterisation of its substrates in biological settings since any derived parameters may not reflect relevant systems. Another assay for determination of P_i employs a complex of Eu^{3+} and tetracycline. Binding of P_i increases the fluorescence. It faces the same challenge, however, as sequestration of P_i could likewise affect the kinetic parameters.[277]

Finally, a recently reported isothermal titration calorimetry (ITC) strategy, called initial rate calorimetry (IrCal), can monitor the activity of AP and other enzymes with biomolecules. This study compared values obtained for pNPP and 4MUP with IrCal and the their respective spectroscopies, and also could be used to monitor the substrate ATP.[100] A faster method with a microfluidic calorimeter was later introduced, but the authors noted that this strategy does not work for large slowly diffusing substrates and that it needs improvement of its sensitivity.[101]

As one can see from this overview of presently available methods, simple spectroscopic assays able to rapidly characterise AP with biomolecular substrates in real time remain highly desirable and an unmet need. To conclude, it is worth repeating why FRET-based assays leveraging conformational change are absent from this discussion: AP is not known to undergo large conformational change while performing its function.

1.5 Tools employed in this project

1.5.1 DNA Nanotechnology

It is well known that DNA plays a role in biology but using DNA to build tools at the nanoscale is often surprising for the non-specialist and scientist alike. There are, nevertheless, numerous advantages to building tools from this incredible class of biomolecule. The well-defined structure of DNA enables the rational design of molecular tools for an intended purpose. DNA can be rapidly synthesised by automated phosphoramidite synthesis (*n.b.,* for principles of the method see section 6.4 Phosphoramidite synthesis of DNA). This enables rapid the exploration of various designs, including DNA switches,[278-281] a topic which we have reviewed.[282] DNA can be designed to respond to various inputs, including temperature,[283-286] pH,[287] small molecules,[288-290] metal ions,[291-293] another DNA strand,[294] or a protein.[295-299] The sensitivity of DNA to these stimuli can often be rationally tuned by changing the sequence. These DNA switches and other structures, when coupled with a signal-generating molecule, can then provide a signal output that is detected by fluorescence spectroscopy, electrochemistry, and many other types of laboratory instrumentation. In this work, we introduce simple fluorescent DNA structures that respond to protein function. Below, several relevant and interesting studies are discussed.

A classic example of DNA nanotechnology is the molecular beacon. It is a ~25 nucleotide strand with a ~5 nucleotide intramolecular complementarity region at its 5′- and 3′-ends, called the stem. The ends are labelled with a fluorophore and quencher pair. The remaining ~15 nucleotide loop region is designed to bind to a target DNA strand. Since the target strand has a stronger interaction with the loop region than the stem does with itself, the binding of this strand will open the loop. This separates the fluorophore and quencher, thereby providing a fluorescent signal increase.[300] Molecular beacons are a popular strategy for sensing in solution,[301] and have been adapted for other platforms, such as electrochemical sensors on a gold surface.[294] By simply changing the sequence of the loop, the molecular beacon can bind another target strand.

Instead of binding a target DNA strand, a similar design can sense temperature as a DNA-based nanothermometer. By changing the composition of the stem, one can tune its sensitivity to temperature. This is due to the Watson-Crick base pairing,[302] whereby it requires more energy to separate guanine (G) and cytosine (C) with three hydrogen bonds than adenine (A) and thymine (T) with two.[302] Thus, by having more G-C pairing than A-T pairing in the stem, one can increase the melting temperature, thereby providing a temperature-sensitive DNA structure with a fluorescence signal output (**Figure 1.9a**).[283-286] Since these nanothermometers require dual-labelling for each temperature range, other designs have leveraged a stabilising strand to adjust the sensing range (**Figure 1.9b**), multimeric nanothermometers that can improve the sensitivity (*e.g.,* triplex DNA via Hoogsteen base pairing; **Figure 1.9c**), and multiple nanothermometers to extend the temperature sensing range (**Figure 1.9d**).[286]

DNA origami enables one to build large self-organised scaffolds on the scale of ~100 nm from hundreds of short DNA sequences.[303] Some researchers have used DNA origami to incorporate DNA nanotechnology with enzymes.[304] In one case, glucose oxidase (GOx) and horseradish peroxidase (HRP) were attached to a DNA scaffold to study the effect of interenzyme distance for a reaction cascade. After GOx coverts glucose and O_2 to gluconic acid and H_2O_2, the H_2O_2 product is subsequently oxidised by HRP, which in the process also converts the electron donor $ABTS^-$ (2,2'-azino-bis(3-ethylbenzothiazoline-6-sulfonic acid)) to $ABTS^{2-}$. Interestingly, having 10 nm between the two enzymes on the DNA origami scaffold enabled a significant enhancement of the activity of the HRP reaction. Therein, the transfer of H_2O_2 followed surface-

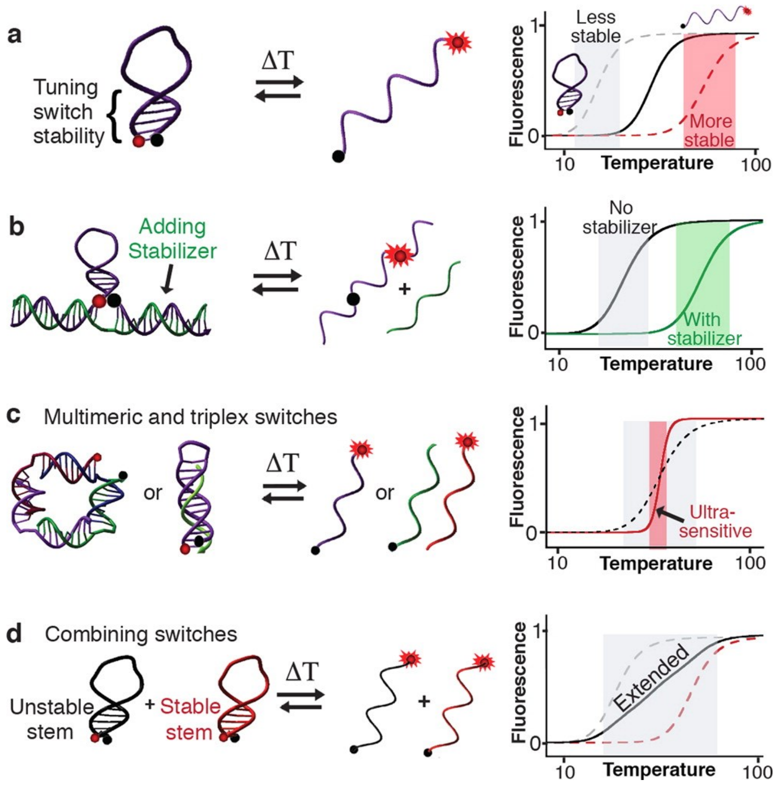

Figure 1.9. – Programmable DNA nanothermometers. (a) Changing the stability of the DNA switch can tune the temperature-sensing dynamic range. (b) Employing stabilising strands enables tuning of the dynamic range without having to synthesise multiple labelled strands. (c) Multimeric nanothermometers can improve the sensitivity. (d) The dynamic range can be extended by using multiple nanothermometers. Reproduced from ref [286] with permission.

limited diffusion, rather than the 3D Brownian diffusion that occurs at larger distances between the enzymes.[305] In a subsequent study, a DNA "swing arm" was used to channel hydrides between two enzymes (**Figure 1.10**). The enzyme glucose-6-phosphate dehydrogenase (G6PDH) oxidises glucose-6-phosphate while reducing NAD^+ to NADH (*n.b.,* NAD = nicotinamide adenine dinucleotide), and the enzyme malic dehydrogenase (MDH) reduces oxaloacetate to malic acid by using the NADH produced by G6PDH. Importantly, NAD^+ was attached halfway between G6PDH and MDH (7 nm between each). Thus, the swing arm mediated the transfer of hydrides between the two enzymes. In addition to the distance dependence between the components to achieve optimal activity, it was also possible to reduce enzyme activity by substituting the ssDNA

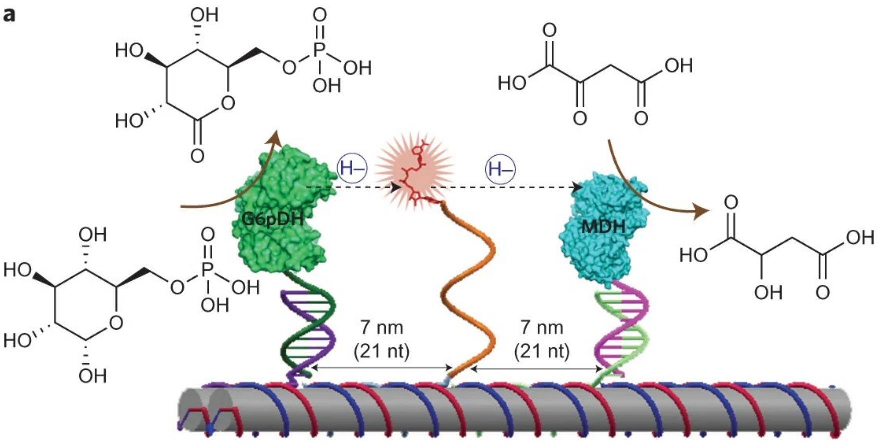

Figure 1.10. – Swing arm concept. By employing a DNA origami scaffold, the swing arm with attached NAD$^+$ facilitates hydride transfer between the enzymes G6PDH and MDH. Reproduced from ref [306] with permission.

swing arm for less flexible dsDNA.[306] Previous works by the same group have also displayed distance dependence, such as a DNA nanotweezer that can bring NAD$^+$ into close proximity with G6PDH.[307]

The above-mentioned studies have used DNA to control enzyme function. Others have done the reverse – using enzymes to control DNA. For example, during the catalysis of glutathione (GSH) and 1-chloro-2,4-dinitrobenzene (CDNB), the enzyme glutathione transferase (GST) produces HCl. This reaction product can then close a pH-sensitive DNA switch. On the contrary, when using the enzyme urease, the pH-sensitive DNA switch could be opened. This is because urease produces NH_3 and CO_2 from urea, and in the process, the produced NH_3 receives a proton from the switch. This could be tuned by varying the concentration of the components (*i.e.*, substrate or enzyme), and it was reversible. It could also be adapted for strand displacement from the switch in the presence of an enzyme.[308]

Some studies have examined enzyme-nucleic acid interaction by modifying a DNA strand with a fluorescent dye. For example, one study labelled ssDNA with a fluorescent dye to study the time-dependent 3′- to 5′-end translocation of the DNA repair protein *E. coli* helicase II (UvrD) along ssDNA. The 5′-end was labelled with the dye, which signalled the arrival of the UvrD.

Interestingly, labelling with fluorescein resulted in fluorescence quenching, but labelling with Cy3 resulted in a fluorescence increase.[309] Subsequent studies from the same group[310-313] and others[314-318] have employed this concept, often with Cy3, to study the kinetics and mechanisms of various protein-nucleic acid interactions. For example, a similar strategy was employed to develop a fluorescence assay for the bacteriophage T7 DNA polymerase and its conformational changes upon binding of a deoxynucleotide triphosphate (dNTP). Notably, this study found that the rate constant of the conformational change is highly dependent on the complementarity of the dNTP substrate in order to prevent the incorporation of an incorrect nucleobase.[314] This approach was later called protein-induced fluorescence enhancement (PIFE) in a study of 5′-triphosphate translocation of the protein retinoic acid inducible–gene I (RIG-I) along viral double-stranded ribonucleic acid (dsRNA).[316] PIFE was shown to display sensitive distance dependence in single-molecule assays of three protein-nucleic acid systems. For example, with a restriction enzyme (BamHI) that binds to a specific six-nucleotide sequence on rigid dsDNA, by shifting this binding site it was possible to measure the distance-dependent fluorescence enhancement with single base pair (bp) resolution.[318] Moreover, PIFE distance dependence was in the range of ~0-3 nm, which is below the FRET range of ~3-9 nm.[318, 319] Subsequent studies have even integrated these two complementary distance-dependent methods.[320-323]

The mechanism for the enhancement of Cy3 fluorescence has been demonstrated to arise via a decrease of photoisomerisation efficiency when the dye is sterically constrained by a protein. This is because the *trans* conformation of Cy3 in the excited state is fluorescent, but the *cis* conformation is not. The energy of activation for *trans*-to-*cis* isomerisation is high in the ground state, but this barrier is lowered in the excited state. However, isomerisation is prevented by steric hindrance when the dye is in close proximity to a protein, thereby favouring the fluorescent *trans* conformation.[324] A recent study also found that while the Cy3 fluorescence lifetime is unaffected by whether the dye is at the 5′- or 3′-end of the DNA, there is a difference observed upon interaction of the DNA with a DNA-binding protein. Thus, the specific amino acids interacting with the dye can modulate the PIFE effect. In contrast to the abovementioned studies, this study further argued that PIFE does *not* display distance dependence. More specifically, the study reported that *E. coli* ssDNA-binding (SSB) protein with 5′- or 3′-labelled DNA will locate the dye in a similar position on the protein, yet they display different fluorescence intensities, further supporting that the PIFE effect is due to specific dye-protein interaction, rather than simply distance. They also noted that PIFE could be achieved with flexible ssDNA that does not locate Cy3 near the binding site, since it can loop back and interact with the protein.[325] Another recent study reported that PIFE depends on the initial fluorescence of the unbound Cy3-labelled DNA due to dye-DNA interaction. Thus, one can change the initial state (*i.e.*, the DNA sequence) to modulate PIFE, and even to achieve an opposite effect, which they called protein-induced fluorescence quenching (PIFQ).[326]

Clearly, there is more to learn about dye-protein interactions and how they can be leveraged to make sensors with DNA nanotechnology.[327] Some studies have attributed the PIFE effect to distance, while others have dissented from this view. Nevertheless, PIFE remains advantageous because it does not require protein labelling and only requires the labelling of DNA with a single fluorophore. One drawback, however, is that it has remained limited to systems involving protein-nucleic acid interaction, which obviously precludes many other functional proteins. As also discussed above, various studies have employed DNA strands of different flexibilities and distances to modulate protein function. This thesis explores similar concepts to monitor protein function by employing various linkers to drive dye-protein interaction.

1.5.2 Biotin-streptavidin interaction

Streptavidin (SA) is a ~52.8 kDa homotetrameric bacterial protein obtained from *Streptomyces avidinii* (*S. avidinii*). It is known for its ability to bind up to four biotin molecules or other molecules with a biotin moiety (*e.g.*, biotinylated DNA or proteins). Binding of biotin to SA occurs with remarkably high affinity; the K_d is about 10^{-14} to 10^{-15} M.[328] This high affinity has been attributed to hydrogen bonding and van der Waals interactions inside the binding site, as well as a loop structure closing over the binding site in a manner that is analogous to a lid closing on a container (**Figure 1.11**).[329, 330] Binding occurs rapidly, and it is typically unaffected by extremes of pH, temperature, organic solvents, denaturing agents (unless SA itself is denatured), and enzymatic degradation.[328, 331, 332] For example, one study reported a method to purify SA from the broth of *S. avidinii*, whereby the SA was first bound to an affinity column at pH 11 via a biotin

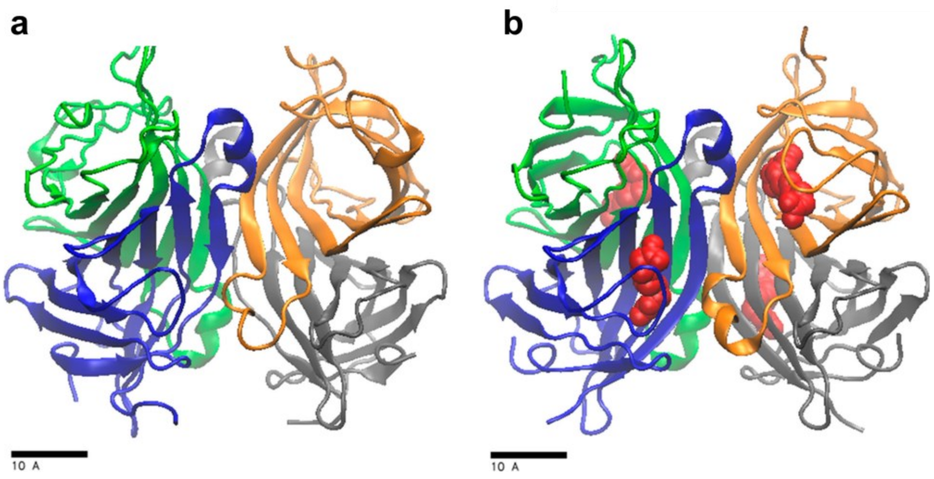

Figure 1.11. – Crystal structure of streptavidin. Here, streptavidin (a) without and (b) with biotin are shown. Shown in different colours are the four subunits of SA (blue, green, grey, orange) and the four bound biotins (red). Figure reproduced from ref. [333] with permission.

analogue that displays pH-dependent binding (iminobiotin), followed by release at pH 4 and quantitative recovery of SA.[334] Thus, SA maintains its function over these pH extremes, but loses affinity for the column due to protonation of the iminobiotin. Another study observed that SA's melting temperature (T_M) midpoint of 75 °C increases to 112 °C upon saturation with biotin.[335]

There are alternatives to SA that also bind biotin, such as avidin from chicken egg white. SA and avidin have low homology for their primary structure, but very similar secondary, tertiary, and quaternary structures.[336] Generally speaking, however, SA is favoured for most applications. This is due to avidin's high positive charge (isoelectric point, pI = 10) relative to SA (pI = 6.8 to 7.5). A modified version of avidin, NeutrAvidin (pI = 6.3), displays similar properties to SA.[337] Another benefit of SA is that its k_{off} for the dissociation of biotin is quite slow, about ~5-7 × 10^{-5} s^{-1}.[338, 339] One study compared SA, avidin, and a new SA analogue called Traptavidin, which has an even slower off rate. As evidenced by the fluorescence increase of biotin-4-fluorescein upon its release in the presence of excess biotin, avidin displayed ~20% dissociation after 2 h, but SA only ~4%, and even less for Traptavidin.[339] Thus, for many applications, the stability of SA ought to be sufficient. It balances commercial availability, cost, and functionality.

SA and biotin are widely used in the field of DNA nanotechnology[340] and in protein immunoassays.[328] For biotinylation of DNA, commercially available reagents allow for the insertion of biotin moieties at the 5′- and 3′-ends, as well as internal modifications.[340] For biotinylation of proteins, this can be achieved by commercially available kits for non-specific biotinylation, and also by precise site-specific labelling.[331] Note that the biotinylation of exposed lysine residues of a protein typically does not affect its function.[341] Thus, for the above reasons, this thesis used SA to connect biotinylated nanoantennas with biotinylated proteins.

1.5.3 Fluorescent dyes

Three naturally occurring amino acids display fluorescence emission: tryptophan (Trp), tyrosine (Tyr), and phenylalanine (Phe). These are abundant in proteins, and they absorb and emit ultraviolet light, but they display relatively low QYs, especially Phe.[342] One benefit of Trp, however, is the high sensitivity of its fluorescence emission to the chemical environment and exposure to the solvent. Thus, it can be exploited to monitor the conformational change of proteins,[55] but it can also suffer from low specificity due to the presence of multiple fluorescent amino acids spread out in several locations in a protein. While many proteins do have multiple fluorescent Trp residues, these provide a weak signal and/or cannot provide site-specific information. Thus, many applications require labelling with a fluorescent dye.

Although numerous fluorescent dyes are available, the most popular is probably fluorescein (**Figure 1.12**). Note that molecular structures of the dyes are provided in Chapter 2 (**Figure S2.7**). Fluorescein is employed in widespread applications, such as staining of cells and microorganisms, tracking the flow of ground water, study of corneal and conjunctival epithelial damage in ophthalmology, and previously, to turn the Chicago River green on Saint Patrick's Day.[343] Various derivatives of fluorescein exist, such as fluorescein isothiocyanate (FITC) and its succinimidyl ester for conjugation to proteins, and carboxyfluorescein amidite (FAM) used in DNA nanotechnology.[344] Although free and oligonucleotide-conjugated fluorescein differ in their fluorescence emission properties due to the local electrostatic potential of the nucleic acid,[345]

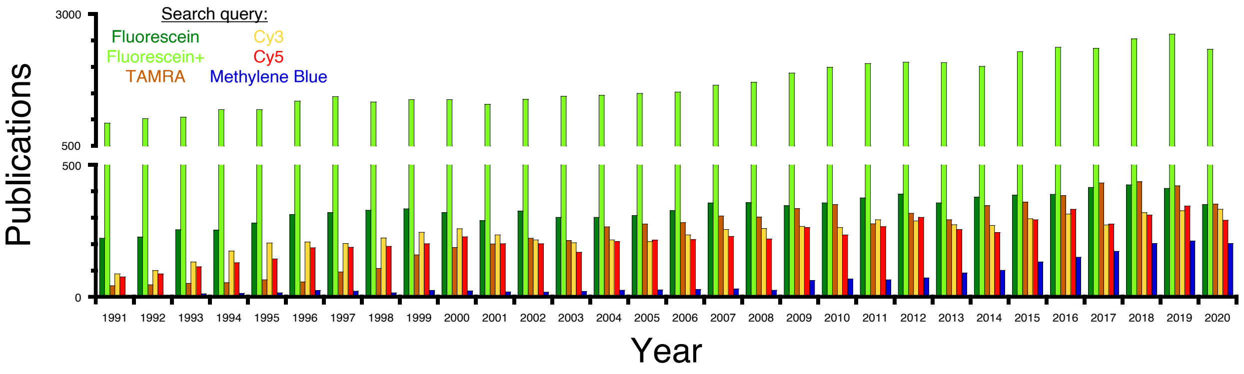

Figure 1.12. – Popularity of fluorescent dyes. Number of publications per year (1991-2020) for several popular fluorescent dyes used in DNA nanotechnology: Fluorescein, Fluorescein+ (wider search), TAMRA, Cy3, Cy5, and Methylene Blue. Overall, fluorescein is somewhat more popular than the other dyes, but when the wider search terms are considered (*e.g.*, FAM), it is significantly more popular than the other dyes. Search queries: **Fluorescein** ("Fluorescein" AND "Fluorescence"), **Fluorescein+** ("Fluorescein" OR "Carboxyfluorescein" OR "5-FAM" OR "6-FAM" OR "FAM" OR "Fluorescein isothiocyanate" OR "FITC" AND "Fluorescence"), **TAMRA** ("TAMRA" OR "Carboxytetramethylrhodamine" OR "TMR" OR "Tetramethylrhodamine" AND "Fluorescence"), **Cyanine 3** ("Cyanine 3" OR "Cyanine3" OR "Cy 3" OR "Cy3" AND "Fluorescence"), **Cyanine 5** ("Cyanine 5" OR "Cyanine5" OR "Cy 5" OR "Cy5" AND "Fluorescence"), and **Methylene Blue** ("Methylene Blue" AND "Fluorescence"). Search performed on Web of Science, 21 December 2020. Search results were not examined in detail, so they likely contained some irrelevant papers, but nevertheless show a general trend.

conjugating different isomers of FAM to oligonucleotides results in their displaying similar, albeit nonidentical, properties. More specifically, the isomers 5-FAM and 6-FAM show no significant difference for their UV-Vis absorption and fluorescence emission intensity, but 5-FAM displays a 3-5 nm redshift and a broader emission spectrum.[346] Thus, in most cases they ought to be interchangeable, but in experiments with multiple dyes, 6-FAM might be better due to less spectral overlap.[346] An important consideration, however, is high sensitivity to experimental conditions. This dye's fluorescence emission is sensitive to conjugation to proteins[347] and to nearby nucleotides, especially guanosine.[348, 349] Furthermore, fluorescein displays lower fluorescence emission at acidic pH due to its protonation state,[350-352] and similar pH sensitivity has been observed for oligonucleotide-conjugated FAM.[353] Various studies have also reported that FAM is insensitive or just moderately sensitive to temperature,[345, 353-355] with differences possibly due to buffer conditions, such as salt concentration.[354] This has enabled the use of FAM in DNA nanothermometers, for example.[286] In addition to sensitivity to the protonation state, as noted above, the sensitivity of fluorophores in general to pH and temperature can be attributed to increased collisional quenching.[355] Some properties of FAM and the other dyes discussed herein are listed in **Table 1.1**.

Table 1.1. – Summary of reported properties for fluorescent dyes used in this project. Dye wavelengths from the websites of Biosearch Technologies (FAM, ROX, Q570, Q670, P650), Glen Research (Cy3, Cy5, TAMRA), and refs [356, 357] (MB).

Name	λ_{ex} (nm)	λ_{em} (nm)	Sensitive to temperature?	Sensitive to pH?	Comment
FAM	498	520	None / Moderate	High	Popular
TAMRA	565	580	Moderate	No	-
ROX	575	602	No	No	-
CAL	540	561	?	?	Relatively new
Cy3 (and Q570)	546 (550)	563 (570)	High	Yes	Fluorescence enhanced by DNA and proteins
Cy5 (and Q670)	646 (644)	662 (670)	High	Yes	Degradation by ozone
MB	670	690	?	No	NIR emission
P650	460	650	?	?	Large Stokes shift

Another popular fluorophore choice is the rhodamine family of dyes. Rhodamines share the same triphenylmethane backbone as fluorescein but differ in that they have nitrogen atoms in the place of fluorescein's exocyclic oxygen atoms. Unlike fluorescein's green fluorescence emission, the rhodamines used in this project emit yellow/orange light (**Table 1.1**). While many types of rhodamine dyes exist, often with ambiguous nomenclature,[358] emphasis here is on those employed in this project, such as carboxytetramethylrhodamine (TAMRA) and carboxyrhodamine

(ROX). Concerning their properties, TAMRA is moderately sensitive to temperature[354], while ROX and the structurally similar Texas Red are not.[354, 355] Both have been reported to be insensitive to pH.[359, 360] Furthermore, TAMRA, and the structurally similar tetramethylrhodamine (TMR), are sensitive to quenching when proximal to guanosine. [348, 361] On the other hand, Texas Red is more sensitive to quenching by adenosine,[348] and presumably, this also applies to ROX. Another rhodamine fluorophore employed herein is Cal Fluor Orange 560 (CAL). Its sensitivity to temperature and pH have not been reported.

The cyanines are another popular family of fluorophores.[362] Here we focus on the well-known Cyanine 3 (Cy3) and Cyanine 5 (Cy5), and their respective analogues with similar properties, Quasar 570 (Q570) and Quasar 670 (Q670). Cy3/Q570 and Cy5/Q670 differ in the length of their polymethine chain, while Cy3 and Q570 (and, likewise, Cy5 and Q670) differ in their chemical connection to the oligonucleotides (*n.b.*, the dye chemistry is discussed and shown later in Chapter 2). Cy3 and Q570 display yellow fluorescence emission, while Cy5 and Q670 display red fluorescence emission. These dyes are popular for protein- and oligonucleotide-labelling applications. The fluorescence emissions of Cy3 and Cy5 are highly sensitive to temperature.[354, 355] The fluorescence of cyanine dyes tends to decrease with temperature, but increases with viscosity.[363] They are also sensitive to pH.[364] Their fluorescence is affected by proximity to nucleotides,[348] and these effects are sequence-dependent.[365-367] Interestingly, while most dyes tend to be quenched by nearby nucleotides, Cy3 undergoes fluorescence enhancement.[348, 365, 366] A similar effect has been observed for its interaction with proteins,[118, 368] which has been exploited in the abovementioned PIFE used to study protein-oligonucleotide interactions.[309, 314, 316, 318-320, 326] This contrasts with fluorescein, which can be quenched by interaction with proteins.[120, 369] Cy3 and Cy5 are also employed as a donor-acceptor pair in FRET, as are fluorescein and Cy3, as well as fluorescein and various rhodamines.[370] Finally, one notable detriment of Cy5 relative to Cy3 is the former’s susceptibility to ozone-induced degradation, which can affect signal intensity reproducibility;[371] a problem this project experienced with Q670.

Lastly, other fluorophores were also employed in this study. Methylene Blue (MB) is best known as a drug to treat the blood disorder methemoglobinemia[372] and as a redox probe in DNA-based electrochemical sensors.[297, 298] MB fluorescence is not sensitive to pH.[356] One advantage of

MB as a fluorophore is that its emission is in the near-infrared (NIR) range, which is useful for the study of samples that exhibit a high fluorescence background in the visible range (*e.g.*, ureters surgery, detection of breast cancer).[356, 357] This study also explored Pulsar 650 (P650), which is based on the Ru(bipyridine)$_3$ complex. Although it emits a weaker fluorescence signal, it displays a large Stokes shift.[373]

1.5.4 Molecular docking simulations

Molecular docking, shortened herein to just "docking", is a form of molecular modelling. It involves prediction of the structure of receptor-ligand complexes and the intermolecular interactions that stabilise the complex. The receptor is typically a protein, and the ligand is either a small molecule or another protein.[28, 374] In the early days of interactive molecular graphics software, researchers would attempt to find apparent chemical and geometric complementarity between two molecules ("Does this fit here?"). Later developments in docking software and protocols automated the search for complementarity and made the process more objective.[374] Early docking involved prediction and reproduction of known protein-ligand complexes, such as heme-myoglobin interaction.[375] Docking is widely used for drug discovery via structure-based drug design (SBDD).[28, 374] This is incredibly useful since it enables rapid *in silico* pre-screening of potentially millions of compounds from a database with a protein target before conducting laboratory experiments to evaluate their bioactive properties (*e.g.*, binding affinity, efficacy). This narrows down the number of candidate drugs for *in vitro* experiments to dozens or hundreds, which might be available or might even require novel chemical synthesis.[28, 376] This process saves time and money, and can enable discovery of drugs that might not have been found otherwise.

Docking relies on experimentally determined 3D protein structures often obtained by XRC, NMR, and cryo-EM[28] that are found in the Protein Data Bank (PDB; https://www.rcsb.org). There are currently more than 170000 macromolecular structures in this database. In spite of this collective achievement, however, only a small fraction of the protein sequences available on the UniProt database (https://www.uniprot.org) have corresponding structures on the PDB.[377, 378] To overcome this limitation, one can build a homology model via a known protein sequence (target) and a known structure of a similar protein (template).[379] This can be achieved, for example, via the SWISS-MODEL web server (https://www.swissmodel.expasy.org).[377, 380]

The principle of docking is summarised here.[28] First, one obtains the structure of the ligand (**Figure 1.13a**) and protein (**Figure 1.13b**). The molecule is docked into the cavity on the protein. On Swiss-Dock (http://www.swissdock.ch), this is done automatically by uploading the two structures. From this step, a variety of potential poses are obtained (**Figure 1.13c**). One then identifies the most likely conformation of the ligand and its interactions with the protein (**Figure 1.13d**), for instance, by the structure with the lowest energy. Determination of this energy involves two steps: 1) exploring the many conformations of various possible binding modes, and 2) prediction of the interaction energy for each conformation. For the first step, structural parameters of the ligand are modified (*e.g.*, torsional degrees of freedom) (**Figure 1.13e**). For this, there are two types of methods to generate an ensemble of all possible conformations to find the lowest energy conformation, systematic and stochastic. A systematic search goes through each rotatable bond while holding others fixed to probe the energy landscape of every possible conformation's interaction with the protein. Eventually, it will converge to the most likely binding mode to find the global minimum. Getting stuck in a local minimum is avoided by starting from multiple distinct conformations (**Figure 1.13f**). The other method, a stochastic search, involves random changes to the ligand's structural parameters to probe the energy landscape (**Figure 1.13g**). For prediction of the interaction energy of ligand-protein complexes, the algorithm considers factors such as intermolecular interactions, desolvation, and entropic effects. More parameters result in greater accuracy but come with a reduction of speed. Thus, energy scoring functions often balance accuracy with speed.[28]

Although most often used to screen drugs *in silico*, docking also has been used to study the interaction of various proteins with dyes, such as fluorescein and its derivatives,[381-384] cyanines,[385, 386] and others.[387, 388] In this project, docking was employed to understand how the dye component of various nanoantennas interacts with the target protein, AP. At present, crystal structure data is only available for APs with various inhibitors[107, 108, 112] as well as product molecules.[108, 389] Docking was performed on the SwissDock webserver,[390, 391] and analysis performed using UCSF Chimera software.[392] SwissDock is advantageous because it is designed for

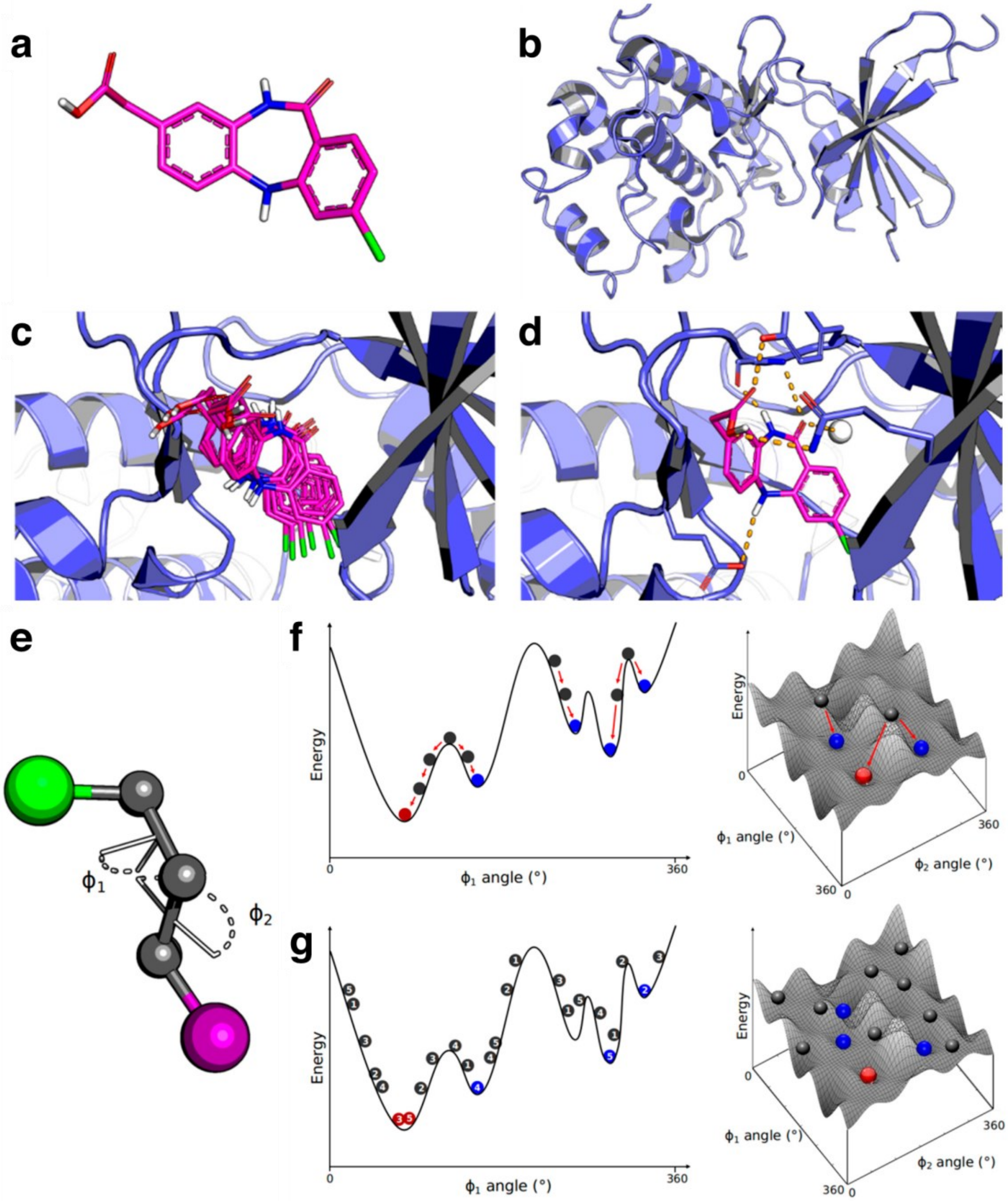

Figure 1.13. – Overview of molecular docking. Example structures of the (a) ligand and (b) protein. (c) The ligand at the binding site of the protein has many possible conformations. (d) After determining the most likely conformation, one can examine the ligand-protein interaction. (e) An example molecule with two dihedral angles (Φ_1 and Φ_2) that determine its conformation. (f) By the systematic search or the (g) stochastic search of the energy landscape, the algorithm can determine the local (blue circles) or global (red circles) energy minimum. Figure reproduced and modified from ref [28] with permission.

use by non-specialists who are outside the field of medicinal chemistry, plus it does not require any coding knowledge. In addition to that, all computations are performed on the server side, so the user does not require complicated software and high-level computational resources.

1.5.5 Molecular dynamics simulations

Molecular dynamics (MD) simulations explore the motions of individual atoms of a larger molecule by modelling the velocity and position of each atom as a function of time, such as the internal motions and conformational changes of proteins.[393, 394] These simulations can investigate events that happen too quickly to be easily measured experimentally[393] and provide mechanistic information about biomolecular phenomena.[29] MD simulations can be used to study protein folding and assembly[395] and ligand-protein interactions.[396, 397]

In an ideal world, one would predict the properties of a (macro)molecule via the time-dependent Schrödinger equation from first principles (*ab initio*).[29] In reality, however, it is necessary to make empirical approximations, especially for large systems consisting of many atoms where the size and timescales become prohibitively expensive in terms of computational resources.[398] MD simulations use macroscopic properties instead of a more precise quantum mechanical wavefunction description of the electrons, and therefore, they leverage a combination of Newtonian mechanics and empirical parameters. These are employed to calculate the interactions, and to describe the energy of a protein (or other system), as a function of its atomic coordinates – called a force field.[29, 398-400] It is also possible to employ more demanding quantum mechanics for a region of interest in order to improve results, such as an active site.[394]

Although MD simulations could be performed in a vacuum, real systems usually have a solvent, so MD simulations typically have one too. In one example for the protein lysozyme, it required 6000 water molecules to solvate. This increased the number of atoms from 2,900 to more than 20000.[29] This illustrates why MD simulations over a long timescale can be computationally demanding and require approximations. After adding the water, the next step is to minimise the system. It is not necessary to reach the energetic minimum, but it is important to not start the simulation very far from equilibrium because it could crash or distort the system. [29]

After running the MD simulation, various results can be obtained. One is the root mean square deviation (RMSD), used to measure changes of the protein backbone from its initial to final conformations over time.[378] This can be used, for example, to investigate the stability of native and mutant forms of a protein,[401] or the stability of a protein-ligand complex.[28] Another result obtained from MD simulations is the root mean square fluctuation (RMSF).[378] For this, the fluctuation of each amino acid is plotted for the entire sequence, and it is also useful for the study of mutations[378] and ligands.[402] Another application is studying the dynamics of complex formation and dissociation, whereby one can observe and even quantify the energy landscape and kinetics of these processes.[376] Finally, one can make a movie of the MD simulation for the purposes of presentation of these processes in a straightforward manner.[29]

This project uses MD simulations for two distinct purposes. In one case, the AP-dye complexes determined by docking were further examined with MD. The purpose of these simulations was to estimate the stability of the predicted binding sites for three dyes on AP. By gaining a better understanding of how dyes interact with AP, it sheds light on the mechanism of how the nanoantenna strategy can monitor enzyme function. In the second case, MD simulations involved the entire nanoantenna-SA-bAP complex. This enabled better understanding and visualisation of dye interaction near the enzyme's active site. Previous works have employed MD simulations to study the interactions of dyes and DNA,[365, 403, 404] dyes and proteins,[387, 388] and DNA and proteins.[405]

Chapter 2 – Fluorescent nanoantennas and their mechanism

2.1 Introduction

In Chapter 1, we discussed the existing methods to characterise protein function, with an emphasis on the enzyme, alkaline phosphatase (AP). These methods were grouped into three categories. First, there are synthetic substrates that, upon hydrolysis, generate a signal change detectable by UV-Vis spectroscopy, fluorescence spectroscopy, or other techniques. Their detriment, however, is that they do not represent biomolecular substrates of the enzyme. Second, there are substrate-specific assays. Their shortcoming is that a different assay will be needed for each substrate, and furthermore, such assays might not be available for other substrates of interest. Moreover, these methods are not typically used to study AP with biomolecular substrates.[138, 141, 168, 406-408] Third, there is the classic malachite green assay,[106] plus new variations of it and other strategies.[253] While useful for biomolecules, this classic assay cannot detect their hydrolysis in real time, plus it is a time-consuming and labourious technique.

We previously summarised the general idea of our biosensing strategy in **Figure 1.7**. This present chapter is about optimisation of our new method and understanding its mechanism. As described in the previous chapter, a nanoantenna has a fluorescent dye at one end, such as fluorescein (FAM), and biotin at the other end. The linker between them can be made from a flexible component, such as single-stranded DNA (ssDNA) or polyethylene glycol (PEG). The experiment starts with the nanoantenna in solution. Streptavidin (SA) is then introduced into the cuvette. This tetrameric protein has four biotin-binding sites that can capture the biotinylated nanoantennas with high affinity. Concurrently, signal quenching is observed due to FAM-SA interaction.[120-122] Together, these are called the nanoantenna-SA platform. Next, biotinylated AP (bAP) is introduced to the cuvette. Although the binding is slower, typically several minutes, a stable nanoantenna-protein complex will eventually form, which is also indicated by a fluorescent signal change due to dye-AP interaction. Finally, we observed that the FAM dye can sense events happening locally at the enzyme. For example, this enables real-time monitoring of the enzyme's transient substrate-bound state.

2.2 Tuning the linker

The nanoantenna-SA platform used to drive dye-protein interaction is convenient because, unlike covalent attachment strategies, it enables rapid testing of different nanoantennas. Indeed, covalently attaching dozens of different labelled DNA strands to a protein of interest could take many weeks of work for synthesis and purification, plus a lot of material. With the nanoantenna-SA platform, many nanoantennas can be assessed in a matter of hours, or at most, a few days. Moreover, in our experience, only a small amount of a given nanoantenna solution needs to be tested, so it can be saved for many other experiments.

We first explored how dye-protein interactions can be impacted by nanoantenna linker length (as measured in number of nucleotides, LX), ratio of nanoantennas to SA, and composition of the nanoantennas. As a “no linker” L0 nanoantenna, we selected a biotin-fluorescein conjugate. A previous study of a similar biotin-fluorescein conjugate and an SA mutant found that upon binding to SA via its biotin, its fluorescein moiety will be located just outside the biotin-binding site.[409] This short nanoantenna displayed significant fluorescence quenching upon binding (**Figure 2.1a**). Using single-stranded DNA (ssDNA), we increased the linker length to L6 and to L12, thereby enabling FAM to interact with more of the SA surface. These nanoantennas displayed moderate quenching but were similar to each other (**Figure 2.1a**), suggesting that their FAMs could bind to similar sites on SA (*n.b.,* this site is explored more in section 2.5). The longer L24 and especially L48 nanoantennas displayed reduced quenching (**Figure 2.1a**), suggesting weaker dye-protein interactions due to the lower effective concentration of the dye near SA. Alternatively, it is also possible that they could reach a higher affinity site, but which results in smaller fluorescence quenching. We also increased the ratio of nanoantennas added per SA. In this case, more quenching was observed with more nanoantennas (**Figure 2.1b**). We then varied the linker composition. A more flexible, hydrophilic, and less charged PEG-based nanoantenna was estimated by density functional theory (DFT) calculations to have a length equivalent to ~21 nucleotides (L21; **Figure 2.2**). This nanoantenna improved the FAM-SA interaction, as evidenced by increased quenching (**Figure 2.1c**). In contrast, a less flexible double-stranded DNA (dsDNA) L24 nanoantenna prevented the FAM-SA interaction (**Figure 2.1c**).

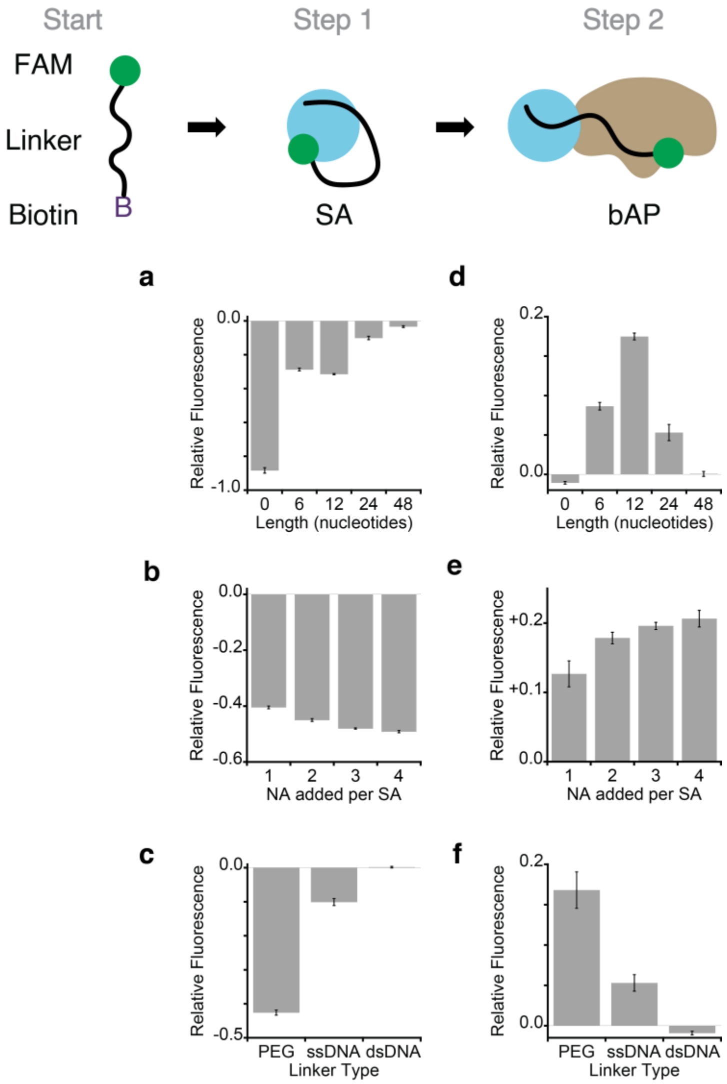

Figure 2.1. – Relative signal change for different linkers. Here, panels (a-c) represent the relative signal change for the nanoantenna binding to SA, and panels (d-f) represent the relative signal change for the subsequent binding of bAP. Parameters changed were the (a,d) linker length, (b,e) ratio of components, and (c,f) linker composition. See Supplementary Figure S2.1 for spectra. The cartoons represent the binding steps as shown in Figure 1.7.

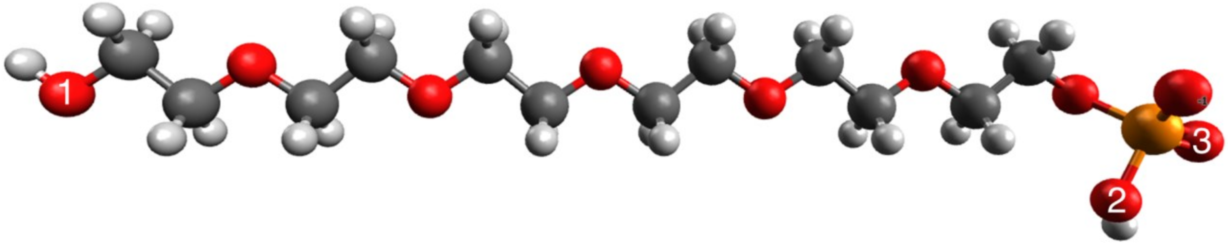

Figure 2.2. – PEG Linker Length. Since we compared nanoantennas based on their length in nucleotides, we aimed to determine the length of the PEG nanoantennas expressed in these units. We performed density functional theory (DFT)[410, 411] computations with the B3LYP functional[412-415] and the 6-311++G** basis set[416-420] to find the length of one PEG unit produced by the Spacer 18 amidite. From Point 1 to Point 2, where the next nucleotides would be located, the computed length is 21.436 Å. From Point 1 to Point 3, the maximum distance, the computed length is 23.547 Å. Based on dsDNA having a length of 3.4 Å per nucleotide,[421] one PEG unit, therefore, corresponds to 6.3 or 6.9 nucleotides, respectively. Since our main PEG-based nanoantenna was made from three PEG units and one unit of FAM-modified thymine (often called T_{FAM} or T 6-FAM), this results in a length of 19.9 or 21.8 nucleotides, respectively. Note that we did not count biotin in the length of any nanoantennas since it will be buried inside of streptavidin. Thus, by analogy, one could call it the *ca.* L21 PEG nanoantenna. We also used a longer PEG nanoantenna in Figure 2.6c, which is made from six PEG units. It similarly corresponds to 38.8 or 42.6 nucleotides, so one could call it the *ca.* L41 PEG nanoantenna. While this comparison with DNA length is imperfect,[422] it nevertheless helps to put the lengths of the nanoantennas into context.

Linker length and composition, and the nanoantenna to SA ratio, likewise affected the monitoring of protein binding to SA. As expected, due to its short length, L0 did not detect the binding of bAP to the nanoantenna-SA platform (**Figure 2.1d**). The longer L6 and especially L12 nanoantennas enabled FAM to detect bAP attachment, but L24 and especially L48 seemed to be too long to result in a high local concentration of FAM near bAP (**Figure 2.1d**). Sensitivity to bAP binding was also affected by the ratio of nanoantennas added per SA. Compared to adding just one nanoantenna per SA, adding two nanoantennas per SA led to higher relative signal increase upon bAP addition, with smaller improvements for three and four nanoantennas. Adding four nanoantennas per SA still resulted in a signal change upon introduction of bAP (**Figure 2.1e**). Since SA has only four biotin-binding sites, this suggests that steric hindrance and/or electrostatic repulsion play a role in assembly.[123] We decided to add 3 nanoantennas per SA to maximise fluorescent signal change without taking the risk of filling all biotin-binding sites, as might occur under a change of conditions. This aspect is discussed in further detail at the end of this section. As expected, we also observed that a flexible PEG linker enabled good FAM-bAP interaction, while a less flexible dsDNA linker did not (**Figure 2.1f**). Moreover, PEG linkers were less sensitive to pH variation, likely due to increased repulsion between negatively charged DNA linkers and proteins (**Figure 2.3**). These factors are summarised in **Figure 2.4.**

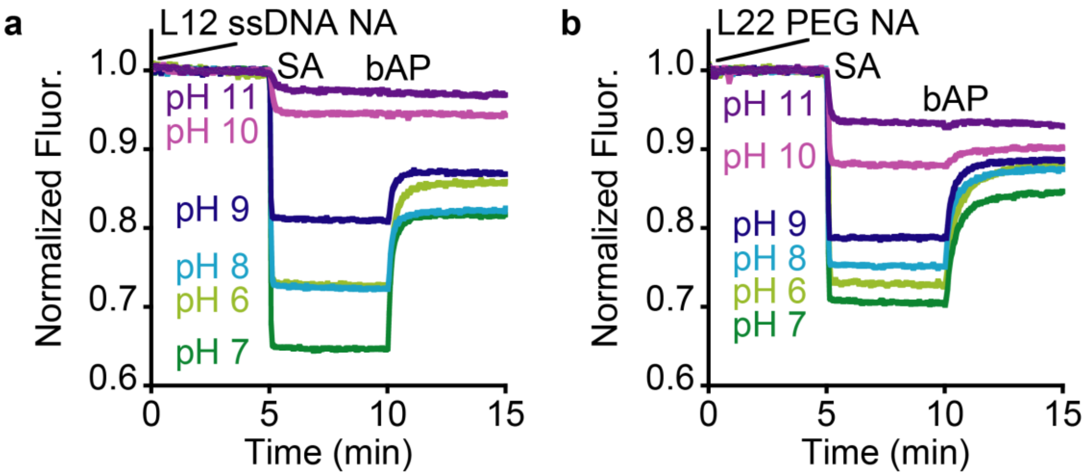

Figure 2.3. – PEG nanoantennas are less sensitive to pH variation than are DNA nanoantennas. The L12 ssDNA nanoantenna is less sensitive to the protein binding steps at alkaline pH, likely due to charge-charge repulsion between the negatively charged DNA linkers and proteins. The PEG nanoantenna has fewer phosphates, and therefore, less negative charge. Note that the isoelectric points (pI) of SA[336, 423] and AP[424, 425] are approximately 6 and 5.5, respectively. Note also that fluorescence signal is normalised due to pH sensitivity of the FAM dye.[426] Conditions: 150 nM L12 ssDNA nanoantenna or L21 PEG nanoantenna, 50 nM SA, and 50 nM bAP in 200 mM Bis-Tris (pH 6.0) or 200 mM Tris (pH 7.0, 8.0, 9.0) or 200 mM CAPS (pH 10.0, 11.0) and 300 mM NaCl (all), 37 °C.

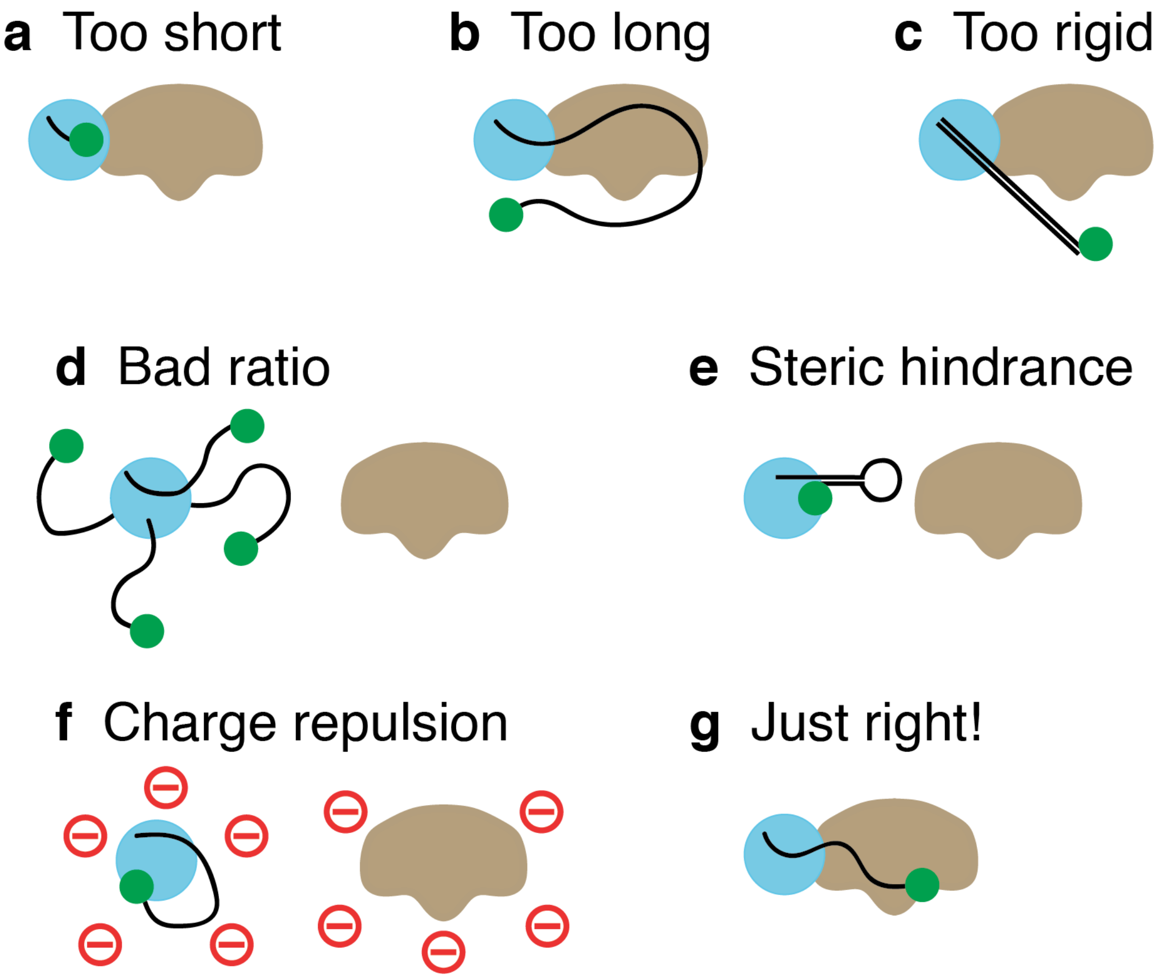

Figure 2.4. – Tuning the nanoantenna linker for optimal signalling. Nanoantennas that are (a) too short, (b) too long, or (c) too rigid will prevent FAM-bAP interaction in the nanoantenna-SA-bAP complex. (d) A bad ratio of components, for example, too many equivalents of nanoantennas added per SA, will prevent bAP from binding to the nanoantenna-SA platform. (e) Likewise, steric hindrance, for example, when employing a bulky molecular beacon nanoantenna, will prevent bAP from binding to the nanoantenna-SA platform. (f) A buffer with high alkaline pH will hinder formation of the nanoantenna-SA-bAP complex due to negative charge-charge repulsion, but this can be mitigated by using PEG-based rather than DNA-based nanoantennas. (f) Representation of a nanoantenna-SA-bAP complex when the nanoantenna is optimised in terms of length, flexibility, ratio of components, *etc*. Note that there are likely more than one nanoantenna and bAP per SA, but one of each is shown here for simplicity.

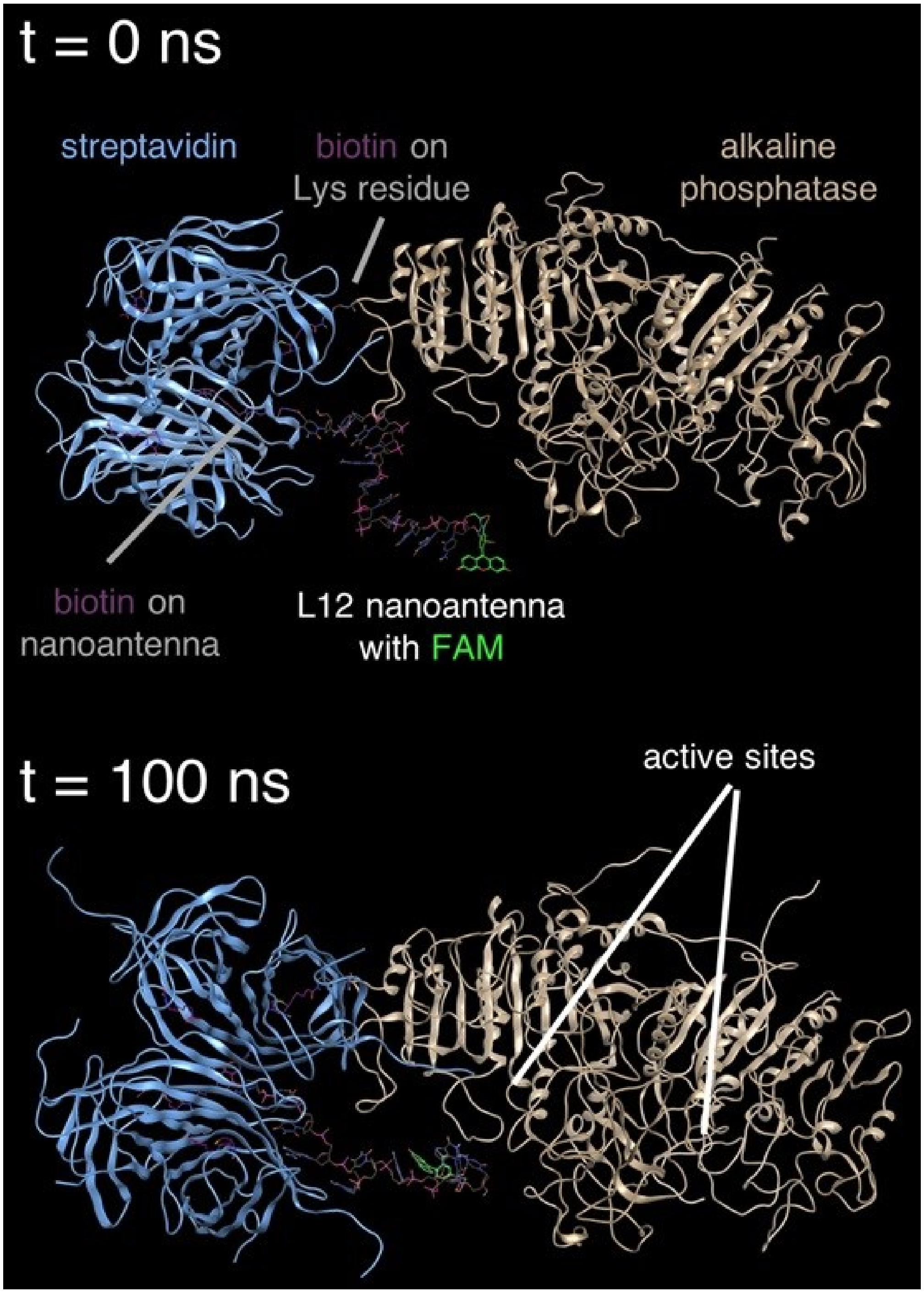

Figure 2.5. – Molecular dynamics (MD) simulation of a possible nanoantenna-SA-bAP complex. During the 100 ns simulation, the nanoantenna locates the FAM dye closer to its binding site near the enzyme's substrate-binding active site.

To further explore our hypothesis of the nanoantenna-SA platform mediating the interaction of FAM with bAP, we employed a molecular dynamics (MD) simulation by working in collaboration with Dr. Maximilian C. C. J. C. Ebert. The complex used in the simulation was based on the L12 optimal length nanoantenna, the crystal structure of SA,[427] and a homology model of AP (*n.b.,* details about the homology model are in section 2.5). However, we did not know which lysine residues of AP are biotinylated by the manufacturer, so we selected an exposed lysine that could plausibly be biotinylated. The MD simulation revealed that the FAM could reach the bound bAP, supporting our hypothesis regarding the dye-enzyme interaction (**Figure 2.5**). Of course, we chose the configuration of the nanoantenna-SA-bAP complex in the MD simulation, whereas in reality, it would consist of many different configurations. Likewise, we choose the exposed lysine residue, but others could be biotinylated too, so this result should be interpreted with that in mind. Nevertheless, if one considers that the nanoantenna's length is comparable to approximately one monomer of the AP dimer, then it is plausible that the nanoantenna could locate its FAM on AP under multiple different configurations of these components. Overall, the simulation supports our hypothesis that FAM on a L12 ssDNA nanoantenna can reach bAP. Note that in section 2.5 the probable FAM binding site on bAP will be discussed.

We next investigated the mechanism by which the nanoantennas generated a transient fluorescence spike during hydrolysis of the substrate, *p*-nitrophenylphosphate (pNPP). As expected, the most sensitive nanoantennas for probing bAP attachment were also the most sensitive for probing its catalytic activity (**Figure 2.6**). The largest fluorescence spike occurs with the L12 ssDNA nanoantenna, when compared to the shorter and longer ssDNA nanoantennas (**Figure 2.6a**). Employing a L12 poly-thymine (PolyT) nanoantenna provides a similar spike intensity to the L12 ssDNA nanoantenna (**Figure 2.6b**). As was the case with the protein binding steps, dsDNA nanoantennas are less sensitive (**Figure 2.6c**), while PEG-based nanoantennas are more sensitive (**Figure 2.6c**). We also explored the ratio of nanoantennas to SA and bAP. A nanoantenna:SA:bAP ratio of 3:1:2 provided a good trade-off between high fluorescence signal and the ability of the biotinylated enzyme to bind the remaining biotin-binding site. This corresponds to most experiments using this ratio with concentrations of 150 nM nanoantenna, 50 nM SA, and 100 nM bAP. Indeed, using a ratio of 12:1:2 prevented monitoring of pNPP hydrolysis (**Figure 2.7**). Furthermore, by employing a 36-nucleotide nanoantenna that forms a molecular beacon,[286, 300] the system requires a ratio of components of 6:1:2 to achieve its optimal signal (**Figure 2.6d**). This is attributed to steric hindrance of the bulky secondary structure of this DNA requiring a higher concentration to drive assembly of the nanoantenna-SA platform, and in turn, this bulkier structure preventing bAP binding.[123]

It is important to note that adding a ratio of 3 nanoantennas per SA does not mean that all SAs in the solution will have three bound nanoantennas. By assuming that all biotin-binding sites are equivalent and that complete binding occurs at nM concentration ($K_d = 10^{-14}$ M), one can calculate which biotin-SA complexes will form via a binomial distribution.[123] For a 3:1 ratio, the calculation indicates that 0.4% of SAs will have zero bound nanoantennas, 4.7% one, 21.1% two, 42.2% three, and 31.6% four. In other words, there will be almost no free streptavidin, few 1:1 complexes will be formed, and the substantial amount of fully saturated 4:1 complexes formed will be unable to bind the bAP. Thus, theoretically, bAP in most cases would only have the possibility to bind to complexes that have two or three nanoantennas. However, the data in **Figure 2.6d** show that unlike in the theoretical calculation's assumption that all nanoantennas bind, in the present experimental system it is clearly not the case. This suggests that steric hindrance and/or electrostatic repulsion reduce binding. Thus, the above calculation should be considered as an example of the diverse population of complexes that could be formed, rather than a concrete determination of the actual ratios formed in this system.

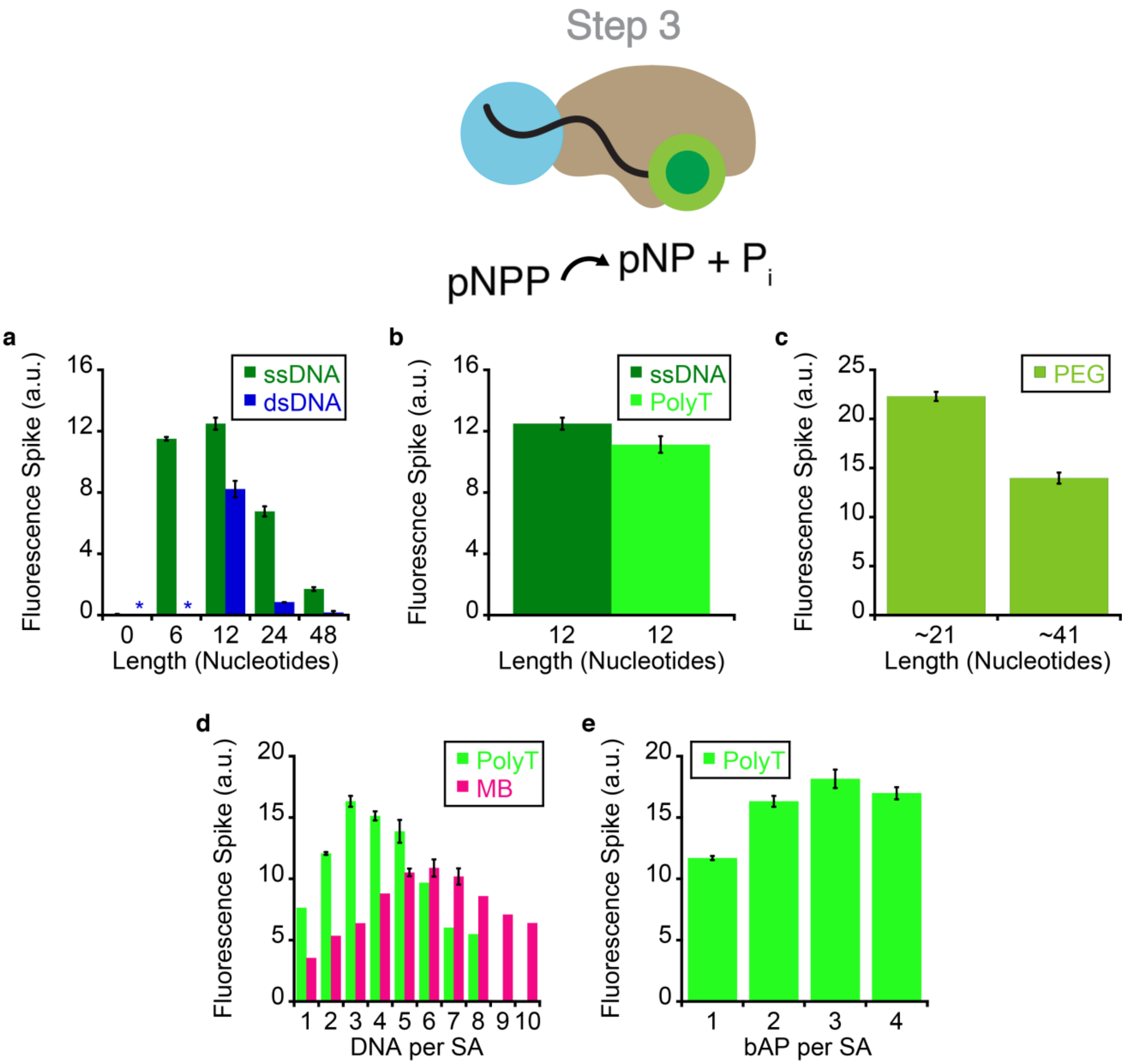

Figure 2.6. – Optimal nanoantenna length, composition, and ratio for monitoring of pNPP hydrolysis. (a) The L12 ssDNA nanoantenna displays the largest spike intensity during pNPP hydrolysis. Nanoantennas that are too short (L0, L06) or too long (L24, L48) have reduced FAM-bAP interaction, and therefore, a weaker signal during hydrolysis. Adding a cDNA strand (L12, L24, L48) to form a dsDNA nanoantenna makes it too rigid for FAM to interact with bAP in most cases, although the L12 dsDNA nanoantenna still provides a good spike intensity during pNPP hydrolysis. (b) L12 ssDNA and L12 PolyT nanoantennas of equal length give similar spike intensities during pNPP hydrolysis. (c) PEG-based nanoantennas also display length

dependence for the spike during pNPP hydrolysis. (d) The spike intensity during pNPP hydrolysis depends on the ratio of nanoantennas added. The nanoantenna:SA:bAP ratio of 3:1:2 gives the best spike intensity with the L12 PolyT nanoantenna, but a bulkier 36-nucleotide molecular beacon nanoantenna requires a ratio of 6:1:2 (*i.e.*, more nanoantennas) for its optimal signal due to steric hindrance. (e) The spike intensity during pNPP hydrolysis also depends on the ratio of bAP added. The nanoantenna:SA:bAP ratio of 3:1:3 is optimal, although to balance enzyme cost versus signal output, in most cases we used 3:1:2. Thus, most experiments used this ratio with concentrations of 150 nM nanoantenna, 50 nM SA, 100 nM bAP. Depending on the enzyme lot-to-lot variation, sometimes less enzyme was used to slow down the overall kinetics to obtain more data points per fluorescence signature in order to increase fitting accuracy (this aspect is discussed later in Chapter 3). Conditions: 100 µM pNPP, 200 mM Tris, 300 mM NaCl, 1 mM $MgCl_2$, pH 7.0, 37 °C. The cartoon represents the catalysis step as shown in Figure 1.7.

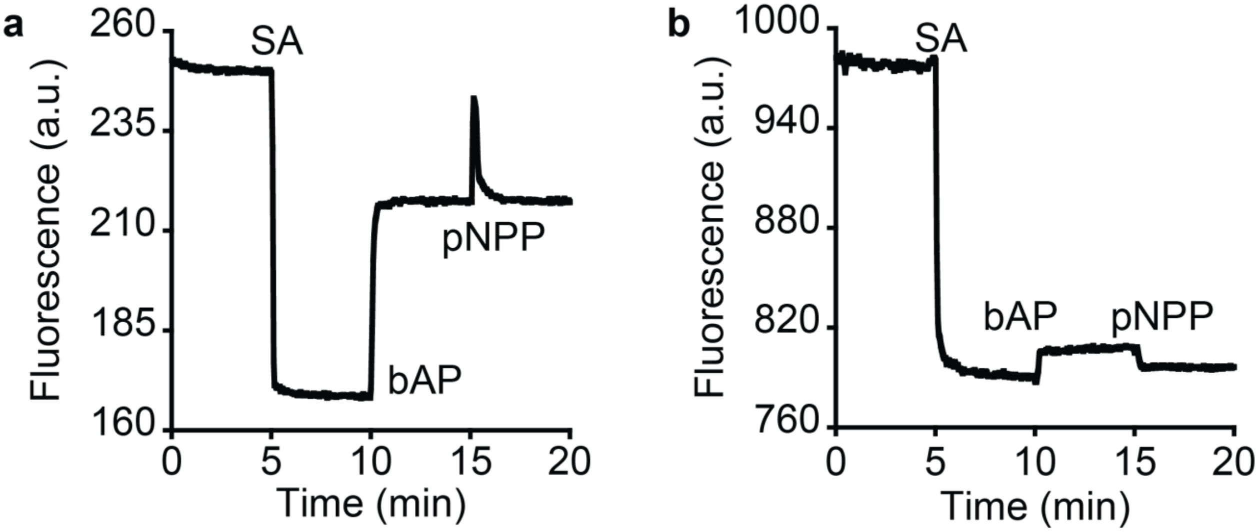

Figure 2.7. – Saturating streptavidin with nanoantennas prevents bAP binding. In (a), the nanoantenna:SA ratio is 3:1, which allows for subsequent binding of bAP and detection of pNPP hydrolysis. In (b), where the ratio is increased to 12:1, the platform is saturated and cannot efficiently detect bAP and pNPP hydrolysis.

2.3 Origin of transient fluorescence spike

We next examined the origin of the fluorescence spike observed during pNPP hydrolysis. No spike occurred when there was no hydrolysis reaction, such as upon addition of the reaction products, *p*-nitrophenol (pNP) and inorganic phosphate (P_i) (**Figure 2.8a-b**), or when using an enzyme without phosphatase activity (**Figure 2.8c**). We then tried a system with two types of nanoantennas: one without biotin but with FAM ("Global") and one with biotin but without FAM ("Dummy"). With these, we also did not observe a spike upon addition of pNPP (**Figure 2.8d**). We further checked whether we could monitor the function of the enzyme by its intrinsic tryptophan (Trp) fluorescence, rather than by using the nanoantennas.[55] For this, we used non-biotinylated AP since the bAP sample has bovine serum albumin (BSA) added by the manufacturer as a stabiliser, which also displays Trp fluorescence. However, we did not observe a signal change upon addition of substrate under various conditions (**Supplementary Figure S2.2**). We also tried to detect the hydrolysis reaction using a protein-binding dye, 8-anilinonaphthalene-1-sulfonic acid (ANS).[57] Although we could detect ANS binding to AP at high concentrations of the enzyme, this dye could not detect AP function (**Supplementary Figure S2.3**). We did, however, observe a spike with other nanoantenna attachment strategies, including covalent attachment to surface-exposed lysine residues of AP (**Figure 2.9a,b;** synthesised by Xiaomeng Wang, see section 6.1.10 Preparation of nanoantenna-AP covalent conjugate), and by using a commercially available SA-AP conjugate (**Figure 2.9c**). We could also observe the spike under various buffer conditions (**Supplementary Figure S2.4**), such as Tris, MOPS, HEPES and PIPES buffers. Furthermore, even after storage of the nanoantenna-SA-bPA complex in our standard buffer for over 100 days in the refrigerator, it was still possible to monitor the pNPP reaction (**Supplementary Figure S2.5**).

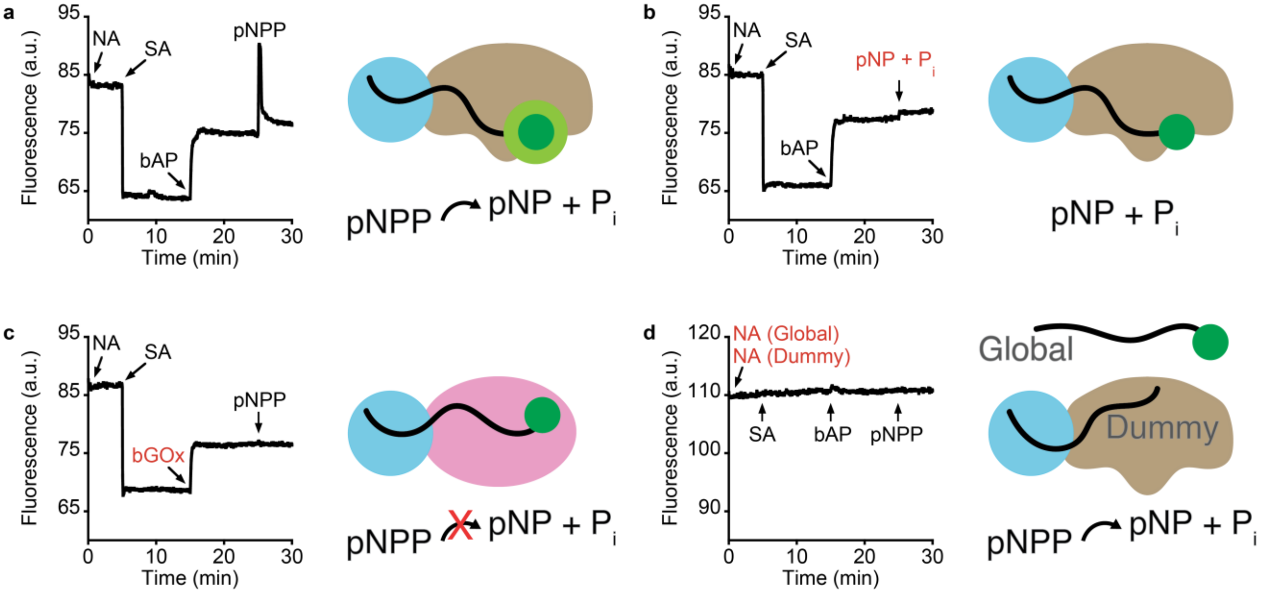

Figure 2.8. – The fluorescence spikes only when there is a hydrolysis reaction and when the nanoantennas are close to the enzyme. The spike is only generated following substrate hydrolysis when bAP is bound to the nanoantenna-SA platform. (a) Typical nanoantenna fluorescence signal used to monitor pNPP hydrolysis. (b) Addition of the reaction products, *p*-nitrophenol (pNP) and inorganic phosphate (P_i), does not give a fluorescence spike because there is no hydrolysis reaction. (c) Using an enzyme without phosphatase activity and which will not hydrolyse pNPP (*e.g.*, biotinylated glucose oxidase, bGOx), does not give a fluorescence spike because there is no hydrolysis reaction. (d) Here, the "Dummy" nanoantenna does not have the dye (*i.e.*, no FAM) but it is still attached to SA via its biotin, while the "Global" nanoantenna has FAM but it is not biotinylated and instead is free in solution. Thus, the hydrolysis reaction of pNPP still occurs, but this system does not monitor it since there is no substantial FAM-bAP interaction. Conditions: 150 nM L12 PolyT nanoantenna, 50 nM SA, 150 nM bAP and 100 µM pNPP in 200 mM Tris, 300 mM NaCl, 1 mM $MgCl_2$, pH 7.0, 37 °C.

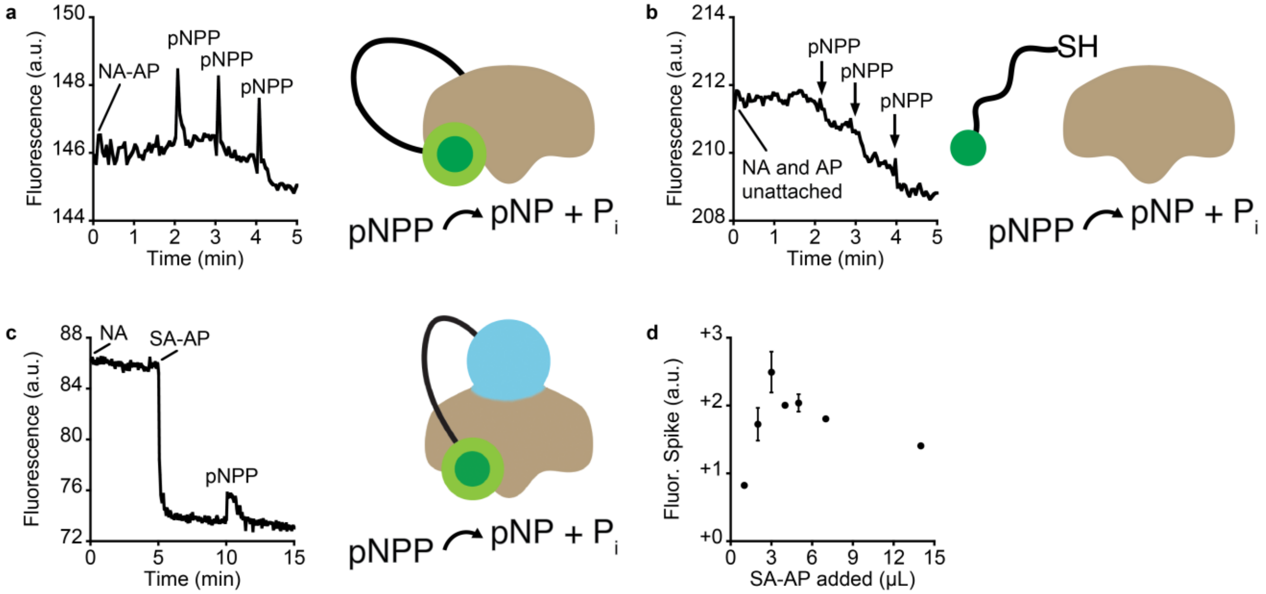

Figure 2.9. – Alternative attachment strategies of nanoantenna to protein also work. (a) Here, 3′-thiolated L12 ssDNA nanoantennas were covalently attached to the lysine residues of AP (see section 6.1.10 for method). Note that calf intestinal AP has 21 lysine residues per monomer.[428] This nanoantenna-AP conjugate displays a spike during pNPP hydrolysis similarly to the nanoantenna-SA-bAP complex. Although significant synthesis steps are involved, it may be desirable for applications for which one does not wish to use the biotin-SA platform. Note that the power was reduced from 635 V to 450 V due to the high baseline. (b) As a control, unattached thiolated nanoantennas and unconjugated AP do not display a spike during pNPP hydrolysis. Conditions: ~40 nM nanoantenna-bAP conjugate and 100 µM pNPP in 200 mM Tris, 300 mM NaCl, 1 mM $MgCl_2$, pH 7.0, 37 °C. (c) Here, a commercially prepared conjugate of SA covalently attached to AP (SA-AP) was used. The kinetic signature is shown for the PolyT L24 nanoantenna binding to SA-AP that results in fluorescence quenching, followed by pNPP hydrolysis (100 µM) that results in a spike. (d) Without knowledge of the protein conjugate's molecular weight due to an unknown number of conjugated SAs added by the manufacturer, we instead optimised using SA-AP volume (1, 2, 3, 4, 5, 7 and 14 µL SA-AP; with triplicate measurements for 2 to 5 µL near the apparent maximum). Even after this optimisation, however, the spike intensity during pNPP hydrolysis remains weaker compared to using the SA and bAP strategy. Overall, these results show that no matter which attachment strategy is used, and despite some being better than others, FAM will still find its binding site on the AP

enzyme. Conditions: 150 nM nanoantenna, 1 to 14 µL SA-AP and 100 µM pNPP in 200 mM Tris, 300 mM NaCl, 1 mM $MgCl_2$, pH 7.0, 37 °C.

2.4 Nanoantennas are sensitive to small chemical modifications

Note to the reader: The previous experiments in this chapter were performed with bAP from a commercial supplier. However, we subsequently experienced substantial lot-to-lot variation. In summary, the first orders of bAP (*n.b.,* several lots but collectively referred to as the first for simplicity) that we used while initially exploring the nanoantenna concept all displayed similar function and kinetics for pNPP hydrolysis. Then, a subsequently received second lot did not work for the nanoantenna sensing strategy. As part of our efforts to overcome this problem, we biotinylated AP ourselves via a biotinylation kit (see section 6.1.9 Preparation of biotinylated AP). We used this bAP in some experiments, including this section. To differentiate it from the commercial bAP, we called it the "homemade bAP". This bAP displayed similar kinetics to the first lots of commercial bAP (details about this are in Chapter 3). However, after discussion with the manufacturer, who agreed to make a new lot of bAP, we found that this third commercial lot worked well again for the nanoantenna strategy, albeit with faster kinetics (also more details in Chapter 3). Although we did not determine why the second lot of bAP did not work, it might be due to enzyme sample variation,[428-433] and if so, this problem could possibly be prevented by employing a recombinant AP.[434] Another possible origin of the problem could be a lack of optimisation of the biotinylation procedure, although we did not explore it. Biotinylation typically does not affect AP function,[435] but the nanoantenna strategy could plausibly be affected by different biotinylation procedures. Overall, these observations suggest that most preparations of bAP should work with the nanoantenna strategy, although there might be some problems concerning enzyme variation and biotinylation procedure standardisation. Note that all comparisons shown in a given figure in this thesis were performed with the same lot of bAP. Incidentally, this problem having occurred at this stage of the project was fitting because this section discusses how subtle differences in chemistry can affect the dye-protein interactions.

We observed that the intensity of a nanoantenna's fluorescence in the different states (*i.e.*, after addition of SA, bAP and pNPP) was sensitive to small chemical modifications. We tested this by employing a dsDNA nanoantenna, whereby the L12 ssDNA nanoantenna with the FAM dye at the 5′-end was bound to a complementary DNA strand (cDNA) containing the chemical modification at its 3′-end (**Figure 2.10a**). These modifications included phosphate, a hydrophobic C_{16} alkane chain, another containing a disulfide, and one with a thiol group (sulfhydryl group) (**Figure 2.10b**). These affected the signal change observed for the SA and bAP binding events, although they did not affect the sensitivity of the nanoantenna toward pNPP hydrolysis (**Figure 2.10c,d**).

Likewise, we also tested distinct locations of FAM on the DNA linker. This was done by comparing 5′-end thymine modified with FAM (T 6-FAM), which was used in the above experiments, with 5′-end 6-FAM, 5′-end 5-FAM, and 3′-end 5-FAM (**Figure 2.11a**). The chemical connection of FAM to the linker differed, so the experiment was not simply a difference of having 5′-end FAM versus 3′-end FAM, but also 5-FAM isomer versus 6-FAM isomer, and two different attachment chemistries for 6-FAM. Another difference is that the chemical connection to the DNA linker of 5′-end 5-FAM is longer than that of 3′-end 5-FAM. These differences in the local environments of the dyes could affect their fluorescence emission. For example, since the quenching efficiency of FAM by nucleobases follows the order of G > A > C ≈ T,[348] and the sequence of this DNA nanoantenna is 5′-TTATTGATCGGC-3′, this resulted in the initial fluorescence of the unbound nanoantennas being dissimilar. More specifically, the fluorescence of the 3′-end 5-FAM was about half as intense as those at the 5′-end. On the other hand, as expected,[346] the 5-FAM and 6-FAM isomers at the 5′-end displayed similar fluorescence. Similarly, the fluorescence did not differ substantially for the two different connection types for T 6-FAM and 6-FAM. We further observed, however, that these changes of dye position and attachment chemistry resulted in the nanoantennas displaying differences in sensitivity to the SA and bAP binding events, as well as to pNPP hydrolysis (**Figure 2.11b**). These modifications are likely to subtly perturb the FAM-bAP interaction, and as a consequence, the ability of FAM to monitor the enzyme's function.

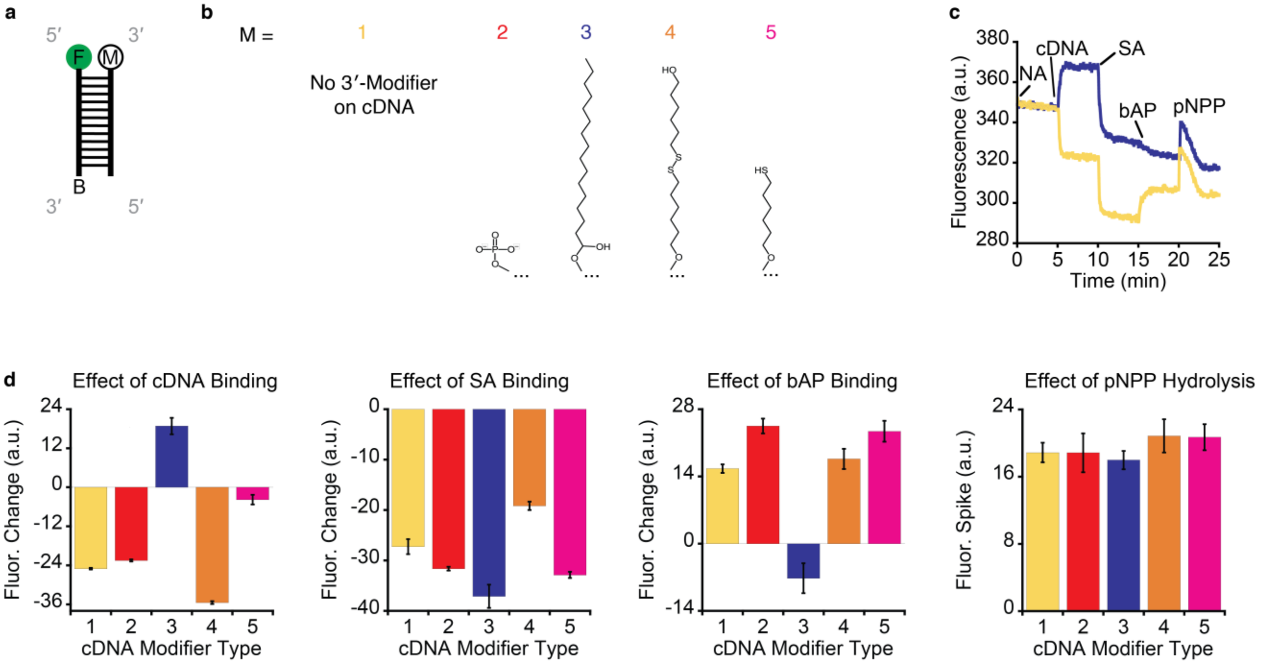

Figure 2.10. – Effect of various chemical modifiers near FAM on signal change upon complementary DNA binding, SA binding, bAP binding, and pNPP hydrolysis. Here, we investigated whether various chemical modifications near the dye ("Modifiers") could affect the fluorescence signal of FAM by changing its interaction with bAP. (a) We used the L12 ssDNA FAM nanoantenna (5′ T 6-FAM) with a complementary DNA strand (cDNA) containing the Modifier located at the 3′-end. (b) The Modifiers are numbered as follows: 1 (yellow) indicates the cDNA without a Modifier; 2 (red) is the cDNA with phosphate; 3 (blue) is the cDNA with a hydrophobic C_{16} alkane chain; 4 (orange) is the cDNA with a modifier that contains a disulfide that would normally be cleaved before use to provide thiol functionality; 5 (pink) is a cDNA with the cleaved thiol. (c) Example kinetic signatures and (d) summary of all results. In short, the SA and bAP binding steps display different intensities with each Modifier, but nevertheless they are qualitatively similar in all cases (*i.e.*, signal up or down). The exception to this is the C_{16} alkane chain, which results in fluorescence quenching when bAP binds. In all cases, the spike intensity during pNPP hydrolysis was similar. Conditions: 15 nM nanoantenna, 75 nM cDNA, 5 nM SA, 10 nM homemade bAP, 25 µM pNPP, pH 8.0, 100 mM Tris, 10 mM NaCl, 37 °C.

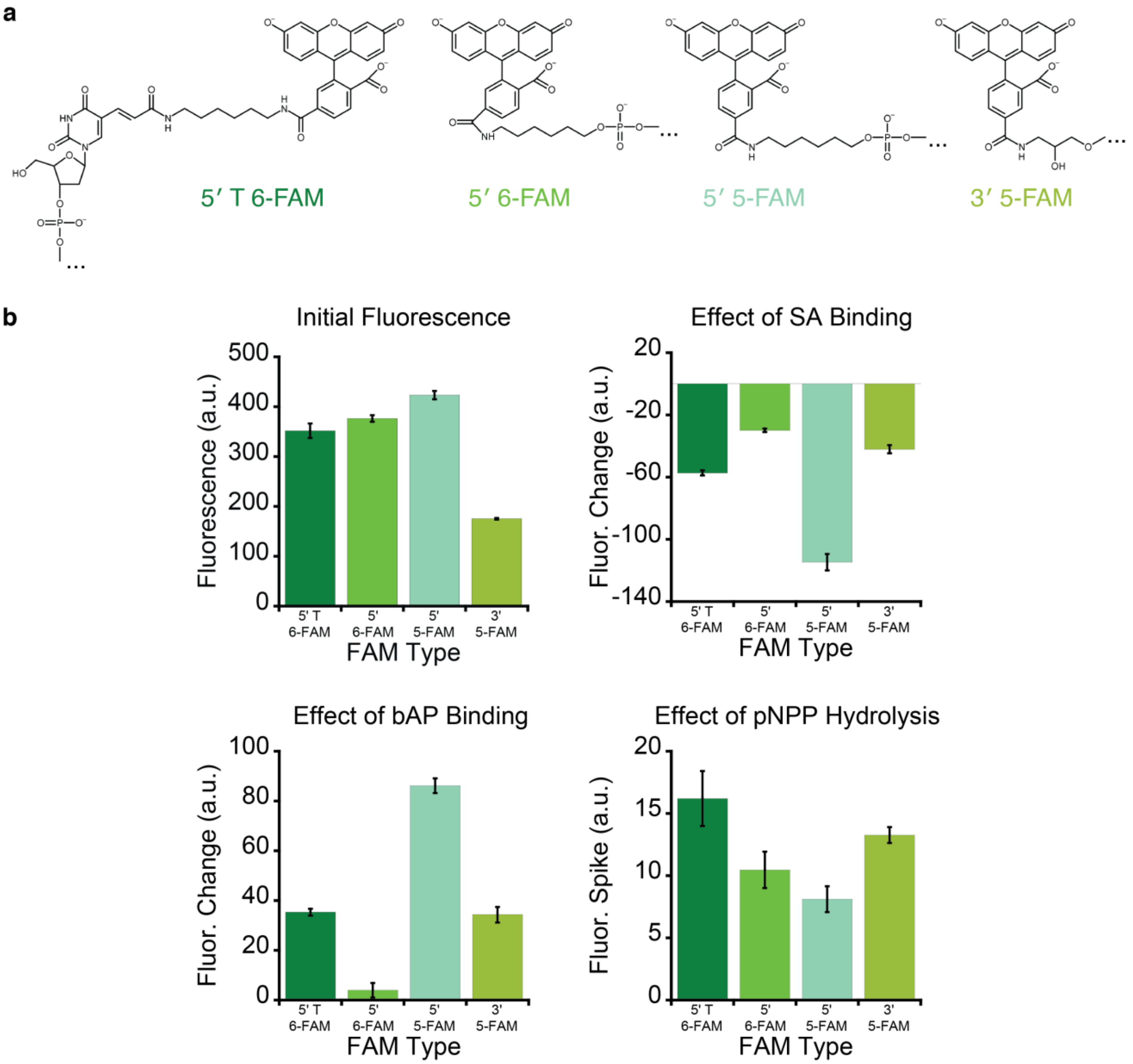

Figure 2.11. – Effect of FAM connections and isomer on SA binding, bAP binding, and pNPP hydrolysis. (a) In most of this study, we used a L12 ssDNA nanoantenna with 5′ thymine 6-carboxyfluorescein (5′ T 6-FAM). Here, however, we also tested other FAM connections on the same DNA sequence: 5′ 6-carboxyfluorescein (5′ 6-FAM), 5′ 5-carboxyfluorescein (5′ 5-FAM), and 3′ 5-carboxyfluorescein (3′ 5-FAM). (b) Shown are the initial fluorescence values, the quenching of fluorescence upon SA binding, the increase of fluorescence upon bAP binding, and the transient fluorescence spike intensity during pNPP hydrolysis. Despite the similar fluorescence emission of 5-FAM and 6-FAM when conjugated to DNA,[346] the various FAM nanoantennas display different trends for protein binding and pNPP hydrolysis. These

differences are likely due to how the chemical connection subtly affects FAM-bAP interaction. Conditions: 15 nM nanoantenna, 5 nM SA, 10 nM homemade bAP, 30 µM pNPP, pH 8.0, 100 mM Tris, 10 mM NaCl, 30 °C. PMT voltage = 800 V.

2.5 FAM binding site on SA and AP

The above results show that the FAM dye on the nanoantenna displays a specific fluorescence signature upon binding to SA, upon subsequent binding to bAP, and during the catalytic function of bAP (*i.e.*, pNPP hydrolysis). A reasonable interpretation would be that the FAM dye is interacting with SA and bAP. The MD simulation, furthermore, backed this hypothesis of the nanoantenna being able to extend the dye toward bAP. But *where* is the dye located on these two proteins? Experimental and computational techniques may shed light on this question.

We first compared the effect of adding excess biotin to cuvettes containing the nanoantenna-SA platform built using either L0 or L12 nanoantennas. The rationale here is that the short L0 nanoantenna's FAM should be located just outside a biotin-binding site,[409] whereas the longer L12 nanoantenna can potentially reach other locations on the protein. When using the L0 nanoantenna, we observed that adding excess biotin does not significantly affect the fluorescence of the nanoantenna-SA platform (**Figure 2.12a**). This indicates that, as expected, the L0 nanoantenna is not replaced by biotin on SA (although it might be after several hours[339]), and that its fluorescein moiety is unaffected by the binding of the incoming biotins at the previously unoccupied biotin-binding site(s), probably 1-2 per SA. In contrast, adding excess biotin results in increased fluorescence of the longer L12 nanoantenna, although not to the initial level of its unbound state (**Figure 2.12b**). This shows that the FAM moiety is affected by the binding of the incoming biotins at the previously unoccupied biotin-binding site(s). This observation for our DNA-based nanoantennas agrees with previous studies of longer biotin-fluorescein conjugates, which can locate their fluorescein moiety just outside unoccupied biotin-binding sites and which can be ejected therefrom by biotin binding.[120, 121] Since the fluorescence does not return to the initial signal baseline in the presence of biotin, the FAM moiety on our nanoantennas likely interacts with some other location(s) on the SA surface that still results in quenching, albeit less.

Next, we consider the effect of excess free biotin on the L0 or L12 nanoantenna-SA-bAP complex. After the addition of bAP to the L0 nanoantenna-SA platform, there is no signal change (**Figure 2.12c**). Subsequent addition of biotin and then pNPP also do not result in an appreciable signal change (**Figure 2.12c**). Thus, the L0 nanoantenna remains unaffected by biotin, and since it cannot reach the bound bAP, it cannot sense the hydrolysis of pNPP either. In contrast, the fluorescence of the L12 nanoantenna increases upon addition of bAP (**Figure 2.12d**). Subsequent addition of excess biotin has only a slight effect (**Figure 2.12d**), supporting the stability of the complex whereby the nanoantenna's biotin moiety is not displaced by the excess free biotin. Furthermore, the sustained ability of the nanoantenna's FAM to sense pNPP hydrolysis suggests the stability of the complex.

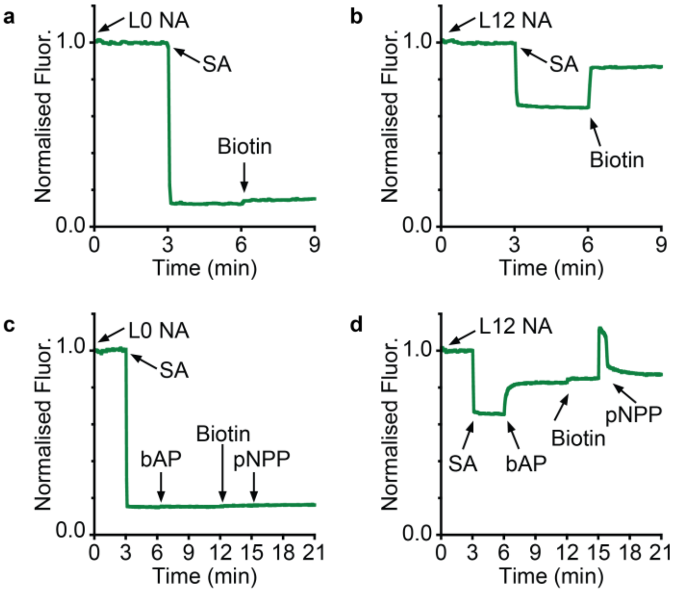

Figure 2.12. – Addition of excess biotin. Effect of biotin on the (a) L0 and (b) L12 nanoantenna-SA platform. Effect of biotin on the (c) L0 or (d) L12 nanoantenna-SA-bAP complex. Data were normalised relative to the initial fluorescence signal before adding SA. Conditions: 150 nM nanoantenna, 50 nM SA and 100 nM bAP in 1000 nM biotin in 200 mM Tris, 300 mM NaCl, 1 mM $MgCl_2$, pH 7.0, 37 °C.

To assess the above hypothesis of where the nanoantenna's FAM is located on SA and bAP, we employed molecular docking. For this, we used Swiss-Dock.[390] A crystal structure of SA was already available (6M9B),[427] but a homology model of AP had to be made from the sequence of bovine intestinal AP (P19111) and the crystal structure of human placental AP (1ZEF).[380, 428, 436, 437] The protonation state of the various ligand molecules was determined by MarvinSketch software and in consultation with the available literature.[343, 350, 438-441]

We started by docking biotin onto SA. Unsurprisingly, the docking resulted in its binding at a biotin-binding site (**Figure 2.13a**).[427] It was reproducible in 10/10 jobs, albeit not always at the same one of the four equivalent sites, and with an average energy score that was negative (-43.33 ± 1.42 kcal/mol), which supports the stability of the binding. Next, we docked the biotin (5-fluorescein) conjugate (*i.e.*, the L0 nanoantenna) onto SA, which resulted in its biotin moiety being in a biotin-binding site, with its fluorescein moiety located just outside (**Figure 2.13a**). This was reproducible in 10/10 jobs, although the orientation of the fluorescein moiety differed from job to job. The average energy score was positive (8.20 ± 1.14 kcal/mol). Since the docking simulation correctly predicted its known binding site,[409] the single-digit positive energy score might reflect the challenges faced for accurately predicting binding affinities.[442] As an approximation of the L12 nanoantenna, we further docked fluorescein onto SA. This resulted in its binding just outside the biotin-binding sites in 9/10 jobs. However, a much higher energy score was determined for fluorescein (57.91 ± 0.31 kcal/mol), which supports that the interaction would be too weak for any significant binding to occur. For comparison, a previous study involving human serum albumin (HSA) and fluorescein indicated a dissociation constant (K_d) of 100 µM.[119] Fluorescein, therefore, would not appreciably bind to SA at nM concentrations. We propose, however, that in the nanoantenna-SA platform, the high local concentration drives dye-protein interaction that would not otherwise occur with free dye. Indeed, the fluorescence quenching observed when the nanoantenna binds to SA suggests that it is at least binding *somewhere* on SA. Based on the molecular docking simulations, we expect that the high local concentration-driven binding site will be just outside an otherwise unoccupied biotin-binding site. Ejection of FAM from its binding site via the incoming higher affinity biotin (K_d in fM range), in a manner reminiscent of host-dye conjugate biosensors with a suitable linker length detecting the binding

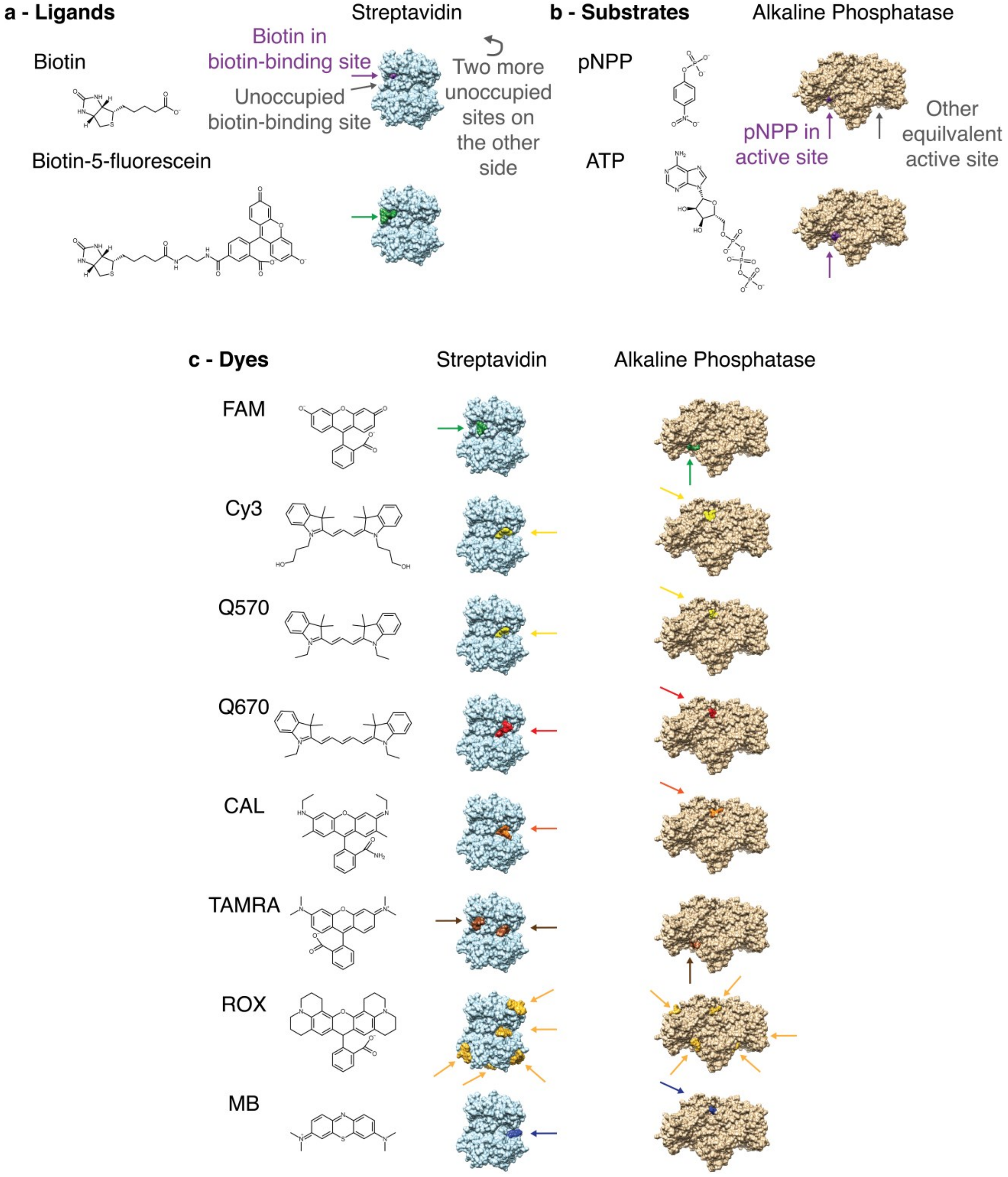

Figure 2.13. – Docking of dyes and substrates with proteins. (a) The simulations predicted that biotin binds in the biotin-binding sites (BBS) of SA.[427] Likewise, biotin-5-fluorescein binds with its biotin moiety in the BBS and its fluorescein moiety outside.[409] (b) The simulations predicted that the substrates pNPP and ATP bind at the active sites of AP. (c) The simulations predicted

that for SA, FAM binds near the BBS,[120, 121, 443] while Cy3, Q570, Q670, CAL, and MB bind in another pocket. TAMRA binds near the BBS and the other pocket in 4/10 and 6/10 jobs, respectively. For AP, FAM and TAMRA bind near the active site, while other dyes bind in a region associated with the catalytic function of mammalian APs.[220] ROX binding was not reproducible for SA and AP (examples shown). Simulations were reproducible in 9/10 or 10/10 jobs, unless noted otherwise.

of a target analyte,[444] is further supported by our above experimental data (**Figure 2.13b**) and previous studies involving similar systems.[120, 121]

Next, we considered the homology model of AP. We docked two substrates, pNPP and adenosine triphosphate (ATP). Again, unsurprisingly, these simulations resulted in the substrates' phosphate moiety being located inside either of the two equivalent active sites of AP and both were reproducible in 10/10 jobs (**Figure 2.13b**).[108] Since the predicted binding sites of biotin with SA, the biotin-fluorescein conjugate with SA, pNPP with AP, ATP with AP, and likely FAM with SA, were all accurate and agree with the available literature[108, 120, 121, 409, 427] and our experiments, we expected that molecular docking might also be able to predict the high local concentration-driven binding site of FAM on AP. We observed that molecular docking predicts that fluorescein binds just outside either of the two equivalent active sites of AP, and this was reproducible in 10/10 jobs (**Figure 2.13c**). Similar to the above results, however, the average energy score for pNPP was negative (-31.10 ± 0.03 kcal/mol) but for fluorescein it was positive (30.54 ± 0.53 kcal/mol). This again shows the necessity of the nanoantenna strategy to drive dye-protein interaction that would not occur otherwise. This predicted binding site is further supported by the large transient spike of FAM fluorescence observed upon addition of a substrate with the nanoantenna-SA-bAP.

2.6 Nanoantennas with different dyes

The testing of chemically diverse dyes on ssDNA L12 nanoantennas provides information about the signalling mechanism and potential universality of the strategy. We started by employing molecular docking to predict where the chemically diverse dyes can bind to AP. These dyes are Cyanine 3 (Cy3), Quasar 570 (Q570), Quasar 670 (Q670), Cal Fluor Orange 560 (CAL), carboxytetramethylrhodamine (TAMRA), carboxyrhodamine (ROX), methylene blue (MB) and Pulsar 650 (P650) (**Figure 2.13c**). Cy3, Q570 and Q670 belong to the cyanine family,[445] while CAL, TAMRA and ROX are in the rhodamine family.[358] In addition to chemical structure, these dyes all display different properties, such as their hydrophobicity (**Supplementary Figure S2.6**), which could affect their binding sites. The docking simulation revealed that TAMRA also likely binds near the AP active sites (9/10 jobs), and that ROX does not have a reproducible binding site. Interestingly, Cy3 (9/10), Q570 (10/10), Q670 (10/10), CAL (10/10) and MB (10/10) were predicted to bind at a location distal to the active sites (**Figure 2.13c**) that has also been associated with catalytic function.[220] Note that the same arguments for FAM concerning the positive energy scores and high local concentration-driven interactions apply to these dyes too. For example, we observed positive average energy scores for Cy3 with SA (26.31 ± 0.72 kcal/mol), CAL with SA (58.23 ± 0.74 kcal/mol), Cy3 with AP (28.37 ± 0.79 kcal/mol), CAL with AP (58.02 ± 0.55 kcal/mol).

We then tested these dyes at the 3′-end of L12 ssDNA fluorescent nanoantennas. Excitingly, all nine dyes tested enabled monitoring of the SA and bAP binding events, albeit weakly in some cases. Shown here for brevity are FAM, CAL, and Cy3 (**Figure 2.14**, see other dyes in **Supplementary Figure S2.7**). In contrast to FAM, Cy3 shows increased fluorescence upon binding to SA and decreased fluorescence upon bAP binding,[316, 318, 319] and it is more sensitive with a dsDNA linker. However, similar to FAM, it is affected by its chemical connection (see Cy3 *vs.* Q570 **in Supplementary Figure S2.7e-f**). We further observed that nanoantennas with FAM, Cy3, and CAL enabled the monitoring of pNPP hydrolysis. Crucially, while the three dyes provided different sensitivities towards the functional events, they all exhibited the same kinetics for pNPP hydrolysis (**Figure 2.15**), indicating that the dye-protein interactions exploited herein did not interfere with protein function. Note that kinetics of substrate hydrolysis observed with different dyes is further examined in the next chapter (end of section 3.5). From a practical perspective, FAM remains the best dye for monitoring AP’s function. However, from a mechanistic perspective, the other dyes provide convincing evidence that nanoantennas employing chemically diverse dyes can probe conformational changes at various locations on the enzyme.

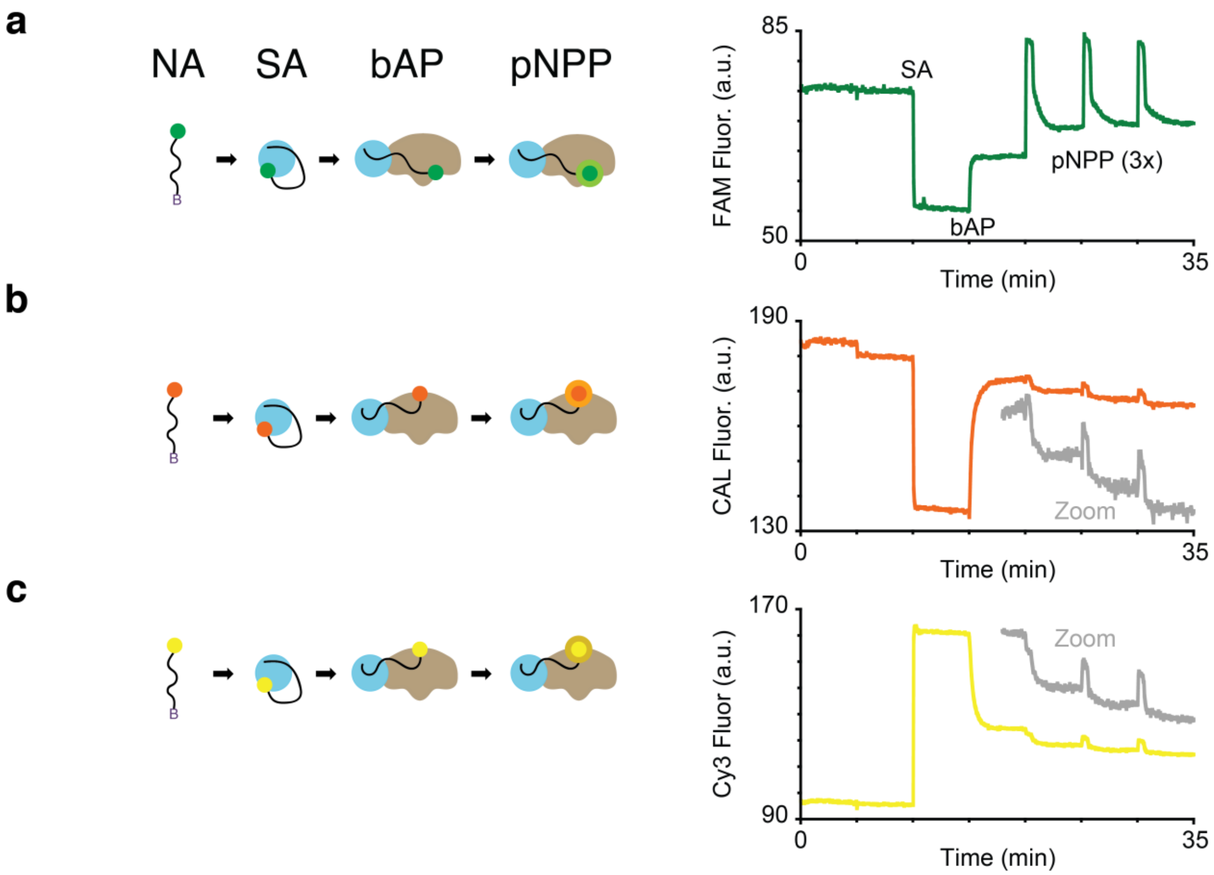

Figure 2.14. – Probing different regions of the AP surface with FAM, CAL and Cy3. Kinetic signatures of ssDNA nanoantennas with (a) FAM, (b) CAL, or (c) Cy3 for SA and bAP binding events as well as for pNPP hydrolysis (3x). Conditions: 150 nM nanoantenna, 50 nM SA, 100 nM bAP and 300 µM pNPP in 200 mM Tris, 300 mM NaCl, 1 mM $MgCl_2$, pH 7.0, 37 °C.

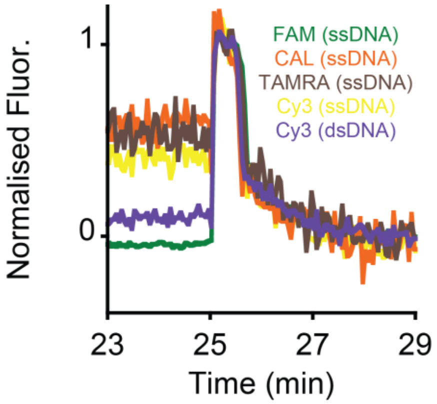

Figure 2.15. – Kinetics of pNPP hydrolysis as monitored by different dyes. Nanoantennas with different FAM, CAL, TAMRA and Cy3 display the same kinetics when monitoring pNPP hydrolysis. For this, we selected the spike observed after the second addition of pNPP in Supplementary Figure S2.7 because 1) FAM displays a different baseline after the first spike but not for subsequent spikes, and 2) for the other dyes, the first injection does not lead to a clear spike while the later injections do. We are not sure why this difference between the first and subsequent substrate additions occurs, but for the purpose of seeing whether the dyes display the same kinetics and do not function as inhibitors, this is confirmed by the second spike for each system. Conditions: 150 nM nanoantenna, 50 nM SA, 100 nM bAP and 300 µM pNPP in 200 mM Tris, 300 mM NaCl, 1 mM $MgCl_2$, pH 7.0, 37 °C.

We then analysed the kinetics of dye-bAP interaction. First, using 3′-end FAM L12 ssDNA nanoantennas, we found that the observed dissociation of FAM from SA and subsequent binding to bAP varies with enzyme concentration, suggesting that dye dissociation is not rate-limiting and that the rate-limiting step of this transition consists of bAP binding to SA (**Figure 2.16**). Next, we monitored this binding step using different nanoantennas (**Figure 2.17**). The rate of nanoantenna dissociation from SA and subsequent binding to bAP varies with nanoantenna properties, including linker and dye. Changing the dye connection to the nanoantenna (3′ *vs*. 5′) does not substantially affect its dissociation rate from SA and binding to bAP (263 *vs.* 300 nM^{-1} s^{-1}), while changing the linker from L12 ssDNA to L21 PEG substantially reduces this dissociation rate (300 *vs.* 73 nM^{-1} s^{-1}). Furthermore, changing the dye (FAM, CAL, TAMRA, Cy3, or Q570) substantially affects the dissociation rate of the nanoantenna from SA and binding to bAP (ranging from 263 to 18 nM^{-1} s^{-1}). These results further suggest that the dye binding location and the nature of the linker may affect the rate at which bAP binds to SA (*e.g.*, through steric hindrance).

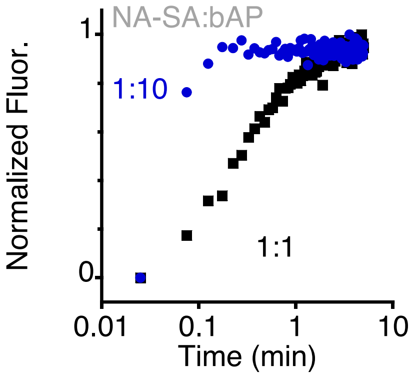

Figure 2.16. – Kinetics of bAP attachment onto SA as monitored by FAM nanoantennas. The rate of dye dissociation from SA and subsequent binding to bAP varies with enzyme concentration, suggesting that dye dissociation is not rate-limiting. Here, nanoantenna-SA platform to bAP ratios (NA-SA:bAP) were 1:1 or 1:10. Ratio of bAP is relative to concentration of SA (assumed to be equal to [nanoantenna-SA platform]). Conditions: 15 nM 3′ 5-FAM L12 ssDNA nanoantenna, 5 nM SA, 5 or 50 nM bAP in 100 mM Tris, 10 mM NaCl, 37 °C, pH 8.0.

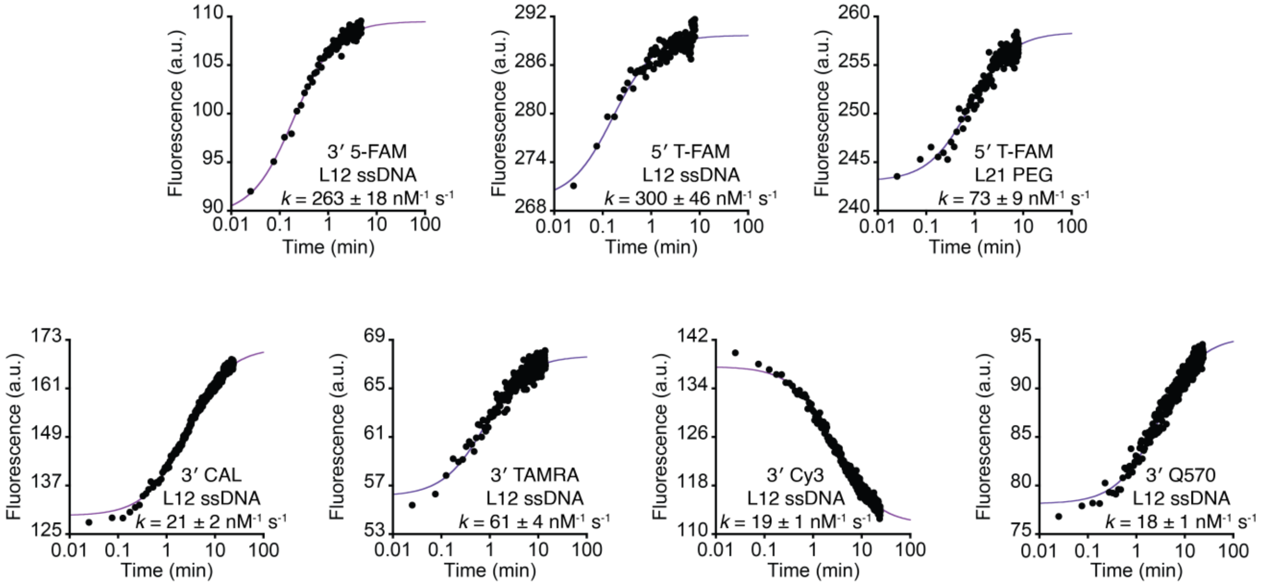

Figure 2.17. – Kinetics of bAP attachment on SA as monitored by different nanoantennas. The rate of nanoantenna dissociation from SA and subsequent binding to bAP varies with nanoantenna properties, including linker and dye. The kinetics of dissociation fit well with a second-order rate constant. Conditions were equivalent to Figure 2.16 with 1x bAP.

We investigated the possible signalling mechanisms of dyes that are predicted to bind at different locations as driven by the high local concentration in the nanoantenna-SA-bAP complex. For nanoantennas with FAM, which is predicted to possibly bind just outside the active site of AP, we proposed three mechanisms for modulation of fluorescence during this enzyme's function: 1) binding of pNPP at the active site directly ejects FAM from its nearby binding site, 2) small conformational changes alter FAM's affinity for AP and release it from the binding site, or 3) small conformational changes perturb the bound FAM's emission. For CAL and Cy3, predicted to possibly bind at locations distal to the active site, we proposed only the latter two mechanisms.

To investigate these proposed mechanisms, once again working in collaboration with Dr. Maximilian C. C. J. C. Ebert, we used MD simulations and examined the trajectories of the bound dyes in the presence or absence of bound pNPP (**Figure 2.18**). FAM remained bound near the active site both in the absence and presence of pNPP, suggesting a strong affinity for this site. In contrast, CAL was not stabilised in its initial binding site in either the absence or presence of pNPP, suggesting low affinity. Interestingly, Cy3 remained bound in the absence of pNPP but dissociated in its presence. Therefore, these simulations suggest a FAM signalling mechanism not based on ejection[444] by pNPP or by a change in affinity, but instead by the sensing of small conformational changes in its local chemical environment. Subtle structural changes could affect photoinduced electron transfer (PET) from amino acids proximal to a bound dye,[369, 446] or affect conditions in its local environment,[447] thereby modulating its fluorescence. This agrees with our observation that, under some conditions, the FAM fluorescence spike intensity during pNPP hydrolysis was significantly greater than the initial fluorescence of the unbound nanoantenna (*e.g.*, **Supplementary Figure S2.8**). We infer that FAM simply being ejected from the active site by the incoming pNPP substrate would likely just return the fluorescence to the initial baseline before protein binding. For CAL, the mechanism remains uncertain, but for Cy3, the simulations suggest that conformational changes during pNPP hydrolysis transiently release the dye. The bound and unbound states of Cy3 could affect its *cis–trans* isomerism, and therefore, its fluorescence signal intensity.[318, 319, 325, 326] Overall, these results reinforce our proposed mechanism that the nanoantenna-mediated dye-enzyme interaction enables monitoring of the conformational changes on the enzyme's surface during its function.

It is important to point out that these MD simulations rely on several assumptions and approximations. For instance, the binding site interactions predicted by the molecular docking simulations would not occur for free fluorophores with AP, but we propose that such interactions are mediated by the nanoantenna-SA-bAP complex. Moreover, the MD simulations involve only the dye and AP, not the entire nanoantenna-SA-bAP complex. Thus, the MD simulations represent a possible signalling mechanism and not a definite proposal. Although extensive computational simulations of dye-protein interactions are beyond the scope of this research project and expertise in our research group, this is an important aspect that deserves appropriate consideration in future works.

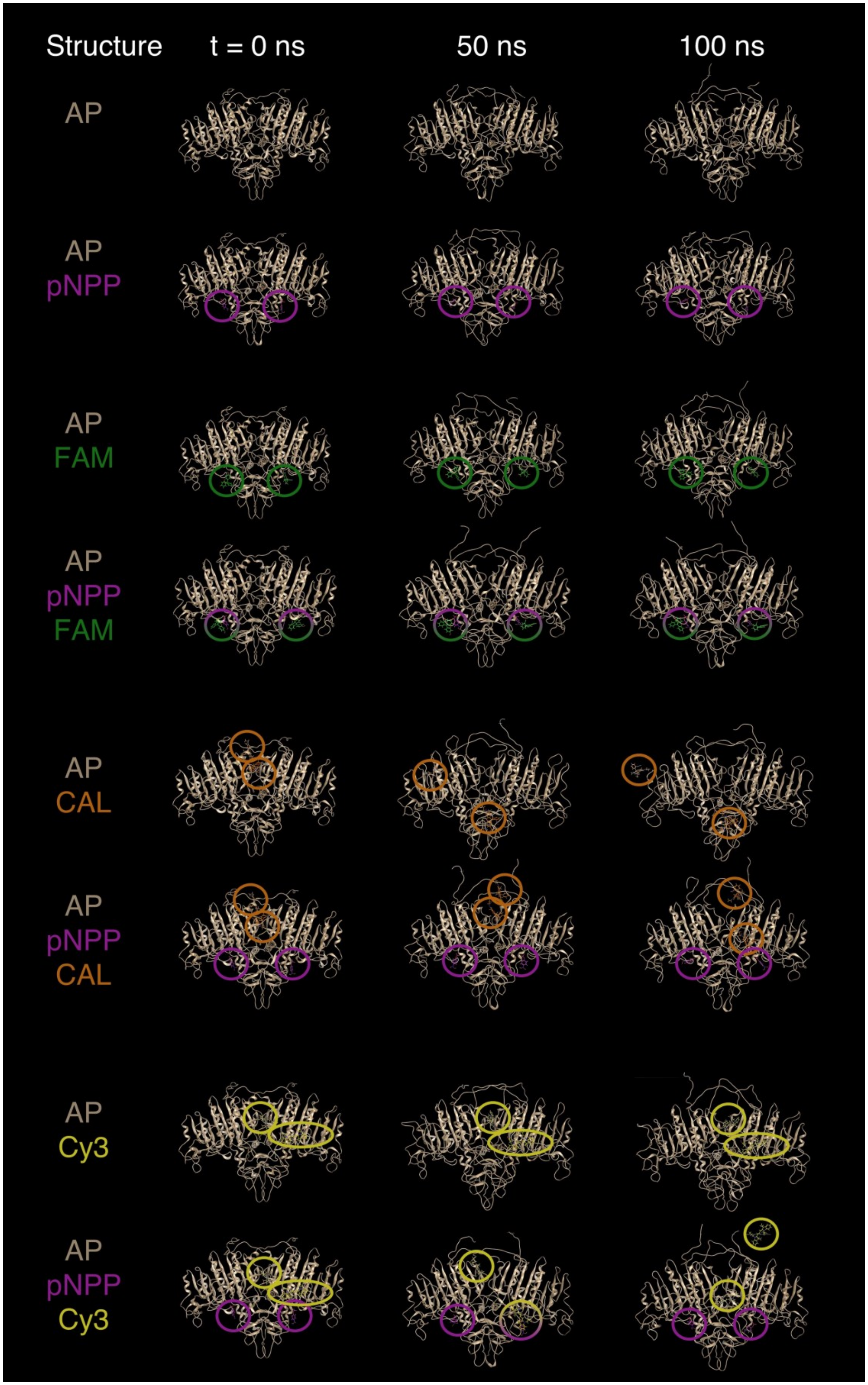
Structure
t = 0 ns
50 ns
100 ns
AP
AP
pNPP
AP
FAM
AP
pNPP
FAM
AP
CAL
AP
pNPP
CAL
AP
Cy3
AP
pNPP
Cy3

Figure 2.18. – Molecular dynamics (MD) trajectories of dyes and/or substrate on AP. The MD simulation of AP with or without a dye (FAM, CAL, Cy3) and with or without a substrate (pNPP). We selected the lowest energy pose (see Figure 2.13) and the next lowest energy pose that we obtained from molecular docking. For visual clarity in the figure, these poses are circled as follows: purple = pNPP, green = FAM, yellow = Cy3, and orange = CAL. In the simulation with pNPP and FAM, one circle is used because they start and remain close together. The simulation was run for 100 ns, with screenshots shown at 0 ns, 50 ns and 100 ns. We also confirmed that the dye pose left the linker connection location exposed, so that the pose is possible via the nanoantenna-driven dye-protein interaction. In all cases, we observed that pNPP remains bound at the active sites. For AP with FAM and with or without pNPP, the position of FAM also remains unchanged. For AP with CAL and with or without pNPP, the CAL dye does not have a stable position. For AP with Cy3 and without pNPP, the Cy3 dye position does not change, but with pNPP, the dye dissociates from the surface.

If a nanoantenna's sensitivity truly depends on whether the dye's binding location experiences conformational change during protein function, one ought to observe a change in its fluorescence signature upon forcing the dye to bind at another location. To test this hypothesis, we employed a dsDNA L12 nanoantenna containing both FAM and CAL. Our reasoning was that the two dyes will compete for their preferred binding sites on bAP. Based on the above MD simulation, we expected that the higher-affinity FAM will bring the lower-affinity CAL along with it. However, as a first step, it was necessary to explore the interactions of FAM and CAL while present on the same nanoantenna. To do this, we compared the fluorescence excitation and emission spectra of nanoantennas with FAM (λ_{ex} = 498 nm and λ_{em} = 520 nm) and/or CAL (λ_{ex} = 540 nm and λ_{em} = 561 nm) as ssDNA, after the binding of complementary DNA (cDNA) to form dsDNA, after the binding of SA, and after the binding of bAP. The cDNA was either unlabelled or labelled with the other dye. For the nanoantenna with both dyes, we checked both sets of wavelengths. As expected, due to the inflexibility of dsDNA, the nanoantennas with only one dye, either FAM (**Figure 2.19a**) or CAL (**Figure 2.19b**), displayed somewhat low sensitivity to the cDNA, SA, and bAP binding events but could still detect them. When both dyes were present after the cDNA binding step, both the FAM (**Figure 2.19c**) and the CAL (**Figure 2.19d**) excitation and emission spectra were drastically affected when proximal to the other dye. This decrease of signal intensity is likely attributable to a contact-mediated quenching mechanism between the dyes.[348] This decrease in fluorescence remains true following the addition of the SA and bAP proteins. Therefore, these dyes seem to remain stacked even after the addition of SA and bAP.

Next, we examined the kinetics of these systems that have nanoantennas with FAM, CAL, or both dyes. We started with the FAM excitation and emission wavelengths and examined the nanoantennas with FAM only and with FAM and CAL together. When following the FAM fluorescence wavelengths, aside from the significant quenching upon binding of the CAL-containing cDNA, we observed that the presence of CAL does not substantially affect the FAM fluorescent signature for the SA and bAP binding events. Also, the FAM signal for the detection of pNPP hydrolysis was only somewhat weaker in the presence of CAL (**Figure 2.20a**). We next used the CAL excitation and emission wavelengths and examined the nanoantennas with CAL only and with FAM and CAL together. In contrast to the previous result, when following the CAL fluorescent nanoantenna, the binding of the FAM-containing cDNA substantially affects the CAL fluorescent signature. Notably, it now enables CAL to efficiently detect a signal during pNPP hydrolysis, likely by sensing the conformational change of the enzyme (**Figure 2.20b**). Given that CAL likely stacks on FAM (**Figure 2.19**), it is plausible that the change of fluorescence signal of CAL is triggered by the same conformational change affecting the FAM dye. The presence of the second dye also did not affect the kinetics of substrate hydrolysis (**Supplementary Figure S2.9**). We further found that employing FAM with other dyes, such as Cy3 or Q670, leads to comparable results (**Supplementary Figure S2.9b-c**). Of note, these changes in the fluorescence signature do not arise due to FAM emitting a signal that overlaps with the other dyes' excitation wavelengths (**Supplementary Figure S2.9d-e**). Thus, these experiments provide strong evidence that FAM can redirect other weaker binding dyes to a location proximal to its own binding site on AP. This observation is consistent with the aforementioned MD simulations, suggesting that FAM is more tightly bound than Cy3 and CAL to AP. Hypothetically, one could rationally employ other non-dye "molecular anchors" to redirect dyes to specific locations on proteins, as FAM does for CAL on AP.

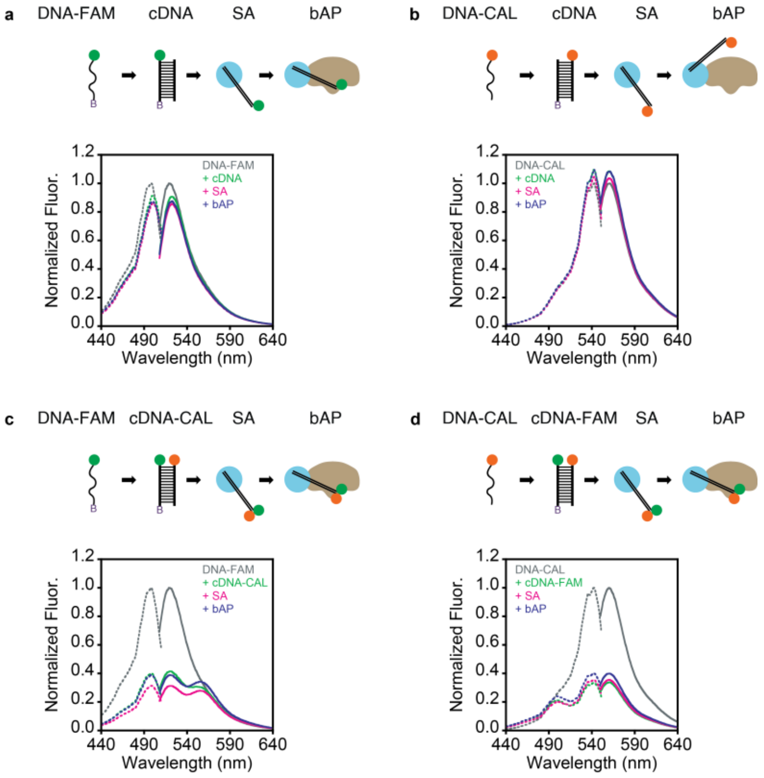

Figure 2.19. – Excitation and emission spectra of dual-dye dsDNA nanoantenna (FAM-CAL) suggest dye stacking. The excitation spectra (dashed line) and emission spectra (solid line) of the formation of the dual-dye dsDNA nanoantenna and protein complex: starting with ssDNA, after binding of cDNA, after binding of SA, and after binding of bAP. In (a), only the FAM dye is present, and excitation and emission of FAM wavelengths (λ_{ex} = 498 nm and λ_{em} = 520 nm) are relatively unaffected by the addition of the complementary DNA (of note, the dsDNA nanoantenna displays little sensitivity to SA and bAP attachment relative to ssDNA nanoantennas). In (b), only the CAL dye is present, and excitation and emission of CAL wavelengths (λ_{ex} = 540 nm and λ_{em} = 561 nm) are relatively unaffected by the addition of the complementary DNA. In (c) and (d), both dyes were present after the cDNA step (*i.e*, the systems were chemically identical), but (c) was measured with the FAM wavelengths and (d) with the CAL wavelengths. We observed that both the FAM and CAL excitation and emission spectra are drastically affected when proximal to the other dye. This remains true even following the addition of the SA and bAP proteins. This decrease of signal intensity is likely attributable to a contact-mediated quenching mechanism between the dyes.[348] These dyes seem to remain stacked even after the addition of SA and bAP.

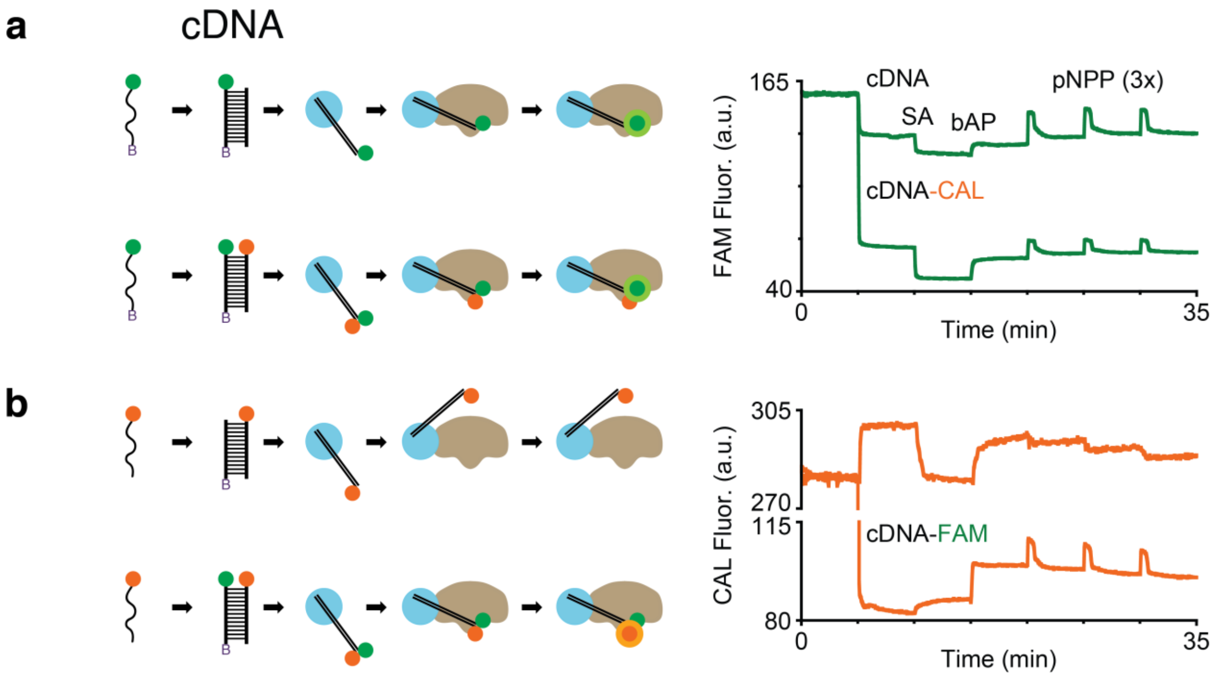

Figure 2.20. – Double-dye competition kinetic signatures. In (a), the top data show the monitoring of FAM fluorescence of a single-dye dsDNA nanoantenna with FAM, and the bottom data show the monitoring of FAM fluorescence of a dual-dye dsDNA nanoantenna with FAM and CAL. In (b), the top data show the monitoring of the CAL fluorescence of a single-dye dsDNA nanoantenna with CAL, and the bottom data show the monitoring of the CAL fluorescence of a dual-dye dsDNA nanoantenna with FAM and CAL. These experiments were performed in the same conditions as Figure 2.14.

2.7 Discussion

This chapter has explored the concept of using fluorescent nanoantennas to monitor the function of our model protein, AP. We optimised the nanoantenna's signal output by tuning the linker length, ratio, and composition. The best nanoantennas to detect binding of bAP to the nanoantenna-SA platform (*i.e.*, L12 ssDNA and *ca.* L21 PEG) are also the best to provide a signal change during bAP catalytic function. This initial observation supported that the nanoantennas, which drive dye-protein interaction via a high local concentration of the dye, can monitor an event occurring on the protein, such as the small conformational change during substrate hydrolysis.

Biotin titration and molecular docking simulations further supported that the nanoantenna's FAM moiety binds near the active sites of AP, an area likely to experience conformational change. MD simulations support that this interpretation of the data is plausible. Further controls, such as with non-biotinylated nanoantennas and the addition of reaction products, revealed that the high local concentration of FAM is necessary to drive dye-enzyme interaction and that a catalytic reaction must occur to provide a signal, respectively. Experiments with different chemical connections of FAM to the DNA linker, and that sometimes the fluorescent spike signal intensity is greater than the initial fluorescence baseline of the unbound nanoantenna, suggested that the nanoantenna's FAM is not simply being ejected from the surface of bAP. This supported our hypothesis of monitoring conformational change, although it is important to note that the nanoantenna strategy is unable to quantify the magnitude of conformational change, as is possible for some proteins with FRET. With the MD simulations, we examined possible signalling mechanisms for FAM and Cy3, but further work is needed to better understand the interactions of these dyes with AP. Finally, in the dye competition experiment, we found that FAM can plausibly relocate the other dyes to its own binding site, which modulated their signal output. With another so-called molecular anchor instead of our proof-of-principle FAM, we speculate that dyes could be rationally designed and synthesised to probe protein function at a specific binding site.

Fluorescent nanoantennas differ from other sensing strategies. Rather than detecting colorimetric or fluorogenic substrates/products that provide a signal change, the mechanism of fluorescent nanoantennas is based on conformational change of the enzyme perturbing or ejecting a fluorescent dye. It also differs from FRET, whereby a protein is labelled with donor and acceptor dyes. FRET is indeed very useful for monitoring conformational change in the ~3-9 nm range,[45, 319] but it is typically unable to sense small conformational changes, such as those that occur for AP.[82, 107] There is one method able to sense smaller conformational changes occurring upon interaction of proteins with fluorescently labelled DNA (typically Cy3), namely, Protein-induced fluorescence enhancement (PIFE).[309, 316] PIFE can sense smaller conformational changes in the ~1-3 nm range,[318, 319] although one recent study has disagreed.[325] We consider how nanoantennas can complement these techniques. As noted, PIFE is based on dye-labelled DNA, so the dye photophysics of PIFE and nanoantennas with Cy3, for example, may be similar (*i.e.*, Cy3 *cis*–*trans* isomerism).[319, 324-326] Nanoantennas differ, however, in that they are not limited to protein systems wherein the DNA is a substrate, which is typically the case with PIFE. Unlike FRET, PIFE, and other techniques, such as PET[448, 449] and tryptophan-induced quenching (TrIQ),[450-452] nanoantennas cannot characterise the magnitude of conformational change. One can, however, envision the integration of nanoantennas with other sensing strategies, as has been achieved with FRET-PIFE[320-323] and FRET-PET.[453, 454] Another benefit of nanoantennas relative to FRET is that they do not require complicated site-specific labelling with fluorophores. Nanoantennas require only non-specific biotinylation (*e.g.*, via exposed lysine residues) of the protein of interest. It cannot be assumed as necessarily true in all cases, but biotinylation often does not affect protein function.[435] In contrast, FRET has been show to affect the function of some proteins, such as with beta-lactamases[44, 455] and dihydrofolate reductase.[456-458] With this in mind, the next chapter of this thesis will examine how nanoantennas can be exploited to characterise the enzyme AP, including its kinetics with biomolecular substrates, and the conformational changes that it experiences in other states, such as with inhibitors and melting. Characterisation of these states agrees with conventional methods, revealing that nanoantennas do not interfere with the measurement, and in other cases, values for AP with various substrates are reported for the first time herein.

2.8 Supplementary figures for Chapter 2

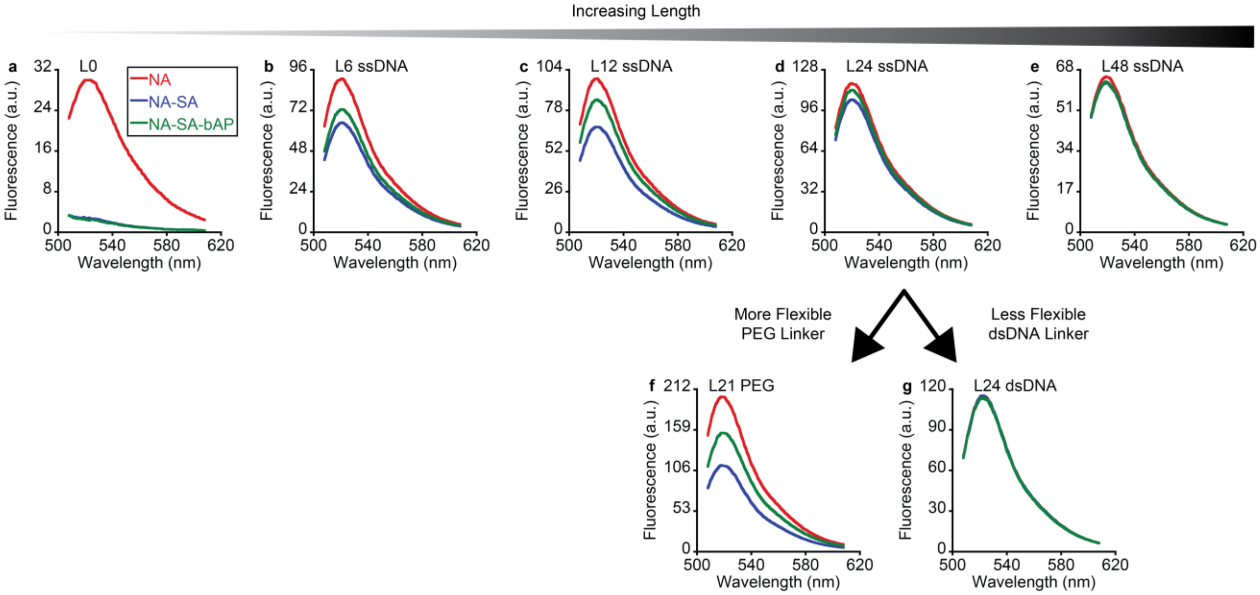

Figure S2.1. – Optimal nanoantenna signalling is obtained at intermediate linker length (L12) with a flexible linker (ssDNA, PEG). These fluorescence spectra were used to generate the panels in Figure 2.1. The spectra show the response of the biotinylated nanoantenna (NA) upon binding to streptavidin (SA), which quenches fluorescence, and then loading of biotinylated alkaline phosphatase (bAP), which increases fluorescence. (a) The biotin-fluorescein conjugate represents a no linker L0 nanoantenna, while (b) L6, (c) L12, (d) L24 and (e) L48 are ssDNA nanoantennas. The optimal linker length to monitor the assembly steps is L12. Compared to the L24, using (f) a more flexible PEG linker improves its response toward bAP, (g) while a less flexible dsDNA effectively shows no signal change. Conditions: 100 nM nanoantenna, 50 nM SA, 100 nM bAP and 1000 nM biotin in 200 mM Tris, 300 mM NaCl, 1 mM $MgCl_2$, pH 7.0, 37 °C.

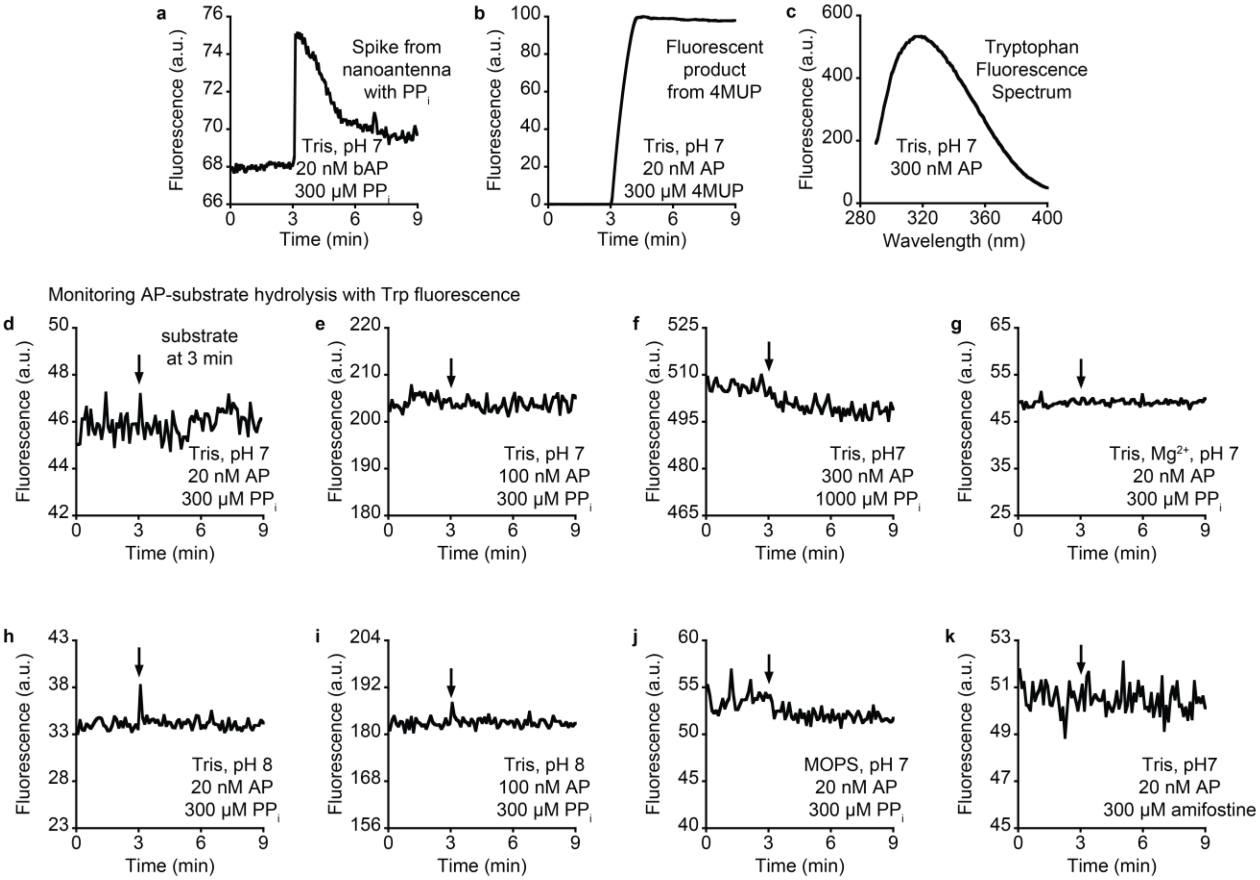

Figure S2.2. – Tryptophan fluorescence does not detect enzyme catalytic activity. (a) PP$_i$ hydrolysis by bAP monitored using nanoantennas and (b) 4MUP hydrolysis by AP monitored by 4MU fluorescence show that the reaction takes about 1-2 minutes. For PP$_i$, conditions were 150 nM nanoantenna, 50 nM SA, 20 nM bAP, 300 µM PP$_i$ in 200 mM Tris, 300 mM NaCl, pH 7.0, 37 °C, PMT voltage = 635 V. For 4MUP, conditions were 20 nM AP, 300 µM 4MUP in 200 mM Tris, 300 mM NaCl, pH 7.0, 37 °C, PMT voltage = 400 V. (c) The AP dimer has eight Trp residues[428] and displays typical fluorescence emission when excited at 280 nm. (d-k) We tried to monitor AP function (PP$_i$ hydrolysis) using Trp fluorescence at 325 nm. Note that PP$_i$ is ideal for this purpose because it will not significantly absorb nor emit light. However, we found no detectable signal change under various conditions, including, (d) 20 nM AP, 300 µM PP$_i$ in 200 mM Tris, 300 mM NaCl, pH 7.0, 37 °C, (e) 100 nM AP and 300 µM PP$_i$ in the same buffer, (f) 300 nM AP and 1000 µM PP$_i$ in the same buffer, (g) 20 nM AP and 300 µM PP$_i$ in the same buffer but also with 1 mM Mg^{2+}, (h) 20 nM AP, 300 µM PP$_i$ in 100 mM Tris, 10 mM NaCl, pH 8.0, 37 °C, (i) 100 nM AP and 300 µM PP$_i$ in the same buffer, (j) 20 nM AP, 300 µM PP$_i$ in 100 mM MOPS, 20 mM NaCl, pH 7.0, 37 °C, and (k) 20 nM AP, 300 µM amifostine in 200 mM Tris, 300 mM NaCl, pH 7.0, 37 °C. For Trp, PMT voltage = 800 V. The arrows indicate addition of substrate at 3 min.

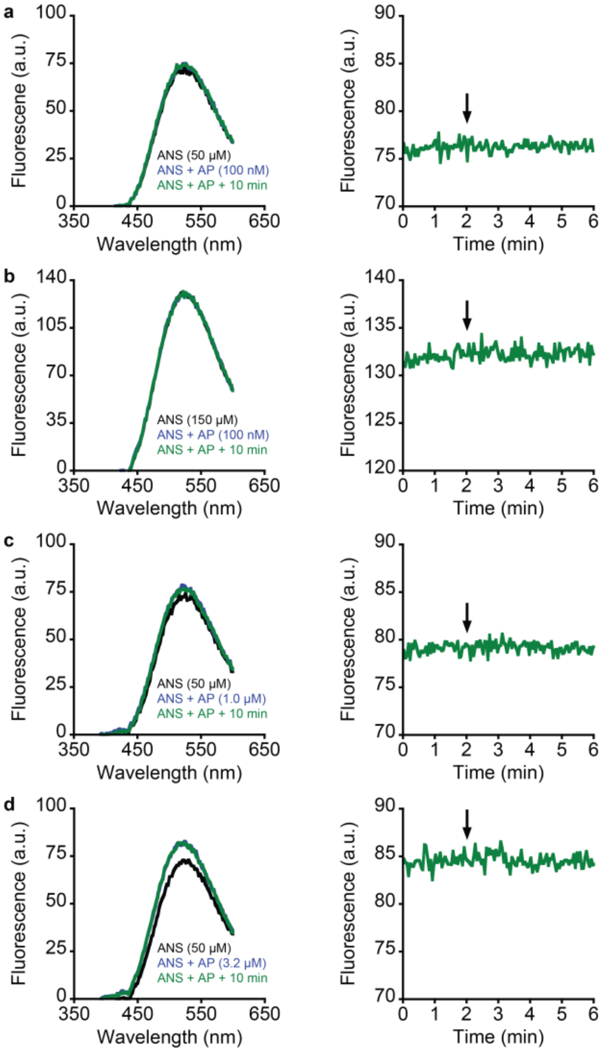

Figure S2.3. – ANS probe does not detect enzyme catalytic activity. (a) Here, we tested 100 nM AP with 50 µM protein-binding dye 8-anilinonaphthalene-1-sulfonic acid (ANS). No significant fluorescence change was observed. We then tried (b) 100 nM AP with 150 µM ANS, (c) 1.0 µM AP with 50 µM ANS, and (d) 3.2 µM AP with 50 µM ANS. Adding more AP led to a small fluorescence increase. Waiting longer, up to one hour, did not lead to a further fluorescence increase. However, in all cases, this approach was not able to detect AP-mediated hydrolysis of amifostine. Note that ANS studies of various APs[56, 459-462] and other proteins[57, 463-465] have used similar concentrations of AP (or other protein) and ANS. PMT voltage = 800 V, *i.e.*, the maximum for our instrument. The arrows indicate addition of substrate at 3 min.

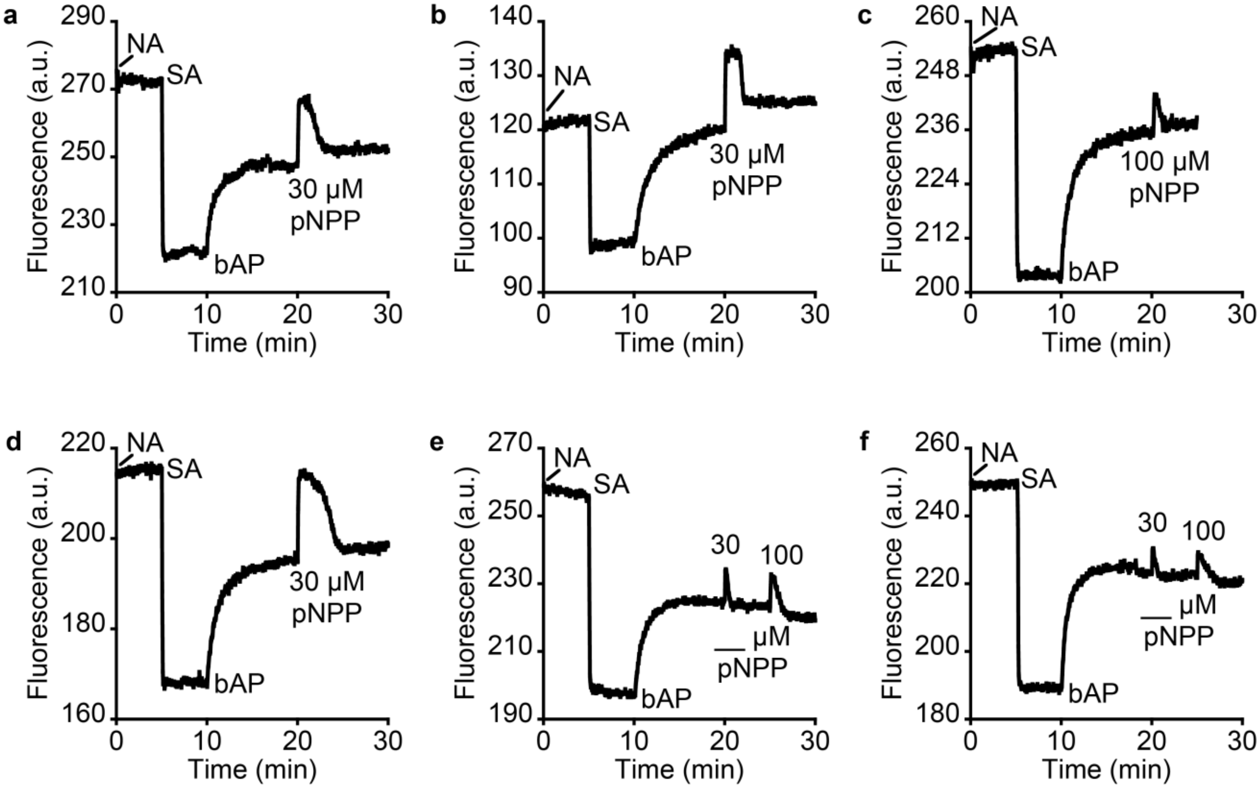

Figure S2.4. – Versatility of nanoantenna in different buffer conditions. To test the versatility of our nanoantenna strategy, we tried it in different buffer conditions. (a) 100 mM Tris, 10 mM NaCl, pH 8.0; (b) 200 mM Tris, 300 mM NaCl, 1 mM Mg^{2+}, pH 7.0; (c) 200 mM Tris, 300 mM NaCl, 1 mM Mg^{2+}, pH 8.0; (d) 100 mM MOPS, 20 mM NaCl, pH 7.0; (e) 10 mM HEPES, 150 mM NaCl, 5 mM KCl, 2 mM $MgCl_2$, pH 7.45; and (f) 50 mM PIPES, 75 mM NaCl, 3 mM $MgCl_2$, pH 7.40. Note that (a-c) represent buffers used in this study, while (d-f) are randomly selected buffers found in the refrigerator of our laboratory. In all cases, we observed the binding steps and the pNPP hydrolysis spike. Conditions were 15 nM PEG nanoantenna, 2.5 nM SA, 10 nM homemade bAP, and pNPP (concentration as indicated). For (c, e, f) the pNPP is quickly hydrolysed likely due to alkaline pH and Mg^{2+}.[216] PMT voltage = 800 V.

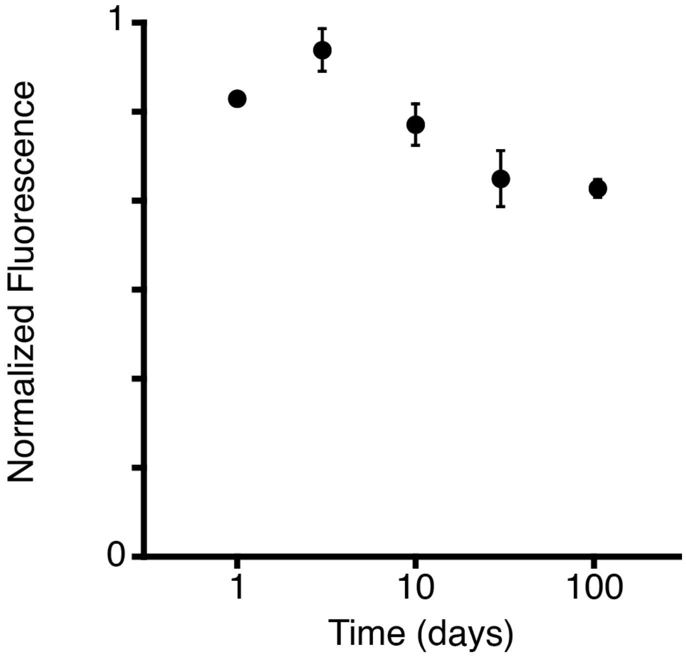

Figure S2.5. – Nanoantenna-protein complex maintains functionality after 100 days. Fluorescence spike intensity for pNPP hydrolysis as a function of storage time after preparation of nanoantenna-protein complex. Even on day 105, the signal intensity during pNPP hydrolysis remains at ~74% compared to day 0. Conditions: 15 nM L12 PolyT nanoantenna, 5 nM SA, 15 nM bAP and 10 µM pNPP in 200 mM Tris, 300 mM NaCl, 1 mM $MgCl_2$, pH 7.0, 37 °C. DNA-protein complex was stored in the same buffer at 4 °C. PMT voltage = 635 V.

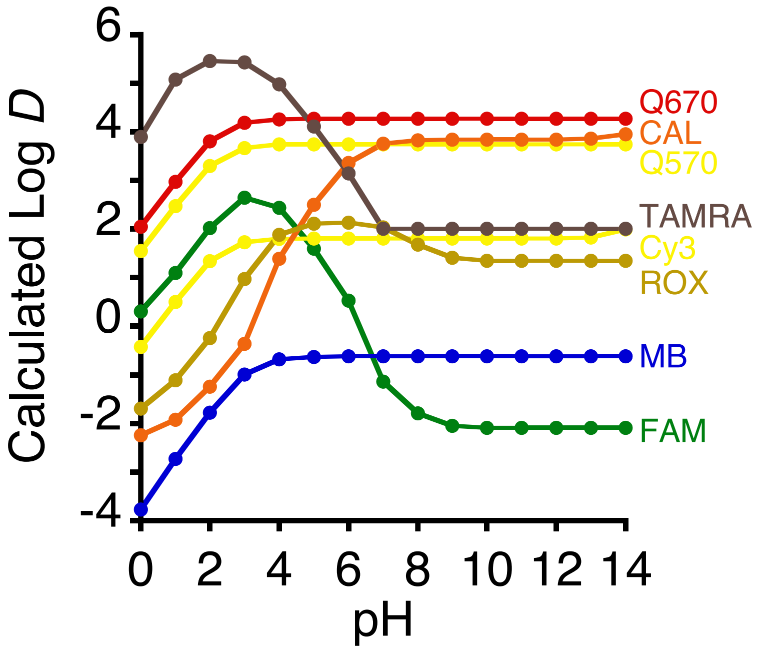

Figure S2.6. – Effect of pH on dye hydrophobicity. Dye hydrophobicity as a function of pH determined by distribution coefficient (log *D*) calculations in MarvinSketch software.[466] Log *D* values greater than zero indicate hydrophobicity, while those less than zero indicate hydrophilicity. At pH 7 or greater, only FAM and MB (Methylene Blue) are hydrophilic. Note that this approach is an approximation, as it only considers the dye itself, but not the entire nanoantenna.

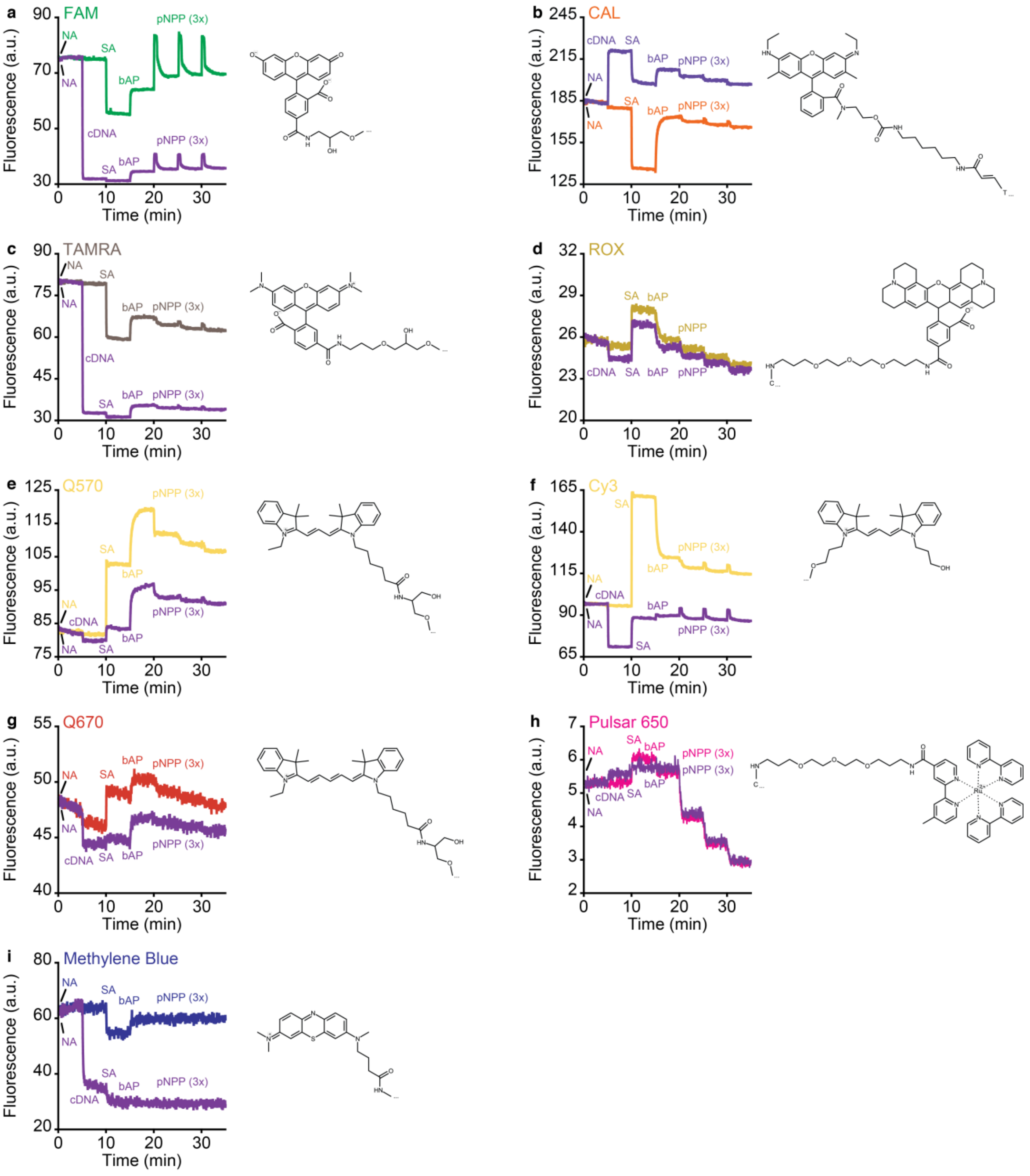

Figure S2.7. – Probing different regions of the protein surface with other dyes. Kinetic signatures of nanoantennas containing (a) FAM (3’ 5-FAM), (b) CAL, (c) TAMRA, (d) ROX, (e) Q570, (f) Cy3, (g) Q670, (h) P650 and (i) MB as ssDNA (various colours) and dsDNA (purple) for SA and bAP binding and pNPP hydrolysis (3x). Conditions: 150 nM nanoantenna, 50 nM

SA, 100 nM bAP and 300 µM pNPP in 200 mM Tris, 300 mM NaCl, 1 mM $MgCl_2$, pH 7.0, 37 °C. Note: FAM, TAMRA, Q570, Cy3 and Q670 are located at the 3'-end of the DNA; CAL is attached to the methyl group of a T nucleotide at the 3'-end; and ROX and P650 to the amino group of a C nucleotide at the 3'-end. MB is connected to an amino group at the 5'-end because the strand sample was borrowed from another project. Molecular structures are based on the manufacturer's description, calculations in MarvinSketch software, and consideration of the available literature.[343, 350, 438-441]

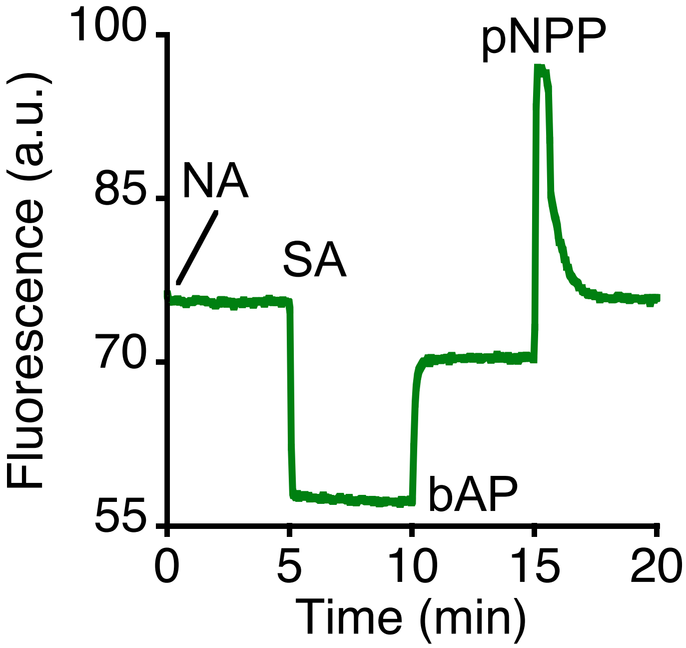

Figure S2.8. – Spike above initial fluorescence baseline suggests a mechanism based on conformational change. Under some conditions, such as 3′ 5-FAM on the L12 ssDNA nanoantenna, the spike intensity during pNPP hydrolysis is higher than that of the initial fluorescence baseline before protein binding. This may support a mechanism whereby during hydrolysis the dye experiences a conformational change of nearby amino acids that increases its fluorescence, as opposed to a simple ejection from the bAP active site into the surrounding buffer. This is because ejection would likely just return the signal to the initial baseline. Conditions: 150 nM nanoantenna, 50 nM SA, 100 nM bAP and 300 µM pNPP in 200 mM Tris, 300 mM NaCl, 1 mM $MgCl_2$, pH 7.0, 37 °C.

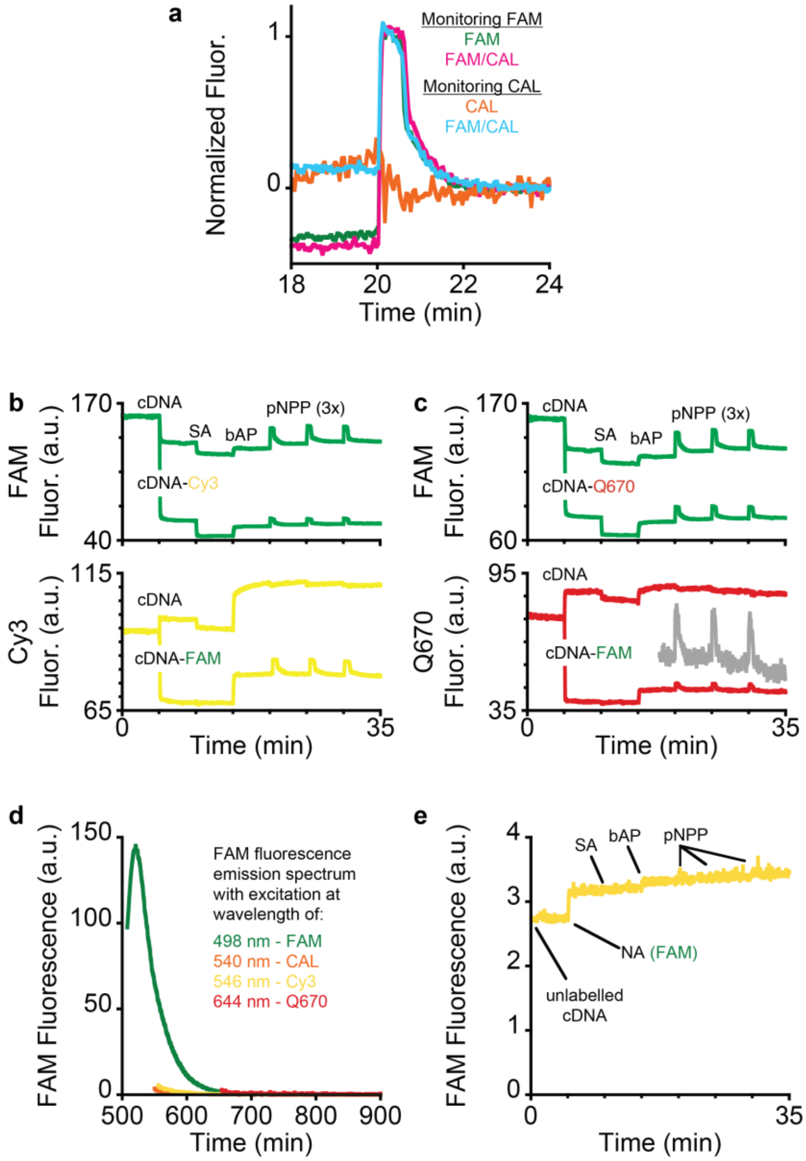

Figure S2.9. – Dual-dye controls. (a) pNPP hydrolysis displays the same kinetics while monitoring FAM (with or without CAL present) and while monitoring CAL (with FAM present). (b-c) Analogous experiments to the dye competition experiment in Figure 2.20 except now with (b) FAM and Cy3 or (c) FAM and Q670. The top data shows that while monitoring FAM, the presence of the other dye does not significantly affect the FAM fluorescence signature (besides some quenching) but monitoring Cy3 or Q670 in the presence of FAM affects their fluorescence signature to the point where it is now possible to efficiently monitor pNPP hydrolysis. (d) As a control, upon excitation of FAM at 498 nm, FAM displays intense fluorescence emission at 520 nm. However, when using the excitation wavelengths optimal for CAL, Cy3 and Q670, FAM does not display fluorescence. (e) For example, in an attempt to monitor the FAM nanoantenna with the excitation (546 nm) and emission (563 nm) wavelengths of Cy3, but otherwise the same conditions, there is no significant fluorescence emission, and it is not possible to monitor SA and bAP binding, nor pNPP hydrolysis. Conditions: 150 nM nanoantenna, 50 nM SA, 100 nM bAP and 300 µM pNPP (3x) in 200 mM Tris, 300 mM NaCl, 1 mM $MgCl_2$, pH 7.0, 37 °C.

Chapter 3 – Characterising conformational states of alkaline phosphatase with fluorescent nanoantennas

3.1 Introduction

Spectroscopic techniques with high temporal resolution can enable real-time characterisation of enzyme kinetics. In the context of alkaline phosphatase (AP), the classic method is to employ ultraviolet-visible (UV-Vis) spectroscopy to monitor the conversion of the chromogenic substrate *p*-nitrophenylphosphate (pNPP) to its products, yellow *p*-nitrophenol (pNP) and inorganic phosphate (P_i).[34] Fluorescence spectroscopy offers analogous procedures, but with the benefit of higher sensitivity. For instance, the fluorogenic substrate 4-methylumbelliferyl phosphate (4MUP) will be hydrolysed by AP to fluorescent 4-methylumbelliferone (4MU) and P_i.[37] The popularity of this general strategy has led to the development of many other molecules that are detectable by fluorescence[229-247, 251] and other spectroscopies,[70, 73, 84-86, 248-250] as well as electrochemical techniques.[91-95, 252] However, their common drawback is that since the detection strategy relies on the specific properties of these substrates or their products to generate a signal, one cannot employ this procedure to characterise biomolecular and medicinal substrates of AP that are of interest in the fields of biology and medicine. To characterise such substrates, one typically employs methods to quantify released P_i after the reaction, often via a phosphomolybdate complex.[106, 115, 467] These methods, however, do not enable real-time analysis of AP function and are time-consuming. Alternatively, some proposed strategies use released P_i to generate a signal by its interaction with another component,[274-277] but it is unclear whether this sequestration of P_i could affect the observed kinetics, since it is not only one of the products of the reaction, but also a competitive inhibitor of AP. Various substrate-specific assays for biomolecules have been reported too.[105, 256-264, 266-273] Many of these can provide results in real time, but they require a totally different detection strategy for each substrate and are not available for many substrates. Moreover, these alternative techniques are not typically used to study AP,[138, 141, 168, 406-408] whereby phosphate quantification has remained the norm.[106] With this in mind, a fluorescence-based method able to rapidly characterise biomolecular substrates of AP in real-time ought to be highly desirable.

This chapter builds on the previous chapter, wherein the signal generated via the fluorescent nanoantennas was linked to the catalytic function of AP. Here, we will demonstrate that the fluorescence "spike" observed upon addition of pNPP substrate initially increases with the concentration of substrate before reaching a plateau at higher concentrations. Furthermore, this fluorescence signal is similar to enzyme-substrate concentration ([ES]) during typical saturation kinetics. By plotting the fluorescence spike intensity versus [pNPP], one observes a saturation binding plot that is reminiscent of Michaelis-Menten kinetics. Then, we show that by mathematical modelling of a fluorescence spike obtained from a single addition of pNPP substrate, it is possible to obtain the Michaelis constant (K_M) and the catalytic rate constant (k_{cat}, also called turnover number), and from these, the catalytic efficiency (k_{cat}/K_M, also called the specificity constant). We tested this substrate characterisation strategy with 15 other substrates of AP, including relevant biomolecular substrates and an AP-activated prodrug used in cancer treatment, and could similarly characterise their kinetics. Values agreed with the literature, when available, while other substrates were characterised for the first time herein. By modelling multiple fluorescence spikes obtained via sequential additions of pNPP to a single enzyme sample, it is also possible to obtain the inhibition constant (K_i) for the product and competitive inhibitor, P_i. Alternatively, we further show for P_i and various other oxyanion inhibitors that one can obtain the K_i by comparing the spikes from samples with or without the added inhibitor. Thus, these fluorescent nanoantennas combined with fitting of the signal for a single enzymatic reaction provide a convenient and versatile strategy for real-time characterisation of enzyme function.

3.2 Fluorescence spike correlates with enzyme-substrate concentration

In the previous chapter, we established that the fluorescence spike observed for the nanoantenna-SA-bAP complex upon addition of the pNPP substrate arises due to substrate binding. Therefore, we expected that one ought to be able to characterise the AP-mediated catalytic reaction by this fluorescence signature. As a simple test of this hypothesis, we monitored the signal upon adding increasing concentrations of pNPP (1, 2, 4, 8, 20, 40, 100 µM) to cuvettes containing the nanoantenna-SA-bAP complex (100 nM bAP; note that we employed ssDNA L12

FAM nanoantennas hereafter). We first observed that the addition of more pNPP increased the spike intensity and duration (**Figure 3.1**). At higher concentrations, however, the intensity no longer increased. The resulting fluorescence signature is reminiscent of the expected profile of the enzyme-substrate concentration ([ES]) during typical saturation kinetics (**Figure 1.6**). The signal rapidly peaked and then maintained a steady state until the substrate had begun to run out. This hypothesis is consistent with the nanoantennas distinguishing between the enzyme and enzyme-substrate conformations.

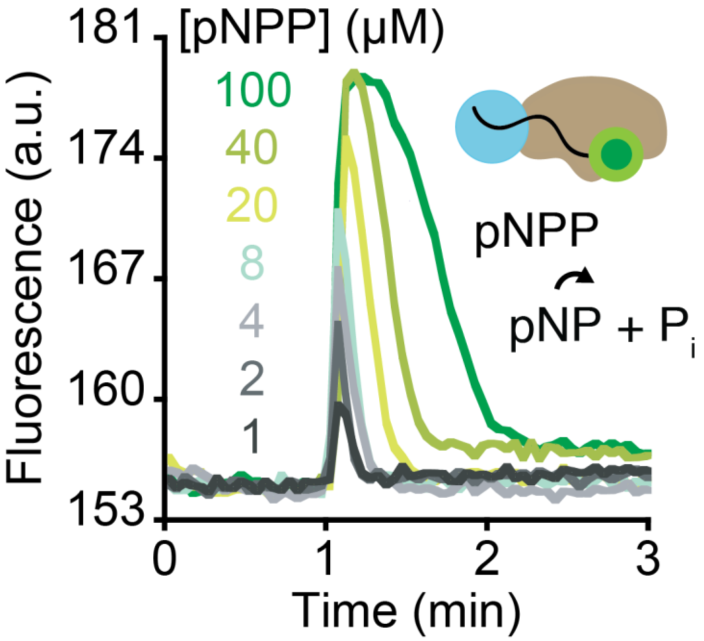

Figure 3.1. – Effect of pNPP concentration of fluorescence spike intensity and time. Here, pNPP was added at concentrations of 1, 2, 4, 8, 20, 40, and 100 µM. Conditions: 150 nM nanoantenna, 50 nM SA, 100 nM bAP, 1-100 µM pNPP, 100 mM Tris, 10 mM NaCl, pH 8.0, and 30 °C.

One benefit of using the pNPP substrate is that its hydrolysis can be detected by two independent strategies, namely, by the fluorescent nanoantennas and by generation of yellow pNP product.[34] Furthermore, by using an instrument with dual fluorescence and absorbance modes, in our case a stopped-flow spectrometer, it is convenient to study the same enzyme and substrate samples by simply changing the detection mode (**Figure 3.2**). First, monitoring pNP generation by UV-Vis displays an increase in absorbance until the substrate begins to run out, whereupon it eventually reaches a plateau. Then, the derivative (or rate) of this data is reminiscent of the transient fluorescence spike observed by the nanoantenna. Indeed, they effectively display the same kinetics. Thus, the link between the fluorescence intensity of the spike and the [ES] is confirmed by the former being proportional to the rate of reaction obtained by monitoring pNP generation by UV-Vis.

We considered that one typically obtains the initial rate (V_0) via the pNP signal shortly after addition of the substrate, which coincides with the maximum intensity of the fluorescence spike. Plotting the spike intensity versus [pNPP], in an analogous manner to V_0 versus [pNPP] for a Michaelis–Menten plot, generated a similar saturation binding curve (**Figure 3.3**). Note that

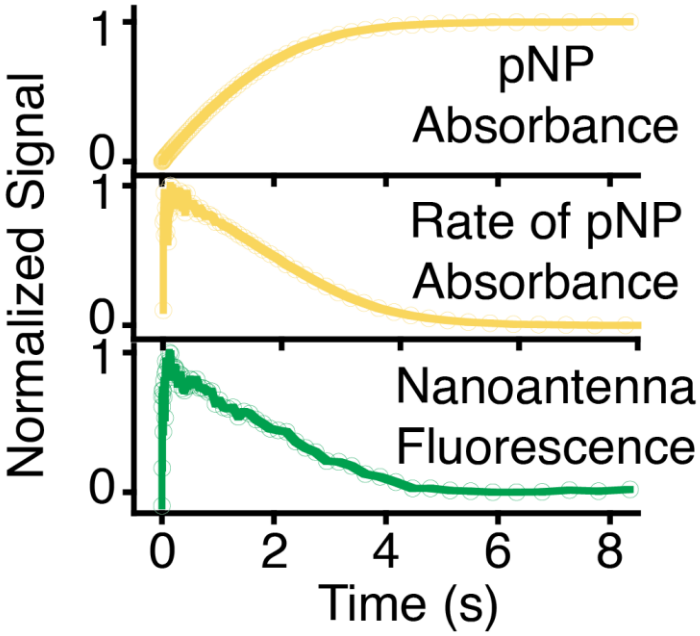

Figure 3.2. – Nanoantenna fluorescence correlates with the rate of reaction determined by monitoring pNP generation with UV-Vis. The rate of pNP generation (slope of absorbance) follows the same profile as the nanoantenna fluorescence.

plotting the area under the spike versus [pNPP] simply generated a linear plot (**Supplementary Figure S3.1**). At lower [pNPP] there is a linear increase in spike intensity, but at higher [pNPP] it tapers off and eventually reaches a plateau at the maximum fluorescence (F_{max}) that is analogous to the maximum rate (V_{max}). Fitting with a modified Michaelis–Menten equation (**Eqn 3.1**), also with fluorescence spike intensity (F_{int}) instead of initial rate, provided a [pNPP] at which the fluorescence spike is half of F_{max}, denoted as $K_{0.5}$ (4.4 ± 0.2 µM). This value is similar to the K_{M} reported in the literature under the same conditions.[100] While the $K_{0.5}$ appears to be equal to the K_{M}, we do not currently have a method to convert the F_{max} (26.2 ± 0.6 a.u.) in units of a.u. to V_{max} in units of M s^{-1}. We demonstrate later, however, how to avoid this limitation. Similar $K_{0.5}$ and F_{max} values were also obtained by plots analogous to the classic Lineweaver–Burk and Hanes–Woolf methods (**Supplementary Figure S3.2**).

$$F_{\text{int}} = \frac{F_{\text{max}}\,[\text{S}]}{K_{0.5} + [\text{S}]} \qquad \textbf{Eqn 3.1}$$

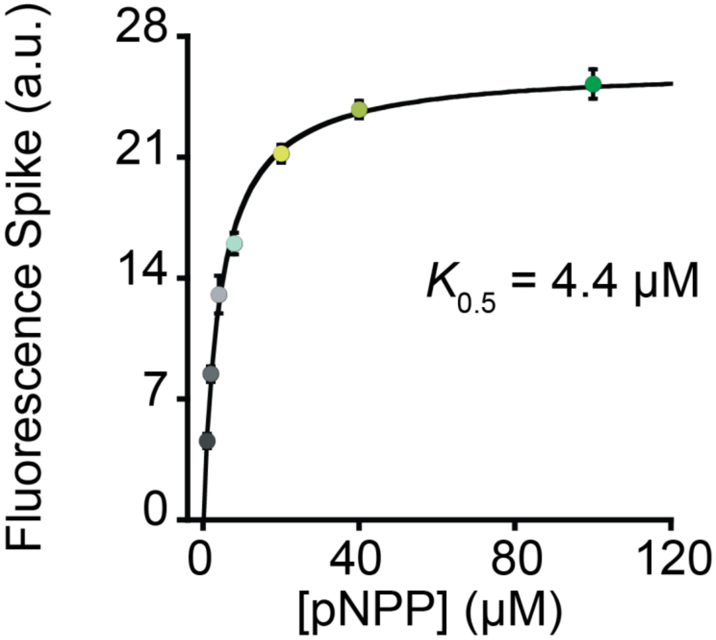

Figure 3.3. – Nanoantenna spike intensity corresponds to reaction rate. Here, the data in Figure 3.1 were plotted as spike intensity *versus* [pNPP] to extract the Michaelis–Menten kinetic parameters by non-linear curve fitting.

3.3 Extraction of parameters: kinetics and inhibition

Nanoantennas enable complete kinetic characterisation of an enzyme in a single experiment. When a reaction product is also an inhibitor, this can enable the study of inhibition with just one enzyme sample without saturating the detector, as could normally occur when using chromogenic and fluorogenic substrates (**Supplementary Figure S3.3**). Indeed, upon performing consecutive pNPP injections, we observed a decrease in spike intensity and an increase in reaction time, consistent with accumulation of one of the products, P_i, a competitive inhibitor of this enzyme (**Figure 3.4**). Inspired by recent ITC studies,[99, 102, 103] we sought to characterise the enzyme kinetics via these fluorescence spikes.

First, by fitting a single fluorescence spike using Michaelis-Menten differential equations with competitive product inhibition,[103] one can extract the K_M and k_{cat} values, and from these, the k_{cat}/K_M (**Figure 3.5, top**). For the kinetic fitting procedure, developed in collaboration with Dominic Lauzon, see sections 6.1.7 Kinetic fitting and 6.5 Script for fitting kinetic data in MATLAB. We determined K_M (5.0 ± 0.1 µM), k_{cat} (32.1 ± 0.9 s^{-1}) and k_{cat}/K_M (6.4 ± 0.3 $\mu M^{-1}\ s^{-1}$) values similar to those reported in the literature under the same conditions (**Table 3.1**).[100] Notably, the $K_{0.5}$

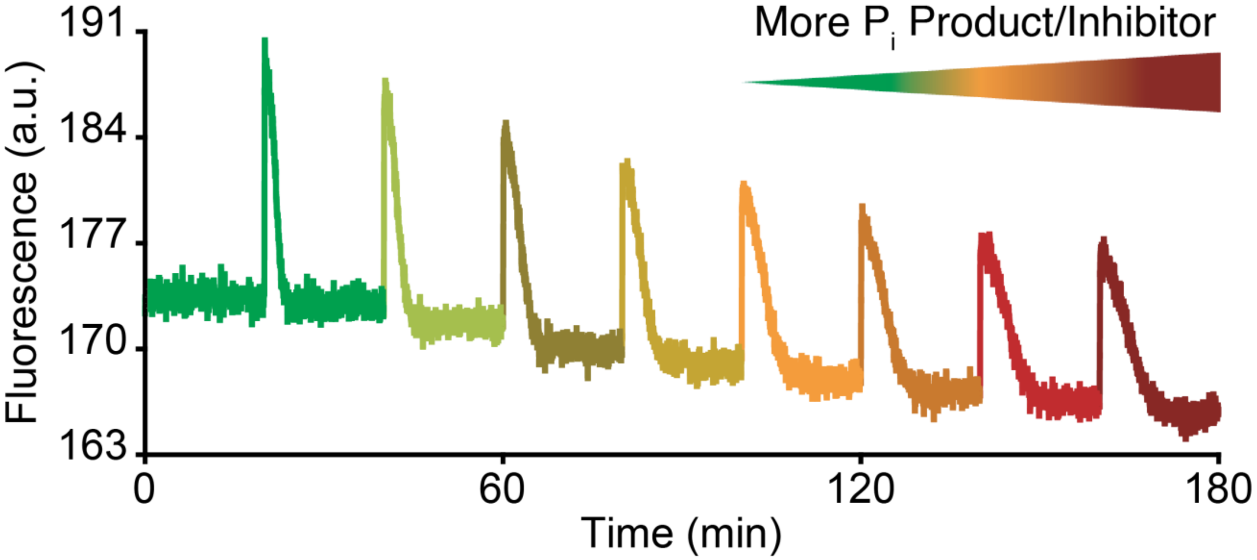

Figure 3.4. – Multiple injections of pNPP. Eight injections of pNPP were added to the same nanoantenna-SA-bAP sample. Each reaction takes longer due to accumulation of P_i.

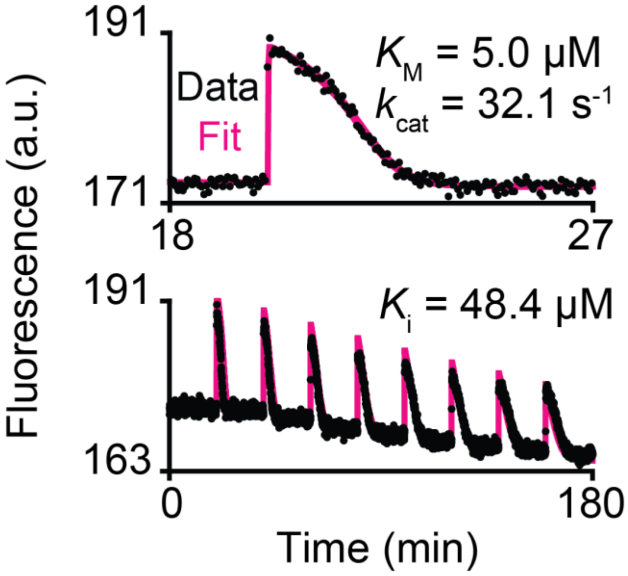

Figure 3.5. – Fitting data to extract the kinetic parameters. Fitting one spike enables extraction of the K_M and k_{cat}, while fitting multiple spikes enables extraction of the K_i.

Table 3.1. – Michaelis–Menten kinetic parameters of AP with pNPP substrate. Shown are values reported in the literature[100] and values determined in our study. Our fitting strategy of the nanoantenna fluorescence shown in Figure 3.5 displays similar parameters. Control experiments with UV-Vis shown in Supplementary Figure S3.4 also display similar parameters.

	Literature ITC	**Literature UV-Vis**	**Nanoantenna Fluorescence (Figure 3.5)**	**Nanoantenna UV-Vis (Figure S3.4a)**	**Dummy – no dye UV-Vis (Figure S3.4b)**	**bAP Only UV-Vis (Figure S3.4c)**
K_M (μM)	7.78	9.31	5.0 ± 0.1	10.1 ± 0.7	11.3 ± 1.0	7.9 ± 0.2
V_{max} (μM s^{-1})	n/a	n/a	0.321 ± 0.0(8)[b]	2.7 ± 0.0(1)	3.3 ± 0.0(5)	3.2 ± 0.0(1)
k_{cat} (s^{-1})	47.36	46.92	32.1 ± 0.8	24.6 ± 0.0(48)	30.4 ± 0.4	30.0 ± 0.1
k_{cat}/K_M (μM^{-1} s^{-1})	6.1[a]	5.0[a]	6.4 ± 0.3	2.5 ± 0.2	2.7 ± 0.2	3.8 ± 0.1

a) These k_{cat}/K_M values differ slightly from what was reported in Table 1 of the cited study, but there seems to be several errors therein because the reported k_{cat}/K_M values do not agree with the corresponding k_{cat} and K_M values, so we recalculated it. The differences are small, and in practical terms, do not matter.

b) This V_{max} was derived by using the k_{cat} value obtained from our fitting procedure and enzyme concentration. Note also that the fluorescence experiment used 10 nM bAP, and the UV-Vis experiments used 109 nM bAP, hence the differing V_{max} values. As expected, the k_{cat} values were effectively the same.

value determined by plotting spike intensity and the K_M value determined by fitting a single spike were in agreement. Crucially, similar values were also obtained by monitoring pNP product generation by using UV-Vis spectroscopy (**Table 3.1** and **Supplementary Figure S3.4**). Importantly, we also found that neither the dye nor SA affected the kinetic parameters of the enzyme (**Table 3.1** and **Supplementary Figure S3.4**). We did find that inaccurate K_M and k_{cat} values were obtained by fitting a single fluorescent spike observed upon addition of a relatively low [pNPP], but this can be avoided by adding higher concentrations of substrate of at least ~3K_M (**Supplementary Figures S3.5, S3.6**). Next, by using a similar fitting procedure, we modelled the eight spikes from the same enzyme sample. From these, we determined the K_i, a measure of the inhibitory effect of the P_i product (**Figure 3.5, bottom**). This K_i (48.4 ± 2.0 µM) was close to the previously reported values (**Table 3.2**). Moreover, the decrease in spike intensities was consistent with the expected decrease in the reaction rate due to the K_i value of the inhibition (**Supplementary Figure S3.5**).

Table 3.2. – Determined K_i values for competitive inhibitor P_i. Also shown are available literature values determined under similar conditions.

Inhibitor	K_i (µM)	pH	Temperature (°C)	Substrate	Reference
P_i	48 ± 2	8.0	30	pNPP (nanoantennas)	This study
phosphate	16.5	9.25	30	4MUP	[468]
	19	9.25	30	ATP	[468]
	21.2	7.5	37	PPi	[256]
	29	9.19	30	PPi	[468]
	33.7	7.0	25	ATP	[100]
	60	8.9	37	PLP	[469, 470]
	68	9.25	30	fluorophosphate	[468]

It is worth discussing some of the details of how we arrived at these values. The first fitting of one spike to obtain the K_M and k_{cat} takes into consideration the inhibitory effects of the released P_i. We needed a K_i value for this, so based on the literature,[100] we assumed a K_i of 33.7 µM. The fit then provided initial K_M (4.2 ± 0.0(2) µM) and k_{cat} (31.4 ± 0.8 s^{-1}) values. The second fitting of all eight spikes to obtain our K_i takes into consideration the K_M and k_{cat} of the enzyme-substrate system, so we used the initial values we had just obtained from the first fit. This provided an initial K_i value (40.8 ± 1.0 µM). From a practical perspective, K_i values of 33.7 µM and 40.8 µM are effectively the same, but their numerical difference could suggest an error in the fitting. To check it, we repeated the fitting of one spike to re-obtain the K_M and k_{cat} values, but now using our own K_i value rather than the literature value. Then, we repeated the fitting of all eight spikes to re-obtain the K_i value, but now using our new K_M and k_{cat} values. After several iterations of this procedure, the values converged with no further change (**Figure 3.6a**). Thus, the final kinetic parameters were those that were provided in the previous paragraph: K_M (5.0 ± 0.1 μM), k_{cat} (32.1 ± 0.9 s^{-1}), k_{cat}/K_M (6.4 ± 0.3 $\mu M^{-1}\ s^{-1}$), and K_i (48.4 ± 2.0 μM).

A criticism here could be that our fitting procedure required the knowledge of a literature K_i value obtained under similar conditions. Thus, instead of this "good guess" for the K_i, we tried a "bad guess" for it. More specifically, we started with a K_i value of 390 μM, as reported for a

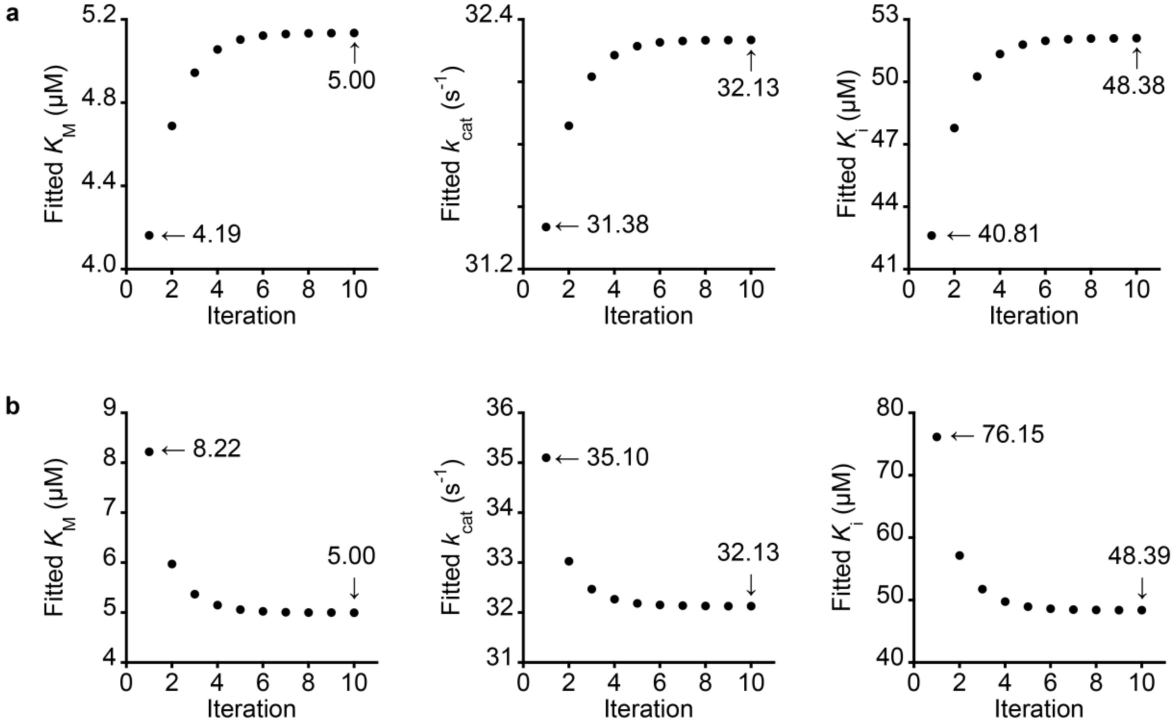

Figure 3.6. – Multiple iterations of data fitting result in their convergence. The first round of data extraction used a literature K_i value to obtain our K_M and k_{cat} values. These were then used to obtain our K_i value. After several iterations of this procedure, the values converge with no further change.

bacterial AP under very different buffer conditions.[219] This led to a somewhat different initial K_M value (8.2 ± 0.0(4) µM) but effectively the same k_{cat} value (35.1 ± 1.0 s^{-1}), and in turn, using these led to a higher K_i value (76.1 ± 2.1 µM). After several iterations of the calculation, however, we obtained the same final kinetic parameters as noted previously (**Figure 3.6b**). Therefore, if one already has a good estimate of the K_i, then the iteration approach may not be necessary for practical purposes (*i.e.*, K_M values of 4.2 µM and 5.0 µM are effectively the same for most applications), but in the absence of a good estimate, one can refine the result.

3.4 Characterising any substrate

The experiments presented above have involved AP-mediated hydrolysis of the substrate pNPP to its products pNP and P_i. However, it is pointless to develop a new fluorescence method to study AP with pNPP – why reinvent the wheel? Remarkably, these fluorescent nanoantennas are not limited to just one substrate. We next demonstrate that fluorescent nanoantennas can be used to monitor the AP-mediated hydrolysis of any substrate, including biomolecules. Note that at this point in the project, we experienced a problem with enzyme batch-to-batch variation,[428-433] so some values presented hereafter are different from those presented above. However, all derived kinetic parameters remained within the expected range. Please see **Supplementary Figure S3.7** for further discussion of this issue. For comparisons of substrates, however, we always used the same batch of enzyme.

We started by characterising the two classic substrates, chromogenic pNPP and fluorogenic 4MUP, with the new batch of bAP. Note that the fluorescent product 4MU, also called hymecromone, has recently received attention for its potential to treat some cancers.[471] Using the fitting protocol described above (without multiple iterations), we extracted their K_M and k_{cat} values, and from these, the k_{cat}/K_M (**Figure 3.7** and **Table 3.3**). While this batch of bAP displayed somewhat different kinetic parameters, the values for pNPP were still within the reported range (K_M = 24.3 ± 1.3 µM, reported = ~4 to ~120 µM; k_{cat} = 178.1 ± 12.8 s^{-1}, reported = ~23 to ~905 s^{-1} or sometimes higher; k_{cat}/K_M = 7.3 ± 0.9 $µM^{-1}$ s^{-1}, reported = ~1 to ~28 $µM^{-1}$ s^{-1} or sometimes higher).[100, 101, 215, 216, 408, 472-475] For 4MUP, the K_M and k_{cat}/K_M were similarly within the reported

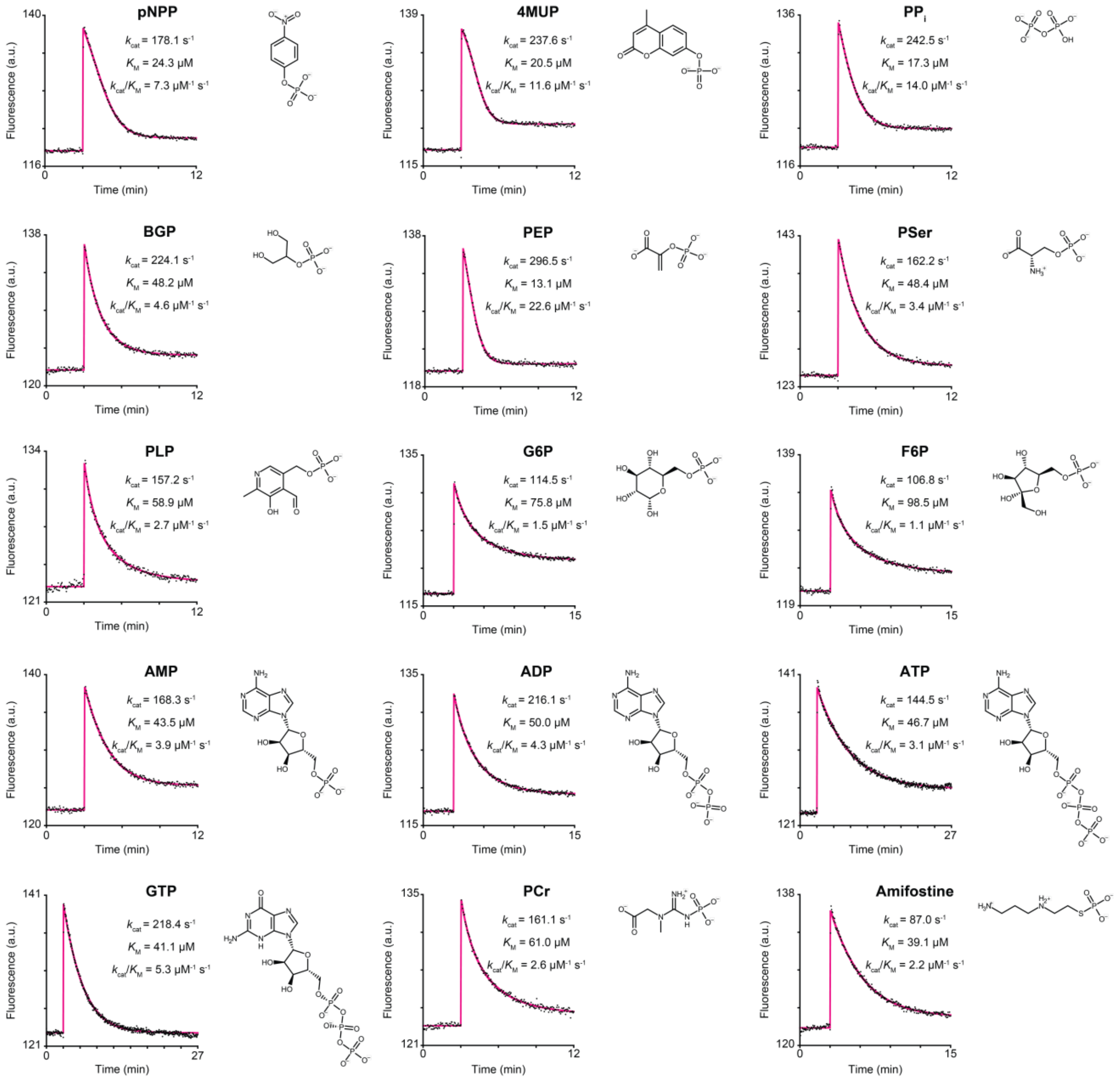

Figure 3.7. – Fluorescent nanoantennas enable real-time monitoring of any substrate hydrolysed by AP. Nanoantenna fluorescence signatures during hydrolysis of pNPP, 4MUP, PP$_i$, BGP, PEP, PSer, PLP, G6P, F6P, AMP, ADP, ATP, GTP, PCr, and amifostine. These experiments were performed in 100 mM Tris, 10 mM NaCl, pH 8.0, and 37 °C.

Table 3.3. – Determined K_M and k_{cat} values for various substrates. Also shown are literature values, listed from low to high K_M, that were determined under similar conditions.[a,b] Our k_{cat} and K_M values, determined at pH 8.0 and 37 °C, are within the typical range for AP values (see pNPP), but are obviously faster when compared to most available values for other substrates determined at somewhat lower pH or temperature.

Substrate	**This study**			**Literature**					
	k_{cat} (s^{-1})	**K_M (µM)**	**k_{cat}/K_M ($\mu M^{-1}\ s^{-1}$)**	**k_{cat} (s^{-1})**	**K_M (µM)**	**k_{cat}/K_M ($\mu M^{-1}\ s^{-1}$)**	**pH**	**T (°C)**	**ref**
pNPP	178.1 ± 12.8	24.3 ± 1.3	7.3 ± 0.9	-	3.6	-	8.0	25	472
				47.36	7.78	6.1[c]	8.0	30	100
				46.92	9.31	5.0[c]	8.0	30	100
				300.3	10.7	28.1	8.0	25	473
				287	18	16.0	8.0	RT	215
				22.5	24	0.93	7.4	25	408
				3580	35	99	8.5	25	101
				905	37.7	24.0	8.0	37	474
				-	~63[d]	-	8.0	-	216
				341.7	119.7	2.9	8.8	37	475
4MUP	237.6 ± 12.9	20.5 ± 0.6	11.6 ± 1.0	39.2	2.2	18	8.0	25	476
				-	2.3[e]	-	7.91	30	37
				9.5	2.5	3.8[c]	8.0	25	100
				7.2	3.2	2.6[c]	8.0	25	100
				-	5.4[e]	-	8.36	30	37
				-	~10	-	8.5	22	477
				-	28	-	8.5	30	478
PP$_i$	242.5 ± 16.7	17.3 ± 0.2	14.0 ± 1.1	-	16	-	8.0	25	472
				36.6[f]	66[f]	0.55[f]	7.4	25	408
BGP	224.1 ± 14.1	48.2 ± 2.8	4.6 ± 0.6	-	15	-	8.0	25	472
PEP	296.5 ± 12.3	13.1 ± 0.2	22.6 ± 1.3	-	5.5	-	8.0	25	472
PSer [f]	162.2 ± 5.2	48.4 ± 1.0	3.4 ± 0.2	-	-	-	-	-	-
PLP	157.2 ± 12.5	58.9 ± 11.6	2.7 ± 0.7	-	3.6	-	7.4	37	267
				17.8	31	0.57	7.4	25	408
G6P [f]	114.5 ± 11.8	75.8 ± 14.3	1.5 ± 0.4	-	-	-	-	-	-
F6P [f]	106.8 ± 3.2	98.5 ± 16.0	1.1 ± 0.2	-	-	-	-	-	-
AMP	168.3 ± 12.4	43.5 ± 2.4	3.9 ± 0.5	-	11.2	-	8.0	30	479
				-	12.0	-	7.4	30	479
				-	18	-	8.0	25	472
				22.6	43	0.52	7.4	25	408
ADP	216.1 ± 14.3	50.0 ± 2.8	4.3 ± 0.5	22.6	20	1.13	7.4	25	408
ATP	144.5 ± 4.0	46.7 ± 2.9	3.1 ± 0.3	3.5	6.8	0.52	7.0	25	100
				-	16	-	8.0	25	472
				-	18.9	-	8.2	25	105
				18.9	31	0.61	7.4	25	408
				-	105	-	7.5	37	266
GTP [f]	218.4 ± 19.6	41.1 ± 1.0	5.3 ± 0.6	-	-	-	-	-	-
PCr [f]	161.1 ± 6.5	61.0 ± 7.0	2.6 ± 0.4	-	-	-	-	-	-
Amifostine [f]	87.0 ± 2.5	39.1 ± 3.9	2.2 ± 0.3	-	-	-	-	-	-

a) Our conditions were 100 mM Tris, 10 mM NaCl, pH 8.0, 37 °C; also 150 nM nanoantenna, 50 nM SA, 20 nM bAP, 300 µM substrate. Literature conditions were mostly Tris buffers, pH ~8, 25-37 °C. We did not consider studies at significantly different pH, nor studies that used other isoforms/species of AP.

b) [Mg^{2+}] can affect the rate of substrate hydrolysis, so values could differ between studies, but likely not enough to make the results non-comparable. For example, in one study at pH 8.0, 1 mM or 5 mM of Mg^{2+} increased the rate by factors of about ~1.7x or ~2.2x, respectively.[216]

c) These k_{cat}/K_M values differ slightly from what was reported in Table 1 of the cited study,[100] but there seems to be several errors therein because the reported k_{cat}/K_M values do not agree with the corresponding k_{cat} and K_M values, so we recalculated it. The differences seem to be larger than rounding errors, but small enough that in practical terms they do not affect the result.

d) This literature pNPP K_M value was not reported directly. We estimated it from the Lineweaver–Burk plot in Figure 3 of the cited study.[216]

e) These literature 4MUP K_M values were not reported directly. We determined them by non-linear fitting with the Michaelis–Menten equation in KaleidaGraph of the data found in Table 2 of the cited study.[37]

f) We could not find any studies reporting kinetic parameters for calf intestinal alkaline phosphatase with some substrates under similar conditions. However, there are studies with various biomolecular substrates that we did not consider for comparison because they employed significantly different conditions (*e.g.*, pH 9-11),[468, 480-483] other bovine isoforms (*e.g.*, kidney),[484-487] other mammalian species (*e.g.*, human, pig, rat),[437, 480, 482, 483, 488-500] or APs from very different species (*e.g.*, fish, bacteria, yeast).[158, 159, 161, 165, 217, 481, 501-508, 509]

range, while the k_{cat} was somewhat faster (K_M = 20.5 ± 0.6 μM, reported = ∼2 to ∼28 μM; k_{cat} = 237.6 ± 12.9 s^{-1}, reported = ∼7 to ∼39 s^{-1}; k_{cat}/K_M = 11.6 ± 1.0 μM^{-1} s^{-1}, reported = ∼3 to ∼18 μM^{-1} s^{-1}).[37, 100, 476-478] This discrepancy for the k_{cat} is probably due to the available literature studies[100, 476] at pH 8 having been conducted at 25 °C, as opposed to our 37 °C, which likely would have made the reaction faster in our case. Based on the success of this comparison with earlier studies, we next considered various biomolecular substrates. Note that although the substrates display different baselines, this is likely due to the phosphate product and sample-to-sample variation (**Supplementary Figures S3.8, S3.9**).

We considered several biomolecular phosphate monoesters. Pyrophosphate (PP_i) and pyridoxal 5'-phosphate (PLP; Vitamin B6) are known substrates of the mammalian tissue-nonspecific isoform of AP (TNAP), and these play a role in skeletal mineralisation and hypophosphatasia.[150-153] β-glycerophosphate (BGP) has also been used to study mineralisation.[156] Glucose-6-phosphate (G6P) and other sugar phosphates have been studied with fungal APs;[158] so G6P and frutose-6-phosphate (F6P) were examined here. One proposed role of intestinal AP is to dephosphorylate phosphoproteins,[109, 149, 161] which contain residues such as phosphoserine (PSer), so we considered that substrate too. Finally, phosphoenolpyruvate (PEP) is the highest energy phosphate found in biology.[1] There have only been a few previous studies of calf intestinal AP with these substrates under similar conditions. For example, we found data for PP_i, BGP, PEP and PLP,[267, 408, 472] but not for G6P, F6P and PSer. Moreover, the data that we could find was often conducted at lower pH and/or temperature, which affects the kinetics. It should also be noted that, specifically for AP and not just as general enzymology advice, there could be some variation for enzyme properties in older literature.[428-433] This scarcity of data reflects the inconvenience involved in studying biomolecular substrates with AP. Nevertheless, these substrates all displayed a fluorescence spike during their hydrolysis by AP. From our fitting procedure, we rapidly obtained their K_M and k_{cat} values. The results were generally in the expected range, especially in consideration of the temperatures used here and in other studies (**Figure 3.7** and **Table 3.3**).

Next, we considered a series of nucleotide substrates: adenosine monophosphate (AMP), adenosine diphosphate (ADP), adenosine triphosphate (ATP), and guanosine triphosphate (GTP). As discussed in Chapter 1, ATP is a known biomolecular substrate of intestinal AP. It has a role in regulating the surface pH of the duodenum and promoting the growth of commensal bacteria in the gut.[142-144, 146, 147] Our nanoantennas and fitting strategy could rapidly characterise these four substrates (**Figure 3.7** and **Table 3.3**). While there were already adequate data available for the K_M of AMP and ATP,[100, 105, 266, 408, 472, 479] few studies had reported the k_{cat} for these important biomolecules.[100, 408] Moreover, there was only one relevant study for ADP,[408] and none for GTP.

All of the substrates tested above are either phosphate monoesters (pNPP, 4MUP, BGP, PEP, PSer, PLP, G6P, F6P, AMP) or contain a pyrophosphate moiety (PP_i, ADP, ATP, GTP). Thus, they all have a P–O bond that can be cleaved by AP. We sought to examine whether the nanoantenna strategy can also characterise the AP-mediated cleavage of other bonds. Phosphocreatine (PCr) is mostly studied in the context of energy metabolism of muscle.[510] However, what is of interest here is that PCr is a phosphoramide. In short, the nanoantenna strategy can also monitor the AP-mediated hydrolysis of the P–N bond. The extracted K_M and k_{cat} values are similar to those of the other small biomolecular substrates (**Figure 3.7** and **Table 3.3**).

Next, we tested amifostine, also called WR-2721 and marketed as Ethyol, which is employed to protect normal tissues against the toxicities of radiation treatment and chemotherapy.[10, 205-207] Intestinal AP putatively dephosphorylates this inactive prodrug to its active form, WR-1065.[208] This metabolite can diffuse into cells, whereupon it protects them during treatment.[206, 207] Here, we show that fluorescent nanoantennas can monitor the AP-mediated hydrolysis of the P–S bond of amifostine. The K_M value is like that of the other substrates, but the k_{cat} is slower (**Figure 3.7** and **Table 3.3**). This could be due to intestinal AP being *able* to hydrolyse the thiophosphate bond, but not having evolved for this purpose.

Finally, we tested a substrate of AP that differs markedly from the others. Lipopolysaccharides (LPS), also called endotoxins, are ~10 kDa macromolecules released from the outer membrane of Gram-negative bacteria, including the intestinal microbiota. As outlined in Chapter 1, a proposed role of intestinal AP is to dephosphorylate LPS, and in turn, reduce its toxicity and inflammation.[134-140] LPS has also been linked to health conditions related to intestinal inflammation.[168, 198] Here, we demonstrate that with the fluorescent nanoantennas, one can monitor the AP-mediated hydrolysis of LPS in real time (**Figure 3.8**). Deriving kinetic parameters for LPS, however, remains challenging due to uncertain sample concentration and number of phosphates per LPS molecule.[511] Nevertheless, the reaction is much slower than an approximately equimolar concentration of pNPP. This could be attributed to the larger size of LPS and/or more phosphates per LPS molecule. Shown alongside the kinetic fluorescence signature is a simplified scheme of LPS structure.[512] Although it can differ between strains of bacteria, generally, it contains acyl chains, several phosphates and various sugars.

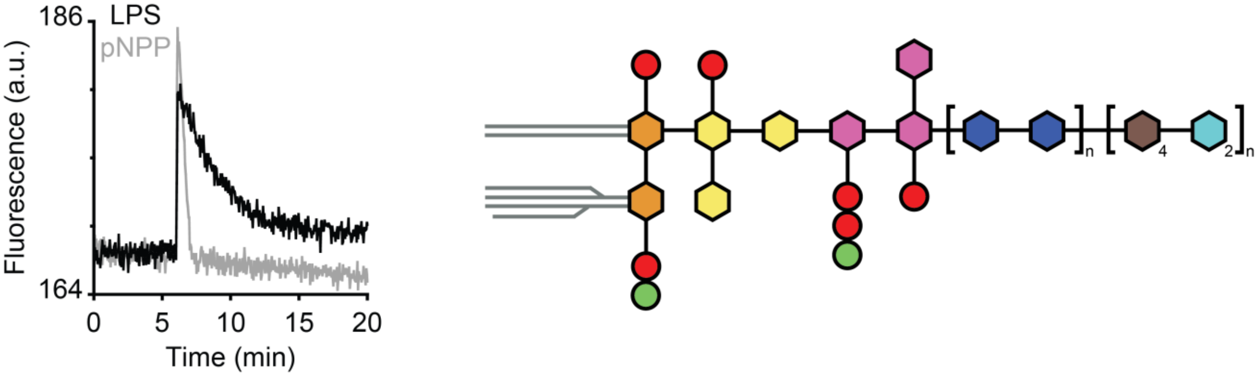

Figure 3.8. – Real-time monitoring of AP function using LPS substrate. Nanoantenna fluorescence signature observed during hydrolysis of ~2.5 µM lipopolysaccharide (LPS) and 2.5 µM pNPP. Shown also is a simplified scheme of LPS structure. LPS was used at a lower concentration than the other substrates due to low concentration of available stock solution. Moreover, due to uncertain LPS molar mass and exact concentration, as well as uncertainty about the number of hydrolysable phosphates, we did not determine the kinetic parameters (K_{M} and k_{cat}). Likewise, kinetic parameters for 2.5 µM pNPP could not be determined due to low concentration being incompatible with our fitting procedure. Conditions: 15 nM PEG nanoantenna, 5 nM SA, 10 nM bAP, 2.5 µM pNPP or ~2.5 µM LPS, in 100 mM Tris, 10 mM NaCl, 37 °C, pH 8.0. The colours in the simplified scheme of LPS represent acyl chains (grey), phosphate (red), ethanolamine (green), N-acetylglucosamine (orange), ketodeoxyoctonic acid (yellow), heptose (violet), glucose (dark blue), neutral sugar (brown), and colitose (light blue).

3.5 “One shot” kinetic fitting saves time and material

When determining the kinetic parameters for an enzyme-substrate system, one must typically determine the initial rates of product generation over a range of ~10 substrate concentrations above and below the K_M.[513] In the context of AP, this is true whether one is using the classic malachite green assay for biomolecules,[106] or detecting the products of pNPP or 4MUP.[34, 37] However, alternative procedures to extract kinetic parameters from progress curves have been proposed.[473, 514, 515] In one study of AP, for example, it was demonstrated that it is possible to obtain accurate K_M and k_{cat} values by fitting two progress curves at different pNPP concentrations.[473] More recently another procedure was shown with the enzyme dihydrofolate reductase (DHFR), whose reaction can be followed by UV-Vis spectroscopy at 340 nm via its cofactor (nicotinamide adenine dinucleotide phosphate, NADPH) and substrate (dihydrofolate, DHF). Therein, the DHFR kinetic parameters were obtained by splitting the progress curve into equal time windows and calculating the mean substrate concentrations and reduction rates for every time interval. This procedure could then be used to conveniently study various mutants of the enzyme.[515] In the present work, since we used just one nanoantenna fluorescent spike for the “one shot” fitting procedure, we further examined how it compares with fitting one progress curve as well as with the classic method at multiple concentrations of substrate.

First, we tried the classic method that employs the fluorogenic substrate 4MUP to determine the initial rates of 4MU product generation at eight different 4MUP concentrations (**Figure 3.9a**). From this, we obtained the K_M and k_{cat} values, which we considered to be the reference values. Then, at one concentration of 4MUP, we found that a single fluorescence spike obtained with our nanoantenna provided K_M and k_{cat} values that agreed with those determined by the traditional method of analysing initial rates of 4MU product generation (**Figure 3.9b**). (As an aside, we performed this analysis several months after the values were obtained for **Figure 3.7** and **Table 3.3**, but we obtained the same result, which shows the reproducibility of the method). In contrast, simply fitting one 4MU progress curve by following fluorescent product generation provided overestimated values for the K_M and k_{cat} (**Figure 3.9c**).

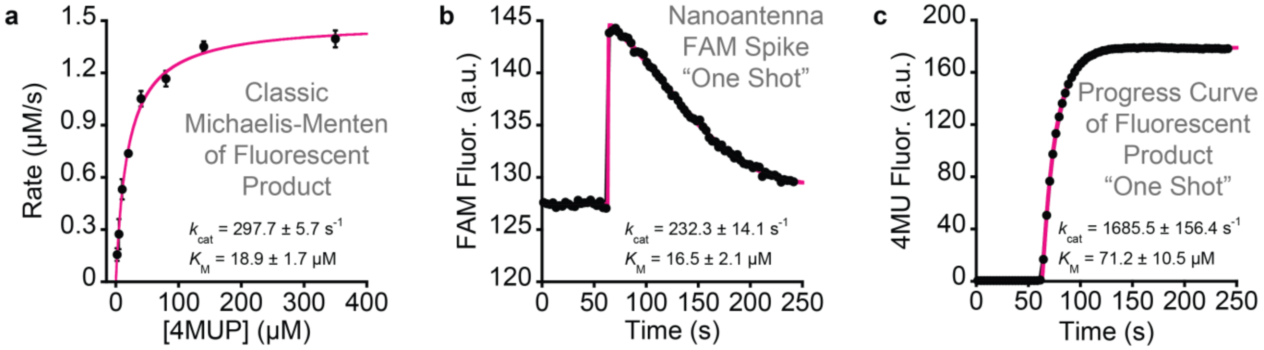

Figure 3.9. – Comparison of methods and error. (a) Classic Michaelis-Menten method to determine k_{cat} and K_{M} values for the 4MUP substrate using the initial rates of 4MU product generation. (b) Nanoantenna "one shot" method to determine k_{cat} and K_{M} values using the FAM fluorescence spike obtained during 4MUP hydrolysis. The values determined using both methods displayed good agreement. (c) We also compared the accuracy of the "one shot" nanoantenna method compared to a similar approach performed using the 4MU progress curve under the same conditions. We found that a "one shot" 4MU progress curve significantly over-estimated both the k_{cat} and K_{M} of the enzyme-substrate system. Conditions were 100 mM Tris, 10 mM NaCl, pH 8.0, 37 °C; also 37.5 nM nanoantenna, 12.5 nM SA, 5 nM bAP, and 2 µM, 5 µM, 10 µM, 20 µM, 40 µM, 80 µM, 140 µM or 350 µM 4MUP in (a), and the same buffer and temperature but with 150 nM nanoantenna, 50 nM SA, 20 nM bAP, and 300 µM 4MUP in (b) and (c). In (a), the concentration of bAP was reduced to facilitate measurement of low 4MUP concentrations, and the nanoantenna and SA concentrations were reduced proportionately. Triplicate experiments were done for each substrate concentration (24 measurements for the classic Michaelis-Menten via initial rates and 3 each for the nanoantenna spike and product progress curve).

These results show the great efficiency of the fluorescent nanoantennas. Since measurements are often taken in triplicate for hard-to-detect spectroscopically silent biomolecules, it is necessary to obtain initial rates for ~30 samples. For substrates that generate a signal, it is also typically necessary to obtain initial rates for ~30 samples, although methods to fit two progress curves at two different substrate concentrations could reduce this to six

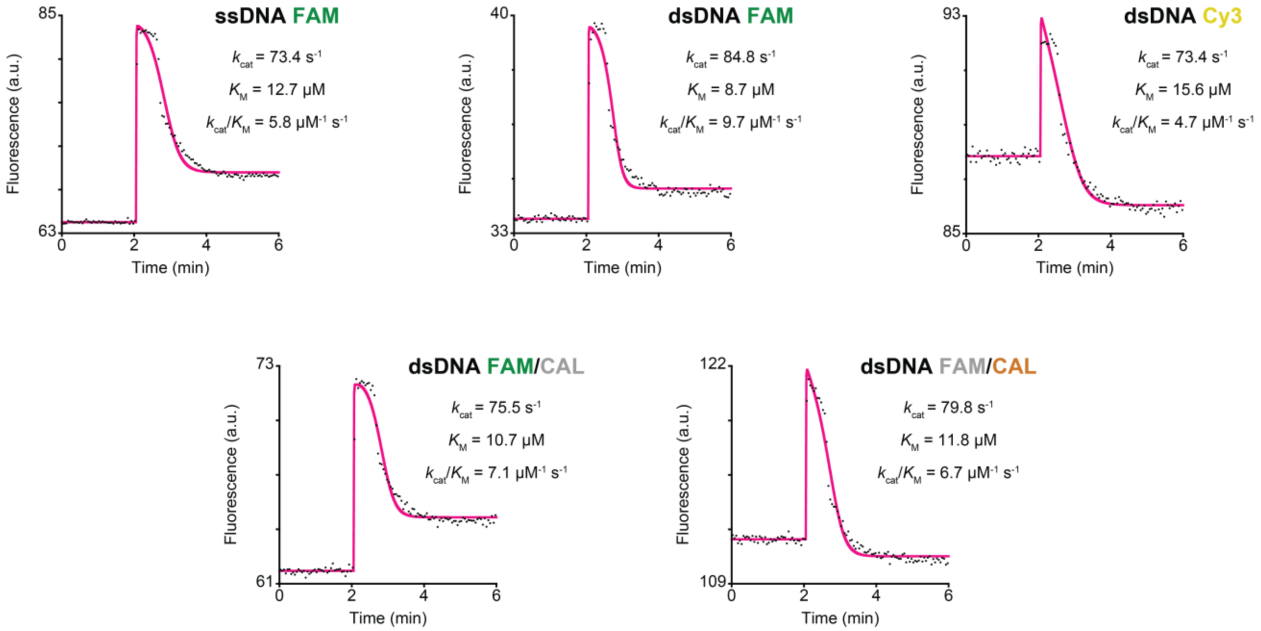

Figure 3.10. – Kinetic parameters can be obtained with various dyes. Here, L12 nanoantennas as ssDNA with FAM, dsDNA with FAM, dsDNA with Cy3, dsDNA with FAM and CAL (monitoring FAM), and dsDNA with FAM and CAL (monitoring CAL) were employed to characterise AP with pNPP. Conditions: 150 nM nanoantenna, 50 nM SA, 100 nM bAP and 300 µM pNPP in 200 mM Tris, 300 mM NaCl, 1 mM $MgCl_2$, pH 7.0, 37 °C. The values of k_{cat} = 77.4 ± 2.2 s^{-1}, K_M = 11.9 ± 1.1 µM and k_{cat}/K_M = 6.8 ± 0.8 µM^{-1} s^{-1} are an average of all five measurements.

samples.[473] Likewise, DHFR and presumably other enzymes can be studied more conveniently by splitting a progress curve into equal time windows, and therefore, only thee samples are needed for a triplicate measurement, as well as an additional calibration curve.[515] With fluorescent nanoantennas and "one shot" fitting, the enzyme-substrate system can be accurately characterised in triplicate with just three samples. Moreover, as shown in the previous section, it is not necessary that the substrate or product molecule generates a signal.

Extraction of the kinetic parameters is not limited to nanoantennas that contain FAM. The fitting procedure was further tested with L12 nanoantennas as ssDNA with FAM, dsDNA with FAM, dsDNA with Cy3, dsDNA with FAM and CAL (monitoring FAM), and dsDNA with FAM and CAL (monitoring CAL) (**Figure 3.10**). Similar k_{cat} and K_M values for pNPP were obtained for all of these nanoantennas. Moreover, these samples were analysed in pH 7 buffer, unlike the rest of this chapter that employed pH 8 buffer. Alkaline phosphatase, as its name implies, displays different activity at different pH levels.[37, 215, 216, 408] At pH 8, the k_{cat} was 178.1 ± 12.8 s^{-1} and now at pH 7 it was 77.4 ± 2.2 s^{-1}. A similar result was reported in the literature, whereby at pH 8 the k_{cat} was 246 s^{-1} and at pH 7 it was 58 s^{-1}.[215] Likewise, at pH 8 the K_M was 24.3 ± 1.3 µM and now at pH 7 it was 11.9 ± 1.1 µM. In the literature example, the K_M shifted from 18 µM to 4 µM.[215]

3.6 Characterising inhibitors

In section 3.3, we showed how it is possible to characterise the K_i of inorganic phosphate (P_i), which is not only a product of substrate hydrolysis but also a competitive inhibitor of the AP enzyme. Here, we show how it is possible to characterise other inhibitors of this enzyme.

First, we considered how inhibitors could impact the shape of the fluorescent spike. To do this, we generated theoretical fluorescence spikes by using our fitting script with the kinetic parameters set as constants. For this section, our focus is on competitive inhibitors, although we also show the results for an uncompetitive inhibitor and a non-competitive inhibitor (**Figure 3.11**). A competitive inhibitor will bind to AP in its active sites, and this enzyme-inhibitor complex prevents the formation of the enzyme-substrate complex. This increases the apparent K_M, but by adding substrate at higher concentration, the apparent V_{max} will be unchanged. Here, we see that compared to having no inhibitor, a relatively weak competitive inhibitor (K_i = 100 µM) will slightly decrease the initial spike intensity and increase the reaction time (~300 s to ~400 s), while a relatively strong competitive inhibitor (K_i = 1 µM) will significantly decrease the spike intensity and increase the reaction time (longer than 600 s).

Next, we used the fluorescent nanoantennas to rapidly characterise the inhibitory effects of five oxyanion competitive inhibitors toward AP with the prodrug substrate amifostine. These five inhibitors were phosphate, molybdate, tungstate, arsenate, and vanadate. We similarly examined Mg^{2+}, a cofactor of AP. We obtained the K_M and k_{cat} of amifostine with AP in the absence and presence of these effectors (**Figure 3.12** and **Table 3.4**). By utilising the Michaelis–

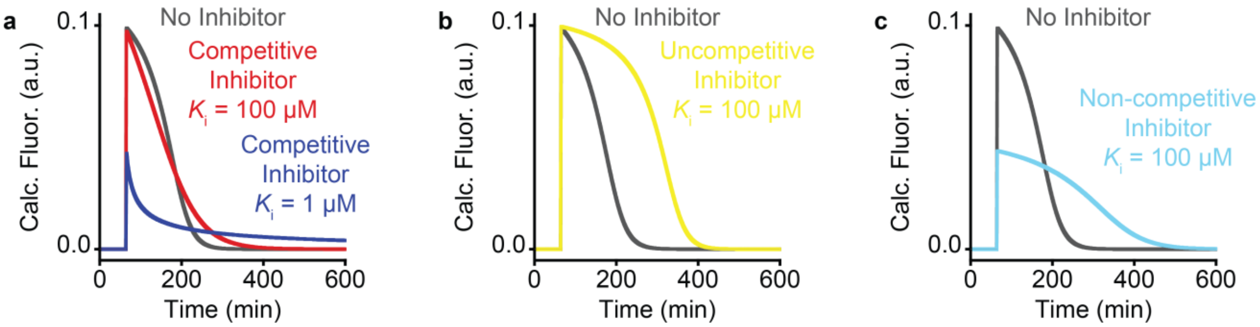

Figure 3.11. – Theoretical nanoantenna kinetic signatures for inhibitors. Here, we generated the expected spike profile of a theoretical system with the parameters: k_{cat} = 100 s^{-1}, K_M = 10 μM, [enzyme] = 100 nM, [substrate] = 1000 μM, and [inhibitor] = 125 μM. Shown are the effects of (a) competitive inhibitors with K_i = 100 μM and K_i = 1 μM, (b) uncompetitive inhibitor with K_i = 100 μM, and (c) non-competitive inhibitor with K_i = 100 μM.

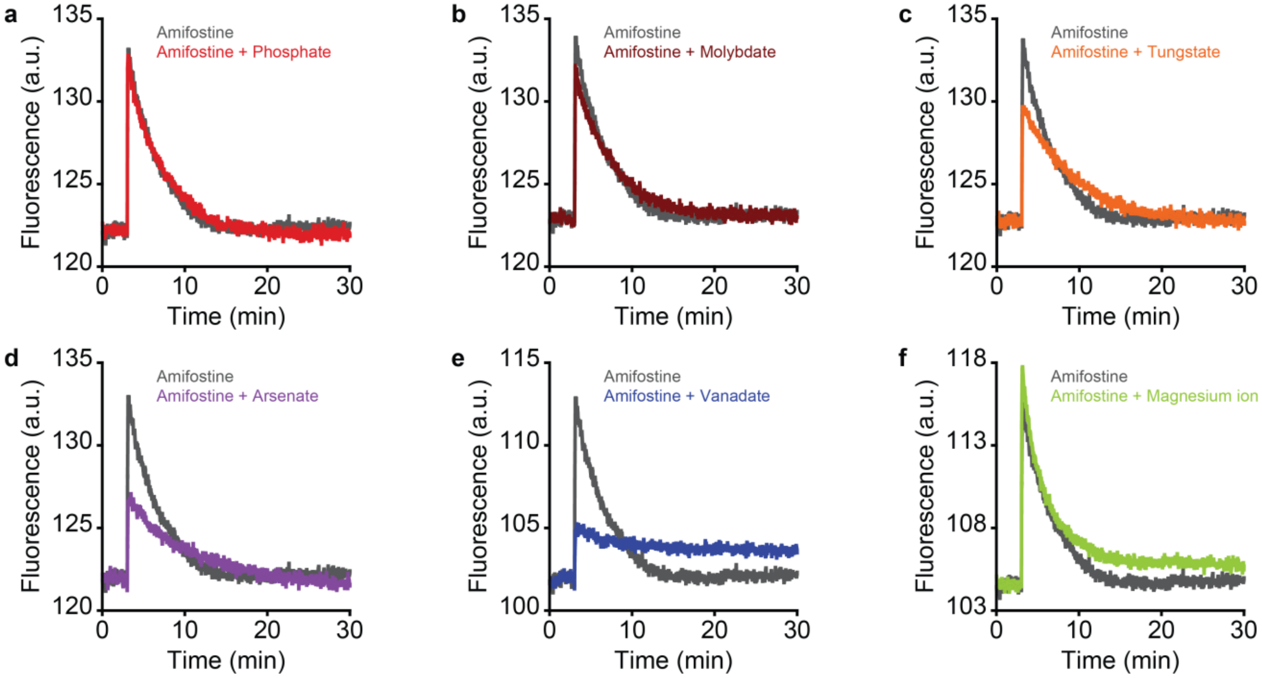

Figure 3.12. – Screening inhibitors by monitoring AP hydrolysis using fluorescent nanoantennas. The inhibitory effects of (a) phosphate, (b) molybdate, (c) tungstate, (d) arsenate, and (e) vanadate on AP with the substrate amifostine, a cancer prodrug that is activated by intestinal AP. Shown also is (f) the effect of Mg^{2+} ion. The baseline of the kinetic

signature without the effector was adjusted for presentation of data (*i.e.*, due to fluorescence quenching caused by vanadate and magnesium ion). Conditions were 300 μM substrate, 30 μM inhibitor or 5 mM Mg^{2+}, and otherwise the same as Figure 3.7. See Table 3.4 for kinetic parameters. The kinetic profiles of phosphate and vanadate follow the theoretical result as shown in Figure 3.11 for relatively weak and strong competitive inhibitors, respectively.

Menten equation for competitive inhibition (provided for reference in **Supplementary Figure S3.7**), we could obtain their K_i values. Whereas a lower K_i indicates a more potent inhibitor, we found that from best to worst, the inhibitors were ranked as vanadate > arsenate > tungstate > molybdate > phosphate (**Table 3.4**). Moreover, as expected, Mg^{2+} increased both the K_M and the k_{cat}.[216]

A search of the literature for various APs – some barely related to intestinal AP – reveals that although our results follow general trends, no single study has characterised all these inhibitors. For example, the order of the potency of vanadate > tungstate > molybdate has been reported for *Escherichia coli* (*E. coli*) AP,[516] sludge-associated AP,[517] and possibly goldfish ovarian tissue AP,[518] but not for any mammalian intestinal APs. Furthermore, vanadate > tungstate > arsenate,[519] tungstate > arsenate > molybdate,[520] vanadate > arsenate,[521] and arsenate > phosphate,[522] have been reported for calf or bovine intestinal AP, as well as vanadate > phosphate for human intestinal AP[523] and bovine kidney AP,[56] arsenate > phosphate for equine plasma AP,[524] and vanadate > arsenate > phosphate for epiphyseal cartilage membrane AP.[525] However, these studies were conducted with substrates that generate an easily detectable signal, such as pNPP. In contrast, using our “one shot” fitting procedure, nanoantennas can rapidly characterise the inhibitors with the spectroscopically silent prodrug amifostine. For a triplicate measurement, this requires only six measurements (*i.e.*, three without inhibitor and three with inhibitor). The standard methods to characterise amifostine with AP would require ~60 measurements (*i.e.*, ~30 without inhibitor and ~30 with inhibitor), using the tedious method of P_i quantification.[106]

Table 3.4. – Kinetic parameters for amifostine with various effectors. Values were determined from the data in Figure 3.12. Fitting was done analogously to Figure 3.7 (not shown), and then the apparent K_M was used to determine the K_i.

Effector	k_{cat} (s^{-1})	K_M (μM)	K_i (μM)
None	76.0 ± 9.4	43.0 ± 5.6	-
phosphate	77.6 ± 5.7	85.1 ± 11.6	30.6 ± 8.2
molybdate	71.3 ± 6.6	107.0 ± 13.8	20.1 ± 5.2
tungstate	46.5 ± 9.8 *	170.6 ± 36.5	10.1 ± 3.5
arsenate	28.6 ± 2.9 *	394.9 ± 52.8	3.7 ± 1.0
vanadate	25.1 ± 4.0 *	1130.7 ± 119.5	1.2 ± 0.3
magnesium ion	116.5 ± 13.9	60.1 ± 8.9	-

* k_{cat} should not decrease for a competitive inhibitor, but we did observe this for tungstate, arsenate, and vanadate. However, we found that fitting the nanoantenna spike without the reaction having finished reduces the determined k_{cat} of the reaction. For example, if we fit phosphate or tungstate data for 30 min or 20 min, its k_{cat} remains effectively unchanged. However, if we instead fit the same data using only a 10 min, 7.5 min, or 5 min time window (*i.e.*, when the reaction is not over), then the determined k_{cat} decreases while there was a smaller effect on the K_M (not shown). This potential artifact of the fitting should be kept in mind when screening inhibitors with high potency and long reaction time.

3.7 Transition state analogue inhibitors

There is an energy barrier for an enzymatic reaction to proceed from substrate(s) to product(s). This may involve alignment of reacting groups, formation of transient unstable charges, bond rearrangements, and so on. For the reaction to proceed, the molecules must overcome this energy barrier, which can be lowered by enzymes. At the top of the "energy hill", decay to substrate(s) or product(s) is equally likely. This is called the transition state ($ES^‡$). However, this state is not stable, and should not be confused with short-lived but stable intermediates, such as the enzyme-substrate complex (ES). Therefore, it is impossible to directly study a transition state by experimental methods.[1] A transition state analogue (TSA), however, occurs when a molecule binds to an enzyme and mimics the geometry of the transition state. This could include, for instance, conformational changes at the active site.[526] This binding is often quite stable, resulting in a relatively low dissociation constant (K_d). When tightly bound at the same location as where a substrate would bind, the TSA can also serve as an inhibitor. Since this enzyme-inhibitor complex is stable, a crystal structure can thus be obtained. This is useful when designing drugs based on inhibition of enzymes,[527] as well as to understand the mechanism of otherwise unstable enzyme transition states.[528]

As discussed in the previous section, vanadate (VO_4^{3-}), also called inorganic vanadate (V_i) by analogy with inorganic phosphate (PO_4^{3-} or P_i), is a competitive inhibitor of APs.[529] Using V_i to inhibit phosphatases and kinases has been studied in the context of various diseases, such as diabetes.[530-534] Crystallographic studies have proposed that V_i is a TSA inhibitor of AP from *E. coli*,[107, 127] as well as other microorganisms.[535] Although there have been no previous crystallographic studies of calf intestinal AP with vanadate, the studies with *E. coli* AP indicate that "the motions required for the formation and breakdown of the transition state are minimal on the part of the enzyme" and are less than 1 Å.[107] This oxyanion acts as a TSA inhibitor because it can form a stable pentavalent complex that is structurally reminiscent of the unstable transition state of a bound phosphate-containing substrate.[107, 127, 536] In other words, the stable AP-V_i complex can be used to study the unobservable transition state. Therefore, the AP-V_i complex represents one of the distinct states of this enzyme, and putatively mimics the transition state (**Figure 3.13**). Furthermore, a recent study has also proposed that inorganic tungstate (W_i) represents a better TSA inhibitor of AP.[114] While it is not the goal of this thesis to wade into a debate of which is the better TSA inhibitor, one should expect that the binding of V_i and W_i would induce specific states in AP that may be detectable by the fluorescent nanoantennas.

With the above in mind, we tested whether the nanoantennas could detect the binding of several oxyanion inhibitors to bAP. First, as a control, we found that vanadate, tungstate, molybdate and phosphate do not substantially affect the fluorescence of the nanoantenna-SA platform via non-specific interaction (**Supplementary Figure S3.8**). Then, we added these oxyanions to cuvettes containing the nanoantenna-SA-bAP complex. Unlike the transient

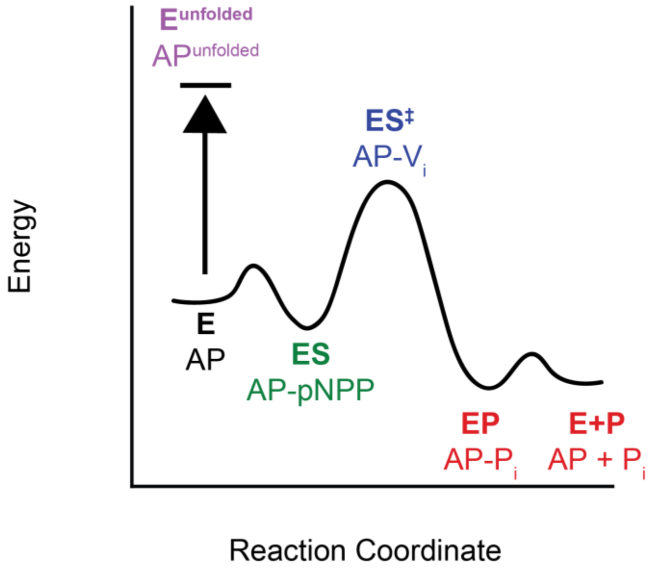

Figure 3.13. – States of AP during enzymatic reaction and denaturation. First, the enzyme (E) is present in solution, followed by the energetically favourable binding of a substrate (*e.g.*, pNPP) to form an enzyme-substrate complex (ES). Next, the high-energy transition state ($ES^{\ddagger}$) is formed. It cannot be observed directly but can be studied via transition state analogue (TSA) inhibitors that mimic its geometry, such as V_i. Note that the AP-V_i complex is stable (*i.e.*, low energy), unlike the transition state whose structure it mimics. After the hydrolysis of pNPP, the bound P_i product (EP) is released from the enzyme (E + P). As a competitive inhibitor, P_i can rebind to the active site. AP can also be unfolded by thermal denaturation ($E^{unfolded}$).

fluorescence spike observed upon addition of a substrate, nanoantennas detect vanadate binding to bAP via large fluorescence quenching (**Figure 3.14a**). This quenching response contrasts with the increase in fluorescence upon substrate binding, further indicating that the FAM of the nanoantenna is not simply being ejected from the active site, but instead it is monitoring enzyme function through distinct conformational changes. Adding increasing concentrations of vanadate led to a binding curve behaviour quenching (**Figure 3.14b**). Furthermore, tungstate binding was found to increase fluorescence (**Figure 3.14b**). The K_d values observed for the binding of vanadate and tungstate (0.54 ± 0.01 µM and 7.6 ± 0.2 µM, respectively) were found to be consistent with their K_i values previously determined using the "one shot" fitting of the fluorescent spike

(1.2 ± 0.3 μM and 10.1 ± 3.5 μM, respectively; see **Table 3.4**). There was also agreement with literature K_i values for vanadate with calf intestinal AP (0.49 μM)[474] and human intestinal AP (0.50 μM).[523] Although there were no K_i values available for intestinal AP with tungstate, a study with *E. coli* AP reported a similar trend for the K_i values of vanadate and tungstate (2.3 μM and 5.9 μM, respectively, at pH 8).[516] Note that while K_d values are determined by binding experiments and K_i values by kinetic experiments, $K_d \approx K_i$ for a competitive inhibitor.[537, 538] In contrast, the phosphate and molybdate binding curves could not be fitted due to the lack of a plateau (**Figure 3.14b**). Thus, here we have shown that the nanoantennas can detect the small conformational changes that occur upon binding of vanadate and tungstate to alkaline phosphatase.

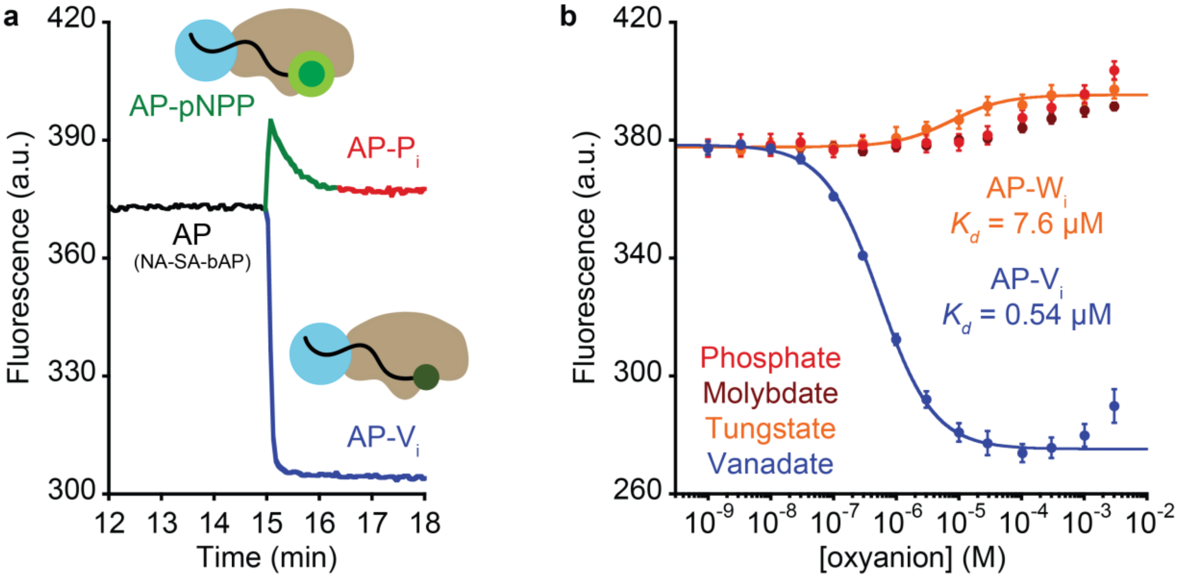

Figure 3.14. – Vanadate and tungstate binding. (a) Unlike the spike during pNPP hydrolysis, V_i binding quenches the nanoantenna's fluorescence. (b) Binding curve of the nanoantenna-SA-bAP complex sensing vanadate (blue) and tungstate (orange). The other competitive inhibitor oxyanions, phosphate (red) and molybdate (maroon), do not exhibit such a large fluorescence change. Note that the final two data points for vanadate were not included in the fit.

3.8 Unfolded state

Thermal denaturation of proteins, often also called protein melting, allows one to determine the thermal stability of a protein as it passes from a highly ordered folded state to an unfolded random state. This information is important in the fields of drug development and protein engineering,[539] as well as for food and biotechnology applications.[540] Upon subjecting the protein sample to a temperature gradient, the inflection point of the signal output is the melting temperature (T_M), which can be determined by taking the derivative of the data or by curve fitting software.[541, 542] Here, we sought to determine whether our fluorescent nanoantennas can be used to monitor large conformational changes, such as protein unfolding by thermal denaturation.

We first recorded the temperature-dependent FAM fluorescence of the nanoantenna, the nanoantenna-SA platform, and the nanoantenna-SA-bAP complex (**Figure 3.15a**). The nanoantenna-SA platform and the nanoantenna-SA-bAP complex displayed transitions, so we used the derivative of the data to find their T_M (**Figure 3.15b**). We also recorded the tryptophan (Trp) fluorescence of SA alone, unbiotinylated AP alone, and the nanoantenna-SA platform (**Figure 3.15c**) and likewise obtained their T_M values (**Figure 3.15d**). Note that we did not record the Trp fluorescence of bAP because it contains bovine serum albumin (BSA) added by the manufacturer as a stabiliser.

Before examining the enzyme, we considered the nanoantenna and SA. Using FAM fluorescence, we see that unbound nanoantennas did not display a transition (**Figure 3.15b**). Using Trp fluorescence, however, we see that SA alone displays a transition at 79.4 ± 1.0 °C (**Figure 3.15d**). This represents the T_M of SA, and it agrees with the reported literature values of 75.5 °C and 84.1 °C.[335, 543] Next, we considered the nanoantenna-SA platform. Using Trp fluorescence, we see that unlike SA alone, it does not display a transition (**Figure 3.15d**). This is presumably due to the enhanced cooperativity of the thermal unfolding of SA upon biotin binding, as a higher T_M value of 112.2 °C has been reported at full biotin saturation.[335] Thus, the nanoantenna-SA platform remains stable over the tested temperature range. Using FAM fluorescence, however, the nanoantenna-SA platform displays a distinct transition at the T_M of 91.7 ± 0.7 °C (**Figure 3.15b**). This likely represents dissociation of FAM from SA, rather than unfolding of SA or detachment of the whole nanoantenna, since the steady Trp fluorescence derivative signal supports that the nanoantenna-SA platform remained stable over this temperature range.[544]

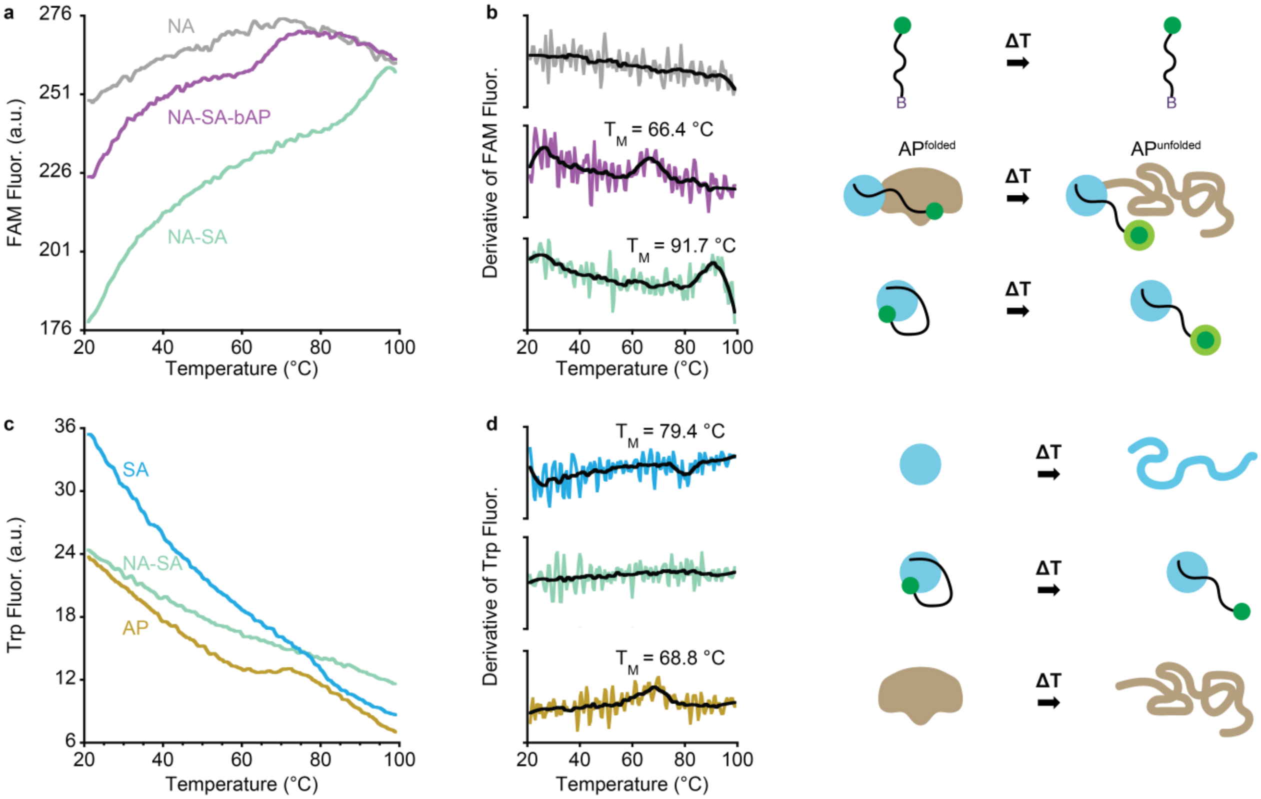

Figure 3.15. – Monitoring protein unfolding with fluorescent nanoantennas. (a) FAM fluorescence melting curves of the nanoantenna (grey), nanoantenna-SA platform (light green) and nanoantenna-SA-bAP complex (light purple). (b) Derivatives of the melting curves with smoothing (black lines) and corresponding cartoons are shown. (c) Trp fluorescence melting curves of SA (blue), the nanoantenna-SA platform (light green) and AP (dark yellow). (d) Derivatives of the melting curves with smoothing and corresponding cartoons are similarly shown. Conditions: 150 nM nanoantenna, 50 nM SA, 100 nM bAP in 100 mM NaCl, 50 mM Na_2HPO_4, pH 6.99, 20-100 °C, 1 °C/min. $\lambda_{ex/em}$ FAM = 498/520 nm, Trp = 280/340 nm. Smoothing of the derivatives was by the Savitzky–Golay method with 25 points.

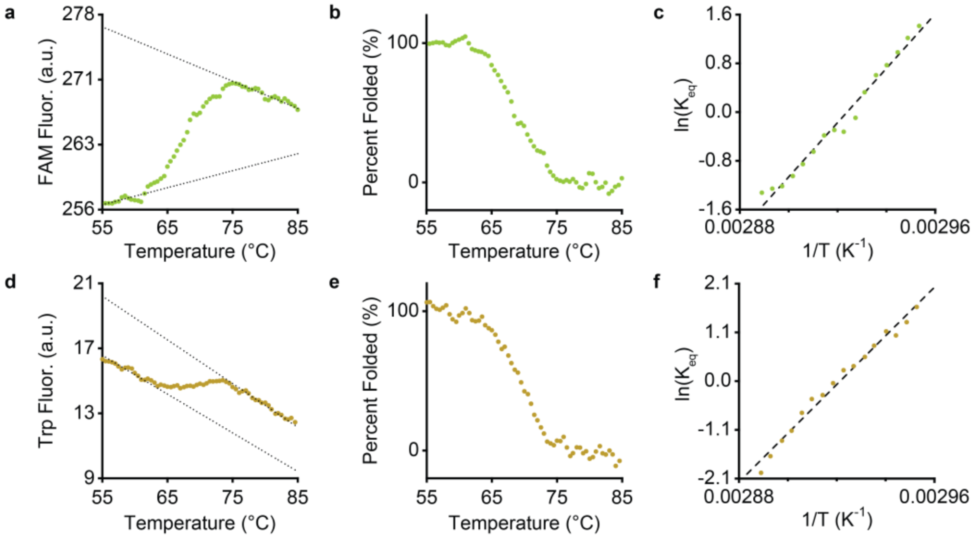

Figure 3.16. – Determination of the apparent Gibbs free energy (Δ*G*) of bAP. (a) Example fitting of the melting curve of the nanoantenna-SA-bAP complex with linear regression to normalise the fluorescence data. (b) The normalised data shows the percent of folded and unfolded conformation. (c) Van't Hoff plot of the data allows one to determine the apparent Δ*G* for the unfolding of bAP. Using the nanoantenna strategy (FAM fluorescence), we determined an apparent Δ*G* of -7.8 ± 0.5 kcal/mol. (d-f) Using the more conventional Trp fluorescence on AP alone, we find a similar value of -9.1 ± 0.3 kcal/mol.

We then considered AP alone and the nanoantenna-SA-bAP complex. Using Trp fluorescence of AP, we observe a transition at 68.8 °C ± 0.4 °C (**Figure 3.15d**), which agrees with the reported literature values of 65 °C and 65.5 °C.[78, 111] Using FAM fluorescence of the nanoantenna-SA-bAP complex, we observed a transition at a T_M of 66.4 °C ± 0.1, which is consistent with the literature values and the above Trp fluorescence measurements (**Figure 3.15b**). The ~2 °C difference could be due to sample-to-sample variation and/or the effect of biotinylation. Notably, the signal with FAM fluorescence is ~10x stronger than with Trp fluorescence. One potential application of T_M determination by fluorescent nanoantennas could be the characterisation of a specific protein in the presence of others (**Supplementary Figure S3.9**). Interestingly, like our previous kinetics studies explored in Chapter 2, we also observed that different connections of FAM to the DNA linker provide differing sensitivity during protein unfolding (**Supplementary Figure S3.10**). Finally, the nanoantennas further enabled derivation of the apparent Gibbs free energy (Δ*G*) for the thermal unfolding of bAP (-7.8 ± 0.5 kcal/mol at T = 37 °C), which was close to the value obtained by Trp fluorescence with AP (-9.1 ± 0.3 kcal/mol) (**Figure 3.16**). Thus, fluorescent nanoantennas can characterise the thermal unfolding of bAP.

3.9 Discussion

There are three general spectroscopic approaches to monitor the catalytic function of AP. The first includes continuous assays for real-time detection of the reaction via a distinct signal change, occasionally a signal decrease for substrate consumption but usually a signal increase for product generation. This includes pNPP with UV-Vis spectroscopy, 4MUP with fluorescence spectroscopy, and many newer examples detectable by fluorescence, electrochemistry, magnetic resonance, and so on. While this general strategy is straightforward, the drawback is that these signal-generating substrates employed with AP do not represent biological enzyme-substrate systems. The second option involves unique substrate-specific assays that provide a signal change in the presence of otherwise spectroscopically silent biomolecular substrates or their products. Their drawback, however, is that a different assay will be needed for each biomolecular substrate, and there might not be one available for some substrates of interest. Furthermore, a cursory search on the Web of Science database of several well-cited substrate-specific AP assays for the substrates ATP and PP_i revealed that while they have been cited in numerous papers reporting new assays for AP or other enzymes, as well as in reviews, they are seemingly not used in biochemical, medical, and enzymology studies of AP. Finally, the third option is quantification of P_i released from biomolecular substrates. Many studies[138, 141, 168, 406-408] of AP continue to employ the literature method[106] or similar commercial kits. This strategy, however, cannot be used to study AP function in real time, plus it is time-consuming since it has several steps.

Fluorescent nanoantennas overcome the drawbacks of these three categories. For example, widely available fluorescence spectroscopy can still be used, but without the limitations of certain synthetic substrates or substrate-specific assays. Fluorescent nanoantennas are not limited to a single substrate – all chemically diverse substrates that we tested herein provided a signal output. These substrates include inorganic PP_i, organic molecules like PSer and G6P, known biological substrates of intestinal AP, such as ATP and macromolecular LPS, and substrates with several types of bonds to cleave, such as the P–N bond of PCr and the P–S bond of amifostine. Unlike the methods based on phosphate quantification, fluorescent nanoantennas enable real-time analysis. Furthermore, fluorescent nanoantennas enabled the rapid characterisation of five oxyanion inhibitors and the cofactor Mg^{2+}. They were also able to detect and characterise the binding of two putative TSA inhibitors, namely, vanadate and tungstate.

Standard methods to determine the Michaelis-Menten kinetic parameters, K_M and k_{cat}, require ~10 measurements of unique samples at different substrate concentrations to capture the roughly linear increase in rate below the K_M and the plateauing region as the rate approaches the V_{max}.[513] This number, of course, increases to ~30 measurements for triplicate testing. The need for ~10 data points typically remains true whether one is conducting real-time measurements with pNPP, 4MUP, or some other substrate that generates a progress curve, and equally, by quantification of P_i.[408] Many papers, including some cited herein that were published in reputable journals, used only a few concentrations in their determination of the parameters. However, it has been shown elsewhere that substrate concentrations should be evenly spaced below, around, and above the K_M, otherwise the derived parameters may be unreliable.[513]

Let us consider two previous studies that reported new assays to monitor calf intestinal AP-mediated hydrolysis of ATP. One used ATP concentrations of 25, 50, 75, and 100 µM, and derived a K_M value of 18.9 µM.[105] The other used 15, 20, 30, and 40 µM, and reported a K_M value of 105 µM.[266] At least according to the mathematical considerations described elsewhere,[513] it remains unclear whether these values are reliable or not. Some explanations for what we see in the literature come to mind. Chemists who develop new enzyme characterisation strategies might be unaware of standard protocols in enzymology. Although one should always perform their due diligence, the chemist author of this thesis can sympathise with such a situation. Another possibility is that enzyme and/or substrate samples are only available or affordable in low amounts, which necessitates fewer measurements. For example, although this was not an issue for us with the small molecule substrates, the LPS used herein was relatively expensive. Based on our estimate of the concentration, we did not have enough LPS to determine the K_M and k_{cat}.

Finally, there remains the unpleasant but sobering possibility that some studies were simply sloppy research, which could be contributing to the scientific reproducibility crisis. Thus, to save time, materials, and money, it is remains important to develop assays that minimise the required amount of enzyme and substrate while still providing reliable kinetic parameters. Fluorescent nanoantennas can meet this need.

Some strategies can characterise AP function without collecting data for $\sim$10 substrate concentrations. For instance, one prominent study immobilised streptavidin-conjugated AP onto biotinylated lipids in a lipid bilayer within a microfluidic system. By employing laminar flow-controlled dilution, this method can characterise the kinetics of the immobilised AP by injecting various concentrations of substrate. The authors also introduced a one-shot approach that generated a range of concentrations via the microfluidic device. In both modes, several concentrations or one-shot, the kinetic parameters were the same for the immobilised AP. On the contrary, while free and immobilised AP displayed similar K_M values, the latter displayed a lower k_{cat}. This discrepancy was attributed to steric hindrance and surface density preventing substrate from reaching some of the active sites, as well as overestimation of the amount of enzyme on the surface.[545] Subsequent studies have reported similar problems for immobilised AP, with higher K_M and/or lower k_{cat}.[546-549] In sharp contrast, our fluorescent nanoantennas that employ biotin-streptavidin non-covalent interaction to bring the dye into close proximity with the enzyme do not significantly affect the kinetic parameters relative to free AP.

Instead of microfluidics, another strategy minimised the number of sample injections by employing a mathematical modelling script of the progress curves from just two sample injections. The derived K_M and k_{cat} values agreed with those obtained by the classic method.[473] However, this strategy still relied on the progress curve signal generated with pNPP. Likewise, the abovementioned microfluidic strategies were also based on 4MUP or an analogue of this molecule. Unlike these methods, our fluorescent nanoantenna strategy enables one-shot characterisation of *any* substrate, including spectroscopically silent biomolecular and medicinal substrates.

A criticism might be that the fitting script employed herein is tedious to learn. While this point is true, it is usually the same procedure each time once one knows how to do it. This is also a software concern rather than an experimental challenge, so one can foresee the development of user-friendly software to fit the data. Furthermore, other works have noted that software-based determinations of initial rates are less susceptible to human bias or error.[550, 551] Similar benefits ought to apply to the modelling of a single fluorescent spike generated by the nanoantennas via differential equations of Michaelis-Menten kinetics.

Isothermal titration calorimetry (ITC) can be employed to characterise enzyme kinetics by studying the heat released upon binding of two components.[96, 97] Similarly to fluorescence, ITC strategies can be based on multiple injections of substrate at different concentrations,[98, 100, 101] or mathematical modelling of a single injection via fitting scripts.[99, 102, 103] The method based on multiple injections of substrate requires determination of the enthalpy (ΔH) of the reaction, which is analogous to having to determine the molar extinction coefficient (ε) of the product for kinetic characterisation by UV-Vis.[100, 101] This is not a significant burden when characterising one substrate, but when characterising multiple biomolecular substrates, it adds additional steps. This could also be problematic for expensive samples. Nevertheless, not all ITC-based strategies require knowledge of the ΔH, which can be determined by integrating the peaks of the ITC data in the single injection strategy.[97] Similarly, fluorescent nanoantennas do not require any previous knowledge about the substrate, aside from the number of reactions (*e.g.*, ATP has three phosphates). A detriment shared by fluorescent nanoantennas and ITC is a relatively long equilibration time. ITC, however, has the benefit of being label-free and able to characterise almost any reaction.[97] At present, this is an obvious advantage of ITC relative to fluorescent nanoantennas, although in principle, our strategy may too work with other proteins – we demonstrate an example in the next chapter. Overall, ITC-based strategies for the characterisation of enzyme kinetics are less amenable to high-throughput screening relative to fluorescence-based methods, but ITC offers more flexibility in terms of systems that can be investigated.

As demonstrated herein, fluorescent nanoantennas can monitor the AP-mediated hydrolysis of amifostine in real time. This drug is in clinical use to protect normal tissues against the toxicities of radiation treatment and chemotherapy.[10, 205-207] There is still more to learn, however, about how it provides this protection. We do know that amifostine is an inactive prodrug that is not taken up by cells. Dephosphorylation by membrane-bound AP generates its active form, called WR-1065, which can diffuse into cells.[206, 207] Although the mechanism remains not entirely understood, it is believed that once inside the cell, WR-1065 serves as an alternative target for reactive alkylating or platinum agents, and also as a scavenger of oxygen free radicals produced by ionising radiation and chemotherapy that would otherwise target cellular nucleic acids.[10, 206] The effectiveness of amifostine has been attributed to normal cells having a higher concentration of WR-1065 than cancer cells due to three factors: 1) normal cells have a higher concentration of membrane-bound AP than cancer cells, 2) reduced circulation to tumours reduces drug availability, and 3) the relatively acidic environment of tumours reduces AP activity toward amifostine.[206] One study proposed that specifically intestinal AP is downregulated in tumour vasculature and stroma, in contrast to its greater expression in normal tissues.[208] Indeed, a more recent study further observed that the conversion of amifostine to WR-1065 was lower in breast cancer MCF-7 cells compared to normal NHDF fibroblasts. Despite that, levels of messenger ribonucleic acids (mRNA) for various isoforms of AP were higher in the MCF-7 cells. This suggests a malfunction of translation of mRNA into protein, for which the cells unsuccessfully try to compensate via more mRNA production.[552] Thus, cancerous cells are prevented from hydrolysing amifostine to the active metabolite, and do not experience its protection during treatments. Of note, there was considerably more mRNA from tissue-nonspecific AP than intestinal AP and placental AP in the MCF-7 cells.[552] Without a doubt, further studies of amifostine are needed to fully understand the mechanism of how this drug works. Some recent studies have reported nanomaterials for colorimetric or fluorescent quantification of amifostine or WR-1065 in the presence of AP.[553-556] While these proposed methods may offer convenience relative to established methods based on liquid chromatography (LC),[553] they nevertheless require significant incubation times and did not enable the study of the kinetic parameters. Therefore, simple tools to monitor and characterise AP-mediated hydrolysis of amifostine in real time, like our fluorescent nanoantennas, could play a pivotal role in understanding the mechanism of this drug. Indeed, to the best of our knowledge, this present work is the first to report the kinetics of

AP-mediated hydrolysis of amifostine. Other prodrugs are also converted to their active form by intestinal AP, such as fosamprenavir to amprenavir, which is used to treat human immunodeficiency virus (HIV) infection.[209-211] Fluorescent nanoantennas might be useful for the study of intestinal AP with prodrug substrates, although challenges remain for the examination of these molecules since there would be interference from other biological substrates (*e.g.,* ATP).

More broadly, one can foresee the potential application of fluorescent nanoantennas to study the hydrolysis of various biological substrates of intestinal AP. This could include examining AMP, ADP, and ATP in the context of purinergic signalling and inflammatory bowel disease (IBD),[557, 558] which was recently linked to deficiency of the gene for intestinal AP.[169] One could investigate, for example, the faster rate of hydrolysis of ADP compared to AMP and ATP with mammalian intestinal AP, as observed in this study and elsewhere,[433, 492] as well as the apparent dependency of this observation on the presence of Mg^{2+}.[492] Furthermore, in a rat model, it was also shown that the activity of intestinal phosphate-dependent glutaminase (PDG), which converts water and the glucose-precursor glutamine to ammonia and glutamate, can be activated by ADP and further modulated by ATP and P_i.[559, 560] We further observed that the two sugar phosphates, G6P and F6P, displayed higher K_M and lower k_{cat} values when compared to the other phosphate monoesters. Higher K_M values for G6P and glucose-1-phosphate (G1P) have also been previously reported with human intestinal AP.[488] Thus, one could investigate the origin of G6P and F6P's apparent lower affinity and slower hydrolysis with intestinal AP and whether this relates to glucose-6-phosphatase (G6Pase) and the putative gluconeogenic role of the small intestine in glucose homeostasis.[561-563] While there is clearly much more to learn about intestinal AP, studying this enzyme with fluorescent nanoantennas might help us to understand the delicate balance of these substrates in the intestine and their relation to biological processes.

Tungstate and especially vanadate induce presumed conformational changes in AP that are detectable by the fluorescent nanoantennas.[107, 114] Moreover, the binding could be characterised in terms of their K_d. This observation suggests that if a binding event causes a conformational change or induces some other factor that can perturb the nanoantenna's dye, then it may be detectable. In the present study, the nanoantenna-SA-bAP complex mediates the binding of FAM near the active site, which is then perturbed by the binding of vanadate or tungstate. Host-guest interactions and the perturbation of fluorophores have been exploited in other (bio)sensors. For example, a conjugate formed between cucurbit[7]uril, a linker, and a dye can sense the Parkinson's disease drug amantadine via dye displacement.[444] In another strategy to detect the anticancer drug methotrexate, a fusion protein was engineered consisting of dihydrofolate reductase (DHFR), NanoLuc luciferase, a polyproline linker, and a SNAP-tag with a fluorophore (Cy3) and a DHFR inhibitor (*e.g.*, trimethoprim). Interaction of the trimethoprim with DHFR brings the fluorophore into proximity with the luciferase, thereby enabling efficient bioluminescent resonance energy transfer (BRET). However, binding of the target methotrexate to DHFR, also a competitive inhibitor, displaces the trimethoprim. BRET efficiency is then reduced due to the separation of the Cy3 and the luciferase.[564] Finally, in another strategy to detect β-Lactam antibiotics, fluorescein was covalently attached near the active site of a β-lactamase. The binding-induced conformational changes could then be monitored by fluorescence spectroscopy.[44] Although no sensing strategy will be suitable for every application, one benefit of fluorescent nanoantennas is that they do not require specific covalent attachment of the fluorophore to the receptor host, and instead only need non-specific biotinylation to enable the dye-protein interaction. Moreover, the putative conformational changes induced by vanadate and tungstate are relatively small, unlike the large conformational changes needed for other strategies. Also, the dye does not necessarily need to be displaced, and instead it responds to slight changes in its environment. Thus, fluorescent nanoantennas represent a new tool among the various options to design protein-based fluorescent biosensors.[565] Furthermore, although several fluorescent sensors for vanadate are available, fluorescent nanoantennas employed with AP represent the first protein-based biosensor for this ion.[566-569] Thus, if other suitable target-protein pairs are found, the nanoantenna strategy may inspire the development of more protein-based biosensors for ions, inhibitors, and other chemical species.

For protein unfolding, there are various thermal shift assays available to obtain the T_M. For example, one can leverage the inherent fluorescence from the amino acids tyrosine, phenylalanine, and especially tryptophan. This provides a signal change when the local environment of the fluorescent amino acid changes during unfolding.[570] Alternatively, for differential scanning fluorimetry (DSF), one can employ a fluorescent dye (*e.g.,* SYPRO Orange).

This dye's fluorescence typically increases during protein unfolding, whereupon it is exposed to hydrophobic regions of the protein with a lower dielectric environment.[571, 572] A drawback of these methods, however, is that they require a pure protein sample. In the first case, the Trp fluorescence signal of other proteins could overlap with that of the target protein, and in the second case, the SYPRO Orange dye could interact with non-target proteins too. Based on our demonstration with AP in the presence of BSA, the nanoantenna strategy could potentially be applied to characterise the unfolding of a specific protein in the presence of other proteins that have an overlapping Trp fluorescence signal.

Overall, we have shown that our nanoantenna strategy enabled detection and characterisation of different conformational states of AP, including the small conformational changes of various enzyme-substrate complexes, the effect of enzyme-inhibitor complexes, as well as transition-state analogue inhibitors, plus the large conformational changes during unfolding. This demonstrates the high sensitivity and versatility of the nanoantenna strategy to potentially detect any conformations of a protein. Moreover, these results suggest that this approach could potentially be universal to monitor the function of other proteins, which we explore in the next chapter.

3.10 Supplementary Figures for Chapter 3

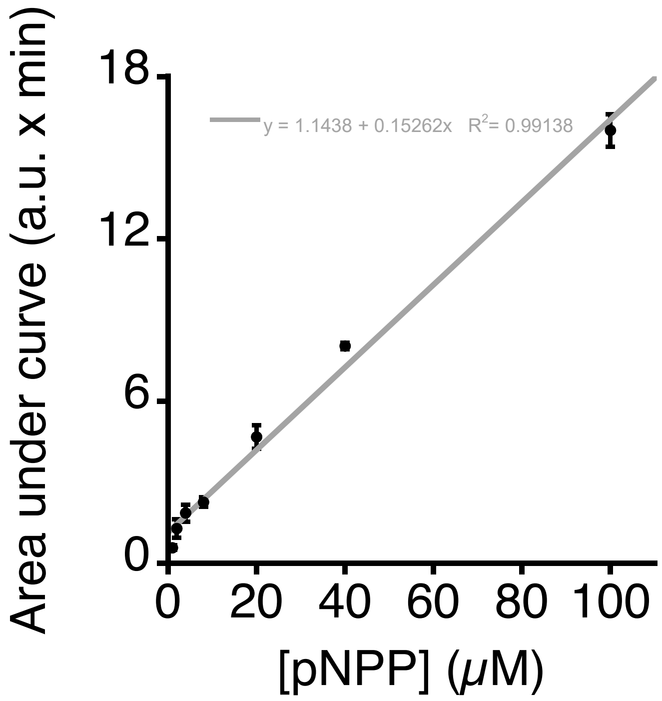

Figure S3.1. – Area under spike increases linearly with pNPP concentration. Here, the fluorescence spikes in Figure 3.1 were integrated with time to obtain the area under the curve (*i.e.*, the spike). The area increases linearly with pNPP concentration.

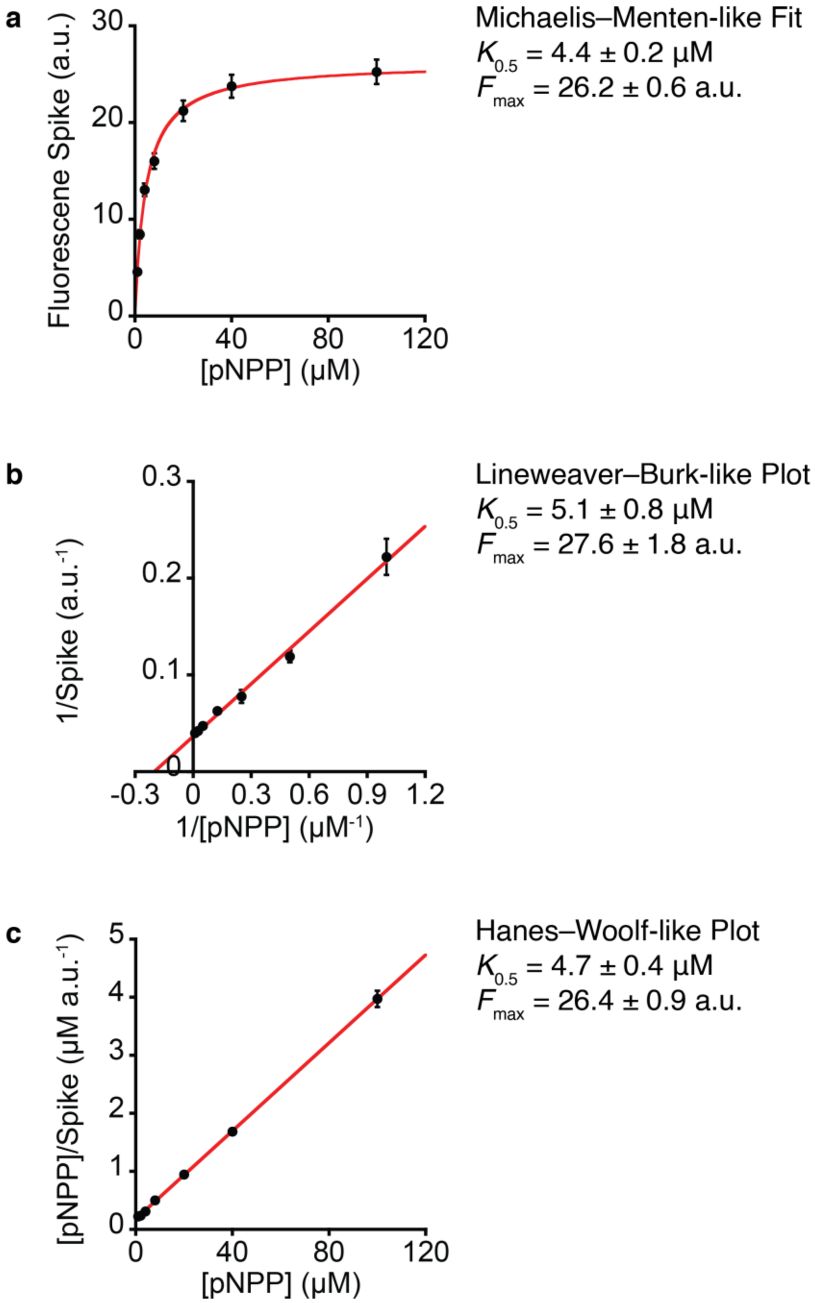

Figure S3.2. – Saturation binding plot. (a) We plotted the fluorescence spike intensity for triplicate injections of 1, 2, 4, 8, 20, 40, and 100 µM pNPP. It displays Michaelis–Menten-like behaviour, whereby the maximum fluorescence (F_{max}) ought to be proportional to the maximum rate (V_{max}) and enzyme-substrate concentration ([ES]). Then, the concentration at half of the F_{max} ($K_{0.5}$) ought to be equal to the Michaelis constant (K_M). Nonlinear fitting of the Michaelis–Menten equation found $K_{0.5}$ and F_{max} values, shown above. The $K_{0.5}$ agrees with the expected K_M under these conditions.[100] We show later how one can convert this fluorescence intensity to rate in µM s^{-1}. Also shown are determination of the kinetic parameters by the classic methods without nonlinear fitting, (b) Lineweaver–Burk-like and (c) Hanes–Woolf-like, which provide similar numerical values. Conditions: 150 nM PEG nanoantenna, 50 nM SA, 100 nM bAP and variable amounts of pNPP in 100 mM Tris, 10 mM NaCl, pH 8.0, 30 °C.

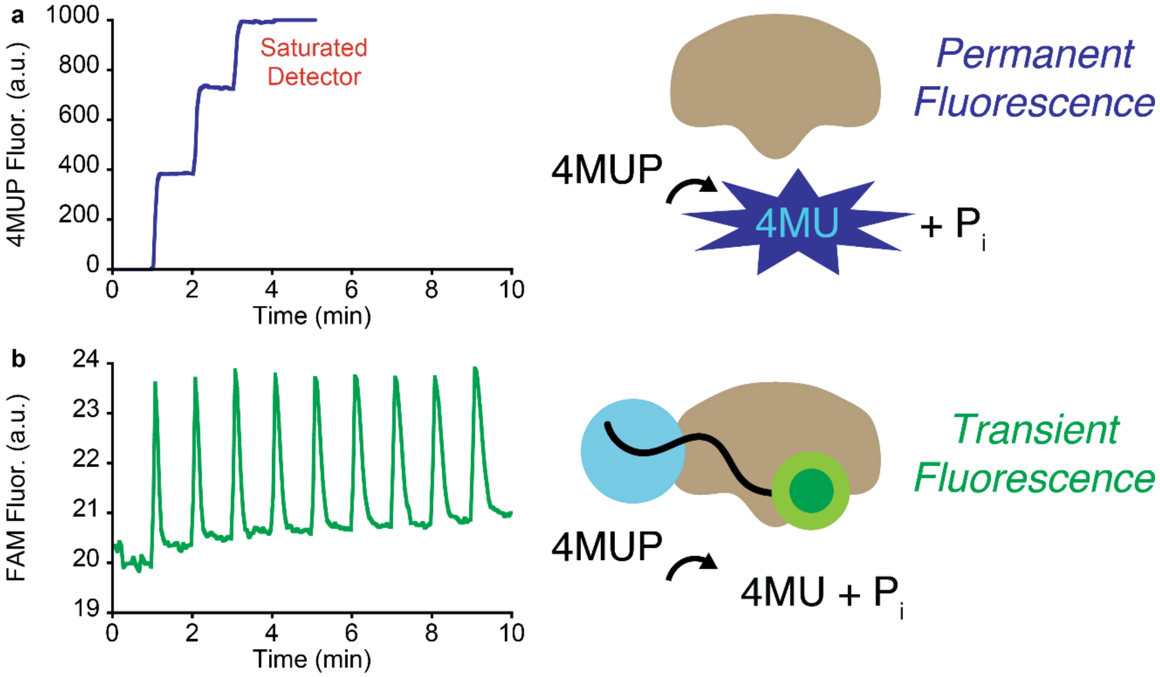

Figure S3.3. – Comparison of classic assay and nanoantennas reveals that nanoantennas allow multiple analyses with the same sample. (a) Real-time fluorescence monitoring of the hydrolysis of 4MUP to fluorescent 4-MU and Pi. Although it works well for the first hydrolysis reaction (injection time = 1 min), if one desires to measure multiple injections of substrate, it will eventually saturate the detector (3 min). Note that we did not bias this experiment to fail, since in most of this paper we used a PMT voltage of 635 V, but in this experiment, we used 500 V, which is between the medium and low power settings on our spectrofluorometer. (b) In contrast, monitoring the hydrolysis reaction by the nanoantenna strategy allows one to perform multiple injections of substrate. Thus, the only limitation is the chemical environment of the system (*i.e.*, stability of enzyme? product inhibition?), rather than a physical or instrumentation limitation. Conditions: 150 nM L12 PolyT nanoantenna, 50 nM SA, 100 nM bAP and 10 µM 4MUP (9x) in 100 mM Tris, 10 mM NaCl, pH 8.0, 30 °C.

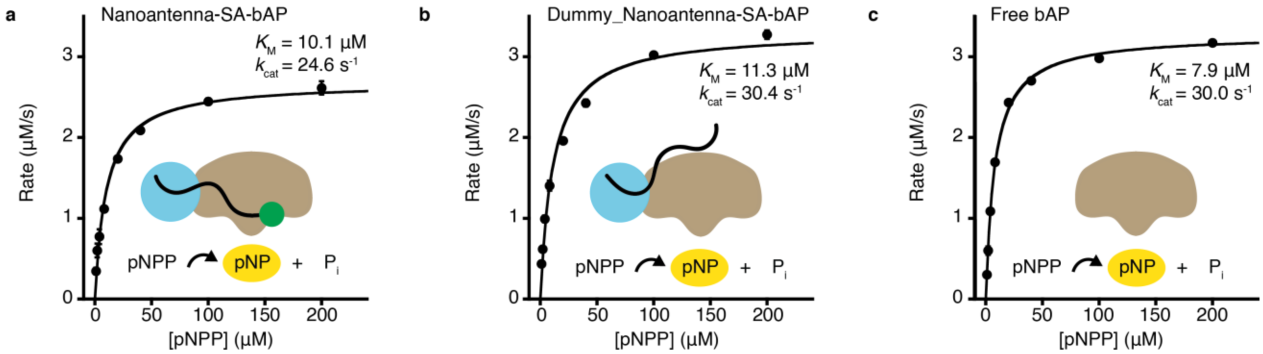

Figure S3.4. – Streptavidin and nanoantennas do not affect the kinetic parameters. Michaelis–Menten kinetics as measured by UV-Vis absorbance of pNP product for (a) the nanoantenna-SA-bAP complex, (b) Dummy nanoantenna-SA-bAP complex (*i.e.*, no FAM on nanoantenna), and (c) free bAP. Conditions: 150 nM nanoantenna, 50 nM SA, 109 nM bAP (not a typo) in 100 mM Tris, 10 mM NaCl, pH 8.0, 30 °C.[435, 573]

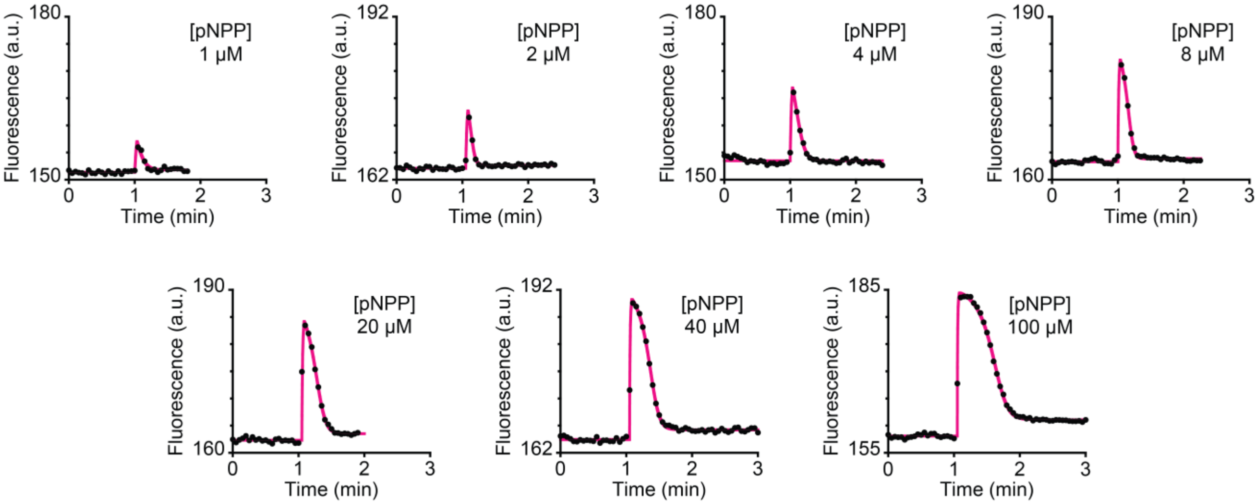

Figure S3.5. – Fitting of the fluorescent spikes to extract kinetic parameters of bAP with [pNPP] = 1, 2, 4, 8, 20, 40 and 100 µM. The data are taken from Figure 3.1 and the extracted parameters are plotted below in Supplementary Figure S3.6.

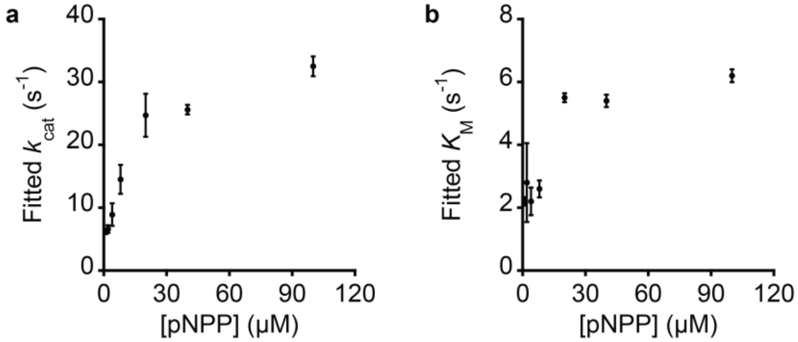

Figure S3.6. – Kinetic parameters of AP determined using different concentrations of substrate (see Figure S3.5). When [pNPP] is less than ~3K_M, the extracted parameters are underestimated, and consequently unreliable, likely due to not enough enzyme-substrate complex being formed. Therefore, we recommend using a sufficiently high concentration of substrate (>3K_M) to perform the one-shot characterisation fitting strategy. Also important is that these parameters for the commercially prepared bAP (20, 40 and 100 µM pNPP) are essentially the same as the parameters determined in Figure 3.5 for our "homemade" bAP (biotinylation of AP ourselves; 30 µM pNPP), which indicates the robustness of our strategy.

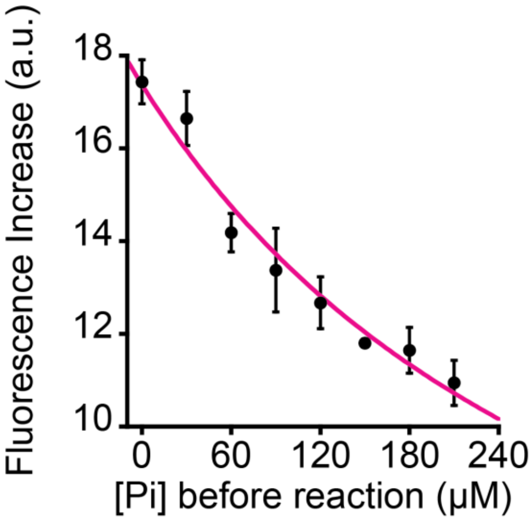

$$V_0 = \frac{V_{\max}\,[\mathrm{S}]}{K_{\mathrm{M}}\left(1 + \frac{[\mathrm{I}]}{K_{\mathrm{i}}}\right) + [\mathrm{S}]}$$

$$V_0 = \frac{20.264\,[30]}{5.00\left(1 + \frac{[\mathrm{I}]}{48.38}\right) + [30]} \qquad \mathrm{R}^2 = 0.97082$$

Figure S3.7. – The spike intensity decreases with increasing inhibitor concentration. Spike intensity, which is proportional to the rate of the reaction, decreases with increasing inhibitor concentration (P_i). This relationship is well modelled using the Michaelis–Menten equation for competitive inhibition by employing the K_M and K_i values determined in the main text. Conditions: 5 nM PEG nanoantenna, 5 nM SA, 10 nM homemade bAP and 30 µM pNPP (8x) in 100 mM Tris, 10 mM NaCl, pH 8.0, 30 °C.

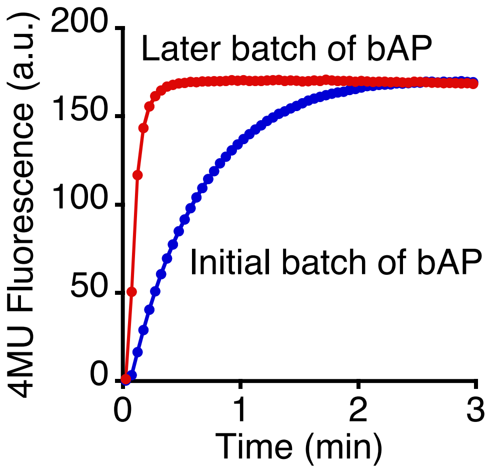

Figure S3.8. – bAP batch-to-batch variation accounts for differences in kinetic parameters. The initial and later batches of bAP used in this study had different rates of substrate hydrolysis, as shown here for the conversion of nonfluorescent 4MUP to fluorescent 4MU and P_i. Thus, differences in determined K_M and k_{cat} between Figure 3.5 and Figure 3.7 can be attributed to the batches (different lots). **Importantly, substrate comparison was done with the same enzyme lot.**

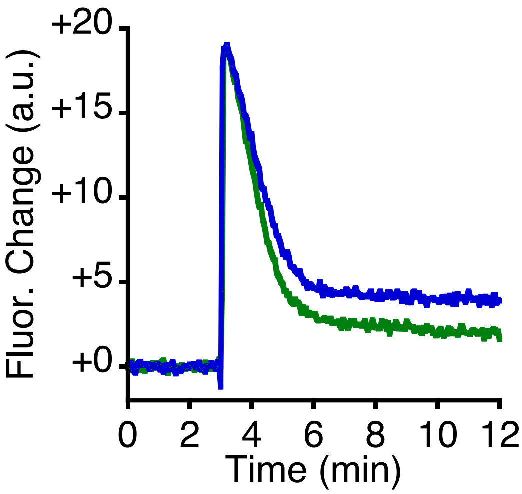

Figure S3.9. – Variation in baseline after substrate hydrolysis. In Figure 3.7, the baseline after the reaction can differ between substrates. However, we observed a similar result for different trials of the same substrate. For example, two trials of 4MUP hydrolysis from Figure 3.7 are shown here. In both cases, the signal increase (~19 a.u.) and the reaction completion time (~6 min) are essentially the same, but the baselines after the reaction are less reproducible. At present, we do not have an explanation for this effect.

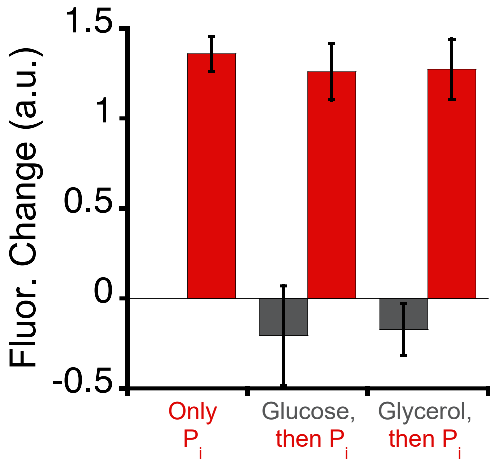

Figure S3.10. – Increase in baseline after the reaction is linked to phosphate. We further explored the origin of the baseline increase observed following hydrolysis for some substrates in Figure 3.7. Here, we explore the effect of adding the product(s) of the reaction to the nanoantenna-SA-bAP complex. We find that only phosphate (P_i) increased the signal baseline, but for example, not the other products of G6P and BGP, namely, glucose and glycerol, respectively.

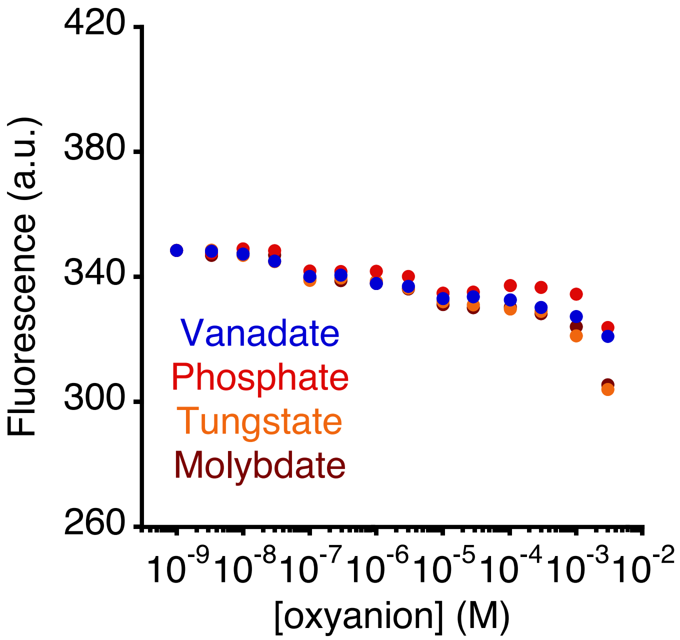

Figure S3.11. – Addition of oxyanions does not affect the fluorescence of our nanoantenna – no bAP present. Fluorescence of the L12 ssDNA nanoantenna attached to SA, but without bAP, was not substantially affected by the addition of vanadate, phosphate, tungstate or molybdate.

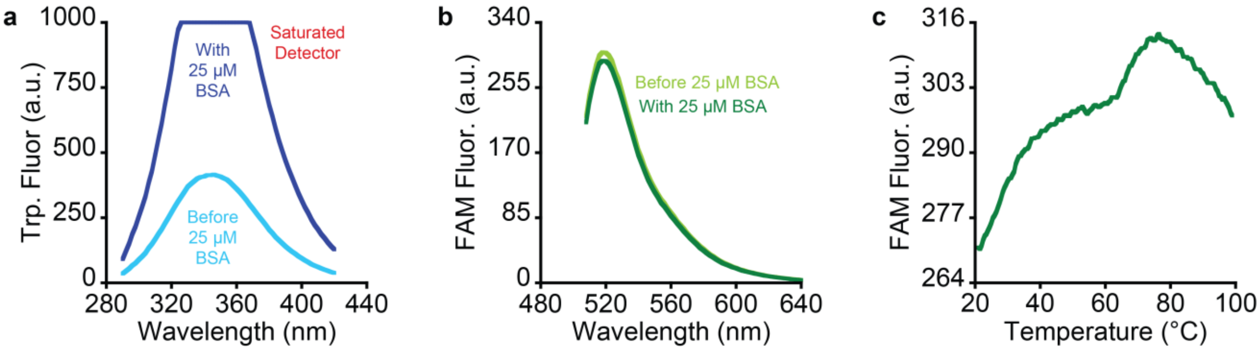

Figure S3.12. – Monitoring unfolding transition of proteins using nanoantenna in a complex sample. (a) Adding BSA to the cuvette results in a tryptophan fluorescence signal that saturates the detector. This reduces the usefulness of tryptophan to monitor the unfolding transition in a complex environment. (b) The same condition does not affect the FAM fluorescence, (c) thereby still allowing specific monitoring of the bAP thermal unfolding transition.

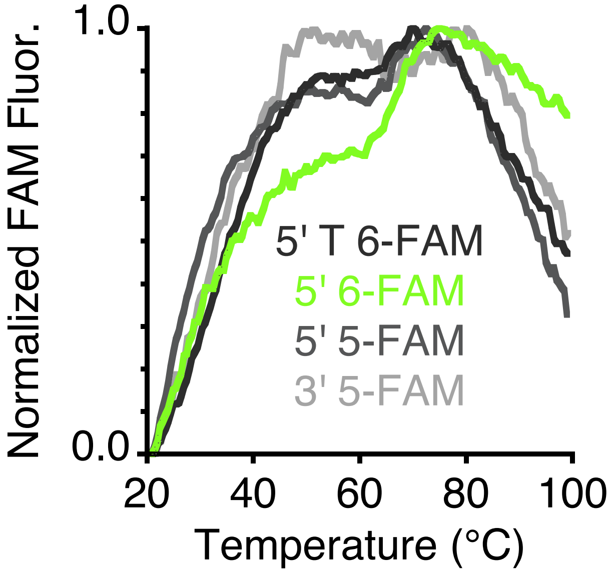

Figure S3.13. – Different FAM connections affect the sensitivity of the nanoantenna towards detecting the melting transition. The L12 nanoantenna with 5′ 6-FAM is more efficient to detect bAP melting compared to analogous nanoantennas with 5′ T 6-FAM, 5′ 5-FAM, or 3′ 5-FAM. See Figure 2.11a for the types of FAM.

Chapter 4 – Rapid screening of nanoantennas to monitor other protein functions

4.1 Introduction

In Chapter 3, we successfully demonstrated that one can characterise various states of alkaline phosphatase (AP) with our fluorescent nanoantenna method. Getting us to that point, in Chapter 2, we explored *many* variations of fluorescent nanoantennas. These variations included trying streptavidin (SA) with a biotinylated enzyme, a streptavidin-conjugated enzyme, or direct covalent attachment of the nanoantennas to the enzyme; linker lengths of 0, 6, 12, 24 or 48 nucleotides; linker compositions of ssDNA, dsDNA, PolyT, or PEG; a handful of ratios of nanoantennas to SA and bAP; four different "Modifiers" adjacent to the FAM dye (*e.g.*, C_{16} alkane chain); four different connections of FAM to the linker; eight other dyes (Cy3, Q570, Q670, CAL, TAMRA, ROX, MB, and P650); and three combinations of dual-dyes (FAM + CAL, Cy3 or Q670). With a list this long, there may have been something else that was omitted here by mistake. Moreover, there are a few other ideas that we could have tried but did not, such as alternatives to streptavidin (*e.g.*, Neutravidin), more dyes, and other types of linkers (*e.g.*, peptide nucleic acids, PNA). From a practical perspective, some of these variables were more important than others and their required optimisation was worth having invested the time, such as linker length. Others, such as the dual-dye nanoantennas, were instead part of our digging into the mechanism of how fluorescent nanoantennas monitor protein function. Nevertheless, even if some less important variations of nanoantennas are omitted, it still might require the testing of a few dozen nanoantennas to the find right one to monitor the function of another protein of interest. Furthermore, just as Förster resonance energy transfer (FRET) does not work for every protein, it is probable that fluorescent nanoantennas also do not work with some proteins. Imagine spending many days testing dozens of fluorescent nanoantennas in cuvettes, just to find out that none of them can monitor the protein's function. This would burn less time than testing an equal number of FRET pairs covalently attached to a protein, but it would be equally disappointing if the protein's function could not be monitored.

In this concise chapter, we decided to facilitate nanoantenna selection and screening assay development by designing a 96-well plate screening assay that takes advantage of the convenience of the nanoantenna-SA platform. This enabled us to rapidly test 12 nanoantennas with different linker lengths, linker types, chemical connection of the fluorophore, and type of fluorophore (dye). With this approach, one can screen for a nanoantenna that works with a protein of interest within one day, rather than spending several days testing many nanoantennas in cuvettes. For this proof-of-concept, we tested fluorescent nanoantennas with another protein, the immunoglobulin-binding Protein G.

4.2 Screening Protein G and immunoglobulin binding

Protein G is obtained from *Streptococcal* bacteria, while Protein A is from the cell wall of *Staphylococcus aureus*. These proteins are mainly of interest for their different binding affinities with various antibodies, which makes them useful for antibody purification, immobilisation, and detection.[574, 575] For example, Protein G will bind goat immunoglobulin G (IgG) with high affinity, but Protein A will not.[576] Thus, we decided to test the nanoantenna strategy with the Protein G system, which in addition to screening, also serves as a model system of protein-protein interaction.

As noted in the Introduction, we wanted to explore rapid and convenient nanoantenna screening with a 96-well plate. Although one could test any number of nanoantennas, we tested 12 different types simply because this number represents one row across the plate. We considered ssDNA nanoantennas with the 5′-end T 6-FAM fluorophore of lengths L6, L12, L24 and L48 (*i.e.*, varying the linker length); 5′-end T 6-FAM fluorophore with L12 dsDNA and L21 PEG linkers (*i.e.*, varying the linker type); 5′-end 6-FAM, 5′-end 5-FAM, and 3′-end 5-FAM on L12 ssDNA nanoantennas (*i.e.*, varying the dye's connection to the linker); and 3′-end Cy3, Q570 and CAL (*i.e.*, varying the fluorescent dye). The principle of detection is straightforward (**Figure 4.1a,b**). We first prepared the well plate by adding the different nanoantennas, followed by the addition of SA. We then added biotinylated Protein G (bPG). After assembly of the nanoantenna-SA-bPG

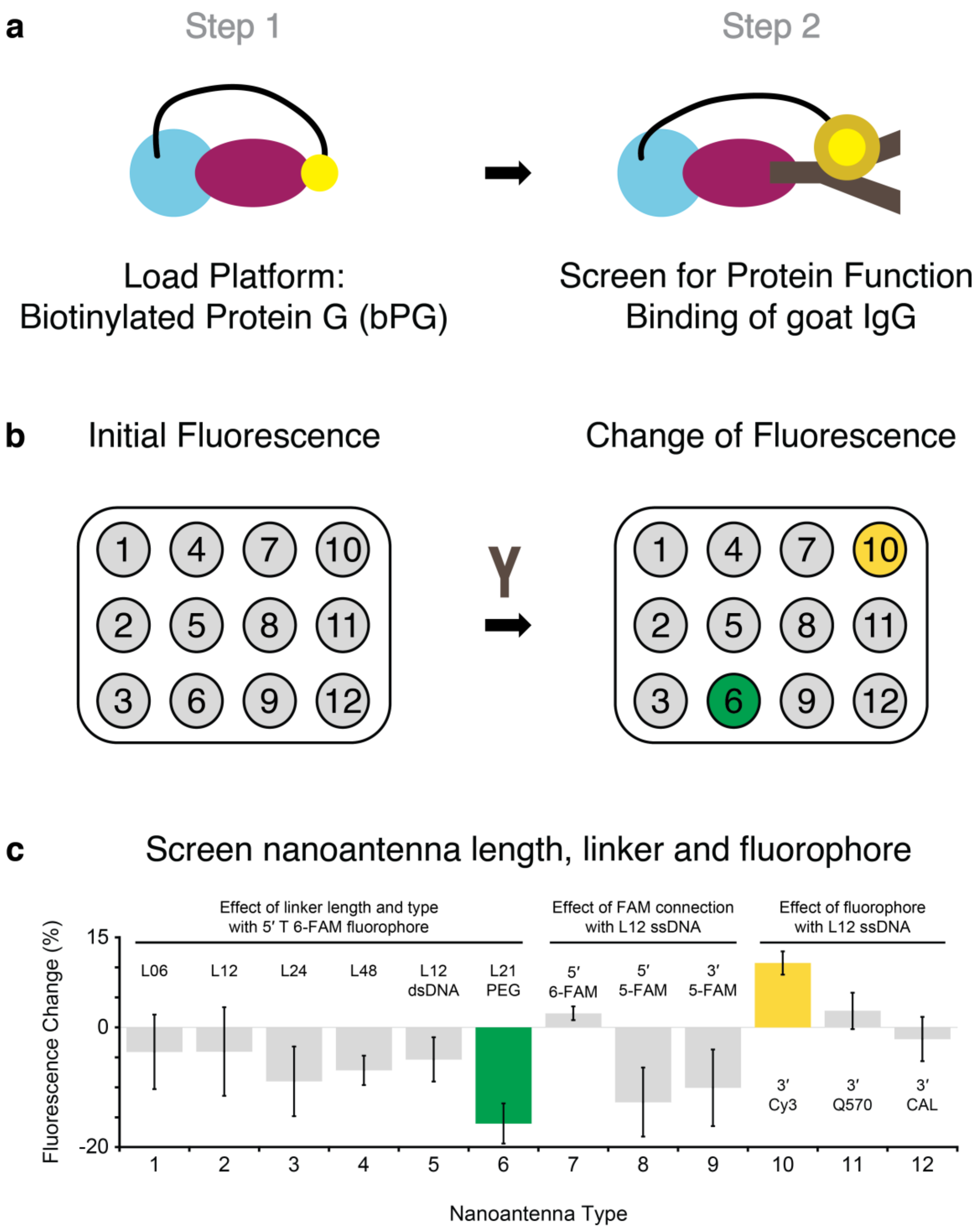

Figure 4.1. – Rapid screening strategy for identification of functional nanoantennas for Protein G binding IgG. (a,b) Plate reader screening strategy to rapidly identify a nanoantenna that reports the binding of goat IgG to biotinylated protein G (bPG) using the nanoantenna-SA platform. (c) Results obtained for rapid screening of 12 nanoantennas for the aforementioned system.

complexes, we recorded the fluorescence intensity in all wells. This is the initial fluorescence signal baseline. Then, we added goat IgG to each well, and recorded the fluorescence again. From this initial screening, we observed that nanoantenna 6 (5′ T 6-FAM L21 PEG) displayed the largest fluorescence quenching, while nanoantenna 10 (3′ Cy3 L12 ssDNA) displayed the largest fluorescence enhancement (**Figure 4.1c**).

After identifying these two candidate nanoantennas, we confirmed their performance in cuvettes, whereupon we observed signal changes in agreement with the screening. Upon IgG binding, nanoantenna 6 (5′ T 6-FAM L21 PEG) again displayed a fluorescence decrease, although now recording the fluorescence versus time in the cuvette, we observed that it continued to drift downward without reaching a plateau (**Figure 4.2**). Nanoantenna 10 (3′ Cy3 L12 ssDNA) displayed a fluorescence increase of 12.4 ± 0.1% in the cuvette (**Figure 4.2**), consistent with the plate reader value of 10.7 ± 2.0%. Furthermore, as a control, the shorter nanoantenna 1 (5′ T 6-FAM L06 ssDNA) did not display a significant fluorescence change (**Figure 4.2**). This screening strategy also offers an opportunity to optimise performance via semi-rational design of the fluorescent nanoantenna. For example, we observed that for this protein function, the flexible L21 PEG nanoantenna enabled the best sensitivity for the T 6-FAM fluorophore (**Figure 4.1c**). Moreover, although the ssDNA nanoantennas with T 6-FAM were not as sensitive in comparison, we noticed that the longer ones were better than the shorter ones (**Figure 4.1c**). Therefore, we subsequently tested a longer PEG nanoantenna (5′ T 6-FAM L41 PEG), not included in our initial screening, and found indeed that it displayed improved sensitivity to goat IgG binding in the cuvette, although also without reaching a plateau (**Figure 4.2**). Thus, this result demonstrates the general principle of semi-rational design of a fluorescent nanoantenna, although in this specific case, PEG-based nanoantennas may not be useful for detecting antibody binding because the signal quenching does not reach a plateau. The reason for this observation remains undetermined.

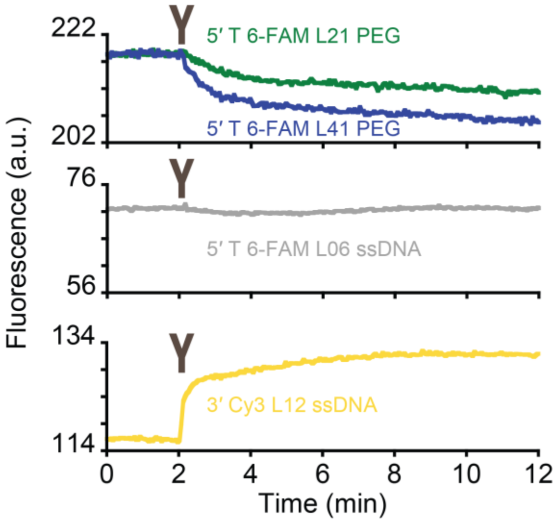

Figure 4.2. – Cuvette validation of nanoantennas. Cuvette validation of results for nanoantennas 1, 6, and 10 displays similar trends to the plate reader format. Also shown is the longer semi-rationally selected longer PEG nanoantenna.

Ultimately, we selected the Cy3 L12 ssDNA nanoantenna for subsequent investigations due to its signal-on fluorescence change. This Cy3 nanoantenna-SA-bPG complex could be adapted as an efficient signal-on biosensor to detect the presence of specific types of antibodies (**Figure 4.3;** bPG + IgG).[576] Indeed, a sample containing SARS-CoV-2 IgG/IgM led to a similar fluorescence increase (**Figure 4.3;** bPG + CoV Ab), while it did not respond to a sample that is negative for SARS-CoV-2 IgG/IgM (**Figure 4.3;** bPG + Ctrl), nor to the presence of the enzyme AP (non-biotinylated) (**Figure 4.3;** bPG + AP). Furthermore, swapping bPG for biotinylated Protein A (bPA), which does not bind goat IgG,[576] also did not display a signal increase (**Figure 4.3;** bPA + IgG; see also **Figure 4.4** for the effect of dilution). This control with bPA further shows that the target goat IgG does not non-specifically interact with the nanoantenna-SA platform.

Overall, these results indicate that fluorescent nanoantennas can be rapidly screened for their ability to monitor distinct protein functions, such as Protein G binding IgG. By switching the bPG/bPA for another biotinylated protein, aptamer, or epitope, this system ought to be adaptable to detect other antibodies and proteins, including more specific interactions.

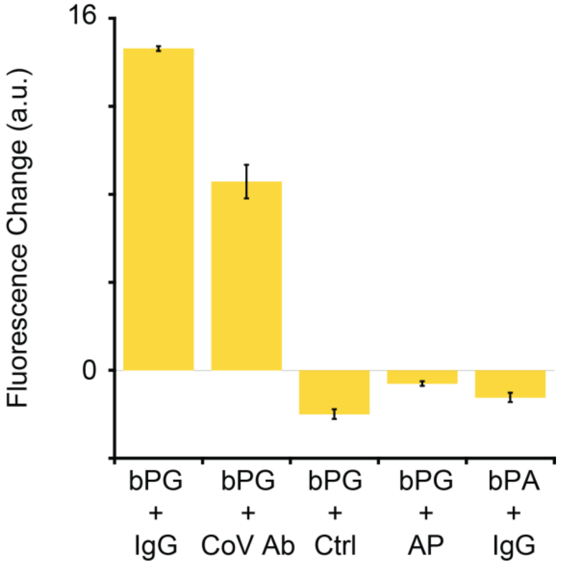

Figure 4.3. – Detection of Antibodies. The nanoantenna-SA-bPG complex detects goat IgG and SARS-CoV-2 IgG/IgM while remaining silent to a sample without SARS-CoV-2 IgG/IgM (Ctrl) and to the enzyme AP. As an additional control, replacing bPG with biotinylated Protein A (bPA), which does not bind goat IgG, does not display a signal change.

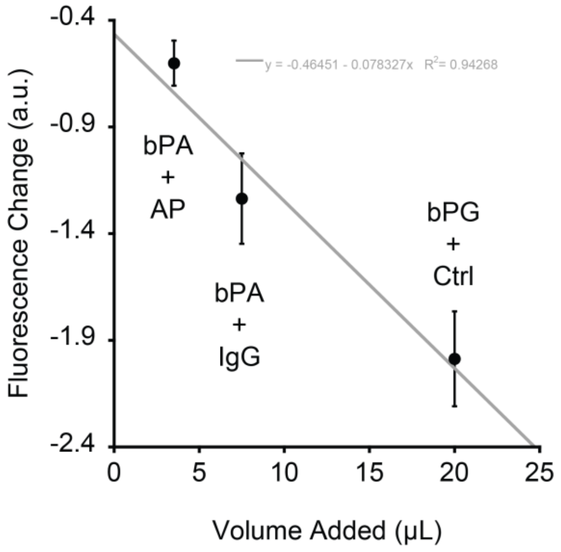

Figure 4.4. – Effect of dilution in control experiments. The signal decrease in the controls in Figure 4.3 correlates with the volume of sample added.

4.3 Discussion

Using a plate reader, we developed a 96-well plate screening strategy to rapidly identify nanoantennas to monitor specific protein functions. In this case, we employed the strategy to identify a nanoantenna that can detect goat IgG binding to Protein G. Thus, in addition to our previous detection of the enzymatic activity of AP, we now show that fluorescent nanoantennas are also able to detect protein-protein interaction. The overall simplicity and rapidity of this method could make fluorescent nanoantennas more attractive for potential users of the method.

Unlike for the stable signal obtained with Protein G, it was not possible with our instrument to screen enzyme function. This was due to the deadtime of the plate reader. After adding substrate to wells containing an enzyme, closing the plate reader cover, and then "pressing go", the instrument takes about one minute to begin collecting the data. Moreover, since multiple wells cannot be scanned simultaneously, a plate with samples in more than one well takes additional time. This situation is incompatible with screening the catalytic function of AP, since under most conditions that we tested the reaction finished in *ca.* 1-3 minutes. However, even for our setup, there may be a workaround. For example, looking back at the results for AP in Chapter 2, we observed that the best nanoantennas to detect bAP function were also the best to detect bAP binding to the nanoantenna-SA platform. While this cannot be assumed as automatically true in all cases, this stable signal change observed upon biotinylated enzyme binding could potentially be used to screen for nanoantennas to detect enzyme function. Moreover, vanadate induced a presumed conformational change in AP that is detectable by the fluorescent nanoantennas as a stable signal change.[107, 114] This binding event could likely also be detected with the plate reader, as probably could the binding of other biotinylated molecules to SA. Therefore, while we have no doubt that there is much more to learn about fluorescent nanoantennas, a concept introduced for the first time in this thesis, we see much potential for fluorescent nanoantennas to rapidly screen and characterise systems involving protein-protein interaction, enzymatic activity, enzyme-inhibitor binding, and protein-ligand binding.

Enzyme-linked immunosorbent assays (ELISA) are established methods to detect antibodies. Although having the advantage of high-throughput, a disadvantage of ELISA is the relatively long assay time. This has spurred the development of faster antibody-based sensing strategies based on surface plasmon resonance (SPR), which can measure adsorption onto surfaces.[577, 578] Relevant to this project, previous SPR studies have reported the detection of antibodies by employing Protein G.[579-581] For example, Protein G tagged with an N-terminal cysteine residue could be linked to an amine-modified ssDNA. This could, in turn, bind to a surface-bound probe with a complementary DNA strand. Using surface plasmon resonance, it was possible to detect the assembly as well as the subsequent addition of various IgGs from human, goat, mouse, and rat origins. The strategy was then further employed to detect human prostate-specific antigen (PSA) via anti-PSA.[581] In comparison to the present work, both methods are able to detect the binding of antibodies to Protein G, although we did not subsequently test the nanoantenna strategy to detect a target antigen. Thus, an interesting future direction for the project could be to determine whether such binding interactions can also perturb the fluorophore and mediate a signal change. Moreover, one could hypothetically employ nanoantennas with different fluorophores to discriminate between various targets.[327] The new biosensing strategy introduced in this project has many potential options for future applications.

Chapter 5 – Overall discussion and conclusions

Here, we have introduced the use of fluorescent nanoantennas as a new strategy to monitor protein function. A platform and linker mediate dye-protein interactions via a high local concentration. Protein conformational changes affecting the dye's chemical environment generate a change in the fluorescence signal. By tuning linker length and dye, we have leveraged this strategy to monitor the functions of three proteins: streptavidin, alkaline phosphatase, and Protein G. Several observations supported our proposed signalling mechanism. First, FAM nanoantennas detected all conformational changes in their surroundings: their binding to SA, subsequent binding of biotin or a biotinylated protein to SA, the function of the biotinylated proteins (*i.e.*, catalytic activity or protein-protein interaction), inhibitor binding and effect, and thermal unfolding. Second, 16 structurally distinct substrates of AP, all hydrolysed by the same mechanism,[108] exhibited similar fluorescence signatures. In contrast, the binding of phosphate at the same location had no significant direct effect on nanoantenna fluorescence (aside from the observed inhibitory effects), while the binding of vanadate, a transition state analogue inhibitor known to induce a small structural change,[107] led to significant fluorescence quenching. Third, nanoantennas employing chemically diverse dyes that bind to various locations on AP differed in sensitivity but displayed the same kinetics during substrate hydrolysis. We also observed similar dye sensitivity for Protein G and streptavidin. Fourth, the strategy was not limited to a single fluorescent dye, since FAM nanoantennas were optimal for monitoring bAP function while the Cy3 nanoantenna was best for bPG. Finally, MD simulations also suggested a signalling mechanism based on conformational change.

A main advantage of fluorescent nanoantennas is their convenience. For example, the nanoantennas can be used with accessible and straightforward fluorescence spectroscopy, as opposed to specialised techniques. Furthermore, various conjugation strategies can be developed to facilitate nanoantenna-protein preparation. For example, here we developed and exploited the modular biotin-SA platform. This requires only non-specific biotinylation of the protein of interest, as opposed to site-specific attachment chemistry of fluorophores. Indeed, lysine residues can be non-specifically biotinylated with a simple commercially available kit. While it cannot be assumed as necessarily true in all cases, biotinylation often does not affect protein function.[435] In comparison, for example, the more complex site-specific labelling needed for FRET strategies has been found in some cases to perturb protein function, such as with beta-lactamases[44, 455] and dihydrofolate reductase.[456-458] In the case where biotinylation would affect a protein's function, other modular attachment strategies could also be developed, for example, one could envision the use of N- or C-terminus affinity tags.[582] When employing a modular attachment strategy, efficient nanoantennas can also be rapidly screened using a 96-well plate, as we demonstrated with bPG.

Another important advantage of fluorescent nanoantennas is their versatility. The findings presented herein suggest that nanoantennas can be used to monitor distinct biomolecular mechanisms in real time. Presumably, this includes both small and large conformational changes, or any other event that can affect the dye's fluorescence emission. Furthermore, since nanoantennas can distinguish between unbound and substrate-bound enzyme conformations, they can supplant non-natural colorimetric[34] and fluorogenic[37, 238, 240] substrates of AP, as well as the malachite green assay used for spectroscopically silent substrates.[106] Indeed, nanoantennas enable real-time, "one-shot" kinetic characterisation of any substrate, such as ATP and amifostine.[143, 146, 150, 208] In contrast, standard methods to determine K_{M} and k_{cat} for spectroscopically silent substrates require ~10 measurements at different substrate concentrations.[106, 513] Fluorescent nanoantennas also compare favourably with other "one-shot" strategies that require microfluidics to generate a range of substrate concentrations, in addition to a fluorescent product.[545] These nanoantennas, however, do have some limitations. For example, unlike other techniques, such as Förster resonance energy transfer (FRET),[45, 583] protein-induced fluorescence enhancement (PIFE),[318, 319] photoinduced electron transfer (PET),[448, 449] and tryptophan-induced quenching (TrIQ),[450-452] nanoantennas cannot quantify specific distance variations. Also, not all dye-protein combinations generate a signal change during protein function; some proteins might not work with any dyes. However, looking to the future, we believe that the universality of the nanoantenna strategy may be improved by screening a larger library of dyes and by further exploring the predictive potential of docking and MD simulations.[584] We anticipate that our fluorescent nanoantennas will find exciting applications in the study of protein structure and function and in high-throughput screening.

Chapter 6 – Materials and methods

6.1 Methods

6.1.1 Oligonucleotide synthesis

Labelled and unlabelled oligonucleotides were made by standard phosphoramidite chemistry with a solid support DNA/RNA H-6 Synthesizer from K&A Laborgeräte (Schaafheim, Germany). Purification of strands with a 5'-protecting group (4,4'-dimethoxytrity (DMT)) was performed with a P-8 oligo purifier. Strands without a protecting group (*e.g.*, 5'-end 6-FAM and 5-FAM) were purified using high performance liquid chromatography (HPLC) with a 1260 Infinity HPLC instrument from Agilent (Santa Clara, CA, USA). The mobile phase was 0.1 M triethylamine with increasing concentration of acetonitrile, and the stationary phase was an XBridge Oligonucleotide BEH C18 OBD Prep Column, 130 Å, 2.5 µm, 10 mm X 50 mm from Waters Corporation (Milford, MA, USA). Extinction coefficients at 260 nm were predicted using the OligoAnalyzer website (https://www.idtdna.com/calc/analyzer) from Integrated DNA Technologies (Coralville, IA, USA). DNA was then quantified by ultraviolent-visible spectroscopy (UV-Vis) with a Cary 60 from Agilent or a NanoDrop 2000c Spectrophotometer from Thermo Fisher Scientific (Waltham, MA, USA). Oligonucleotides were prepared as ~800 µM stock solutions, with 100 µM intermediate solutions of 1 mL; all stored at -20 °C.

6.1.2 Fluorescence

Fluorescence spectroscopy was recorded with a Cary Eclipse Fluorescence Spectrophotometer from Agilent. For measurements in quartz cuvettes, it was equipped with a Peltier Thermostatted Multicell Holder Accessory from Agilent. For the plate-reader measurements, it was equipped with a Microplate Reader ACCY from Varian (Palo Alto, CA, USA) and used Nunc MaxiSorp 350 µL black 96-well plates from Thermo Fisher Scientific. Typical settings were ex/em slit widths 5 nm, excitation 498 nm, and emission 520 nm for Fluorescein (FAM; wavelengths are denoted hereafter in the format of 498/520), Cal Fluor Orange 560 (CAL) 540/561, Carboxyrhodamine (ROX) 575/602, Carboxytetramethylrhodamine (TAMRA) 565/580, Cyanine 3 (Cy3) 546/563, Quasar 570 (Q570) 550/570, Quasar 670 (Q670) 644/670, Pulsar 650 (P650) 460/650, and Methylene Blue (MB) 670/690. The PMT detector voltage was typically set at 635 V for 150 nM fluorescent nanoantennas, but 800 V for those with MB or P650, as well as 800 V for experiments with 15 nM FAM nanoantennas. For plate-reader measurements, it was 600 V. For kinetics, we typically used Avg time 3.0 s and Cycle 0.04 min. For spectra, we typically used CAT mode with 10 scans at “medium” speed (scan rate 600 nm/minute, averaging time 0.1 s, data interval 1 nm).

A typical study of nanoantenna fluorescence emission over time was as follows: the intermediate nanoantenna stock solution was added to buffer in a quartz cuvette (150 nM), followed by waiting 5-10 min for the fluorescence signal to equilibrate. After observing a stable signal, we performed subsequent additions of complementary DNA (cDNA), proteins, substrates, *etc*. Final volume at addition of substrate was 1 mL. We typically mixed the solution by rapidly pipetting ~10x using ~50 µL volume while being careful to not pipette bubbles into the solution. A waiting time of 3-10 minutes for each step was taken to ensure binding and equilibration. In most cases, cDNA and SA bound very quickly after several seconds, but biotinylated proteins often took longer, sometimes up to several minutes. In a typical experiment, we added SA (50 nM) and then bAP (100 nM) for a nanoantenna:SA:bAP ratio of 3:1:2. For some faster lots of enzyme, we added less enzyme, as indicated. Lastly, we added the substrate (*e.g.*, pNPP). To make the effects of dilution negligible, most additions were aliquots of several µL.

For dual absorbance and fluorescence kinetics of the same sample, we used a SX20 Stopped Flow Spectrometer from Applied Photophysics (Surrey, England, UK) with a 495 nm cut-off filter. Nanoantenna-protein complex was prepared in one syringe and substrate in the other syringe, which were then mixed during the measurement.

6.1.3 Buffer conditions

In our initial studies of the nanoantenna concept with AP and of various dyes (Figure 2.1, Figure 2.14), buffer conditions were 200 mM Tris, 300 mM NaCl, 1 mM $MgCl_2$, pH 7.0, and 37 °C, with 100 nM bAP and 50 nM SA. A ratio of three nanoantennas per SA, for example, used 150 nM nanoantennas. Later, for comparison with another recent study,[100] buffer conditions were then

100 mM Tris, 10 mM NaCl, pH 8.0, and 30 °C, with either 100 nM bAP (Figure 3.1) or 10 nM bAP (Figure 3.4; nanoantennas and SA were adjusted proportionally). For the characterisation of substrates (Figure 3.7) and inhibitors (Figure 3.12), the same buffer was used but at 37 °C with 150 nM nanoantennas, 50 nM SA, and 20 nM bAP. Less bAP was used because this lot of bAP enzyme displayed faster substrate hydrolysis kinetics than previous lots that we had purchased. For vanadate experiments (Figure 3.14), the same buffer was also used but with 100 nM bAP. In experiments for thermal denaturation of AP (Figure 3.15), to reduce pH variation with temperature, we changed the buffer conditions to 100 mM NaCl, 50 mM Na_2HPO_4, pH 7.0, 37 °C, and used 100 nM bAP. For experiments with Protein G in the 96-well plate (Figure 4.1), buffer conditions were 200 mM Tris, 300 mM NaCl, pH 7.0, room temperature with 500 nM nanoantennas, 167 nM SA, 167 nM bPG, and 1000 nM goat IgG. For subsequent experiments with Protein G in cuvettes, the same buffer was used at 37 °C with 150 nM nanoantennas, 50 nM SA, 50 nM bPG, and 500 nM goat IgG. Other figures typically used the same conditions as associated experiments in the main text, but see also their caption.

6.1.4 Software

Data analysis was performed in KaleidaGraph from Synergy Software (Reading, PA, USA), OriginPro 9.0 from OriginLab Corporation (Northampton, MA, USA), and Excel from Microsoft (Redmond, WA, USA), with all data plotted in KaleidaGraph. The logD calculations, as a measure of hydrophobicity,[466] were done with MarvinSketch software from ChemAxon (Budapest, Hungary). Molecular structure images were also generated with MarvinSketch.

6.1.5 Molecular docking simulations

Docking was performed on the SwissDock web server (http://www.swissdock.ch)[390, 391] from the Swiss Institute of Bioinformatics (Lausanne, Switzerland). The “Target” protein structure for streptavidin was 6M9B (*Streptomyces avidinii).*[427] Since there was no crystal structure available for the AP used in this study, we instead built a homology model on the SWISS-MODEL web server (https://www.swissmodel.expasy.org) from the sequence of P19111 (*Bos taurus* intestinal alkaline phosphatase) and the structure of 1ZEF (*Homo sapiens* placental alkaline phosphatase) as the template.[428, 436, 437] The Global Model Quality Estimation (GMQE) was 0.79, Quaternary Structure Quality Estimate (QSQE) was 0.93, and the Identity was 75.52. “Ligand” structures (*e.g.*, biotin, pNPP, dyes, *etc*.) were determined to be the major microspecies at pH 7.0 using MarvinSketch software, the manufacturer’s product description, and the available literature,[343, 350, 438-441] followed by optimisation in Avogadro software.[585] Analysis of the docking simulation was done in UCSF Chimera software using the View Dock tool (Type Selection: Dock 4, 5 or 6).[392] Note that dyes in the simulation did not include the attachment chemistry to the DNA, nor the DNA itself, and are accordingly an estimation of the binding site. Docking simulations were repeated ten times to confirm reproducibility (or lack thereof) for the binding site.

6.1.6 Molecular dynamics simulations

Structure preparation. All protein-ligand complexes were prepared using the AP homology model. Two sets of complexes were generated for three fluorophores (FAM, CAL and Cy3) in the complex with or without pNPP substrate. From the docking study of FAM, we chose the best pose (“position”) that would have the *para* and *ortho* connection of the DNA linker attachment point accessible by the solvent. Since AP is a homodimer, both binding locations were populated with different ligand conformations for double sampling. In the case of the substrate-bound pNPP/FAM complex, the FAM ligand was redocked to the AP active site with the substrate present. Again, the best scoring pose of the pNPP/FAM ligand complex from the docking run was chosen. The QuickPrep application of MOE2019 software,[586] with default parameters, was used to create a fully parameterised all-atomistic model, which was then used to generate the input files for all MD simulations. Separately, the model of the nanoantenna-SA-bAP complex was built using the streptavidin/biotin complex (6M9B),[427] the AP homology model, and the rL12 nanoantenna sequence with 3' 5-FAM and 5' T biotin. The all-atomistic model was again generated using the QuickPrep application. A lysine residue in proximity to the AP binding site was biotinylated and the biotin moiety was placed in the streptavidin active site in a non-clashing conformation. Note that the manufacturer would not disclose the exact composition of the biotin connectivity to AP. The DNA linker was constructed using the MOE2019 DNA/RNA builder starting from the crystallised biotin molecule in the neighbouring streptavidin active site. Finally, the FAM fluorophore was attached to the 3'-end of the DNA linker and the entire complex’s energy was minimised using the MOE2019 built-in energy minimisation application.

MD Simulation. The simulation cell and AMBER20[587] input files were generated using MOE2019. The crystallographic water molecules were removed prior to solvation. Next, the protein/ligand complexes and AP apo structure were embedded in a TIP3P water box with cubic periodic boundary conditions, keeping a distance of 10 Å between the boundaries and the protein. The net charge of the protein was neutralised with 100 mM NaCl. For energy minimisation and MD simulations, the AMBER14:EHT force field was used and the electrostatic interactions were evaluated by the particle-mesh Ewald method. Each system was energy-minimised for 5000 steps using the Conjugate Gradient method. For equilibration, the system was subjected to a 100 ps simulation to gradually heat the system from 10K to 300K. Next, a 100 ps NVT ensemble was generated at 300K followed by an NPT ensemble for 200 ps at 300K and 1 bar. Then, for each complex, a 100 ns production trajectory was generated for further analysis. The trajectory analysis and frame export for the video was done using scripts shared by the CCG support group.

6.1.7 Kinetic fitting (K_M, k_{cat}, K_i)

Fitting was performed using MATLAB (version R2019a) from Mathworks (Natick, MA, USA) by following a method with a script obtained from the author.[588] Briefly, Michaelis-Menten differential equations with competitive product inhibition (Eqns. 6.1 to 6.6) were integrated using Euler's method with a time step of dt = 0.1 s, where K_M is the Michaelis constant, K_i is the product inhibition constant, and k_{cat} is the catalytic rate constant (turnover number). $[S]_t$, $[P]_t$ and $[ES]_t$ are the concentration of substrate, product, and enzyme-substrate complex at time = t, respectively. $Rate_{dil}$ is the rate of dilution of the substrate from the pipette to the cuvette and is estimated to be 2 s during the dilution and 0 otherwise. $[S]_0$ is the initial concentration of substrate in the syringe prior to dilution. $[E]_0$ is the concentration of enzyme in the cuvette and is assumed to remain constant throughout the course of the kinetics. Note that substrate addition typically dilutes the enzyme by less than 1% and therefore is negligible.

$$\frac{d[P]_t}{dt} = \frac{[E]_0 \cdot k_{cat} \cdot [S]_t}{\left(K_M\left(1 + \frac{[P]_t}{K_I}\right) + [S]_t\right)} \qquad \textbf{Eqn. 6.1}$$

$$[P]_{t+dt} = [P]_t + \frac{d[P]_t}{dt} \cdot dt \qquad \textbf{Eqn. 6.2}$$

$$\frac{d[S]_t}{dt} = -\frac{d[P]_t}{dt} + [S]_0 \cdot Rate_{dil} \qquad \textbf{Eqn. 6.3}$$

$$[S]_{t+dt} = [S]_t + \frac{d[S]_t}{dt} \cdot dt \qquad \textbf{Eqn. 6.4}$$

$$[ES]_t = \frac{[E]_0 \cdot [S]_t}{\left(K_M\left(1 + \frac{[P]_t}{K_I}\right) + [S]_t\right)} \qquad \textbf{Eqn. 6.5}$$

$$F_{spike} = Baseline + F_{max} \cdot [ES]_t + F_{prod} \cdot [P]_t \qquad \textbf{Eqn. 6.6}$$

The fluorescence signal was found to be correlated with the concentration of ES and is fit according to Eqn. 6.6, where the baseline is the native signal of the nanoantenna-SA-bAP complex, F_{max} is the fluorescence signal of the nanoantenna-SA-bAP complex when all the enzyme is bound with substrate (*i.e.*, high substrate concentration), and F_{prod} is the impact of the product concentration on the fluorescence signal of the nanoantenna-SA-bAP complex. Fitting was performed by using the nonlinear least-squares solver *lsqcurvefit* in MATLAB which minimises the sum of the squares of the residuals between the raw data and the computed data. Then, when applicable, the 95% confidence interval of each parameter is calculated using the *nlparci* function in MATLAB.

Enzymatic equations were sometimes modified to accommodate specific characteristics of some substrates. For example, PP_i upon cleavage generates two phosphate products, rather than one phosphate as is generated for pNPP or 4MUP. Therefore, $d[P]_t/dt$ was multiplied by 2. ADP, ATP and GTP can react multiple times and this was considered by multiplying $[S]_0$ with the number of reactive groups. All experiments were done in triplicate.

6.1.8 Density functional theory computations

To estimate nanoantenna length, DFT quantum mechanical computations were performed with the General Atomic and Molecular Electronic Structure System (GAMESS)[411] via the website Chem Compute (https://www.chemcompute.org)[410] on the Comet cluster of the San Diego Supercomputing Center. We used the B3LYP functional and the 6-311++G(d,p) basis set with diffuse functions for the negative charge. The optimised structures displayed no negative vibrational frequencies, which confirmed optimisation to the ground state. Since we examined DNA nanoantennas based on their length in nucleotides, we needed to make a comparison for the PEG nanoantennas. The molecular structure of one unit produced by Spacer 18 amidite was first drawn in Avogadro software, followed by DFT computations. The optimised geometry was then examined in Avogadro with the Measure tool to determine its length in Å. We converted Å to nucleotides based on dsDNA having a length of 3.4 Å per nucleotide.[421]

6.1.9 Preparation of biotinylated AP

For most of this project, we used commercially prepared biotinylated alkaline phosphatase (bAP). We also prepared our own biotinylated AP to explore lot-to-lot variation issues (used in Figures 2.10, 2.11, and 3.4 plus its associated figures). For this, we used unconjugated AP from Rockland and a Biotin Protein Labeling Kit from Roche Diagnostics (Mannheim, Germany). To avoid unwanted side reactions, we removed Tris from the enzyme's buffer with a Nanosep Centrifugal Device with Omega Membrane 30K from Pall Corporation (Port Washington, NY, USA) by rinsing 10x. Then, we followed the manufacturer's instructions for the biotinylation kit by following "Procedure 2: Polyclonal antibody" based on the mass of the protein.

6.1.10 Preparation of nanoantenna-AP covalent conjugate

AP was first diluted to 40 µM using PBS buffer (pH 7). Then, we added 3 equivalents of freshly prepared SPDP reagent (20 mM) in DMSO. AP was incubated with SPDP solution at room temperature for 30 min. Next, we used a Zeba spin desalting column to exchange the SPDP-modified protein reaction buffer for 10 mM HEPES, 150 mM NaCl, pH 8, and to remove reaction by-products and excess nonreacted SPDP reagent. Separately, we incubated the DNA nanoantenna (5′ T 6-FAM, 3′ SH) with 1 M dithiothreitol (DTT) in 40 µL TE buffer for 30 min at

37 °C. Then, we extracted with ethyl acetate, and combined the aqueous phases. We then added 8 equivalents of reduced thiol DNA to the SPDP-modified AP and let it react for 1 h at room temperature. Note that to avoid side reactions, we used a DNA strand that did not contain guanine.

6.1.11 Presentation of data

Error bars on graphs and expressed values represent mean ± standard error of the mean (SEM) for three distinct measurements. Typically, experiments were performed in triplicate, with the following exceptions: Figure 2.1 and Figure 2.6 (ratios) for values not near the maximum, Figure 2.9 (covalent attachment of nanoantenna to AP) which had three injections of pNPP to the same sample, as well as Figure 2.8 and Figure 2.18 (MD simulations) that were performed once. Also, all molecular docking simulations were performed ten times.

6.2 List of reagents

6.2.1 Enzymes and proteins

Alkaline phosphatase (AP) was from calf intestinal mucosa of *Bos taurus*. Unconjugated AP (19.83 mg/ml, in 0.05 M Tris Chloride, 0.005 M $MgCl_2$, 0.0001 M $ZnCl_2$, 50% (v/v) Glycerol, pH 7.0; >6,000 units/mg, where unit = hydrolysis of ~6 mM p-nitrophenol phosphate/minute at 37 °C at pH 9.8), biotin-conjugated AP (bAP; 1 mg/ml, in 0.05 M Tris Chloride, 0.15 M NaCl, 0.001 M $MgCl_2$, 0.0001 M $ZnCl_2$, 50% (v/v) Glycerol; pH 8.0, 0.05% (w/v) Sodium Azide as a preservative, 10 mg/mL Bovine Serum Albumin (BSA) as a stabiliser), streptavidin-conjugated AP (SA-AP; 1 mg/ml, in the same buffer from the manufacturer), biotin-conjugated glucose oxidase (bGOX; 0.01 M Sodium Phosphate, 0.15 M Sodium Chloride, pH 7.2), Protein G Biotin Conjugated (bPG; lyophilised, 1.0 mg/ml, 0.02 M Potassium Phosphate, 0.15 M Sodium Chloride, pH 7.2, 0.01% (w/v) Sodium Azide as a preservative, 10 mg/mL Bovine Serum Albumin (BSA) as a stabiliser), Protein A Biotin Conjugated (bPA; lyophilised, 1.0 mg/mL, 0.02 M Potassium Phosphate, 0.15 M Sodium Chloride, pH 7.2, 0.01% (w/v) Sodium Azide as a preservative, 10 mg/mL Bovine Serum Albumin (BSA) as a stabiliser), and Goat IgG whole molecule (lyophilised, 11.0 mg/ml, 0.02 M Potassium Phosphate, 0.15 M Sodium Chloride, pH 7.2, 0.01% (w/v) Sodium Azide as a preservative, lot # 32090) were from Rockland Immunochemicals (Limerick, PA, USA). Streptavidin from *Streptomyces avidinii* (SA; 1 mg/ml, in 140 mM NaCl, 8 mM Sodium Phosphate, 2 mM Potassium Phosphate, 10 mM Potassium Chloride, pH 7.4) was from New England Biolabs (Ipswich, MA, USA). VIROTROL SARS-CoV-2 (Reactive for SARS-CoV-2 total IgG/IgM and IgG antibodies; human plasma based; lot # 390300) and VIROCLEAR SARS-CoV-2 (Non-reactive for SARS-CoV-2 total IgG/IgM and IgG antibodies; human plasma based; lot # 390600) were from Bio-Rad Laboratories (Hercules, CA, USA). Bovine Serum Albumin (BSA; cold ethanol fraction, pH 5.2, ≥96%) was from Sigma-Aldrich (St. Louis, MO, USA).

6.2.2 Substrates and inhibitors

p-nitrophenylphosphate (pNPP, 500 mM solution) was from New England Biolabs. Adenosine 5′-triphosphate (ATP; 100 mM solution, pH 7.0) was from Bio Basic (Markham, ON, Canada). Pyridoxal-5'-phosphate monohydrate (PLP; ≥95%) and creatine phosphate disodium tetrahydrate (PCr; ≥98%) were from BioShop (Burlington, ON, Canada). Amifostine (≥98%) was from BioVision (Milpitas, CA, USA). 4-Methylumbelliferyl phosphate (4MUP; ≥98%), sodium pyrophosphate tetrabasic decahydrate (PP_i; ≥99%), β-glycerophosphate disodium salt hydrate (BGP; “cell culture tested”), phospho(enol)pyruvic acid monopotassium salt (PEP; 99%), O-phospho-L-serine (PSer; ≥98%), D-glucose 6-phosphate sodium salt (G6P; ≥98%), D-fructose 6-phosphate disodium salt (F6P; ≥98%), adenosine 5′-monophosphate monohydrate (AMP; ≥95%), adenosine 5′-diphosphate sodium salt (ADP; ≥95%), guanosine 5′-triphosphate sodium salt hydrate (GTP; ≥95%), 4-nitrophenol (PNP; “spectroscopic grade”), sodium orthovanadate (99.98%), sodium molybdate dihydrate (≥99%), potassium arsenate monobasic (≥99.9%), and α-D-glucose (anhydrous, 96%) were from Sigma-Aldrich. Lipopolysaccharide (LPS) solution from *Escherichia coli* O26:B6 (eBioscience, “sterile aqueous buffer, no sodium azide”) was from Thermo Fisher Scientific (Waltham, MA, USA). Sodium tungstate dihydrate was from MCB (Norwood, OH, USA). Glycerol (99.5%) was from American Chemicals.

6.2.3 Oligonucleotide synthesis reagents

3′-Modifications were from controlled pore glass (CPG) columns and 5′-modifications were from phosphoramidites. Biotin (B), Quasar 570 (Q570), Quasar 670 (Q670), fluorescein (5-FAM), rhodamine-X (ROX), CAL Fluor Orange 560 (CAL), phosphate (P), C_{16} spacer (C_{16}), thiol C6 (S-S; S-H after treatment with dithiothreitol) CPG columns, as well as Fluorescein T Amidite (T 6-FAM or T_{FAM}), 6-FAM Amidite (6-FAM), 5-FAM Amidite (5-FAM), Biotin T C6 Amidite (T biotin or T_B), Spacer 18 Amidite (DMT-Hexa(ethylene glycol)) (S18), and Methylene Blue Succinimidyl Ester (MB) were from Biosearch Technologies (Petaluma, CA, USA). Tetramethylrhodamine (TAMRA) and Cyanine 3 (Cy3) CPG columns were from Glen Research (Stirling, VA, USA). Standard A, G, C, and T CPG columns were from Biosearch. Acetonitrile (wash grade), DMT removal (3% trichloroacetic acid/dichloromethane), CAP A (Acetic Anhydride/Pyridine/THF), CAP B (16% N-Methylimidazole in THF), Oxidation Solution (0.1M Iodine/Pyridine/H_2O/THF), Activation Reagent (0.25 M 5-ethylthio Tetrazole in ACN), deoxycytadine (n-acetyl) CED phosphoramidite, deoxyguanosine (n-ibu) CED phosphoramidite, deoxyadenosine (n-bz) CED phosphoramidite, and thymidine CED phosphoramidite were from ChemGenes (Wilmington, MA, USA). For purification, glacial acetic acid (99.7%) and triethylamine (99%) were from Thermo Fisher Scientific, acetonitrile (≥99.9%) was from Sigma-Aldrich, and trifluoroacetic acid (99%) was from Alfa Aesar (Ward Hill, MA, USA). MicroPure II columns for DNA purification were from Biosearch.

6.2.4 Miscellaneous reagents

Biotin (5-fluorecein) conjugate (≥90%) used as the L0 nanoantenna was from Sigma-Aldrich, 8-Anilino-1-naphthalenesulfonic acid ammonium salt hydrate (ANS probe; 97%), CAPS (≥99%), MOPS sodium salt (≥99.5%), Bis-Tris (≥98.0%) and hydrochloric acid (37%) were from Sigma-Aldrich. D-Biotin (99.0%), Tris (99.9%), sodium chloride (≥99.5%), sodium hydroxide (98%), PIPES (99%) and sodium phosphate dibasic were from BioShop. Magnesium chloride anhydrous (99%) was from Alfa Aesar. Sodium phosphate monobasic anhydrous (≥99.5%) and ammonium hydroxide (28-30%) were from VWR (Radnor, PA, USA). HEPES was from MP Biomedicals (Solon, OH, USA). All reagents were stored at -20°C, -4 °C, or at room temperature, as appropriate. All solutions were prepared in ultrapure water from a Milli-Q Biocel filtration device from EMD Millipore (Burlington, MA, USA).

6.3 List of oligonucleotides sequences

All sequences listed here are in the direction of 5′ to 3′.

PEG nanoantennas:

~**L21:** T_{FAM}-S18-S18-S18-Biotin (S18 = Spacer 18)
~**L41:** T_{FAM}-S18-S18-S18-S18-S18-S18-Biotin

ssDNA nanoantennas with $T_{6\text{-}FAM}$:

L06: $T_{6\text{-}FAM}$-TATTG-Biotin
L12: $T_{6\text{-}FAM}$-TATTGATCGGC-Biotin
L24: $T_{6\text{-}FAM}$-TATTGATCGGCGTTTTAAAGTG T-Biotin
L48: $T_{6\text{-}FAM}$-TATTGATCGGCGTTTTAAAGTGTCCAGGGTGTTTGTGTATTACTCGA-Biotin
PolyT12: $T_{6\text{-}FAM}$-TTTTTTTTTTT-Biotin

ssDNA nanoantennas with other FAMs:

L12 (6-FAM version): 6-FAM-TTATTGATCGGC-Biotin
L12 (5-FAM version): 5-FAM-TTATTGATCGGC-Biotin

Note that 5-FAM and 6-FAM are isomers (see Figure 2.11). Therefore, the nanoantennas L12, L12 (6-FAM version), and L12 (5-FAM version) differ in their connectivity of FAM at the 5′-end. In addition, we also used rL12 (5-FAM), see below, which had the dye at the 3′-end.

cDNA to form dsDNA nanoantennas:

cL12: GCCGATCAATAA
cL24: ACACTTTAAAACGCCGATCAATAA
cL48: TCGAGTAATACACAAACACCCTGGACACTTTAAAACGCCGATCAATAA

L12 with other dyes:

To test various dyes, we used a “reverse” version of the L12 nanoantenna (rL12).
rL12 (Dye): T_{Biotin}-TATTGATCGGC-Dye; where dye = 5-FAM, TAMRA, Cy3, Q570, or Q670

Some dyes were directly attached to a nucleobase, so the sequence was modified accordingly.
rL12 (Dye): T_{Biotin}-TATTGATCGG-C_{Dye}; Dye = ROX or P650
rL12 (Dye): T_{Biotin}-TATTGATCGG-T_{Dye}; Dye = CAL
Thus, for dsDNA with CAL, the cL12’s G at 5′ was replaced by A.

The MB strand was from another project in our lab and was kindly donated by Dr. Guichi Zhu.
MB-CCAGAGACCACGGACT-Biotin

Modifiers:

To test chemical modifications near FAM, we used cL12 strand with the Modifier at the 3′-end.
Here, Modifier = phosphate, C_{16}, S-S or S-H.
GCCGATCAATAA-Modifier

Dye competition:

For dual-dye studies, we used the standard L12 FAM nanoantenna with versions of the cL12 nanoantenna containing CAL, Cy3 or Q670 at the 3′-end. We also used a capture strand analogous to L12 but without the $T_{6\text{-FAM}}$.

Controls:

Molecular beacon: $T_{6\text{-FAM}}$*CCGC*GATCGGCGTTTTA*GCGGA*TCCTGGGTGTTAG-Biotin
Global: $T_{6\text{-FAM}}$-TTTTTTTTTTT
Dummy: TTTTTTTTTTTT-Biotin

Covalent attachment:

For nanoantenna-AP covalent attachment, the strand had a thiol moiety. Also, it did not have guanine to avoid side reactions.

$T_{6\text{-FAM}}$-CCATACATCCC-SH

6.4 Phosphoramidite synthesis of DNA

This section begins by briefly discussing biological synthesis of DNA; not to review the fundamentals of biology,[589] but instead to emphasise the differences from the phosphoramidite synthesis method. DNA synthesis starts with the precursor molecules, deoxynucleoside triphosphates (dNTP). DNA polymerase attaches a phosphate of one dNTP to the sugar of the second dNTP. Two phosphates are released from the first dNTP to provide energy for the reaction. This process is repeated until the DNA strand is complete. The DNA polymerase also requires a template strand to mediate the process. The enzyme moves along the template strand in the 3′-to-5′ direction, and due to the antiparallel orientation of double-stranded DNA (dsDNA), it synthesises the new strand in the 5′-to-3′ direction. Other enzymes are also involved, such as nucleases that can break strands, DNA ligases that can join two strands to form a longer strand, primases that make RNA primers to start the synthesis of DNA, and various other proteins. Sometimes DNA replication results in errors, which includes having the wrong base pair in a mismatch (*e.g.*, G and T). To avoid mutations and potential harm to the organism, DNA polymerase stops the process until an editing protein can fix the error, or if at the 3′-end, by removal with a 3′ exonuclease. The strands generated by this process are very long. For example, each *E. coli* DNA strand contains about 4.7 million nucleotides.[589] However, DNA synthesis by the phosphoramidite method differs markedly from this biosynthetic process. As will be explained below, the precursor and waste molecules differ, the process does not employ enzymes, synthesis occurs in the 3′-to-5′ direction to yield single-stranded DNA (ssDNA), errors are prevented by a chemical approach, and oftentimes, strands cannot be longer than ~200 nucleotides.

DNA synthesis employing phosphoramidite chemistry occurs on a solid-phase support. Unlike the early days of DNA synthesis by hand,[590] the process is now automated once the reagents are added to the instrument and the desired sequence has been entered into the computer. The synthesis occurs within the tubing of the oligonucleotide synthesiser through which the reagents are pumped. Also, the processes remain similar regardless of whether one is synthesising DNA that is unlabelled, DNA with 3′ or 5′ terminal modifications (*e.g.,* fluorescent dyes, biotin), or DNA with internal modifications (*e.g.*, polyethylene glycol). These differences do affect some of the final steps, which are addressed below.

DNA synthesis begins on a solid support, such as controlled pore glass (CPG) (**Figure 6.1**). The CPG is designed to not influence the synthesis, whereby it has pores large enough to contain the oligonucleotides and it should not allow any side reactions.[591] There is also a covalent linker between the support itself and the first nucleoside (the 3′-end nucleoside), which will later be cleaved.[591] With this in place, the first step of the synthesis is called "detritylation" or "deblocking". The 3′-end nucleoside on the solid support has an acid-labile 4,4'-dimethoxytrityl (DMT) protecting group at its 5′-end hydroxyl group (5'-OH). The DMT is removed by 2% trichloroacetic acid (TCA) in inert dichloromethane (DCM). It is then rinsed away by acetonitrile, as are all subsequent waste products. With the DMT gone, the starting nucleoside now has a reactive 5'-end hydroxyl group (5'-OH).[592, 593] The released orange DMT carbocation absorbs light at ~498 nm and is used to quantify the reaction.[592]

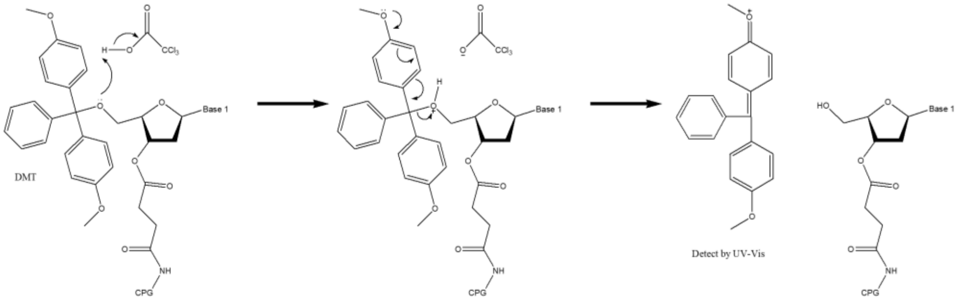

Figure 6.1. – Solid support and detritylation step. Starting with 3′-end nucleoside attached to the controlled pore glass (CPG) solid support, the 4,4'-dimethoxytrityl (DMT) is removed by trichloroacetic acid (TCA). The 5′-end hydroxyl group (5'-OH) is now available for the next step. The DMT is detected by UV-Vis to quantify the reaction.

Before describing the next steps of the reaction, it is prudent to first review the composition of a phosphoramidite (**Figure 6.2**).[592] It contains the following components: the desired nucleotide, its 5'-OH protected by a DMT (similar to what is on the solid support), a protecting group on the amino functionality,[594-596] as well as β-cyanoethyl and diisopropylamine protecting groups on the phosphite.[592, 593, 597] To prevent unwanted side reactions, the amino group of the 2'-deoxyadenosine and 2'-deoxycytidine is protected by a benzoyl (dA^{Bz}) or an acetyl group (dC^{Ac}), respectively.[594, 595] Conversely, while the amino group of 2'-deoxyguanosine is less reactive, the isobutyryl protecting group also makes it more soluble (dG^{iBu}).[596] Thymidine does not have an amino group, so there is no protecting group (T; equivalent to deoxythymidine, dT).

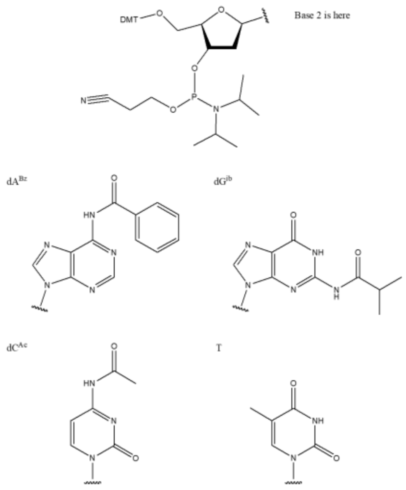

Figure 6.2. – Composition of a phosphoramidite. The phosphoramidite contains the desired nucleotide and amino protecting groups, its 5'-OH protected by a DMT, and β-cyanoethyl and diisopropylamine protecting groups on the phosphite. The amino protecting groups are shown below.

The second step is called “coupling” or “activation” (**Figure 6.3**). The purpose of this step is to add the next nucleotide (or modification) in the sequence, which comes from the phosphoramidite. In acetonitrile, the diisopropylamino group of the phosphoramidite is protonated (“activated”) by a weakly acidic catalyst. In our typical methodology, the catalyst is 5-ethylthiotetrazole,[598-600] although others are also available.[601] The activated phosphoramidite undergoes nucleophilic attack by the 5'-OH, which releases the diisopropylamino group and forms a phosphite triester.[592, 593]

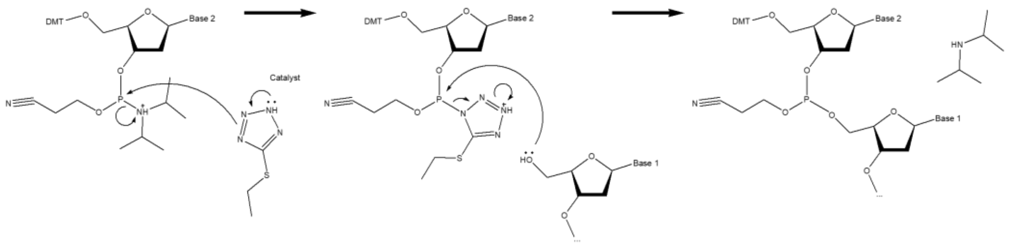

Figure 6.3. – Coupling step. The phosphoramidite is attached to the 3′-end nucleoside on the CPG solid support (...) via its 5'-OH with the aid of 5-ethylthiotetrazole as a catalyst.

The third step is called “oxidation” (**Figure 6.4**). Its purpose is to covert the unstable phosphite triester linkage to a stable phosphotriester. The phosphotriester is oxidised by reaction with iodine dissolved in water, pyridine, and tetrahydrofuran (THF).[592, 593] This involves the formation of an iodine-pyridine adduct on the phosphite triester, which is displaced by water to form the oxidised phosphate. Pyridine also neutralises the hydrogen iodide by-product.[592, 593]

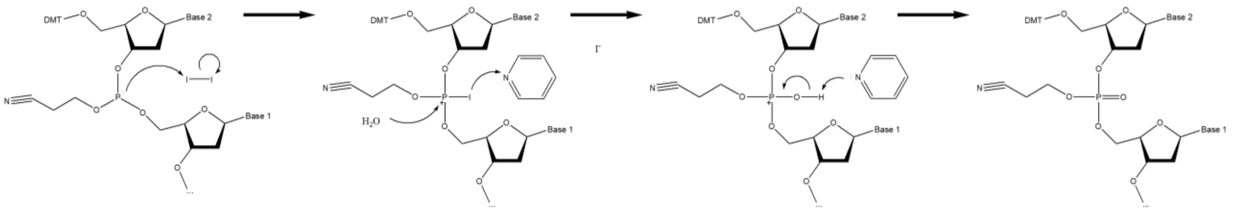

Figure 6.4. – Oxidation step. The unstable phosphite triester linkage is converted to the more stable phosphotriester via reaction with iodine in the presence of water, pyridine, and THF.

The fourth step is called “capping” (**Figure 6.5**). This purpose of this step is to prevent the formation of strands with a missing base since the efficiency of the coupling step is not 100% (*i.e.*, there could be some unreacted 5'-OH remaining). In THF and pyridine, N-methylimidazole reacts with acetic anhydride to form an intermediate, which then reacts with the unreacted (5'-OH) to form an acetylated ester 5'-OH.[592, 593] This is unaffected by subsequent cycles of reaction, and it will later be removed. The preceding steps are repeated until the sequence is complete.[592, 593]

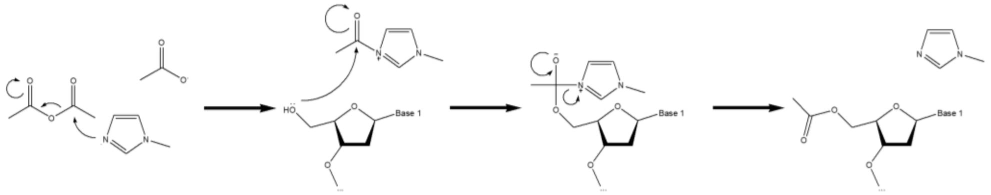

Figure 6.5. – Capping step. Capping unreacted 5'-OH groups as an acetylated ester via reaction of N-methylimidazole with acetic anhydride in the presence of THF and pyridine to prevent the formation of strands with a missing base.

After the synthesis, the oligonucleotide must be cleaved from the CPG (**Figure 6.6**). This is typically done via concentrated ammonium hydroxide in water. The succinyl linker to the CPG is cleaved, which leaves the oligonucleotide with a 3'-OH.[592, 593] Another step, which typically happens concurrently, is deprotection. This involves heating the solution overnight to remove the protecting groups from dA, dC, and dG (**Figure 6.7**).[592, 593] The β-cyanoethyl group is also removed from the phosphate in this step (**Figure 6.8**).[592, 593] Note that this is the general procedure, which will differ if using faster deprotecting groups and/or dyes that are sensitive to degradation.

After cleavage and deprotection, the next step is to purify the DNA. The reader might have noticed that the final nucleotide added at the 5'-end will still have a DMT. This 5′-DMT enables purification by reversed-phase chromatography (RPC). In this technique, the stationary phase is hydrophobic polymeric resin, which has a high affinity for the hydrophobic DMT, but not for truncated sequences (from the capping step) and other impurities that do not have a 5′-DMT moiety.[592, 593] After purification, treatment with acid removes the DMT, followed by elution of the purified strand with 20% acetonitrile. Strands without a 5′-DMT can be purified by high-performance liquid chromatography (HPLC).[592, 593] In most cases, these are sequences with 5′-end fluorescent dyes. The dye makes it convenient for separation by HPLC, since one can monitor the oligonucleotide by UV-Vis at 260 nm, as well as the dye itself by UV-Vis and fluorescence.

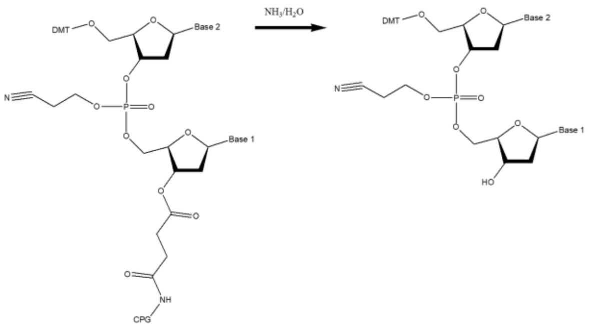

Figure 6.6. – Cleavage step. The 3'-end nucleotide's succinyl linker to the CPG is cleaved by ammonium hydroxide.

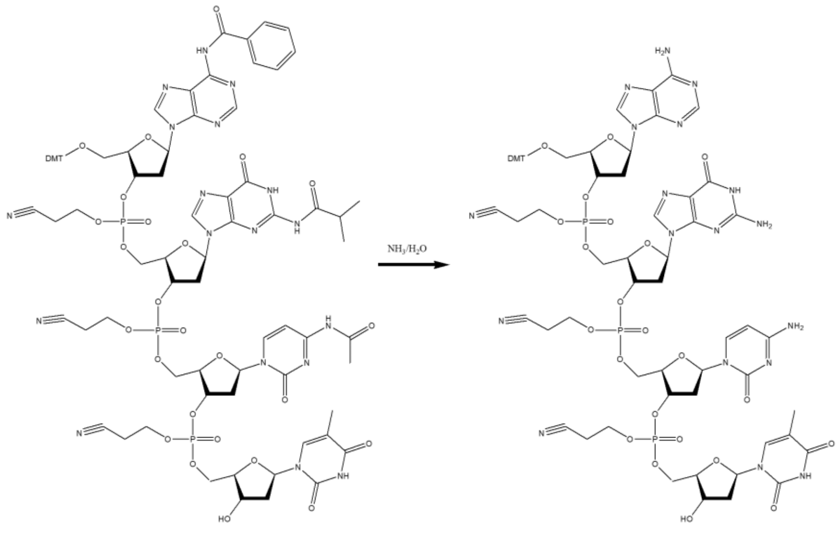

Figure 6.7. – Deprotection step (#1). Concurrent with the cleavage step, the protecting groups are removed from A, G, and C. There is no protecting group on T.

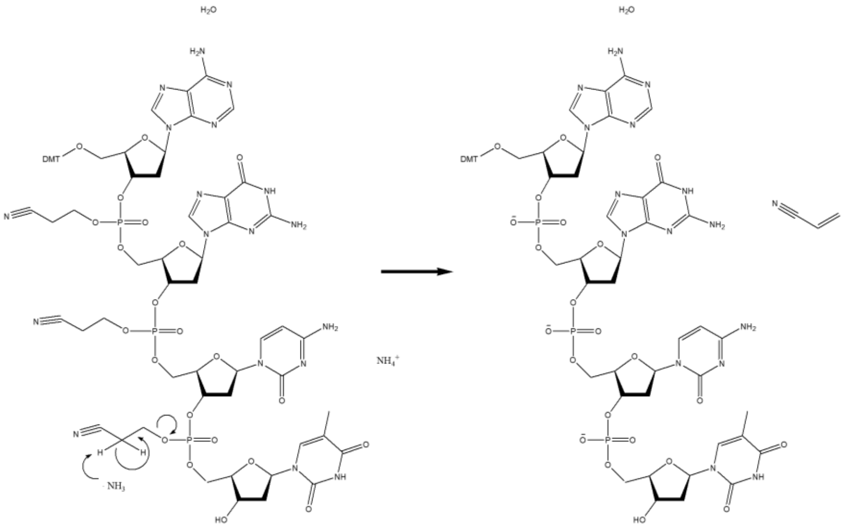

Figure 6.8. – Deprotection step (#2). During deprotection, the β-cyanoethyl group is also removed from the phosphate.

6.5 Script for fitting kinetic data in MATLAB

1) Model function. This function contains the differential equations of the Michaelis-Menten enzymatic kinetics.

```matlab
function [Tim,ES2] = Model(Eo,Csub,tdil,kcat,Km,Fmax,Fprod)
%Open the Data. Here the data was named Conc100uM1.
load('Conc100uM1')
tdata=Conc100uM1(:,1);
ydata=Conc100uM1(:,2);
%Initial values and time definition
dt = 0.1; %Intervals of 0.1 sec
time = 0:dt:300; %300sec = time of the reaction. Need to be adjusted to the data.
Etot(1,1) = Eo;
S(1,1) = 0;
P(1,1) = 0;
T(1,1) = 0;
ES(1,1) = 0;
%Calculate the Baseline, average of the fluorescence for the first 60 sec (< 63 sec).
ooo = 1:(length(tdata));
logic = tdata(ooo) < 63;
L=length(nonzeros(logic));
Baseline = mean(ydata(1:L));
%We found that it takes about 2 s (tdil) for the substrate to dilute evenly inside the cuvette.
Ratedil=1./tdil;
%Loop calculation of the Michaelis-Menten differential equation.
for o = 1:(length(time)-1)
   if o*dt <= tdil
      Rl = Ratedil;
   else
      Rl = 0;
   end
   %Rate
   dSdt(o,1) = -Eo.*((kcat.*S(o,1)))./(Km*(1+P(o,1)./48.38) + S(o,1)) + Rl.*Csub;
   S(o+1,1) = dSdt(o,1).*dt + S(o,1);
   dPdt(o,1) = Eo.*((kcat.*S(o,1)))./(Km*(1+P(o,1)./48.38) + S(o,1));
   P(o+1,1) = dPdt(o,1).*dt + P(o,1);
   ES(o,1) = Eo.*S(o,1)./(Km*(1+P(o,1)./48.38) + S(o,1));
   Tim(o,1) = time(1,o);
   Prod = P(2:end);
end
% Transforming the ES curve from the Michaelis-Menten into a fluorescence signal.
% From 0 to 60 sec Fluo = Baseline
% From 60 sec to the end Fluo = Baseline + Fmax * [ES] + [P]*Fprod where Fmax is the maximal fluorescent of the nanoantenna when bound to the ES complex, and Fprod is the fluorescence impact of the product on the nanoantenna
for oo = 1:(length(Tim))
logic2 = Tim <= 63;
L2=length(nonzeros(logic2));
   if Tim(oo) <= 63
      ES2(oo) = Baseline;
   else
      ES2(oo) = Baseline+Fmax.*ES(oo-L2)+Prod(oo-L2).*Fprod;
   end
```

```
end
```

2) tofit function. This function calculates the Michaelis-Menten curves for specific values of k_{cat}, K_M, F_{max} and F_{prod} defined by the vector k.

```
function ypred = tofit(k,tdata)
Eo=0.1;% The concentration of enzyme in µM.
tdil=2;% The dilution time of the substrate in s.
Csub=100;% Concentration of substrate in µM.
kcat=k(1); % kcat.
Km=k(2); % KM.
Fmax=k(3); % Maximal fluorescence of the spike.
Fprod=k(4);% Fluorescence impact of the product in a.u./µM.
[t,y] = Model(Eo,Csub,tdil,kcat,Km,Fmax,Fprod);
%% find predicted values y(tdata)
ypred = interp1(t,y,tdata);
end
```

3) Workplace. Using the tofit function, this script performs a nonlinear curve-fitting to find the best values for k_{cat}, K_M, F_{max} and F_{prod}.

```
%% Loading Data
load('Conc100uM1')
tdata=Conc100uM1(:,1); % x-axis data
ydata=Conc100uM1(:,2); % y-axis data
%% Solve nonlinear curve-fitting (data-fitting) problems in least-squares sense
lb = [1;0.1;200;-1];  %lower boundaries
ub = [100;100;500;1]; %upper boundaries
x0=0.5*[ub-lb]+lb;    %initial point (mid-point of boundaries)
% Nonlinear curve-fitting using the function lsqcurvefit
[x,resnorm,residual,exitflag,output,lambda,jacobian]=lsqcurvefit(@tofit,x0,tdata,ydata,lb,ub,optimset('Displ
ay','off'));
% Calculate the 95% confidence interval using the function nlparci
conf=nlparci(x,residual,'jacobian',jacobian,'alpha',0.05);
CI_low=conf(:,1); % Extract the CI lower limit
CI_upp=conf(:,2); % Extract the CI upper limit
Value=x; % Fittted value
CI=(CI_upp-CI_low)/2; % 95% confidence interval
%Create a vector containing all values and CIs.
Results=[Value(1),CI(1),Value(2),CI(2),Value(3),CI(3),Value(4),CI(4)]
```

References

1. Nelson, D.L., Lehninger, A.L. & Cox, M.M. Lehninger Principles of Biochemistry. 71-233 (W. H. Freeman, New York; 2008s).
2. Ambrogelly, A., Palioura, S. & Söll, D. Natural expansion of the genetic code. *Nat. Chem. Biol.* **3**, 29-35 (2007).
3. Turcotte, S. et al. Azasulfurylpeptide Modulation of CD36-Mediated Inflammation Without Effect on Neovascularization. *Biomedicines* **6**, 98 (2018).
4. Danelius, E. et al. Dynamic Chirality in the Mechanism of Action of Allosteric CD36 Modulators of Macrophage-Driven Inflammation. *J. Med. Chem.* **62**, 11071-11079 (2019).
5. Kim, E.E. & Wyckoff, H.W. Reaction mechanism of alkaline phosphatase based on crystal structures: Two-metal ion catalysis. *J. Mol. Biol.* **218**, 449-464 (1991).
6. Nyblom, M. et al. Crystal Structure of Na+, K+-ATPase in the Na+-Bound State. *Science* **342**, 123-127 (2013).
7. Harrington, W.F. & Rodgers, M.E. MYOSIN. *Annu. Rev. Biochem.* **53**, 35-73 (1984).
8. Schnell, J.D. & Hicke, L. Non-traditional functions of ubiquitin and ubiquitin-binding proteins. *J. Biol. Chem.* **278**, 35857-35860 (2003).
9. Wang, C. et al. A human monoclonal antibody blocking SARS-CoV-2 infection. *Nat. Commun.* **11**, 2251 (2020).
10. Millán, J.L. Mammalian Alkaline Phosphatases: From Biology to Applications in Medicine and Biotechnology. (John Wiley & Sons, 2006s).
11. Vogt, A.D. & Di Cera, E. Conformational Selection or Induced Fit? A Critical Appraisal of the Kinetic Mechanism. *Biochemistry* **51**, 5894-5902 (2012).
12. Gregorio, G.G. et al. Single-molecule analysis of ligand efficacy in β2AR–G-protein activation. *Nature* **547**, 68 (2017).
13. Soucy, T.A. et al. An inhibitor of NEDD8-activating enzyme as a new approach to treat cancer. *Nature* **458**, 732-736 (2009).
14. Fairhead, M. & Thöny-Meyer, L. Bacterial tyrosinases: old enzymes with new relevance to biotechnology. *New Biotechnol.* **29**, 183-191 (2012).
15. Ma, X., Hortelão, A.C., Patiño, T. & Sánchez, S. Enzyme Catalysis To Power Micro/Nanomachines. *ACS Nano* **10**, 9111-9122 (2016).
16. Robinson, P.K. Enzymes: principles and biotechnological applications. *Essays Biochem.* **59**, 1-41 (2015).
17. Richard, J.P. Protein Flexibility and Stiffness Enable Efficient Enzymatic Catalysis. *J. Am. Chem. Soc.* **141**, 3320-3331 (2019).
18. Andrews, L.D., Fenn, T.D. & Herschlag, D. Ground State Destabilization by Anionic Nucleophiles Contributes to the Activity of Phosphoryl Transfer Enzymes. *PLOS Biol.* **11**, e1001599 (2013).
19. Aledo, J.C., Lobo, C. & del Valle, A.E. Energy diagrams for enzyme-catalyzed reactions: Concepts and misconcepts. *Biochem. Mol. Biol. Educ.* **31**, 234-236 (2003).
20. Menten, L. & Michaelis, M. Die kinetik der invertinwirkung. *Biochem. Z.* **49**, 5 (1913).

21. Johnson, K.A. & Goody, R.S. The Original Michaelis Constant: Translation of the 1913 Michaelis–Menten Paper. *Biochemistry* **50**, 8264-8269 (2011).
22. Prjibelski, A.D., Korobeynikov, A.I. & Lapidus, A.L. in Encyclopedia of Bioinformatics and Computational Biology. (eds. S. Ranganathan, M. Gribskov, K. Nakai & C. Schönbach) 292-322 (Academic Press, Oxford; 2019).
23. Manz, A., Dittrich, P.S., Pamme, N. & Iossifidis, D. Bioanalytical Chemistry, Edn. Second Edition. 117-141, 203-223 (Imperial College Press, London; 2015s).
24. Callahan, N., Tullman, J., Kelman, Z. & Marino, J. Strategies for Development of a Next-Generation Protein Sequencing Platform. *Trends Biochem. Sci.* **45**, 76-89 (2020).
25. Shi, Y. A Glimpse of Structural Biology through X-Ray Crystallography. *Cell* **159**, 995-1014 (2014).
26. Shen, Y. et al. Consistent blind protein structure generation from NMR chemical shift data. *Proc. Natl. Acad. Sci. U.S.A.* **105**, 4685-4690 (2008).
27. Cheng, Y., Grigorieff, N., Penczek, Pawel A. & Walz, T. A Primer to Single-Particle Cryo-Electron Microscopy. *Cell* **161**, 438-449 (2015).
28. Ferreira, L.G., Dos Santos, R.N., Oliva, G. & Andricopulo, A.D. Molecular docking and structure-based drug design strategies. *Molecules* **20**, 13384-13421 (2015).
29. Lindahl, E.R. in Molecular Modeling of Proteins. (ed. A. Kukol) 3-23 (Humana Press, Totowa, NJ; 2008).
30. Rajagopala, S.V. et al. The binary protein-protein interaction landscape of Escherichia coli. *Nat. Biotechnol.* **32**, 285-290 (2014).
31. Pavia, D.L., Lampman, G.M., Kriz, G.S. & Vyvyan, J.R. Introduction to Spectroscopy. 381-417 (Brooks/Cole, Cengage Learning, Belmont, CA; 2009s).
32. Skoog, D.A., West, D.M., Crouch, S.R. & Holler, F.J. Fundamentals of Analytical Chemistry. 784-838 (Thomson-Brooks/Cole, Belmont, CA; 2004s).
33. Zhou, F. et al. Sensitive sandwich ELISA based on a gold nanoparticle layer for cancer detection. *Analyst* **137**, 1779-1784 (2012).
34. Bessey, O.A., Lowry, O.H. & Brock, M.J. A method for the rapid determination of alkaline phosphatase with five cubic millimeters of serum. *J. Biol. Chem.* **164**, 321-329 (1946).
35. Hötzer, B., Medintz, I.L. & Hildebrandt, N. Fluorescence in Nanobiotechnology: Sophisticated Fluorophores for Novel Applications. *Small* **8**, 2297-2326 (2012).
36. Lévesque, É. et al. General C–H Arylation Strategy for the Synthesis of Tunable Visible Light-Emitting Benzo[a]imidazo[2,1,5-c,d]indolizine Fluorophores. *J. Org. Chem.* **82**, 5046-5067 (2017).
37. Fernley, H. & Walker, P. Kinetic behaviour of calf-intestinal alkaline phosphatase with 4-methylumbelliferyl phosphate. *Biochem. J.* **97**, 95-103 (1965).
38. Briciu-Burghina, C., Heery, B. & Regan, F. Continuous fluorometric method for measuring β-glucuronidase activity: comparative analysis of three fluorogenic substrates. *Analyst* **140**, 5953-5964 (2015).
39. Leight, J.L., Alge, D.L., Maier, A.J. & Anseth, K.S. Direct measurement of matrix metalloproteinase activity in 3D cellular microenvironments using a fluorogenic peptide substrate. *Biomaterials* **34**, 7344-7352 (2013).
40. Toutchkine, A., Kraynov, V. & Hahn, K. Solvent-Sensitive Dyes to Report Protein Conformational Changes in Living Cells. *J. Am. Chem. Soc.* **125**, 4132-4145 (2003).

41. Anai, T., Nakata, E., Koshi, Y., Ojida, A. & Hamachi, I. Design of a Hybrid Biosensor for Enhanced Phosphopeptide Recognition Based on a Phosphoprotein Binding Domain Coupled with a Fluorescent Chemosensor. *J. Am. Chem. Soc.* **129**, 6232-6239 (2007).
42. Strunk, J.J. et al. Probing Protein Conformations by in Situ Non-Covalent Fluorescence Labeling. *Bioconjugate Chem.* **20**, 41-46 (2009).
43. Luitz, M.P. et al. Covalent dye attachment influences the dynamics and conformational properties of flexible peptides. *PLOS ONE* **12**, e0177139 (2017).
44. Au, H.-W., Tsang, M.-W., So, P.-K., Wong, K.-Y. & Leung, Y.-C. Thermostable β-Lactamase Mutant with Its Active Site Conjugated with Fluorescein for Efficient β-Lactam Antibiotic Detection. *ACS Omega* **4**, 20493-20502 (2019).
45. Lerner, E. et al. Toward dynamic structural biology: Two decades of single-molecule Förster resonance energy transfer. *Science* **359**, eaan1133 (2018).
46. Obeng, E.M., Dullah, E.C., Danquah, M.K., Budiman, C. & Ongkudon, C.M. FRET spectroscopy—towards effective biomolecular probing. *Anal. Methods* **8**, 5323-5337 (2016).
47. Dittrich, P.S., Müller, B. & Schwille, P. Studying reaction kinetics by simultaneous FRET and cross-correlation analysis in a miniaturized continuous flow reactor. *Phys. Chem. Chem. Phys.* **6**, 4416-4420 (2004).
48. Comstock, M.J. et al. Direct observation of structure-function relationship in a nucleic acid–processing enzyme. *Science* **348**, 352-354 (2015).
49. Diez, M. et al. Proton-powered subunit rotation in single membrane-bound F0F1-ATP synthase. *Nat. Struct. Mol. Biol.* **11**, 135-141 (2004).
50. Zhang, Z., Rajagopalan, P.T.R., Selzer, T., Benkovic, S.J. & Hammes, G.G. Single-molecule and transient kinetics investigation of the interaction of dihydrofolate reductase with NADPH and dihydrofolate. *Proc. Natl. Acad. Sci. U.S.A.* **101**, 2764-2769 (2004).
51. Antikainen, N.M., Smiley, R.D., Benkovic, S.J. & Hammes, G.G. Conformation Coupled Enzyme Catalysis: Single-Molecule and Transient Kinetics Investigation of Dihydrofolate Reductase. *Biochemistry* **44**, 16835-16843 (2005).
52. Wang, Y. & Lu, H.P. Bunching Effect in Single-Molecule T4 Lysozyme Nonequilibrium Conformational Dynamics under Enzymatic Reactions. *J. Phys. Chem. B* **114**, 6669-6674 (2010).
53. Devost, D. et al. Conformational Profiling of the AT1 Angiotensin II Receptor Reflects Biased Agonism, G Protein Coupling, and Cellular Context. *J. Biol. Chem.* **292**, 5443-5456 (2017).
54. Bourque, K. et al. Distinct Conformational Dynamics of Three G Protein-Coupled Receptors Measured Using FlAsH-BRET Biosensors. *Front. Endocrinol.* **8** (2017).
55. Vallée-Bélisle, A. & Michnick, S.W. Visualizing transient protein-folding intermediates by tryptophan-scanning mutagenesis. *Nat. Struct. Mol. Biol.* **19**, 731 (2012).
56. Mordente, A. et al. Mixed function oxidation and enzymes: Kinetic and structural properties of an oxidatively modified alkaline phosphatase. *Arch. Biochem. Biophys.* **264**, 502-509 (1988).
57. Deetanya, P. et al. Interaction of 8-anilinonaphthalene-1-sulfonate with SARS-CoV-2 main protease and its application as a fluorescent probe for inhibitor identification. *Comput. Struct. Biotechnol. J.* **19**, 3364-3371 (2021).

58. Kovermann, M., Rogne, P. & Wolf-Watz, M. Protein dynamics and function from solution state NMR spectroscopy. *Q. Rev. Biophys.* **49**, e6 (2016).
59. Lisi, G.P. & Patrick Loria, J. Using NMR spectroscopy to elucidate the role of molecular motions in enzyme function. *Prog. Nucl. Magn. Reson. Spectrosc.* **92-93**, 1-17 (2016).
60. Jiang, Y. & Kalodimos, C.G. NMR Studies of Large Proteins. *J. Mol. Biol.* **429**, 2667-2676 (2017).
61. Eisenmesser, E.Z., Bosco, D.A., Akke, M. & Kern, D. Enzyme Dynamics During Catalysis. *Science* **295**, 1520-1523 (2002).
62. Ullrich, S.J., Hellmich, U.A., Ullrich, S. & Glaubitz, C. Interfacial enzyme kinetics of a membrane bound kinase analyzed by real-time MAS-NMR. *Nat. Chem. Biol.* **7**, 263-270 (2011).
63. Her, C., Alonzo, A.P., Vang, J.Y., Torres, E. & Krishnan, V.V. Real-Time Enzyme Kinetics by Quantitative NMR Spectroscopy and Determination of the Michaelis–Menten Constant Using the Lambert-W Function. *J. Chem. Educ.* **92**, 1943-1948 (2015).
64. Kern, D., Eisenmesser, E.Z. & Wolf-Watz, M. Enzyme Dynamics During Catalysis Measured by NMR Spectroscopy. *Methods Enzymol.* **394**, 507-524 (2005).
65. Baldwin, A.J. & Kay, L.E. NMR spectroscopy brings invisible protein states into focus. *Nat. Chem. Biol.* **5**, 808-814 (2009).
66. Corazza, A. et al. Native-unlike Long-lived Intermediates along the Folding Pathway of the Amyloidogenic Protein β2-Microglobulin Revealed by Real-time Two-dimensional NMR. *J. Biol. Chem.* **285**, 5827-5835 (2010).
67. Haupt, C. et al. Transient Enzyme–Substrate Recognition Monitored by Real-Time NMR. *J. Am. Chem. Soc.* **133**, 11154-11162 (2011).
68. Irague, R. et al. NMR-Based Structural Glycomics for High-Throughput Screening of Carbohydrate-Active Enzyme Specificity. *Anal. Chem.* **83**, 1202-1206 (2011).
69. Coleman, J.E. Structure and mechanism of alkaline phosphatase. *Annu. Rev. Biophys. Biomol. Struct.* **21**, 441-483 (1992).
70. Tanaka, K., Kitamura, N. & Chujo, Y. Bimodal Quantitative Monitoring for Enzymatic Activity with Simultaneous Signal Increases in 19F NMR and Fluorescence Using Silica Nanoparticle-Based Molecular Probes. *Bioconjugate Chem.* **22**, 1484-1490 (2011).
71. Klare, J.P. Site-directed spin labeling EPR spectroscopy in protein research. *Biol. Chem.* **394**, 1281-1300 (2013).
72. Heidarsson, P.O., Sigurdsson, S.T. & Ásgeirsson, B. Structural features and dynamics of a cold-adapted alkaline phosphatase studied by EPR spectroscopy. *FEBS J.* **276**, 2725-2735 (2009).
73. Sanzhaeva, U. et al. Imaging of Enzyme Activity by Electron Paramagnetic Resonance: Concept and Experiment Using a Paramagnetic Substrate of Alkaline Phosphatase. *Angew. Chem. Int. Ed.* **57**, 11701-11705 (2018).
74. Kelly, S.M., Jess, T.J. & Price, N.C. How to study proteins by circular dichroism. *Biochim. Biophys. Acta Proteins Proteom.* **1751**, 119-139 (2005).
75. Rogers, D.M. et al. Electronic Circular Dichroism Spectroscopy of Proteins. *Chem* **5**, 2751-2774 (2019).

76. Boulanger, R.R. & Kantrowitz, E.R. Characterization of a monomeric Escherichia coli alkaline phosphatase formed upon a single amino acid substitution. *J. Biol. Chem.* **278**, 23497-23501 (2003).
77. Schweitzer-Stenner, R. Advances in vibrational spectroscopy as a sensitive probe of peptide and protein structure: A critical review. *Vib. Spectrosc.* **42**, 98-117 (2006).
78. Bortolato, M., Besson, F. & Roux, B. Role of metal ions on the secondary and quaternary structure of alkaline phosphatase from bovine intestinal mucosa. *Proteins* **37**, 310-318 (1999).
79. Fabian, H. & Mäntele, W. in Handbook of Vibrational Spectroscopy. (eds. J.M. Chalmers & P.R. Griffiths) 3999-3425 (John Wiley & Sons, 2006).
80. Ma, J., Pazos, I.M., Zhang, W., Culik, R.M. & Gai, F. Site-Specific Infrared Probes of Proteins. *Annu. Rev. Phys. Chem.* **66**, 357-377 (2015).
81. Barth, A. & Zscherp, C. Substrate binding and enzyme function investigated by infrared spectroscopy. *FEBS Lett.* **477**, 151-156 (2000).
82. Zhang, L., Buchet, R. & Azzar, G. Phosphate Binding in the Active Site of Alkaline Phosphatase and the Interactions of 2-Nitrosoacetophenone with Alkaline Phosphatase-Induced Small Structural Changes. *Biophys. J.* **86**, 3873-3881 (2004).
83. Rygula, A. et al. Raman spectroscopy of proteins: a review. *J. Raman Spectrosc.* **44**, 1061-1076 (2013).
84. Sun, D., Xu, W. & Xu, S. Ultrasensitive Raman sensing of alkaline phosphatase activity in serum based on an enzyme-catalyzed reaction. *Anal. Methods* **11**, 3501-3505 (2019).
85. Ruan, C., Wang, W. & Gu, B. Detection of Alkaline Phosphatase Using Surface-Enhanced Raman Spectroscopy. *Anal. Chem.* **78**, 3379-3384 (2006).
86. Sun, D., Xu, W., Liang, C., Shi, W. & Xu, S. A Smart Surface-Enhanced Resonance Raman Scattering Nanoprobe for Monitoring Cellular Alkaline Phosphatase Activity during Osteogenic Differentiation. *ACS Sens.* (2020).
87. Chen, C. et al. Recent advances in electrochemical glucose biosensors: a review. *RSC Adv.* **3**, 4473-4491 (2013).
88. Choi, Y. et al. Single-Molecule Lysozyme Dynamics Monitored by an Electronic Circuit. *Science* **335**, 319-324 (2012).
89. Chiku, M., Nakamura, J., Fujishima, A. & Einaga, Y. Conformational Change Detection in Nonmetal Proteins by Direct Electrochemical Oxidation Using Diamond Electrodes. *Anal. Chem.* **80**, 5783-5787 (2008).
90. Fernandes, I.P.G. & Oliveira-Brett, A.M. Calcium-induced calmodulin conformational change. Electrochemical evaluation. *Bioelectrochemistry* **113**, 69-78 (2017).
91. Gyurcsányi, R.E., Bereczki, A., Nagy, G., Neuman, M.R. & Lindner, E. Amperometric microcells for alkaline phosphatase assay. *Analyst* **127**, 235-240 (2002).
92. Szydłowska, D., Campàs, M., Marty, J.-L. & Trojanowicz, M. Catechol monophosphate as a new substrate for screen-printed amperometric biosensors with immobilized phosphatases. *Sens. Actuators B Chem.* **113**, 787-796 (2006).
93. Goggins, S., Naz, C., Marsh, B.J. & Frost, C.G. Ratiometric electrochemical detection of alkaline phosphatase. *Chem. Commun.* **51**, 561-564 (2015).

94. Ciana, L.D., Bernacca, G., Bordin, F., Fenu, S. & Garetto, F. Highly sensitive amperometric measurement of alkaline phosphatase activity with glucose oxidase amplification. *J. Electroanal. Chem.* **382**, 129-135 (1995).
95. Serra, B., Morales, M.D., Reviejo, A.J., Hall, E.H. & Pingarrón, J.M. Rapid and highly sensitive electrochemical determination of alkaline phosphatase using a composite tyrosinase biosensor. *Anal. Biochem.* **336**, 289-294 (2005).
96. Saboury, A.A. A review on the ligand binding studies by isothermal titration calorimetry. *J. Iran. Chem. Soc.* **3**, 1-21 (2006).
97. Wang, Y., Wang, G., Moitessier, N. & Mittermaier, A.K. Enzyme Kinetics by Isothermal Titration Calorimetry: Allostery, Inhibition, and Dynamics. *Front. Mol. Biosci.* **7** (2020).
98. Todd, M.J. & Gomez, J. Enzyme Kinetics Determined Using Calorimetry: A General Assay for Enzyme Activity? *Anal. Biochem.* **296**, 179-187 (2001).
99. Transtrum, M.K., Hansen, L.D. & Quinn, C. Enzyme kinetics determined by single-injection isothermal titration calorimetry. *Methods* **76**, 194-200 (2015).
100. Honarmand Ebrahimi, K., Hagedoorn, P.-L., Jacobs, D. & Hagen, W.R. Accurate label-free reaction kinetics determination using initial rate heat measurements. *Sci. Rep.* **5**, 16380 (2015).
101. van Schie, M.M.C.H., Ebrahimi, K.H., Hagen, W.R. & Hagedoorn, P.-L. Fast and accurate enzyme activity measurements using a chip-based microfluidic calorimeter. *Anal. Biochem.* **544**, 57-63 (2018).
102. Di Trani, J.M., Moitessier, N. & Mittermaier, A.K. Measuring Rapid Time-Scale Reaction Kinetics Using Isothermal Titration Calorimetry. *Anal. Chem.* **89**, 7022-7030 (2017).
103. Di Trani, J.M., Moitessier, N. & Mittermaier, A.K. Complete Kinetic Characterization of Enzyme Inhibition in a Single Isothermal Titration Calorimetric Experiment. *Anal. Chem.* **90**, 8430-8435 (2018).
104. Di Trani, J.M. et al. Rapid measurement of inhibitor binding kinetics by isothermal titration calorimetry. *Nat. Commun.* **9**, 893 (2018).
105. Chen, J. et al. Real-Time Fluorescence Turn-On Detection of Alkaline Phosphatase Activity with a Novel Perylene Probe. *Chem. Asian J.* **8**, 276-281 (2013).
106. Baykov, A.A., Evtushenko, O.A. & Avaeva, S.M. A malachite green procedure for orthophosphate determination and its use in alkaline phosphatase-based enzyme immunoassay. *Anal. Biochem.* **171**, 266-270 (1988).
107. Holtz, K.M., Stec, B. & Kantrowitz, E.R. A Model of the Transition State in the Alkaline Phosphatase Reaction. *J. Biol. Chem.* **274**, 8351-8354 (1999).
108. Stec, B., Holtz, K.M. & Kantrowitz, E.R. A revised mechanism for the alkaline phosphatase reaction involving three metal ions. *J. Mol. Biol.* **299**, 1303-1311 (2000).
109. Le Du, M.H., Stigbrand, T., Taussig, M.J., Ménez, A. & Stura, E.A. Crystal Structure of Alkaline Phosphatase from Human Placenta at 1.8 Å Resolution: IMPLICATION FOR A SUBSTRATE SPECIFICITY. *J. Biol. Chem.* **276**, 9158-9165 (2001).
110. de Backer, M. et al. The 1.9Å Crystal Structure of Heat-labile Shrimp Alkaline Phosphatase. *J. Mol. Biol.* **318**, 1265-1274 (2002).
111. Ghosh, K. et al. Crystal structure of rat intestinal alkaline phosphatase – Role of crown domain in mammalian alkaline phosphatases. *J. Struct. Biol.* **184**, 182-192 (2013).

112. Ásgeirsson, B., Markússon, S., Hlynsdóttir, S.S., Helland, R. & Hjörleifsson, J.G. X-ray crystal structure of Vibrio alkaline phosphatase with the non-competitive inhibitor cyclohexylamine. *Biochem. Biophys. Rep.* **24**, 100830 (2020).
113. Wende, A. et al. Structural and Biochemical Characterization of a Halophilic Archaeal Alkaline Phosphatase. *J. Mol. Biol.* **400**, 52-62 (2010).
114. Peck, A., Sunden, F., Andrews, L.D., Pande, V.S. & Herschlag, D. Tungstate as a Transition State Analog for Catalysis by Alkaline Phosphatase. *J. Mol. Biol.* **428**, 2758-2768 (2016).
115. Ames, B.N. [10] Assay of inorganic phosphate, total phosphate and phosphatases. *Methods Enzymol.* **8**, 115-118 (1966).
116. Tenboer, J. et al. Time-resolved serial crystallography captures high-resolution intermediates of photoactive yellow protein. *Science* **346**, 1242-1246 (2014).
117. Lobb, R.R. & Auld, D.S. Determination of enzyme mechanisms by radiationless energy transfer kinetics. *Proc. Natl. Acad. Sci. U.S.A.* **76**, 2684-2688 (1979).
118. Pisoni, D.S. et al. Symmetrical and Asymmetrical Cyanine Dyes. Synthesis, Spectral Properties, and BSA Association Study. *J. Org. Chem.* **79**, 5511-5520 (2014).
119. Abou-Zied, O.K. & Sulaiman, S.A.J. Site-specific recognition of fluorescein by human serum albumin: A steady-state and time-resolved spectroscopic study. *Dyes Pigm.* **110**, 89-96 (2014).
120. Buranda, T. et al. Ligand Receptor Dynamics at Streptavidin-Coated Particle Surfaces: A Flow Cytometric and Spectrofluorimetric Study. *J. Phys. Chem. B* **103**, 3399-3410 (1999).
121. Kada, G., Falk, H. & Gruber, H.J. Accurate measurement of avidin and streptavidin in crude biofluids with a new, optimized biotin–fluorescein conjugate. *Biochim. Biophys. Acta* **1427**, 33-43 (1999).
122. Wu, Y., Simons, P.C., Lopez, G.P., Sklar, L.A. & Buranda, T. Dynamics of fluorescence dequenching of ostrich-quenched fluorescein biotin: A multifunctional quantitative assay for biotin. *Anal. Biochem.* **342**, 221-228 (2005).
123. Neish, C.S., Martin, I.L., Henderson, R.M. & Edwardson, J.M. Direct visualization of ligand-protein interactions using atomic force microscopy. *Br. J. Pharmacol.* **135**, 1943-1950 (2002).
124. Siller, A.F. & Whyte, M.P. Alkaline Phosphatase: Discovery and Naming of Our Favorite Enzyme. *J. Bone Miner. Res.* **33**, 362-364 (2018).
125. Riedel, C. et al. The heat released during catalytic turnover enhances the diffusion of an enzyme. *Nature* **517**, 227-230 (2015).
126. Millán, J.L. Alkaline Phosphatases. *Purinergic Signal.* **2**, 335 (2006).
127. Holtz, K.M. & Kantrowitz, E.R. The mechanism of the alkaline phosphatase reaction: insights from NMR, crystallography and site-specific mutagenesis. *FEBS Lett.* **462**, 7-11 (1999).
128. Fawley, J. & Gourlay, D.M. Intestinal alkaline phosphatase: a summary of its role in clinical disease. *J. Surg. Res.* **202**, 225-234 (2016).
129. Sharma, U., Pal, D. & Prasad, R. Alkaline Phosphatase: An Overview. *Ind. J. Clin. Biochem.* **29**, 269-278 (2014).
130. Le Du, M.-H. & Millán, J.L. Structural evidence of functional divergence in human alkaline phosphatases. *J. Biol. Chem.* **277**, 49808-49814 (2002).

131. Rader, B.A. Alkaline Phosphatase, an Unconventional Immune Protein. *Front. Immunol.* **8**, 897 (2017).
132. Orimo, H. The mechanism of mineralization and the role of alkaline phosphatase in health and disease. *J. Nippon Med. Sch.* **77**, 4-12 (2010).
133. Golub, E.E. & Boesze-Battaglia, K. The role of alkaline phosphatase in mineralization. *Curr. Opin. Orthop.* **18** (2007).
134. Vaishnava, S. & Hooper, L.V. Alkaline Phosphatase: Keeping the Peace at the Gut Epithelial Surface. *Cell Host Microbe* **2**, 365-367 (2007).
135. Bates, J.M., Akerlund, J., Mittge, E. & Guillemin, K. Intestinal Alkaline Phosphatase Detoxifies Lipopolysaccharide and Prevents Inflammation in Zebrafish in Response to the Gut Microbiota. *Cell Host Microbe* **2**, 371-382 (2007).
136. Poelstra, K. et al. Dephosphorylation of endotoxin by alkaline phosphatase in vivo. *Am. J. Pathol.* **151**, 1163 (1997).
137. Bentala, H. et al. Removal of Phosphate from Lipid A as a Strategy to Detoxify Lipopolysaccharide. *Shock* **18** (2002).
138. Goldberg, R.F. et al. Intestinal alkaline phosphatase is a gut mucosal defense factor maintained by enteral nutrition. *Proc. Natl. Acad. Sci. U.S.A.* **105**, 3551-3556 (2008).
139. Liu, W. et al. Intestinal Alkaline Phosphatase Regulates Tight Junction Protein Levels. *J. Am. Coll. Surg.* **222**, 1009-1017 (2016).
140. Singh, S.B., Carroll-Portillo, A., Coffman, C., Ritz, N.L. & Lin, H.C. Intestinal Alkaline Phosphatase Exerts Anti-Inflammatory Effects Against Lipopolysaccharide by Inducing Autophagy. *Sci. Rep.* **10**, 3107 (2020).
141. Moss, A.K. et al. Intestinal alkaline phosphatase inhibits the proinflammatory nucleotide uridine diphosphate. *Am. J. Physiol. Gastrointest. Liver Physiol.* **304**, G597-G604 (2013).
142. Akiba, Y., Mizumori, M., Guth, P.H., Engel, E. & Kaunitz, J.D. Duodenal brush border intestinal alkaline phosphatase activity affects bicarbonate secretion in rats. *Am. J. Physiol. Gastrointest. Liver Physiol.* **293**, G1223-G1233 (2007).
143. Mizumori, M. et al. Intestinal alkaline phosphatase regulates protective surface microclimate pH in rat duodenum. *J. Physiol.* **587**, 3651-3663 (2009).
144. Kaunitz, J.D. & Akiba, Y. Purinergic regulation of duodenal surface pH and ATP concentration: implications for mucosal defence, lipid uptake and cystic fibrosis. *Acta Physiol.* **201**, 109-116 (2011).
145. Malo, M.S. et al. Intestinal alkaline phosphatase preserves the normal homeostasis of gut microbiota. *Gut* **59**, 1476-1484 (2010).
146. Malo, M.S. et al. Intestinal alkaline phosphatase promotes gut bacterial growth by reducing the concentration of luminal nucleotide triphosphates. *Am. J. Physiol. Gastrointest. Liver Physiol.* **306**, G826-G838 (2014).
147. Lallès, J.-P. Luminal ATP: the missing link between intestinal alkaline phosphatase, the gut microbiota, and inflammation? *Am. J. Physiol. Gastrointest. Liver Physiol.* **306**, G824-G825 (2014).
148. Meštrović, V. & Pavela-Vrančič, M. Inhibition of alkaline phosphatase activity by okadaic acid, a protein phosphatase inhibitor. *Biochimie* **85**, 647-650 (2003).
149. Sarrouilhe, D., Lalégerie, P. & Baudry, M. Endogenous phosphorylation and dephosphorylation of rat liver plasma membrane proteins, suggesting a 18 kDa

phosphoprotein as a potential substrate for alkaline phosphatase. *Biochim. Biophys. Acta, Protein Struct. Mol. Enzymol.* **1118**, 116-122 (1992).
150. Waymire, K.G. et al. Mice lacking tissue non–specific alkaline phosphatase die from seizures due to defective metabolism of vitamin B–6. *Nat. Genet.* **11**, 45-51 (1995).
151. Whyte, M.P. et al. Alkaline phosphatase: placental and tissue-nonspecific isoenzymes hydrolyze phosphoethanolamine, inorganic pyrophosphate, and pyridoxal 5'-phosphate. Substrate accumulation in carriers of hypophosphatasia corrects during pregnancy. *J. Clin. Investig.* **95**, 1440-1445 (1995).
152. Whyte, M.P. Hypophosphatasia and the Role of Alkaline Phosphatase in Skeletal Mineralization*. *Endocr. Rev.* **15**, 439-461 (1994).
153. Whyte, M.P. Physiological role of alkaline phosphatase explored in hypophosphatasia. *Ann. N. Y. Acad. Sci.* **1192**, 190-200 (2010).
154. Millán, J.L. & Whyte, M.P. Alkaline Phosphatase and Hypophosphatasia. *Calcif. Tissue Int.* **98**, 398-416 (2016).
155. Narisawa, S., Yadav, M.C. & Millán, J.L. In Vivo Overexpression of Tissue-Nonspecific Alkaline Phosphatase Increases Skeletal Mineralization and Affects the Phosphorylation Status of Osteopontin. *J. Bone Miner. Res.* **28**, 1587-1598 (2013).
156. Hui, M., Li, S.Q., Holmyard, D. & Cheng, P.T. Stable Transfection of Nonosteogenic Cell Lines with Tissue Nonspecific Alkaline Phosphatase Enhances Mineral Deposition Both in the Presence and Absence of β-Glycerophosphate: Possible Role for Alkaline Phosphatase in Pathological Mineralization. *Calcif. Tissue Int.* **60**, 467-472 (1997).
157. Sumikawa, K., Okochi, T. & Adachi, K. Differences in phosphatidate hydrolytic activity of human alkaline phosphatase isozymes. *Biochim. Biophys. Acta, Lipids Lipid Metab.* **1046**, 27-31 (1990).
158. Ezawa, T., Kuwahara, S.-y., Sakamoto, K., Yoshida, T. & Saito, M. Specific inhibitor and substrate specificity of alkaline phosphatase expressed in the symbiotic phase of the arbuscular mycorrhizal fungus, Glomus etunicatum. *Mycologia* **91**, 636-641 (1999).
159. Fernandez, M.P., Gascon, S. & Schwencke, J. Some enzymatic properties of vacuolar alkaline phosphatase from yeast. *Curr. Microbiol.* **6**, 121-126 (1981).
160. Kizawa, K., Aono, T. & Ohtomo, R. PHO8 gene coding alkaline phosphatase of Saccharomyces cerevisiae is involved in polyphosphate metabolism. *J. Gen. Appl. Microbiol.* **62**, 297-302 (2016).
161. Tuleva, B., Vasileva-Tonkova, E. & Galabova, D. A specific alkaline phosphatase from Saccharomyces cerevisiae with protein phosphatase activity. *FEMS Microbiol. Lett* **161**, 139-144 (1998).
162. Kuenzler, E.J. GLUCOSE-6-PHOSPHATE UTILIZATION BY MARINE ALGAE1. *J. Phycol.* **1**, 156-164 (1965).
163. Lin, X., Zhang, H., Huang, B. & Lin, S. Alkaline Phosphatase Gene Sequence And Transcriptional Regulation By Phosphate Limitation In Amphidinium Carterae (Dinophyceae). *J. Phycol.* **47**, 1110-1120 (2011).
164. Zhang, C., Luo, H., Huang, L. & Lin, S. Molecular mechanism of glucose-6-phosphate utilization in the dinoflagellate Karenia mikimotoi. *Harmful Algae* **67**, 74-84 (2017).

165. Xie, E., Su, Y., Deng, S., Kontopyrgou, M. & Zhang, D. Significant influence of phosphorus resources on the growth and alkaline phosphatase activities of Microcystis aeruginosa. *Environ. Pollut.* **268**, 115807 (2021).
166. Bilski, J. et al. The Role of Intestinal Alkaline Phosphatase in Inflammatory Disorders of Gastrointestinal Tract. *Mediators Inflamm.* **2017**, 9074601 (2017).
167. Lallès, J.-P. Recent advances in intestinal alkaline phosphatase, inflammation, and nutrition. *Nutr. Rev.* **77**, 710-724 (2019).
168. Yang, W.H. et al. Recurrent infection progressively disables host protection against intestinal inflammation. *Science* **358**, eaao5610 (2017).
169. Parlato, M. et al. Human ALPI deficiency causes inflammatory bowel disease and highlights a key mechanism of gut homeostasis. *EMBO Mol. Med.* **10**, e8483 (2018).
170. Kilby, K., Mathias, H., Boisvenue, L., Heisler, C. & Jones, J.L. Micronutrient Absorption and Related Outcomes in People with Inflammatory Bowel Disease: A Review. *Nutrients* **11**, 1388 (2019).
171. Yang, Y., Millán, J.L., Mecsas, J. & Guillemin, K. Intestinal Alkaline Phosphatase Deficiency Leads to Lipopolysaccharide Desensitization and Faster Weight Gain. *Infect. Immun.* **83**, 247-258 (2015).
172. Kaliannan, K. et al. Intestinal alkaline phosphatase prevents metabolic syndrome in mice. *Proc. Natl. Acad. Sci. U.S.A.* **110**, 7003-7008 (2013).
173. Malo, M.S. A High Level of Intestinal Alkaline Phosphatase Is Protective Against Type 2 Diabetes Mellitus Irrespective of Obesity. *EBioMedicine* **2**, 2016-2023 (2015).
174. Lassenius, M.I. et al. Intestinal alkaline phosphatase at the crossroad of intestinal health and disease – a putative role in type 1 diabetes. *J. Intern. Med.* **281**, 586-600 (2017).
175. Tsai, L.-C. et al. Expression and regulation of alkaline phosphatases in human breast cancer MCF-7 cells. *Eur. J. Biochem.* **267**, 1330-1339 (2000).
176. Guerreiro, S. et al. Distinct modulation of alkaline phosphatase isoenzymes by 17β-estradiol and xanthohumol in breast cancer MCF-7 cells. *Clin. Biochem.* **40**, 268-273 (2007).
177. Said, N.M. Three gold indicators for breast cancer prognosis: a case–control study with ROC analysis for novel ratios related to CBC with (ALP and LDH). *Mol. Biol. Rep.* **46**, 2013-2027 (2019).
178. Sharma, U., Pal, D., Singh, S.K., Kakkar, N. & Prasad, R. Reduced L/B/K alkaline phosphatase gene expression in renal cell carcinoma: Plausible role in tumorigenesis. *Biochimie* **104**, 27-35 (2014).
179. Ishisaki, A. Property of alkaline phosphatase of a human oral squamous cell carcinoma cell line. *Jpn. J. Oral. Biol.* **35**, 38-50 (1993).
180. Xiao, B. et al. Inhibition of growth and increase of alkaline phosphatase activity in cultured human oral cancer cells by all-trans retinoic acid. *Int. J. Oral Maxillofac. Surg.* **35**, 643-648 (2006).
181. Rao, S.R. et al. Tumour-derived alkaline phosphatase regulates tumour growth, epithelial plasticity and disease-free survival in metastatic prostate cancer. *Br. J. Cancer* **116**, 227-236 (2017).
182. Hung, H.-Y. et al. Preoperative alkaline phosphatase elevation was associated with poor survival in colorectal cancer patients. *Int. J. Colorectal Dis.* **32**, 1775-1778 (2017).

183. Saif, M.W., Alexander, D. & Wicox, C.M. Serum Alkaline Phosphatase Level as a Prognostic Tool in Colorectal Cancer: A Study of 105 patients. *J. Appl. Res.* **5**, 88-95 (2005).
184. Namikawa, T. et al. Prognostic significance of serum alkaline phosphatase and lactate dehydrogenase levels in patients with unresectable advanced gastric cancer. *Gastric Cancer* **22**, 684-691 (2019).
185. Usoro, N.I., Omabbe, M.C., Usoro, C.A. & Nsonwu, A. Calcium, inorganic phosphates, alkaline and acid phosphatase activities in breast cancer patients in Calabar, Nigeria. *Afr. Health Sci.* **10**, 9 (2010).
186. Li, S.-J. et al. Albumin-to-alkaline phosphatase ratio as a novel prognostic indicator for patients undergoing minimally invasive lung cancer surgery: Propensity score matching analysis using a prospective database. *Int. J. Surg.* **69**, 32-42 (2019).
187. Barseghyan, K., Gayer, C. & Azhibekov, T. Differences in Serum Alkaline Phosphatase Levels in Infants with Spontaneous Intestinal Perforation versus Necrotizing Enterocolitis with Perforation. *Neonatology* **117**, 349-357 (2020).
188. Park, J.-B. et al. Serum alkaline phosphatase is a predictor of mortality, myocardial infarction, or stent thrombosis after implantation of coronary drug-eluting stent. *Eur. Heart J.* **34**, 920-931 (2012).
189. Kabootari, M. et al. Serum alkaline phosphatase and the risk of coronary heart disease, stroke and all-cause mortality: Tehran Lipid and Glucose Study. *BMJ Open* **8**, e023735 (2018).
190. Sasaki, S. et al. A Role of Intestinal Alkaline Phosphatase 3 (Akp3) in Inorganic Phosphate Homeostasis. *Kidney Blood Press. Res.* **43**, 1409-1424 (2018).
191. Alvarenga, L., Cardozo, L.F.M.F., Lindholm, B., Stenvinkel, P. & Mafra, D. Intestinal alkaline phosphatase modulation by food components: predictive, preventive, and personalized strategies for novel treatment options in chronic kidney disease. *EPMA J.* **11**, 565-579 (2020).
192. To, K.K.-W. et al. Temporal profiles of viral load in posterior oropharyngeal saliva samples and serum antibody responses during infection by SARS-CoV-2: an observational cohort study. *Lancet Infect. Dis.* **20**, 565-574 (2020).
193. Ali, A.T., Paiker, J.E. & Crowther, N.J. The Relationship Between Anthropometry and Serum Concentrations of Alkaline Phosphatase Isoenzymes, Liver Enzymes, Albumin, and Bilirubin. *Am. J. Clin. Pathol.* **126**, 437-442 (2006).
194. Beumer, C. et al. Calf Intestinal Alkaline Phosphatase, a Novel Therapeutic Drug for Lipopolysaccharide (LPS)-Mediated Diseases, Attenuates LPS Toxicity in Mice and Piglets. *J. Pharmacol. Exp. Ther.* **307**, 737-744 (2003).
195. Wang, W. et al. Intestinal Alkaline Phosphatase Inhibits the Translocation of Bacteria of Gut-Origin in Mice with Peritonitis: Mechanism of Action. *PLOS ONE* **10**, e0124835 (2015).
196. Hamarneh, S.R. et al. Intestinal Alkaline Phosphatase Attenuates Alcohol-Induced Hepatosteatosis in Mice. *Dig. Dis. Sci.* **62**, 2021-2034 (2017).
197. Riggle, K.M. et al. Intestinal alkaline phosphatase prevents the systemic inflammatory response associated with necrotizing enterocolitis. *J. Surg, Res.* **180**, 21-26 (2013).
198. Yang, Y. et al. Ontogeny of alkaline phosphatase activity in infant intestines and breast milk. *BMC Pediatr.* **19**, 2 (2019).

199. Lallès, J.-P. Dairy products and the French paradox: Could alkaline phosphatases play a role? *Med. Hypotheses* **92**, 7-11 (2016).
200. Lukas, M. et al. Exogenous alkaline phosphatase for the treatment of patients with moderate to severe ulcerative colitis. *Inflamm. Bowel Dis.* **16**, 1180-1186 (2009).
201. Peters, E., Heemskerk, S., Masereeuw, R. & Pickkers, P. Alkaline Phosphatase: A Possible Treatment for Sepsis-Associated Acute Kidney Injury in Critically Ill Patients. *Am. J. Kidney Dis.* **63**, 1038-1048 (2014).
202. Peters, E. et al. Alkaline phosphatase protects against renal inflammation through dephosphorylation of lipopolysaccharide and adenosine triphosphate. *Br. J. Pharmacol.* **172**, 4932-4945 (2015).
203. Peters, E. et al. Study protocol for a multicentre randomised controlled trial: Safety, Tolerability, efficacy and quality of life Of a human recombinant alkaline Phosphatase in patients with sepsis-associated Acute Kidney Injury (STOP-AKI). *BMJ Open* **6**, e012371 (2016).
204. Genova, J. et al. A summary of feed additives, intestinal health and intestinal alkaline phosphatase in piglet nutrition. *Czech J. Anim. Sci.* **65**, 281-294 (2020).
205. Pfaff, A.R., Beltz, J., King, E. & Ercal, N. Medicinal thiols: current status and new perspectives. *Mini. Rev. Med. Chem.* **20**, 513-529 (2020).
206. King, M. et al. Use of Amifostine for Cytoprotection during Radiation Therapy: A Review. *Oncology* **98**, 61-80 (2020).
207. Kouvaris, J.R., Kouloulias, V.E. & Vlahos, L.J. Amifostine: the first selective-target and broad-spectrum radioprotector. *Oncologist* **12** (2007).
208. Giatromanolaki, A., Sivridis, E., Maltezos, E. & Koukourakis, M.I. Down-regulation of intestinal-type alkaline phosphatase in the tumor vasculature and stroma provides a strong basis for explaining amifostine selectivity. *Semin. Oncol.* **29**, 14-21 (2002).
209. Furfine, E.S. et al. Preclinical Pharmacology and Pharmacokinetics of GW433908, a Water-Soluble Prodrug of the Human Immunodeficiency Virus Protease Inhibitor Amprenavir. *Antimicrob. Agents Chemother.* **48**, 791-798 (2004).
210. Brouwers, J., Tack, J. & Augustijns, P. In vitro behavior of a phosphate ester prodrug of amprenavir in human intestinal fluids and in the Caco-2 system: Illustration of intraluminal supersaturation. *Int. J. Pharm.* **336**, 302-309 (2007).
211. Braeckmans, M. et al. The influence of gastric motility on the intraluminal behavior of fosamprenavir. *Eur. J. Pharm. Sci.* **142**, 105117 (2020).
212. Bowers, G.N., Jr., McComb, R.B., Christensen, R.G. & Schaffer, R. High-purity 4-nitrophenol: purification, characterization, and specifications for use as a spectrophotometric reference material. *Clin. Chem.* **26**, 724-729 (1980).
213. Lazdunski, M. & Ouellet, L. PHOSPHATASE ALCALINE INTESTINALE: CINÉTIQUE DE L'HYDROLYSE DU PHOSPHATE DE p-NITROPHÉNYLE. *Can. J. Chem.* **39**, 1298-1308 (1961).
214. Chaudhuri, G., Chatterjee, S., Venu-Babu, P., Ramasamy, K. & Thilagaraj, W.R. Kinetic behaviour of calf intestinal alkaline phosphatase with pNPP. *Indian J. Biochem. Biophys.* **50**, 64-71 (2013).
215. Sancenon, V. et al. Development, validation and quantitative assessment of an enzymatic assay suitable for small molecule screening and profiling: A case-study. *Biomol. Detect. Quantif.* **4**, 1-9 (2015).

216. Dean, R.L. Kinetic studies with alkaline phosphatase in the presence and absence of inhibitors and divalent cations. *Biochem. Mol. Biol. Educ.* **30**, 401-407 (2002).
217. Hjörleifsson, J.G. & Ásgeirsson, B. pH-Dependent Binding of Chloride to a Marine Alkaline Phosphatase Affects the Catalysis, Active Site Stability, and Dimer Equilibrium. *Biochemistry* **56**, 5075-5089 (2017).
218. Cherenok, S. et al. Calix[4]arene α-Aminophosphonic Acids: Asymmetric Synthesis and Enantioselective Inhibition of an Alkaline Phosphatase. *Org. Lett.* **8**, 549-552 (2006).
219. Gudjónsdóttir, K. & Ásgeirsson, B. Effects of replacing active site residues in a cold-active alkaline phosphatase with those found in its mesophilic counterpart from Escherichia coli. *FEBS J.* **275**, 117-127 (2008).
220. Hoylaerts, M.F., Ding, L., Narisawa, S., Van Kerckhoven, S. & Millán, J.L. Mammalian alkaline phosphatase catalysis requires active site structure stabilization via the N-terminal amino acid microenvironment. *Biochemistry* **45**, 9756-9766 (2006).
221. Aschaffenburg, R. & Mullen, J.E.C. 381. A rapid and simple phosphatase test for milk. *J. Dairy Res.* **16**, 58-67 (1949).
222. Rankin, S.A., Christiansen, A., Lee, W., Banavara, D.S. & Lopez-Hernandez, A. Invited review: The application of alkaline phosphatase assays for the validation of milk product pasteurization. *J. Dairy Sci.* **93**, 5538-5551 (2010).
223. Tabatabai, M.A. & Bremner, J.M. Use of p-nitrophenyl phosphate for assay of soil phosphatase activity. *Soil Biol. Biochem.* **1**, 301-307 (1969).
224. Montalibet, J., Skorey, K.I. & Kennedy, B.P. Protein tyrosine phosphatase: enzymatic assays. *Methods* **35**, 2-8 (2005).
225. Gee, K.R. et al. Fluorogenic Substrates Based on Fluorinated Umbelliferones for Continuous Assays of Phosphatases and β-Galactosidases. *Anal. Biochem.* **273**, 41-48 (1999).
226. Jiang, Y., Li, X. & Walt, D.R. Single-Molecule Analysis Determines Isozymes of Human Alkaline Phosphatase in Serum. *Angew. Chem. Int. Ed.* **59**, 18010-18015 (2020).
227. Niu, X., Ye, K., Wang, L., Lin, Y. & Du, D. A review on emerging principles and strategies for colorimetric and fluorescent detection of alkaline phosphatase activity. *Anal. Chim. Acta* **1086**, 29-45 (2019).
228. Han, Y., Chen, J., Li, Z., Chen, H. & Qiu, H. Recent progress and prospects of alkaline phosphatase biosensor based on fluorescence strategy. *Biosens. Bioelectron.* **148**, 111811 (2020).
229. Zhou, W. et al. Self-Cleavable Bioluminogenic Luciferin Phosphates as Alkaline Phosphatase Reporters. *ChemBioChem* **9**, 714-718 (2008).
230. Levine, M.N. & Raines, R.T. Sensitive fluorogenic substrate for alkaline phosphatase. *Anal. Biochem.* **418**, 247-252 (2011).
231. Tan, Y. et al. Reaction-Based Off–On Near-infrared Fluorescent Probe for Imaging Alkaline Phosphatase Activity in Living Cells and Mice. *ACS Appl. Mater. Interfaces* **9**, 6796-6803 (2017).
232. Liu, H.-W. et al. In vivo imaging of alkaline phosphatase in tumor-bearing mouse model by a promising near-infrared fluorescent probe. *Talanta* **175**, 421-426 (2017).
233. Li, S.-J. et al. Facile and Sensitive Near-Infrared Fluorescence Probe for the Detection of Endogenous Alkaline Phosphatase Activity In Vivo. *Anal. Chem.* **89**, 6854-6860 (2017).

234. Liu, H.-W. et al. In Situ Localization of Enzyme Activity in Live Cells by a Molecular Probe Releasing a Precipitating Fluorochrome. *Angew. Chem. Int. Ed.* **56**, 11788-11792 (2017).
235. Kim, T.-I., Kim, H., Choi, Y. & Kim, Y. A fluorescent turn-on probe for the detection of alkaline phosphatase activity in living cells. *Chem. Commun.* **47**, 9825-9827 (2011).
236. Park, J. & Kim, Y. An improved fluorogenic substrate for the detection of alkaline phosphatase activity. *Bioorg. Med. Chem. Lett.* **23**, 2332-2335 (2013).
237. Song, Z. et al. A Ratiometric Fluorescent Probe Based on ESIPT and AIE Processes for Alkaline Phosphatase Activity Assay and Visualization in Living Cells. *ACS Appl. Mater. Interfaces* **6**, 17245-17254 (2014).
238. Liang, J., Kwok, R.T.K., Shi, H., Tang, B.Z. & Liu, B. Fluorescent Light-up Probe with Aggregation-Induced Emission Characteristics for Alkaline Phosphatase Sensing and Activity Study. *ACS Appl. Mater. Interfaces* **5**, 8784-8789 (2013).
239. Paragas, V.B., Zhang, Y.-Z., Haugland, R.P. & Singer, V.L. The ELF-97 Alkaline Phosphatase Substrate Provides a Bright, Photostable, Fluorescent Signal Amplification Method for FISH. *J. Histochem. Cytochem.* **45**, 345-357 (1997).
240. Deng, J., Yu, P., Wang, Y. & Mao, L. Real-time Ratiometric Fluorescent Assay for Alkaline Phosphatase Activity with Stimulus Responsive Infinite Coordination Polymer Nanoparticles. *Anal. Chem.* **87**, 3080-3086 (2015).
241. Hou, X., Yu, Q., Zeng, F., Ye, J. & Wu, S. A ratiometric fluorescent probe for in vivo tracking of alkaline phosphatase level variation resulting from drug-induced organ damage. *J. Mater. Chem. B* **3**, 1042-1048 (2015).
242. Zhang, X. et al. A high-sensitivity fluorescent probe with a self-immolative spacer for real-time ratiometric detection and imaging of alkaline phosphatase activity. *New J. Chem.* **43**, 11887-11892 (2019).
243. Zhang, P., Fu, C., Zhang, Q., Li, S. & Ding, C. Ratiometric Fluorescent Strategy for Localizing Alkaline Phosphatase Activity in Mitochondria Based on the ESIPT Process. *Anal. Chem.* **91**, 12377-12383 (2019).
244. Zhao, L. et al. Ratiometric fluorescent response of electrospun fibrous strips for real-time sensing of alkaline phosphatase in serum. *Biosens. Bioelectron.* **91**, 217-224 (2017).
245. Tian, M. et al. Design of ratiometric monoaromatic fluorescence probe via modulating intramolecular hydrogen bonding: A case study of alkaline phosphatase sensing. *Anal. Chim. Acta* **1143**, 144-156 (2021).
246. Zhang, H. et al. Construction of an alkaline phosphatase-specific two-photon probe and its imaging application in living cells and tissues. *Biomaterials* **140**, 220-229 (2017).
247. Dong, L., Miao, Q., Hai, Z., Yuan, Y. & Liang, G. Enzymatic Hydrogelation-Induced Fluorescence Turn-Off for Sensing Alkaline Phosphatase in Vitro and in Living Cells. *Anal. Chem.* **87**, 6475-6478 (2015).
248. Sun, J., Zhao, J., Bao, X., Wang, Q. & Yang, X. Alkaline Phosphatase Assay Based on the Chromogenic Interaction of Diethanolamine with 4-Aminophenol. *Anal. Chem.* **90**, 6339-6345 (2018).
249. Daryaei, I., Mohammadebrahim Ghaffari, M., Jones, K.M. & Pagel, M.D. Detection of Alkaline Phosphatase Enzyme Activity with a CatalyCEST MRI Biosensor. *ACS Sens.* **1**, 857-861 (2016).

250. Lu, F. et al. Colorimetric alkaline phosphatase activity detection by integrating phosphorylation-mediated sulfydryl protection/deprotection and fluorosurfactant stabilized gold nanoparticles. *Sens. Actuators B Chem.* **325**, 128959 (2020).
251. Freeman, R., Finder, T., Gill, R. & Willner, I. Probing Protein Kinase (CK2) and Alkaline Phosphatase with CdSe/ZnS Quantum Dots. *Nano Lett.* **10**, 2192-2196 (2010).
252. Mazzei, F. et al. Alkaline phosphatase inhibition based electrochemical sensors for the detection of pesticides. *J. Electroanal. Chem.* **574**, 95-100 (2004).
253. Martínez Gache, S.A., Recoulat Angelini, A.A., Sabeckis, M.L. & González Flecha, F.L. Improving the stability of the malachite green method for the determination of phosphate using Pluronic F68. *Anal. Biochem.* **597**, 113681 (2020).
254. Webb, M.R. A continuous spectrophotometric assay for inorganic phosphate and for measuring phosphate release kinetics in biological systems. *Proc. Natl. Acad. Sci. U.S.A.* **89**, 4884-4887 (1992).
255. Brune, M., Hunter, J.L., Corrie, J.E.T. & Webb, M.R. Direct, Real-Time Measurement of Rapid Inorganic Phosphate Release Using a Novel Fluorescent Probe and Its Application to Actomyosin Subfragment 1 ATPase. *Biochemistry* **33**, 8262-8271 (1994).
256. Liu, Y. & Schanze, K.S. Conjugated Polyelectrolyte-Based Real-Time Fluorescence Assay for Alkaline Phosphatase with Pyrophosphate as Substrate. *Anal. Chem.* **80**, 8605-8612 (2008).
257. Raj, P. et al. Pyrophosphate Prompted Aggregation-Induced Emission: Chemosensor Studies, Cell Imaging, Cytotoxicity, and Hydrolysis of the Phosphoester Bond with Alkaline Phosphatase. *Eur. J. Inorg. Chem.* **2019**, 628-638 (2019).
258. Ni, P. et al. Spectrophotometric determination of the activity of alkaline phosphatase and detection of its inhibitors by exploiting the pyrophosphate-accelerated oxidase-like activity of nanoceria. *Microchim. Acta* **186**, 320 (2019).
259. Hou, L. et al. A ratiometric multicolor fluorescence biosensor for visual detection of alkaline phosphatase activity via a smartphone. *Biosens. Bioelectron.* **143**, 111605 (2019).
260. Zhang, L. et al. Inhibition of dsDNA-Templated Copper Nanoparticles by Pyrophosphate as a Label-Free Fluorescent Strategy for Alkaline Phosphatase Assay. *Anal. Chem.* **85**, 3797-3801 (2013).
261. Ma, J.-L., Yin, B.-C., Wu, X. & Ye, B.-C. Copper-Mediated DNA-Scaffolded Silver Nanocluster On–Off Switch for Detection of Pyrophosphate and Alkaline Phosphatase. *Anal. Chem.* **88**, 9219-9225 (2016).
262. Zhao, W., Chiuman, W., Lam, J.C.F., Brook, M.A. & Li, Y. Simple and rapid colorimetric enzyme sensing assays using non-crosslinking gold nanoparticle aggregation. *Chem. Commun.*, 3729-3731 (2007).
263. Wei, H., Chen, C., Han, B. & Wang, E. Enzyme Colorimetric Assay Using Unmodified Silver Nanoparticles. *Anal. Chem.* **80**, 7051-7055 (2008).
264. Nutiu, R., Yu, J.M.Y. & Li, Y. Signaling Aptamers for Monitoring Enzymatic Activity and for Inhibitor Screening. *ChemBioChem* **5**, 1139-1144 (2004).
265. Dsouza, R.N., Hennig, A. & Nau, W.M. Supramolecular Tandem Enzyme Assays. *Chem. Eur. J.* **18**, 3444-3459 (2012).

266. Wang, K., Cui, J.-H., Xing, S.-Y. & Dou, H.-X. A calixpyridinium-based supramolecular tandem assay for alkaline phosphatase and its application to ATP hydrolysis reaction. *Org. Biomol. Chem.* **14**, 2684-2690 (2016).
267. Yue, Y.-X. et al. Supramolecular Tandem Assay for Pyridoxal-5′-phosphate by the Reporter Pair of Guanidinocalix[5]Arene and Fluorescein. *ChemistryOpen* **8**, 1437-1440 (2019).
268. Liu, Y.-C., Peng, S., Angelova, L., Nau, W.M. & Hennig, A. Label-Free Fluorescent Kinase and Phosphatase Enzyme Assays with Supramolecular Host-Dye Pairs. *ChemistryOpen* **8**, 1350-1354 (2019).
269. Liu, Y. et al. Selective Sensing of Phosphorylated Peptides and Monitoring Kinase and Phosphatase Activity with a Supramolecular Tandem Assay. *J. Am. Chem. Soc.* **140**, 13869-13877 (2018).
270. Zhou, X., Khusbu, F.Y., Chen, H. & Ma, C. A turn-on fluorescence assay of alkaline phosphatase activity based on an enzyme-triggered conformational switch of G-quadruplex. *Talanta* **208**, 120453 (2020).
271. Chen, C. et al. Logically Regulating Peroxidase-Like Activity of Gold Nanoclusters for Sensing Phosphate-Containing Metabolites and Alkaline Phosphatase Activity. *Anal. Chem.* **91**, 15017-15024 (2019).
272. Chen, C. et al. Fluorescence assay for alkaline phosphatase based on ATP hydrolysis-triggered dissociation of cerium coordination polymer nanoparticles. *Analyst* **143**, 3821-3828 (2018).
273. Ma, C. et al. A terbium chelate based fluorescent assay for alkaline phosphatase in biological fluid. *Sens. Actuators B Chem.* **202**, 683-689 (2014).
274. Qian, Z. et al. Carbon Quantum Dots-Based Recyclable Real-Time Fluorescence Assay for Alkaline Phosphatase with Adenosine Triphosphate as Substrate. *Anal. Chem.* **87**, 2966-2973 (2015).
275. Chen, L., Yang, G., Wu, P. & Cai, C. Real-time fluorescence assay of alkaline phosphatase in living cells using boron-doped graphene quantum dots as fluorophores. *Biosens. Bioelectron.* **96**, 294-299 (2017).
276. Chen, C., Zhao, J., Lu, Y., Sun, J. & Yang, X. Fluorescence Immunoassay Based on the Phosphate-Triggered Fluorescence Turn-on Detection of Alkaline Phosphatase. *Anal. Chem.* **90**, 3505-3511 (2018).
277. Schrenkhammer, P., Rosnizeck, I.C., Duerkop, A., Wolfbeis, O.S. & Schäferling, M. Time-Resolved Fluorescence-Based Assay for the Determination of Alkaline Phosphatase Activity and Application to the Screening of Its Inhibitors. *J. Biomol. Screen.* **13**, 9-16 (2008).
278. Sundquist, W.I. & Klug, A. Telomeric DNA dimerizes by formation of guanine tetrads between hairpin loops. *Nature* **342**, 825-829 (1989).
279. Gehring, K., Leroy, J.-L. & Guéron, M. A tetrameric DNA structure with protonated cytosine-cytosine base pairs. *Nature* **363**, 561-565 (1993).
280. Zeraati, M. et al. I-motif DNA structures are formed in the nuclei of human cells. *Nat. Chem.* **10**, 631-637 (2018).
281. Hu, Y., Cecconello, A., Idili, A., Ricci, F. & Willner, I. Triplex DNA Nanostructures: From Basic Properties to Applications. *Angew. Chem. Int. Ed.* **56**, 15210-15233 (2017).

282. Harroun, S.G. et al. Programmable DNA switches and their applications. *Nanoscale* **10**, 4607-4641 (2018).
283. Ke, G. et al. l-DNA Molecular Beacon: A Safe, Stable, and Accurate Intracellular Nano-thermometer for Temperature Sensing in Living Cells. *J. Am. Chem. Soc.* **134**, 18908-18911 (2012).
284. Jonstrup, A.T., Fredsøe, J. & Andersen, A.H. DNA hairpins as temperature switches, thermometers and ionic detectors. *Sensors* **13**, 5937-5944 (2013).
285. Ebrahimi, S., Akhlaghi, Y., Kompany-Zareh, M. & Rinnan, Å. Nucleic Acid Based Fluorescent Nanothermometers. *ACS Nano* **8**, 10372-10382 (2014).
286. Gareau, D., Desrosiers, A. & Vallée-Bélisle, A. Programmable Quantitative DNA Nanothermometers. *Nano Lett.* **16**, 3976-3981 (2016).
287. Idili, A., Vallée-Bélisle, A. & Ricci, F. Programmable pH-Triggered DNA Nanoswitches. *J. Am. Chem. Soc.* **136**, 5836-5839 (2014).
288. Baker, B.R. et al. An Electronic, Aptamer-Based Small-Molecule Sensor for the Rapid, Label-Free Detection of Cocaine in Adulterated Samples and Biological Fluids. *J. Am. Chem. Soc.* **128**, 3138-3139 (2006).
289. Stojanovic, M.N., de Prada, P. & Landry, D.W. Aptamer-Based Folding Fluorescent Sensor for Cocaine. *J. Am. Chem. Soc.* **123**, 4928-4931 (2001).
290. Mahshid, S.S., Ricci, F., Kelley, S.O. & Vallée-Bélisle, A. Electrochemical DNA-Based Immunoassay That Employs Steric Hindrance To Detect Small Molecules Directly in Whole Blood. *ACS Sens.* **2**, 718-723 (2017).
291. Porchetta, A., Vallée-Bélisle, A., Plaxco, K.W. & Ricci, F. Allosterically Tunable, DNA-Based Switches Triggered by Heavy Metals. *J. Am. Chem. Soc.* **135**, 13238-13241 (2013).
292. Narayanaswamy, N. et al. A pH-correctable, DNA-based fluorescent reporter for organellar calcium. *Nat. Methods* **16**, 95-102 (2019).
293. Liu, C.-W., Huang, C.-C. & Chang, H.-T. Highly Selective DNA-Based Sensor for Lead(II) and Mercury(II) Ions. *Anal. Chem.* **81**, 2383-2387 (2009).
294. Fan, C., Plaxco, K.W. & Heeger, A.J. Electrochemical interrogation of conformational changes as a reagentless method for the sequence-specific detection of DNA. *Proc. Natl. Acad. Sci. U.S.A.* **100**, 9134-9137 (2003).
295. Ranallo, S., Rossetti, M., Plaxco, K.W., Vallée-Bélisle, A. & Ricci, F. A Modular, DNA-Based Beacon for Single-Step Fluorescence Detection of Antibodies and Other Proteins. *Angew. Chem. Int. Ed.* **54**, 13214-13218 (2015).
296. Vallée-Bélisle, A., Ricci, F., Uzawa, T., Xia, F. & Plaxco, K.W. Bioelectrochemical switches for the quantitative detection of antibodies directly in whole blood. *J. Am. Chem. Soc.* **134**, 15197-15200 (2012).
297. Mahshid, S.S., Camiré, S., Ricci, F. & Vallée-Bélisle, A. A Highly Selective Electrochemical DNA-Based Sensor That Employs Steric Hindrance Effects to Detect Proteins Directly in Whole Blood. *J. Am. Chem. Soc.* **137**, 15596-15599 (2015).
298. Mahshid, S.S., Mahshid, S., Vallée-Bélisle, A. & Kelley, S.O. Peptide-Mediated Electrochemical Steric Hindrance Assay for One-Step Detection of HIV Antibodies. *Anal. Chem.* **91**, 4943-4947 (2019).

299. Vallée-Bélisle, A., Bonham, A.J., Reich, N.O., Ricci, F. & Plaxco, K.W. Transcription Factor Beacons for the Quantitative Detection of DNA Binding Activity. *J. Am. Chem. Soc.* **133**, 13836-13839 (2011).

300. Tyagi, S. & Kramer, F.R. Molecular Beacons: Probes that Fluoresce upon Hybridization. *Nat. Biotechnol.* **14**, 303-308 (1996).

301. Zheng, J. et al. Rationally designed molecular beacons for bioanalytical and biomedical applications. *Chem. Soc. Rev.* **44**, 3036-3055 (2015).

302. Watson, J.D. & Crick, F.H.C. Molecular Structure of Nucleic Acids: A Structure for Deoxyribose Nucleic Acid. *Nature* **171**, 737-738 (1953).

303. Rothemund, P.W.K. Folding DNA to create nanoscale shapes and patterns. *Nature* **440**, 297-302 (2006).

304. Grossi, G., Dalgaard Ebbesen Jepsen, M., Kjems, J. & Andersen, E.S. Control of enzyme reactions by a reconfigurable DNA nanovault. *Nat. Commun.* **8**, 992 (2017).

305. Fu, J., Liu, M., Liu, Y., Woodbury, N.W. & Yan, H. Interenzyme Substrate Diffusion for an Enzyme Cascade Organized on Spatially Addressable DNA Nanostructures. *J. Am. Chem. Soc.* **134**, 5516-5519 (2012).

306. Fu, J. et al. Multi-enzyme complexes on DNA scaffolds capable of substrate channelling with an artificial swinging arm. *Nature Nanotechnol.* **9**, 531 (2014).

307. Liu, M. et al. A DNA tweezer-actuated enzyme nanoreactor. *Nat. Commun.* **4**, 2127 (2013).

308. Del Grosso, E., Dallaire, A.-M., Vallée-Bélisle, A. & Ricci, F. Enzyme-Operated DNA-Based Nanodevices. *Nano Lett.* **15**, 8407-8411 (2015).

309. Fischer, C.J., Maluf, N.K. & Lohman, T.M. Mechanism of ATP-dependent Translocation of E.coli UvrD Monomers Along Single-stranded DNA. *J. Mol. Biol.* **344**, 1287-1309 (2004).

310. Niedziela-Majka, A., Chesnik, M.A., Tomko, E.J. & Lohman, T.M. Bacillus stearothermophilus PcrA Monomer Is a Single-stranded DNA Translocase but Not a Processive Helicase in Vitro. *J. Biol. Chem.* **282**, 27076-27085 (2007).

311. Wong, C.J. & Lohman, T.M. Kinetic Control of Mg2+-dependent Melting of Duplex DNA Ends by Escherichia coli RecBC. *J. Mol. Biol.* **378**, 761-777 (2008).

312. Wu, C.G., Bradford, C. & Lohman, T.M. Escherichia coli RecBC helicase has two translocase activities controlled by a single ATPase motor. *Nat. Struct. Mol. Biol.* **17**, 1210-1217 (2010).

313. Tomko, E.J., Fischer, C.J. & Lohman, T.M. Ensemble methods for monitoring enzyme translocation along single stranded nucleic acids. *Methods* **51**, 269-276 (2010).

314. Luo, G., Wang, M., Konigsberg, W.H. & Xie, X.S. Single-molecule and ensemble fluorescence assays for a functionally important conformational change in T7 DNA polymerase. *Proc. Natl. Acad. Sci. U.S.A.* **104**, 12610-12615 (2007).

315. Sorokina, M., Koh, H.-R., Patel, S.S. & Ha, T. Fluorescent Lifetime Trajectories of a Single Fluorophore Reveal Reaction Intermediates During Transcription Initiation. *J. Am. Chem. Soc.* **131**, 9630-9631 (2009).

316. Myong, S. et al. Cytosolic Viral Sensor RIG-I Is a 5'-Triphosphate–Dependent Translocase on Double-Stranded RNA. *Science* **323**, 1070-1074 (2009).

317. Park, J. et al. PcrA Helicase Dismantles RecA Filaments by Reeling in DNA in Uniform Steps. *Cell* **142**, 544-555 (2010).

318. Hwang, H., Kim, H. & Myong, S. Protein induced fluorescence enhancement as a single molecule assay with short distance sensitivity. *Proc. Natl. Acad. Sci. U.S.A.* **108**, 7414-7418 (2011).
319. Hwang, H. & Myong, S. Protein induced fluorescence enhancement (PIFE) for probing protein–nucleic acid interactions. *Chem. Soc. Rev.* **43**, 1221-1229 (2014).
320. Ploetz, E. et al. Förster resonance energy transfer and protein-induced fluorescence enhancement as synergetic multi-scale molecular rulers. *Sci. Rep.* **6**, 33257 (2016).
321. Lerner, E., Ploetz, E., Hohlbein, J., Cordes, T. & Weiss, S. A Quantitative Theoretical Framework For Protein-Induced Fluorescence Enhancement–Förster-Type Resonance Energy Transfer (PIFE-FRET). *J. Phys. Chem. B* **120**, 6401-6410 (2016).
322. Sreenivasan, R. et al. Fluorescence Resonance Energy Transfer Characterization of DNA Wrapping in Closed and Open Escherichia coli RNA Polymerase−λPR Promoter Complexes. *Biochemistry* **55**, 2174-2186 (2016).
323. Gidi, Y., Götte, M. & Cosa, G. Conformational Changes Spanning Angstroms to Nanometers via a Combined Protein-Induced Fluorescence Enhancement–Förster Resonance Energy Transfer Method. *J. Phys. Chem. B* **121**, 2039-2048 (2017).
324. Stennett, E.M.S., Ciuba, M.A., Lin, S. & Levitus, M. Demystifying PIFE: The Photophysics Behind the Protein-Induced Fluorescence Enhancement Phenomenon in Cy3. *J. Phys. Chem. Lett.* **6**, 1819-1823 (2015).
325. Nguyen, B., Ciuba, M.A., Kozlov, A.G., Levitus, M. & Lohman, T.M. Protein Environment and DNA Orientation Affect Protein-Induced Cy3 Fluorescence Enhancement. *Biophys. J.* **117**, 66-73 (2019).
326. Rashid, F. et al. Initial state of DNA-Dye complex sets the stage for protein induced fluorescence modulation. *Nat. Commun.* **10**, 2104 (2019).
327. Pode, Z. et al. Protein recognition by a pattern-generating fluorescent molecular probe. *Nat. Nanotechnol.* **12**, 1161-1168 (2017).
328. Luong, J.H.T. & Vashist, S.K. Chemistry of Biotin–Streptavidin and the Growing Concern of an Emerging Biotin Interference in Clinical Immunoassays. *ACS Omega* **5**, 10-18 (2020).
329. Weber, P., Ohlendorf, D., Wendoloski, J. & Salemme, F. Structural origins of high-affinity biotin binding to streptavidin. *Science* **243**, 85-88 (1989).
330. Le Trong, I. et al. Streptavidin and its biotin complex at atomic resolution. *Acta Crystallogr. D Biol. Crystallogr.* **67**, 813-821 (2011).
331. Dundas, C.M., Demonte, D. & Park, S. Streptavidin–biotin technology: improvements and innovations in chemical and biological applications. *Appl. Microbiol. Biotechnol.* **97**, 9343-9353 (2013).
332. González, M.n., Argaraña, C.E. & Fidelio, G.D. Extremely high thermal stability of streptavidin and avidin upon biotin binding. *Biomol. Eng.* **16**, 67-72 (1999).
333. Sarter, M. et al. Strong Adverse Contribution of Conformational Dynamics to Streptavidin–Biotin Binding. *J. Phys. Chem. B* **124**, 324-335 (2020).
334. Hofmann, K., Wood, S.W., Brinton, C.C., Montibeller, J.A. & Finn, F.M. Iminobiotin affinity columns and their application to retrieval of streptavidin. *Proc. Natl. Acad. Sci. U.S.A.* **77**, 4666-4668 (1980).
335. González, M. et al. Interaction of Biotin with Streptavidin: Thermostability and Conformational Changes upon Binding. *J. Biol. Chem.* **272**, 11288-11294 (1997).

336. Laitinen, O.H., Hytönen, V.P., Nordlund, H.R. & Kulomaa, M.S. Genetically engineered avidins and streptavidins. *Cell. Mol. Life Sci.* **63**, 2992-3017 (2006).
337. Jain, A., Barve, A., Zhao, Z., Jin, W. & Cheng, K. Comparison of Avidin, Neutravidin, and Streptavidin as Nanocarriers for Efficient siRNA Delivery. *Mol. Pharmaceutic.* **14**, 1517-1527 (2017).
338. Chilkoti, A. & Stayton, P.S. Molecular Origins of the Slow Streptavidin-Biotin Dissociation Kinetics. *J. Am. Chem. Soc.* **117**, 10622-10628 (1995).
339. Chivers, C.E. et al. A streptavidin variant with slower biotin dissociation and increased mechanostability. *Nat. Methods* **7**, 391-393 (2010).
340. Madsen, M. & Gothelf, K.V. Chemistries for DNA Nanotechnology. *Chem. Rev.* **119**, 6384-6458 (2019).
341. Bayer, E.A. & Wilchek, M. [14] Protein biotinylation. *Methods Enzymol.* **184**, 138-160 (1990).
342. Chen, R.F. Fluorescence Quantum Yields of Tryptophan and Tyrosine. *Anal. Lett.* **1**, 35-42 (1967).
343. Cooksey, C. Quirks of dye nomenclature. 9. Fluorescein. *Biotech. Histochem.* **92**, 506-512 (2017).
344. Brush, C.K. (US5371241A, 1994).
345. Sjöback, R., Nygren, J. & Kubista, M. Characterization of fluorescein–oligonucleotide conjugates and measurement of local electrostatic potential. *Biopolymers* **46**, 445-453 (1998).
346. Kvach, M.V. et al. 5(6)-Carboxyfluorescein Revisited: New Protecting Group, Separation of Isomers, and their Spectral Properties on Oligonucleotides. *Bioconjugate Chem.* **18**, 1691-1696 (2007).
347. Lavis, L.D., Rutkoski, T.J. & Raines, R.T. Tuning the pKa of Fluorescein to Optimize Binding Assays. *Anal. Chem.* **79**, 6775-6782 (2007).
348. Marras, S.A.E., Kramer, F.R. & Tyagi, S. Efficiencies of fluorescence resonance energy transfer and contact ‐ mediated quenching in oligonucleotide probes. *Nucleic Acids Res.* **30**, e122-e122 (2002).
349. Nazarenko, I., Pires, R., Lowe, B., Obaidy, M. & Rashtchian, A. Effect of primary and secondary structure of oligodeoxyribonucleotides on the fluorescent properties of conjugated dyes. *Nucleic Acids Res.* **30**, 2089-2195 (2002).
350. Sjöback, R., Nygren, J. & Kubista, M. Absorption and fluorescence properties of fluorescein. *Spectrochim. Acta A* **51**, L7-L21 (1995).
351. Klonis, N. & Sawyer, W.H. Spectral properties of the prototropic forms of fluorescein in aqueous solution. *J. Fluoresc.* **6**, 147-157 (1996).
352. Smith, S.A. & Pretorius, W.A. Spectrophotometric determination of pKa values for fluorescein using activity coefficient corrections. *Water SA* **28**, 395-402 (2002).
353. Schneider, U.V. et al. A novel FRET pair for detection of parallel DNA triplexes by the LightCycler. *BMC Biotechnol.* **10**, 4 (2010).
354. Liu, W.-T., Wu, J.-H., Li, E.S.-Y. & Selamat, E.S. Emission Characteristics of Fluorescent Labels with Respect to Temperature Changes and Subsequent Effects on DNA Microchip Studies. *Appl. Environ. Microbiol.* **71**, 6453-6457 (2005).

355. Marras, S.A. Interactive fluorophore and quencher pairs for labeling fluorescent nucleic acid hybridization probes. *Mol. Biotechnol.* **38**, 247-255 (2008).

356. Matsui, A. et al. Real-time, near-infrared, fluorescence-guided identification of the ureters using methylene blue. *Surgery* **148**, 78-86 (2010).

357. Tummers, Q.R.J.G. et al. Real-time intraoperative detection of breast cancer using near-infrared fluorescence imaging and Methylene Blue. *Eur. J. Surg. Oncol.* **40**, 850-858 (2014).

358. Cooksey, C.J. Quirks of dye nomenclature. 5. Rhodamines. *Biotech. Histochem.* **91**, 71-76 (2016).

359. Ke, G. et al. A Cell-Surface-Anchored Ratiometric Fluorescent Probe for Extracellular pH Sensing. *ACS Appl. Mater. Interfaces* **6**, 15329-15334 (2014).

360. Elbaz, J., Shimron, S. & Willner, I. pH-triggered switchable Mg2+-dependent DNAzymes. *Chem. Commun.* **46**, 1209-1211 (2010).

361. Unruh, J.R., Gokulrangan, G., Wilson, G.S. & Johnson, C.K. Fluorescence Properties of Fluorescein, Tetramethylrhodamine and Texas Red Linked to a DNA Aptamer. *Photochem. Photobiol.* **81**, 682-690 (2005).

362. Levitus, M. & Ranjit, S. Cyanine dyes in biophysical research: the photophysics of polymethine fluorescent dyes in biomolecular environments. *Q. Rev. Biophys.* **44**, 123-151 (2011).

363. Aramendia, P.F., Negri, R.M. & Roman, E.S. Temperature Dependence of Fluorescence and Photoisomerization in Symmetric Carbocyanines.Influence of Medium Viscosity and Molecular Structure. *J. Phys. Chem.* **98**, 3165-3173 (1994).

364. Han, J. & Burgess, K. Fluorescent Indicators for Intracellular pH. *Chem. Rev.* **110**, 2709-2728 (2010).

365. Spiriti, J., Binder, J.K., Levitus, M. & van der Vaart, A. Cy3-DNA Stacking Interactions Strongly Depend on the Identity of the Terminal Basepair. *Biophys. J.* **100**, 1049-1057 (2011).

366. Kretschy, N., Sack, M. & Somoza, M.M. Sequence-Dependent Fluorescence of Cy3- and Cy5-Labeled Double-Stranded DNA. *Bioconjugate Chem.* **27**, 840-848 (2016).

367. Kretschy, N. & Somoza, M.M. Comparison of the Sequence-Dependent Fluorescence of the Cyanine Dyes Cy3, Cy5, DyLight DY547 and DyLight DY647 on Single-Stranded DNA. *PLOS ONE* **9**, e85605 (2014).

368. Gruber, H.J. et al. Anomalous Fluorescence Enhancement of Cy3 and Cy3.5 versus Anomalous Fluorescence Loss of Cy5 and Cy7 upon Covalent Linking to IgG and Noncovalent Binding to Avidin. *Bioconjugate Chem.* **11**, 696-704 (2000).

369. Togashi, D.M., Szczupak, B., Ryder, A.G., Calvet, A. & O'Loughlin, M. Investigating Tryptophan Quenching of Fluorescein Fluorescence under Protolytic Equilibrium. *J. Phys. Chem. A* **113**, 2757-2767 (2009).

370. Wu, L. et al. Förster resonance energy transfer (FRET)-based small-molecule sensors and imaging agents. *Chem. Soc. Rev.* **49**, 5110-5139 (2020).

371. Fare, T.L. et al. Effects of Atmospheric Ozone on Microarray Data Quality. *Anal. Chem.* **75**, 4672-4675 (2003).

372. Cooksey, C.J. Quirks of dye nomenclature. 8. Methylene blue, azure and violet. *Biotech. Histochem.* **92**, 347-356 (2017).

373. Clarise R. Starr, E.T.V., Richard R. Chapleau, David L. Masserang Optimizing the Roche LightCycler(R) for Single-Tube Multiplexed RT-PCR Assays. *J. Clin. Diagn. Res.* **9**, DM01-DM03 (2015).
374. Brooijmans, N. & Kuntz, I.D. Molecular recognition and docking algorithms. *Annu. Rev. Biophys. Biomol. Struct.* **32**, 335-373 (2003).
375. Kuntz, I.D., Blaney, J.M., Oatley, S.J., Langridge, R. & Ferrin, T.E. A geometric approach to macromolecule-ligand interactions. *J. Mol. Biol.* **161**, 269-288 (1982).
376. Śledź, P. & Caflisch, A. Protein structure-based drug design: from docking to molecular dynamics. *Curr. Opin. Struct. Biol.* **48**, 93-102 (2018).
377. Bienert, S. et al. The SWISS-MODEL Repository—new features and functionality. *Nucleic Acids Res.* **45**, D313-D319 (2016).
378. Shukla, R. & Tripathi, T. in Computer-Aided Drug Design. (ed. D.B. Singh) 133-161 (Springer Singapore, Singapore; 2020).
379. Martí-Renom, M.A. et al. Comparative protein structure modeling of genes and genomes. *Annu. Rev. Biophys. Biomol. Struct.* **29**, 291-325 (2000).
380. Waterhouse, A. et al. SWISS-MODEL: homology modelling of protein structures and complexes. *Nucleic Acids Res.* **46**, W296-W303 (2018).
381. Fatima, S., Anwar, T., Ahmad, N., Islam, A. & Sen, P. Non-enzymatic glycation enhances human serum albumin binding capacity to sodium fluorescein at room temperature: A spectroscopic analysis. *Clin. Chim. Acta* **469**, 180-186 (2017).
382. Wang, Y. et al. Discovery of FDA-Approved Drugs as Inhibitors of Fatty Acid Binding Protein 4 Using Molecular Docking Screening. *J. Chem. Inf. Model.* **54**, 3046-3050 (2014).
383. Mahajan, P.G. et al. Synthesis and Studies of Fluorescein Based Derivatives for their Optical Properties, Urease Inhibition and Molecular Docking. *J. Fluoresc.* **28**, 1305-1315 (2018).
384. Stefanucci, A. et al. Fluorescent-labeled bioconjugates of the opioid peptides biphalin and DPDPE incorporating fluorescein–maleimide linkers. *Future Med. Chem.* **9**, 859-869 (2017).
385. Muddana, H.S., Sengupta, S., Sen, A. & Butler, P.J. Enhanced brightness and photostability of cyanine dyes by supramolecular containment. *arXiv preprint arXiv:1410.0844* (2014).
386. Vus, K. et al. Cyanine dyes derived inhibition of insulin fibrillization. *J. Mol. Liq.* **276**, 541-552 (2019).
387. Haghshenas, H., Kay, M., Dehghanian, F. & Tavakol, H. Molecular dynamics study of biodegradation of azo dyes via their interactions with AzrC azoreductase. *J. Biomol. Struct. Dyn.* **34**, 453-462 (2016).
388. Millan, S. et al. A Spectroscopic and Molecular Simulation Approach toward the Binding Affinity between Lysozyme and Phenazinium Dyes: An Effect on Protein Conformation. *J. Phys. Chem. B* **121**, 1475-1484 (2017).
389. Stec, B., Cheltsov, A. & Millán, J.L. Refined structures of placental alkaline phosphatase show a consistent pattern of interactions at the peripheral site. *Acta Crystallogr. Sect. F Struct. Biol. Cryst. Commun.* **66**, 866-870 (2010).
390. Grosdidier, A., Zoete, V. & Michielin, O. SwissDock, a protein-small molecule docking web service based on EADock DSS. *Nucleic Acids Res.* **39**, W270-W277 (2011).
391. Grosdidier, A., Zoete, V. & Michielin, O. Fast docking using the CHARMM force field with EADock DSS. *J. Comput. Chem.* **32**, 2149-2159 (2011).

392. Pettersen, E.F. et al. UCSF Chimera—a visualization system for exploratory research and analysis. *J. Comput. Chem.* **25**, 1605-1612 (2004).
393. Karplus, M. & McCammon, J.A. Molecular dynamics simulations of biomolecules. *Nat. Struct. Biol.* **9**, 646-652 (2002).
394. Ramanan, R., Dubey, K.D., Wang, B., Mandal, D. & Shaik, S. Emergence of Function in P450-Proteins: A Combined Quantum Mechanical/Molecular Mechanical and Molecular Dynamics Study of the Reactive Species in the H2O2-Dependent Cytochrome P450SPα and Its Regio- and Enantioselective Hydroxylation of Fatty Acids. *J. Am. Chem. Soc.* **138**, 6786-6797 (2016).
395. Bermudez, M., Mortier, J., Rakers, C., Sydow, D. & Wolber, G. More than a look into a crystal ball: protein structure elucidation guided by molecular dynamics simulations. *Drug Discov. Today* **21**, 1799-1805 (2016).
396. Ebert, M.C.C.J.C., Dürr, S.L., A. Houle, A., Lamoureux, G. & Pelletier, J.N. Evolution of P450 Monooxygenases toward Formation of Transient Channels and Exclusion of Nonproductive Gases. *ACS Catal.* **6**, 7426-7437 (2016).
397. Huang, D. & Caflisch, A. The free energy landscape of small molecule unbinding. *PLOS Comput. Biol.* **7**, e1002002 (2011).
398. González, M.A. Force fields and molecular dynamics simulations. *Collection SFN* **12**, 169-200 (2011).
399. Guvench, O. & MacKerell, A.D. in Molecular Modeling of Proteins. (ed. A. Kukol) 63-88 (Humana Press, Totowa, NJ; 2008).
400. Boldon, L., Laliberte, F. & Liu, L. Review of the fundamental theories behind small angle X-ray scattering, molecular dynamics simulations, and relevant integrated application. *Nano Rev.* **6**, 25661 (2015).
401. Shukla, H., Shukla, R., Sonkar, A. & Tripathi, T. Alterations in conformational topology and interaction dynamics caused by L418A mutation leads to activity loss of Mycobacterium tuberculosis isocitrate lyase. *Biochem. Biophys. Res. Commun.* **490**, 276-282 (2017).
402. Evoli, S., Guzzi, R. & Rizzuti, B. Molecular simulations of β-lactoglobulin complexed with fatty acids reveal the structural basis of ligand affinity to internal and possible external binding sites. *Proteins* **82**, 2609-2619 (2014).
403. Iqbal, A., Wang, L., Thompson, K.C., Lilley, D.M.J. & Norman, D.G. The Structure of Cyanine 5 Terminally Attached to Double-Stranded DNA: Implications for FRET Studies. *Biochemistry* **47**, 7857-7862 (2008).
404. Unruh, J.R., Gokulrangan, G., Lushington, G.H., Johnson, C.K. & Wilson, G.S. Orientational Dynamics and Dye-DNA Interactions in a Dye-Labeled DNA Aptamer. *Biophys. J.* **88**, 3455-3465 (2005).
405. D'Annessa, I. et al. Simulations of DNA topoisomerase 1B bound to supercoiled DNA reveal changes in the flexibility pattern of the enzyme and a secondary protein–DNA binding site. *Nucleic Acids Res.* **42**, 9304-9312 (2014).
406. Katsipis, G. et al. In vitro and in silico evaluation of the inhibitory effect of a curcumin-based oxovanadium (IV) complex on alkaline phosphatase activity and bacterial biofilm formation. *Appl. Microbiol. Biotechnol.* **105**, 147-168 (2021).

407. Deshwal, A. & Maiti, S. Macromolecular Crowding Effect on the Activity of Liposome-Bound Alkaline Phosphatase: A Paradoxical Inhibitory Action. *Langmuir* **37**, 7273-7284 (2021).
408. Kiffer-Moreira, T. et al. Catalytic signature of a heat-stable, chimeric human alkaline phosphatase with therapeutic potential. *PLOS One* **9**, e89374 (2014).
409. Fairhead, M., Krndija, D., Lowe, E.D. & Howarth, M. Plug-and-Play Pairing via Defined Divalent Streptavidins. *J. Mol. Biol.* **426**, 199-214 (2014).
410. Perri, M.J. & Weber, S.H. Web-Based Job Submission Interface for the GAMESS Computational Chemistry Program. *J. Chem. Educ.* **91**, 2206-2208 (2014).
411. Schmidt, M.W. et al. General atomic and molecular electronic structure system. *J. Comput. Chem.* **14**, 1347-1363 (1993).
412. Becke, A.D. Density-functional thermochemistry. III. The role of exact exchange. *J. Chem. Phys.* **98**, 5648-5652 (1993).
413. Lee, C., Yang, W. & Parr, R.G. Development of the Colle-Salvetti correlation-energy formula into a functional of the electron density. *Phys. Rev. B* **37**, 785-789 (1988).
414. Vosko, S.H., Wilk, L. & Nusair, M. Accurate spin-dependent electron liquid correlation energies for local spin density calculations: a critical analysis. *Can. J. Phys.* **58**, 1200-1211 (1980).
415. Stephens, P.J., Devlin, F.J., Chabalowski, C.F. & Frisch, M.J. Ab Initio Calculation of Vibrational Absorption and Circular Dichroism Spectra Using Density Functional Force Fields. *J. Phys. Chem.* **98**, 11623-11627 (1994).
416. Krishnan, R., Binkley, J.S., Seeger, R. & Pople, J.A. Self‐consistent molecular orbital methods. XX. A basis set for correlated wave functions. *J. Chem. Phys.* **72**, 650-654 (1980).
417. McLean, A.D. & Chandler, G.S. Contracted Gaussian basis sets for molecular calculations. I. Second row atoms, Z=11–18. *J. Chem. Phys.* **72**, 5639-5648 (1980).
418. Francl, M.M. et al. Self-consistent molecular orbital methods. XXIII. A polarization-type basis set for second-row elements. *J. Chem. Phys.* **77**, 3654-3665 (1982).
419. Clark, T., Chandrasekhar, J., Spitznagel, G.W. & Schleyer, P.V.R. Efficient diffuse function-augmented basis sets for anion calculations. III. The 3-21+G basis set for first-row elements, Li–F. *J. Comput. Chem.* **4**, 294-301 (1983).
420. Spitznagel, G.W., Clark, T., von Ragué Schleyer, P. & Hehre, W.J. An evaluation of the performance of diffuse function-augmented basis sets for second row elements, Na-Cl. *J. Comput. Chem.* **8**, 1109-1116 (1987).
421. Watson, J.D. & Crick, F.H. Molecular structure of nucleic acids. *Nature* **171**, 737-738 (1953).
422. Roth, E., Glick Azaria, A., Girshevitz, O., Bitler, A. & Garini, Y. Measuring the Conformation and Persistence Length of Single-Stranded DNA Using a DNA Origami Structure. *Nano Lett.* **18**, 6703-6709 (2018).
423. Aslan, F.M., Yu, Y., Vajda, S., Mohr, S.C. & Cantor, C.R. Engineering a novel, stable dimeric streptavidin with lower isoelectric point. *J. Biotechnol.* **128**, 213-225 (2007).
424. Vega-Warner, A.V., Wang, C.-H., Smith, D.M. & Ustunol, Z. Milk Alkaline Phosphatase Purification and Production of Polyclonal Antibodies. *J. Food Sci.* **64**, 601-605 (1999).
425. Chuang, N.-N. & Yang, B.-C. A comparative study of alkaline phosphatases among human placenta, bovine milk, hepatopancreases of shrimp Penaeus monodon (Crustacea: Decapoda) and clam Meretrix lusoria (Bivalvia: Veneidae): To obtain an alkaline

phosphatase with improved characteristics as a reporter. *Comp. Biochem. Physiol. B* **96**, 787-789 (1990).

426. Martin, M.M. & Lindqvist, L. The pH dependence of fluorescein fluorescence. *J. Lumin.* **10**, 381-390 (1975).
427. Basu, S., Finke, A., Vera, L., Wang, M. & Olieric, V. Making routine native SAD a reality: lessons from beamline X06DA at the Swiss Light Source. *Acta Crystallogr. D* **75**, 262-271 (2019).
428. Weissig, H., Schildge, A., Hoylaerts, M.F., Iqbal, M. & Millán, J.L. Cloning and expression of the bovine intestinal alkaline phosphatase gene: biochemical characterization of the recombinant enzyme. *Biochem. J.* **290**, 503-508 (1993).
429. Manes, T. et al. Genetic Complexity, Structure, and Characterization of Highly Active Bovine Intestinal Alkaline Phosphatases *. *J. Biol. Chem.* **273**, 23353-23360 (1998).
430. Besman, M. & Coleman, J.E. Isozymes of bovine intestinal alkaline phosphatase. *J. Biol. Chem.* **260**, 11190-11193 (1985).
431. Behal, F.J. & Center, M. Heterogeneity of calf intestinal alkaline phosphatase. *Arch. Biochem. Biophys.* **110**, 500-505 (1965).
432. Ueno, H., Kato, M., Minagawa, Y., Hirose, Y. & Noji, H. Elucidation and control of low and high active populations of alkaline phosphatase molecules for quantitative digital bioassay. *Protein Sci.* **30**, 1628-1639 (2021).
433. Kaufmann, C.M., Graßmann, J., Treutter, D. & Letzel, T. Utilization of real-time electrospray ionization mass spectrometry to gain further insight into the course of nucleotide degradation by intestinal alkaline phosphatase. *Rapid Commun. Mass Spectrom.* **28**, 869-878 (2014).
434. Susini, V., Rossi, V.L., Sanesi, A. & Drazek, L. Kinetics study on recombinant alkaline phosphatase and correlation with the generated fluorescent signal. *J. Immunoass. Immunochem.* **39**, 108-118 (2018).
435. Iyer, A., Chandra, A. & Swaminathan, R. Hydrolytic enzymes conjugated to quantum dots mostly retain whole catalytic activity. *Biochim. Biophys. Acta, Gen. Subj.* **1840**, 2935-2943 (2014).
436. Llinas, P. et al. Structural Studies of Human Placental Alkaline Phosphatase in Complex with Functional Ligands. *J. Mol. Biol.* **350**, 441-451 (2005).
437. Harada, T. et al. Characterization of structural and catalytic differences in rat intestinal alkaline phosphatase isozymes. *FEBS J.* **272**, 2477-2486 (2005).
438. Gracie, K. et al. Interaction of fluorescent dyes with DNA and spermine using fluorescence spectroscopy. *Analyst* **139**, 3735-3743 (2014).
439. Stennett, E.M.S., Ciuba, M.A. & Levitus, M. Photophysical processes in single molecule organic fluorescent probes. *Chem. Soc. Rev.* **43**, 1057-1075 (2014).
440. Marr III, H.E., Stewart, J.M. & Chiu, M.F. The crystal structure of methylene blue pentahydrate. *Acta Cryst. B* **29**, 847-853 (1973).
441. Hähner, G., Marti, A., Spencer, N.D. & Caseri, W.R. Orientation and electronic structure of methylene blue on mica: A near edge x-ray absorption fine structure spectroscopy study. *J. Chem. Phys.* **104**, 7749-7757 (1996).

442. Guedes, I.A., Pereira, F.S.S. & Dardenne, L.E. Empirical Scoring Functions for Structure-Based Virtual Screening: Applications, Critical Aspects, and Challenges. *Front. Pharmacol.* **9** (2018).
443. Marmé, N., Knemeyer, J.-P., Sauer, M. & Wolfrum, J. Inter- and Intramolecular Fluorescence Quenching of Organic Dyes by Tryptophan. *Bioconjugate Chem.* **14**, 1133-1139 (2003).
444. Hu, C. et al. Covalent cucurbit[7]uril–dye conjugates for sensing in aqueous saline media and biofluids. *Chem. Sci.* (2020).
445. Shindy, H.A. Fundamentals in the chemistry of cyanine dyes: A review. *Dyes Pigm.* **145**, 505-513 (2017).
446. Chen, H., Ahsan, S.S., Santiago-Berrios, M.E.B., Abruña, H.D. & Webb, W.W. Mechanisms of Quenching of Alexa Fluorophores by Natural Amino Acids. *J. Am. Chem. Soc.* **132**, 7244-7245 (2010).
447. Klonis, N. & Sawyer, W.H. Effect of Solvent–Water Mixtures on the Prototropic Equilibria of Fluorescein and on the Spectral Properties of the Monoanion. *Photochem. Photobiol.* **72**, 179-185 (2000).
448. Pantazis, A., Westerberg, K., Althoff, T., Abramson, J. & Olcese, R. Harnessing photoinduced electron transfer to optically determine protein sub-nanoscale atomic distances. *Nat. Commun.* **9**, 4738 (2018).
449. Jarecki, Brian W. et al. Tethered Spectroscopic Probes Estimate Dynamic Distances with Subnanometer Resolution in Voltage-Dependent Potassium Channels. *Biophys. J.* **105**, 2724-2732 (2013).
450. Mansoor, S.E., McHaourab, H.S. & Farrens, D.L. Determination of Protein Secondary Structure and Solvent Accessibility Using Site-Directed Fluorescence Labeling. Studies of T4 Lysozyme Using the Fluorescent Probe Monobromobimane. *Biochemistry* **38**, 16383-16393 (1999).
451. Mansoor, S.E., McHaourab, H.S. & Farrens, D.L. Mapping Proximity within Proteins Using Fluorescence Spectroscopy. A Study of T4 Lysozyme Showing That Tryptophan Residues Quench Bimane Fluorescence. *Biochemistry* **41**, 2475-2484 (2002).
452. Mansoor, S.E., DeWitt, M.A. & Farrens, D.L. Distance Mapping in Proteins Using Fluorescence Spectroscopy: The Tryptophan-Induced Quenching (TrIQ) Method. *Biochemistry* **49**, 9722-9731 (2010).
453. Haenni, D., Zosel, F., Reymond, L., Nettels, D. & Schuler, B. Intramolecular Distances and Dynamics from the Combined Photon Statistics of Single-Molecule FRET and Photoinduced Electron Transfer. *J. Phys. Chem. B* **117**, 13015-13028 (2013).
454. Ahmed, I.A., Rodgers, J.M., Eng, C., Troxler, T. & Gai, F. PET and FRET utility of an amino acid pair: tryptophan and 4-cyanotryptophan. *Phys. Chem. Chem. Phys.* **21**, 12843-12849 (2019).
455. Chan, P.-H. et al. Rational Design of a Novel Fluorescent Biosensor for β-Lactam Antibiotics from a Class A β-Lactamase. *J. Am. Chem. Soc.* **126**, 4074-4075 (2004).
456. Rajagopalan, P.T.R. et al. Interaction of dihydrofolate reductase with methotrexate: Ensemble and single-molecule kinetics. *Proc. Natl. Acad. Sci. U.S.A.* **99**, 13481-13486 (2002).

457. Talukder, P. et al. Cyanotryptophans as Novel Fluorescent Probes for Studying Protein Conformational Changes and DNA–Protein Interaction. *Biochemistry* **54**, 7457-7469 (2015).

458. Chen, S. et al. Detection of Dihydrofolate Reductase Conformational Change by FRET Using Two Fluorescent Amino Acids. *J. Am. Chem. Soc.* **135**, 12924-12927 (2013).

459. Hung, H.-C. & Chang, G.-G. Multiple unfolding intermediates of human placental alkaline phosphatase in equilibrium urea denaturation. *Biophys. J.* **81**, 3456-3471 (2001).

460. Ásgeirsson, B. & Guðjónsdóttir, K. Reversible inactivation of alkaline phosphatase from Atlantic cod (Gadus morhua) in urea. *Biochim. Biophys. Acta Proteins Proteom.* **1764**, 190-198 (2006).

461. Wang, Z.-J., Ma, W., Yang, J.-M., Kang, Y. & Park, Y.-D. Effects of Cu2+ on alkaline phosphatase from Macrobrachium rosenbergii. *Int. J. Biol. Macromol.* **117**, 116-123 (2018).

462. Abdolrazghi, Z. & Butterworth, P.J. Interaction of Calf Intestinal Alkaline Phosphatase with 8-Anilinonaphthalene-1-Sulphonate. *Enzyme* **30**, 129-133 (1983).

463. Martinez-Gonzalez, A.I., Díaz-Sánchez, Á.G., de la Rosa, L.A., Bustos-Jaimes, I. & Alvarez-Parrilla, E. Inhibition of α-amylase by flavonoids: Structure activity relationship (SAR). *Spectrochim. Acta A* **206**, 437-447 (2019).

464. Thompson, W. & Yielding, K.L. 8-Anilino naphthalene sulfonate binding as a probe for conformational changes induced in glutamate dehydrogenase by regulatory reagents. *Arch. Biochem. Biophys.* **126**, 399-406 (1968).

465. Deshpande, M. & Sathe, S.K. Interactions with 8-Anilinonaphthalene-1-sulfonic Acid (ANS) and Surface Hydrophobicity of Black Gram (Vigna mungo) Phaseolin. *J. Food Sci.* **83**, 1847-1855 (2018).

466. Zanetti-Domingues, L.C., Tynan, C.J., Rolfe, D.J., Clarke, D.T. & Martin-Fernandez, M. Hydrophobic fluorescent probes introduce artifacts into single molecule tracking experiments due to non-specific binding. *PLoS One* **8**, e74200 (2013).

467. Li, H., Sun, Y., Li, Y. & Du, J. Alkaline phosphatase activity assay with luminescent metal organic frameworks-based chemiluminescent resonance energy transfer platform. *Microchem. J.* **160**, 105665 (2021).

468. Fernley, H. & Walker, P. Studies on alkaline phosphatase. Inhibition by phosphate derivatives and the substrate specificity. *Biochem. J.* **104**, 1011-1018 (1967).

469. TURNER, J. Pyridoxal phosphate breakdown by an alkaline-phosphatase preparation. *Biochem. J.* **80**, 663-668 (1961).

470. Coburn, S.P., Mahuren, J.D., Jain, M., Zubovic, Y. & Wortsman, J. Alkaline Phosphatase (EC 3.1.3.1) in Serum Is Inhibited by Physiological Concentrations of Inorganic Phosphate1. *J. Clin. Endocrinol. Metab.* **83**, 3951-3957 (1998).

471. Nagy, N. et al. 4-Methylumbelliferone Treatment and Hyaluronan Inhibition as a Therapeutic Strategy in Inflammation, Autoimmunity, and Cancer. *Front. Immunol.* **6** (2015).

472. Chappelet-Tordo, D., Fosset, M., Iwatsubo, M., Gache, C. & Lazdunski, M. Intestinal alkaline phosphatase. Catalytic properties and half of the sites reactivity. *Biochemistry* **13**, 1788-1795 (1974).

473. Palmier, M.O. & Van Doren, S.R. Rapid determination of enzyme kinetics from fluorescence: Overcoming the inner filter effect. *Anal. Biochem.* **371**, 43-51 (2007).

474. Ziegler, A.J., Florian, J., Ballicora, M.A. & Herlinger, A.W. Alkaline phosphatase inhibition by vanadyl-β-diketone complexes: electron density effects. *J. Enzyme Inhib. Med. Chem.* **24**, 22-28 (2009).

475. Jain, M., Vaze, R.G., Ugrani, S.C. & Sharma, K.P. Mechanoresponsive and recyclable biocatalytic sponges from enzyme-polymer surfactant conjugates and nanoparticles. *RSC Adv.* **8**, 39029-39038 (2018).

476. Finkler, B. et al. Monomolecular pyrenol-derivatives as multi-emissive probes for orthogonal reactivities. *Photochem. Photobiol. Sci.* **15**, 1544-1557 (2016).

477. Weis, D.D. & Nardozzi, J.D. Enzyme Kinetics in Acoustically Levitated Droplets of Supercooled Water: A Novel Approach to Cryoenzymology. *Anal. Chem.* **77**, 2558-2563 (2005).

478. Lewis, W.H. & Rutan, S.C. Guanidinium-induced differential kinetic denaturation of alkaline phosphatase isozymes. *Anal. Chem.* **63**, 627-629 (1991).

479. Zhu, S. et al. The measurement of cyclic nucleotide phosphodiesterase 4 activities via the quantification of inorganic phosphate with malachite green. *Anal. Chim. Acta* **636**, 105-110 (2009).

480. Kearney, A.S. & Stella, V.J. The in Vitro Enzymic Labilities of Chemically Distinct Phosphomonoester Prodrugs. *Pharm. Res.* **9**, 497-503 (1992).

481. Ásgeirsson, B., Hartemink, R. & Chlebowski, J.F. Alkaline phosphatase from Atlantic cod (Gadus morhua). Kinetic and structural properties which indicate adaptation to low temperatures. *Comp. Biochem. Physiol. B* **110**, 315-329 (1995).

482. Motzok, I. & Branion, H.D. Studies on alkaline phosphatases. 2. Factors influencing pH optima and Michaelis constant. *Biochem. J.* **72**, 177-183 (1959).

483. Duncan, P.H., McKneally, S.S., MacNeil, M.L., Fast, D.M. & Bayse, D.D. Development of a reference material for alkaline phosphatase. *Clin. Chem.* **30**, 93-97 (1984).

484. Cathala, G., Brunel, C., Chappelet-Tordo, D. & Lazdunski, M. Bovine kidney alkaline phosphatase. Catalytic properties, subunit interactions in the catalytic process, and mechanism of Mg2+ stimulation. *J. Biol. Chem.* **250**, 6046-6053 (1975).

485. Brunel, C., Cathala, G. & Saintot, M. Purification et propriétés de la phosphatase alcaline du cerveau de bœuf. *Biochim. Biophys. Acta, Enzymol.* **191**, 621-635 (1969).

486. Zittle, C.A. & Bingham, E.W. Action of Purified Milk Phosphatase on Phosphoserine and on Casein. *J. Dairy Sci.* **42**, 1772-1780 (1959).

487. Kumon, A., Kodama, H., Kondo, M., Yokoi, F. & Hiraishi, H. Nω-Phosphoarginine Phosphatase (17 kDa) and Alkaline Phosphatase as Protein Arginine Phosphatases. *J. Biochem.* **119**, 719-724 (1996).

488. Narayanan, S. & Appleton, H.D. Specificity studies on human intestinal alkaline phosphatase. *Biochim. Biophys. Acta* **284**, 175-182 (1972).

489. Trubowitz, S., Feldman, D., Morgenstern, S. & Hunt, V. The isolation, purification and some properties of the alkaline phosphatase of human leucocytes. *Biochem. J.* **80**, 369-374 (1961).

490. Smith, G.P. & Peters, T.J. Purification and properties of alkaline phosphatase from human polymorphonuclear leukocytes. *Int. J. Biochem.* **17**, 209-215 (1985).

491. Harkness, D.R. Studies on human placental alkaline phosphatase: II. Kinetic properties and studies on the apoenzyme. *Arch. Biochem. Biophys.* **126**, 513-523 (1968).

492. Eaton, R.H. & Moss, D.W. Organic pyrophosphates as substrates for human alkaline phosphatases. *Biochem. J.* **105**, 1307-1312 (1967).

493. Wennberg, C. et al. Structure, genomic DNA typing, and kinetic characterization of the D allozyme of placental alkaline phosphatase (PLAP/ALPP). *Hum. Mutat.* **19**, 258-267 (2002).

494. Hiwada, K. & Wachsmuth, E.D. Catalytic properties of alkaline phosphatase from pig kidney. *Biochem. J.* **141**, 283-291 (1974).

495. Simão, A.M.S. et al. Membrane-bound alkaline phosphatase from ectopic mineralization and rat bone marrow cell culture. *Comp. Biochem. Physiol. A: Mol. Integr. Physiol.* **146**, 679-687 (2007).

496. Müller, K., Schellenberger, V., Borneleit, P. & Treide, A. The alkaline phosphatase from bone: transphosphorylating activity and kinetic mechanism. *Biochim. Biophys. Acta, Protein Struct. Mol. Enzymol.* **1076**, 308-313 (1991).

497. Saini, P.K. & Done, J. The diversity of alkaline phosphatase from rat intestine: Isolation and purification of the enzyme(s). *Biochim. Biophys. Acta, Enzymol.* **258**, 147-153 (1972).

498. Rindi, G., Ricci, V., Gastaldi, G. & Patrini, C. Intestinal Alkaline Phosphatase can Transphosphorylate Thiamin to Thiamin Monophosphate During Intestinal Transport in the Rat. *Arch. Physiol. Biochem.* **103**, 33-38 (1995).

499. Murdoch, R., E Buxton, L. & Kay, D. Mouse Uterine Alkaline Phosphatase: Improved Purification by Affinity Chromatography and Further Characterization of the Enzyme. *Aust. J. Biol. Sci.* **33**, 279-294 (1980).

500. van Belle, H. Kinetics and inhibition of alkaline phosphatases from canine tissues. *Biochim. Biophys. Acta, Enzymol.* **289**, 158-168 (1972).

501. Baracchini Buainain, L., Kimiko Kadowaki, M., de Lourdes Polizeli, M., Francisco Terenzi, H. & Atilio Jorge, J. Characterization of a conidial alkaline phosphatase from the thermophilic fungus Humicola grisea var. thermoidea. *J. Basic Microbiol.* **38**, 85-94 (1998).

502. Lee, D.-H. et al. A novel psychrophilic alkaline phosphatase from the metagenome of tidal flat sediments. *BMC Biotechnol.* **15**, 1 (2015).

503. Adler, L. Properties of alkaline phosphatase of the halotolerant yeast Debaryomyces hansenii. *Biochim. Biophys. Acta, Enzymol.* **522**, 113-121 (1978).

504. de Oliveira Ornela, P.H. & Guimarães, L.H.S. Purification and characterization of an iron-activated alkaline phosphatase produced by Rhizopus microsporus var. microsporus under submerged fermentation using rye flour. *J. Appl. Biol. Biotech.* **8**, 16-25 (2020).

505. Golotin, V., Balabanova, L., Likhatskaya, G. & Rasskazov, V. Recombinant Production and Characterization of a Highly Active Alkaline Phosphatase from Marine Bacterium Cobetia marina. *Mar. Biotechnol.* **17**, 130-143 (2015).

506. Meng, D. et al. An alkaline phosphatase from Bacillus amyloliquefaciens YP6 of new application in biodegradation of five broad-spectrum organophosphorus pesticides. *J. Environ. Sci. Health B* **54**, 336-343 (2019).

507. Claussen, J.C. et al. Probing the Enzymatic Activity of Alkaline Phosphatase within Quantum Dot Bioconjugates. *J. Phys. Chem. C* **119**, 2208-2221 (2015).

508. Zhang, R.-Q. et al. Inhibition kinetics of green crab (Scylla serrata) alkaline phosphatase by zinc ions: a new type of complexing inhibition. *Biochim. Biophys. Acta, Protein Struct. Mol. Enzymol.* **1545**, 6-12 (2001).
509. Pétursson, B., BSc Thesis (University of Iceland, 2014).
510. Clark, J.F. Creatine and phosphocreatine: a review of their use in exercise and sport. *J. Athl. Train.* **32**, 45-51 (1997).
511. Komazin, G. et al. Substrate structure-activity relationship reveals a limited lipopolysaccharide chemotype range for intestinal alkaline phosphatase. *J. Biol. Chem.* **294**, 19405-19423 (2019).
512. Mangoni, M.L. et al. Lipopolysaccharide, a key molecule involved in the synergism between temporins in inhibiting bacterial growth and in endotoxin neutralization. *J. Biol. Chem.* **283**, 22907-22917 (2008).
513. Ritchie, R.J. & Prvan, T. A Simulation Study on Designing Experiments to Measure the Km of Michaelis-Menten Kinetics Curves. *J. Theor. Biol.* **178**, 239-254 (1996).
514. Zimmerle, C.T. & Frieden, C. Analysis of progress curves by simulations generated by numerical integration. *Biochem. J.* **258**, 381-387 (1989).
515. Tamer, Y.T. et al. High-Order Epistasis in Catalytic Power of Dihydrofolate Reductase Gives Rise to a Rugged Fitness Landscape in the Presence of Trimethoprim Selection. *Mol. Biol. Evol.* **36**, 1533-1550 (2019).
516. Stankiewicz, P.J. & Gresser, M.J. Inhibition of phosphatase and sulfatase by transition-state analogs. *Biochemistry* **27**, 206-212 (1988).
517. Böger, B. et al. Inhibition of the activated sludge-associated enzyme phosphatase by transition metal oxyanions. *Water Sci. Technol.* **83**, 2629-2639 (2021).
518. Hsu, S.Y. & Goetz, F.W. Oxoanions stimulate in vitro ovulation and signal transduction pathways in goldfish (Carassius auratus) follicles. *Am. J. Physiol. Endocrinol. Metab.* **263**, E943-E949 (1992).
519. Koncki, R., Rudnicka, K. & Tymecki, Ł. Flow injection system for potentiometric determination of alkaline phosphatase inhibitors. *Anal. Chim. Acta* **577**, 134-139 (2006).
520. Reker, C.E., Lapointe, M.C., Kovačič-Milivojević, B., Chiou, W.J.H. & Vedeckis, W.V. A possible role for dephosphorylation in glucocorticoid receptor transformation. *J. Steroid Biochem.* **26**, 653-665 (1987).
521. Whisnant, A.R. & Gilman, S.D. Studies of reversible inhibition, irreversible inhibition, and activation of alkaline phosphatase by capillary electrophoresis. *Anal. Biochem.* **307**, 226-234 (2002).
522. Morton, R.K. The substrate specificity and inhibition of alkaline phosphatases of cow's milk and calf intestinal mucosa. *Biochem. J.* **61**, 232-240 (1955).
523. Stinson, R.A. & Seargeant, L.E. Comparative studies of pure alkaline phosphatases from five human tissues. *Clin. Chim. Acta* **110**, 261-272 (1981).
524. Murakami, M. Equine Alkaline Phosphatase: III. Some Biochemical Properties of Equine Plasma Alkaline Phosphatase. *Exp. Rep. Equine Hlth. Lab.* **1971**, 110-125 (1971).
525. Cyboron, G., Vejins, M. & Wuthier, R. Activity of epiphyseal cartilage membrane alkaline phosphatase and the effects of its inhibitors at physiological pH. *J. Biol. Chem.* **257**, 4141-4146 (1982).

526. Schramm, V.L. Enzymatic Transition State Theory and Transition State Analogue Design *. *J. Biol. Chem.* **282**, 28297-28300 (2007).
527. Gutierrez, J.A. et al. Transition state analogs of 5′-methylthioadenosine nucleosidase disrupt quorum sensing. *Nat. Chem. Biol.* **5**, 251-257 (2009).
528. Shi, W. et al. The 2.0 Å structure of human hypoxanthine-guanine phosphoribosyltransferase in complex with a transition-state analog inhibitor. *Nat. Struct. Biol.* **6**, 588-593 (1999).
529. Seargeant, L.E. & Stinson, R.A. Inhibition of human alkaline phosphatases by vanadate. *Biochem. J.* **181**, 247-250 (1979).
530. Rehder, D. The potentiality of vanadium in medicinal applications. *Future Med. Chem.* **4**, 1823-1837 (2012).
531. Crans, D.C. Antidiabetic, Chemical, and Physical Properties of Organic Vanadates as Presumed Transition-State Inhibitors for Phosphatases. *J. Org. Chem.* **80**, 11899-11915 (2015).
532. Rehder, D. The future of/for vanadium. *Dalton Trans.* **42**, 11749-11761 (2013).
533. Rehder, D. The role of vanadium in biology. *Metallomics* **7**, 730-742 (2015).
534. Laizé, V., Tiago, D.M., Aureliano, M. & Cancela, M.L. New insights into mineralogenic effects of vanadate. *Cell. Mol. Life Sci.* **66**, 3831-3836 (2009).
535. Yong, S.C. et al. A complex iron-calcium cofactor catalyzing phosphotransfer chemistry. *Science* **345**, 1170-1173 (2014).
536. McLauchlan, C.C., Peters, B.J., Willsky, G.R. & Crans, D.C. Vanadium–phosphatase complexes: Phosphatase inhibitors favor the trigonal bipyramidal transition state geometries. *Coord. Chem. Rev.* **301-302**, 163-199 (2015).
537. Dubois, B.W., Cherian, S.F. & Evers, A.S. Volatile anesthetics compete for common binding sites on bovine serum albumin: a 19F-NMR study. *Proc. Natl. Acad. Sci. U.S.A.* **90**, 6478-6482 (1993).
538. Todd, M.J. & Hausinger, R.P. Competitive Inhibitors of Klebsiella aerogenes Urease: Mechanisms of interaction with the nickel active site. *J. Biol. Chem.* **264**, 15835-15842 (1989).
539. Yang, H., Liu, L., Li, J., Chen, J. & Du, G. Rational Design to Improve Protein Thermostability: Recent Advances and Prospects. *ChemBioEng Rev.* **2**, 87-94 (2015).
540. Relkin, P. & Mulvihill, D.M. Thermal unfolding of β-lactoglobulin, α-lactalbumin, and bovine serum albumin. A thermodynamic approach. *Crit. Rev. Food Sci. Nutr.* **36**, 565-601 (1996).
541. Schellman, J.A. The thermodynamic stability of proteins. *Ann. Rev. Biophys. Biophys. Chem.* **16**, 115-137 (1987).
542. Kotov, V. et al. In-depth interrogation of protein thermal unfolding data with MoltenProt. *Protein Sci.* **30**, 201-217 (2021).
543. Weber, P.C., Pantoliano, M.W., Simons, D.M. & Salemme, F.R. Structure-Based Design of Synthetic Azobenzene Ligands for Streptavidin. *J. Am. Chem. Soc.* **116**, 2717-2724 (1994).
544. Kurzban, G.P., Gitlin, G., Bayer, E.A., Wilchek, M. & Horowitz, P.M. Biotin binding changes the conformation and decreases tryptophan accessibility of streptavidin. *J. Protein Chem.* **9**, 673-682 (1990).

545. Mao, H., Yang, T. & Cremer, P.S. Design and Characterization of Immobilized Enzymes in Microfluidic Systems. *Anal. Chem.* **74**, 379-385 (2002).
546. Kerby, M.B., Legge, R.S. & Tripathi, A. Measurements of Kinetic Parameters in a Microfluidic Reactor. *Anal. Chem.* **78**, 8273-8280 (2006).
547. Hughes, A.J. & Herr, A.E. Quantitative Enzyme Activity Determination with Zeptomole Sensitivity by Microfluidic Gradient-Gel Zymography. *Anal. Chem.* **82**, 3803-3811 (2010).
548. Neira, H.D. & Herr, A.E. Kinetic Analysis of Enzymes Immobilized in Porous Film Arrays. *Anal. Chem.* **89**, 10311-10320 (2017).
549. Wang, J., Morabito, K., Erkers, T. & Tripathi, A. Capture and separation of biomolecules using magnetic beads in a simple microfluidic channel without an external flow device. *Analyst* **138**, 6573-6581 (2013).
550. Olp, M.D., Kalous, K.S. & Smith, B.C. ICEKAT: an interactive online tool for calculating initial rates from continuous enzyme kinetic traces. *BMC Bioinform.* **21**, 186 (2020).
551. Pinto, M.F. et al. interferENZY: A Web-Based Tool for Enzymatic Assay Validation and Standardized Kinetic Analysis. *J. Mol. Biol.*, 166613 (2020).
552. Hofer, M. et al. Two New Faces of Amifostine: Protector from DNA Damage in Normal Cells and Inhibitor of DNA Repair in Cancer Cells. *J. Med. Chem.* **59**, 3003-3017 (2016).
553. Ke, C.-B., Lu, T.-L. & Chen, J.-L. Fluorometric determination of amifostine and alkaline phosphatase on amphiprotic molecularly imprinted silica crosslinked with binary functional silanes and carbon dots. *Biosens. Bioelectron.* **151**, 111965 (2020).
554. Na, W., Liu, S., Liu, X. & Su, X. Ultrasensitive detection of amifostine and alkaline phosphatase based on the growth of CdS quantum dots. *Talanta* **144**, 1059-1064 (2015).
555. Li, N., Na, W., Liu, H. & Su, X. Dual mode detection of amifostine based on gold nanoparticles and sulfanilic acid functionalized graphene quantum dots. *New. J. Chem.* **42**, 12126-12133 (2018).
556. Luo, M. et al. Determination of alkaline phosphatase activity based on enzyme-triggered generation of a thiol and the fluorescence quenching of silver nanoclusters. *Microchim. Acta* **186**, 180 (2019).
557. Eltzschig, H.K., Sitkovsky, M.V. & Robson, S.C. Purinergic Signaling during Inflammation. *N. Engl. J. Med.* **367**, 2322-2333 (2012).
558. Longhi, M.S., Moss, A., Jiang, Z.G. & Robson, S.C. Purinergic signaling during intestinal inflammation. *J. Mol. Med.* **95**, 915-925 (2017).
559. Masola, B. & Ngubane, N.P. The activity of phosphate-dependent glutaminase from the rat small intestine is modulated by ADP and is dependent on integrity of mitochondria. *Arch. Biochem. Biophys.* **504**, 197-203 (2010).
560. Croset, M. et al. Rat Small Intestine Is an Insulin-Sensitive Gluconeogenic Organ. *Diabetes* **50**, 740-746 (2001).
561. Mithieux, G., Rajas, F. & Gautier-Stein, A. A Novel Role for Glucose 6-Phosphatase in the Small Intestine in the Control of Glucose Homeostasis *. *J. Biol. Chem.* **279**, 44231-44234 (2004).
562. Gautier-Stein, A., Rajas, F. & Mithieux, G. Intestinal gluconeogenesis and protein diet: future directions. *Proc. Nutr. Soc.*, 1-8 (2020).
563. Varga, V. et al. Species-Specific Glucose-6-Phosphatase Activity in the Small Intestine—Studies in Three Different Mammalian Models. *Int. J. Mol. Sci.* **20**, 5039 (2019).

564. Griss, R. et al. Bioluminescent sensor proteins for point-of-care therapeutic drug monitoring. *Nat. Chem. Biol.* **10**, 598-603 (2014).

565. Tamura, T. & Hamachi, I. Recent Progress in Design of Protein-Based Fluorescent Biosensors and Their Cellular Applications. *ACS Chem. Biol.* **9**, 2708-2717 (2014).

566. Zhang, X.-a. & Woggon, W.-D. A Supramolecular Fluorescence Sensor for Pyrovanadate as a Functional Model of Vanadium Haloperoxidase. *J. Am. Chem. Soc.* **127**, 14138-14139 (2005).

567. Zhou, Y. et al. A Novel Supermolecular Tetrameric Vanadate-Selective Colorimetric and "Off–On" Sensor with Pyrene Ligand. *Org. Lett.* **13**, 2742-2745 (2011).

568. Jeong, H., Lee, B.-I. & Byeon, S.-H. Antenna Effect on the Organic Spacer-Modified Eu-Doped Layered Gadolinium Hydroxide for the Detection of Vanadate Ions over a Wide pH Range. *ACS Appl. Mater. Interfaces* **8**, 10946-10953 (2016).

569. Huo, F.-J. et al. A rhodamine-based dual chemosensor for the visual detection of copper and the ratiometric fluorescent detection of vanadium. *Dyes Pigm.* **86**, 50-55 (2010).

570. Garidel, P., Hegyi, M., Bassarab, S. & Weichel, M. A rapid, sensitive and economical assessment of monoclonal antibody conformational stability by intrinsic tryptophan fluorescence spectroscopy. *Biotechnol. J.* **3**, 1201-1211 (2008).

571. Lo, M.-C. et al. Evaluation of fluorescence-based thermal shift assays for hit identification in drug discovery. *Anal. Biochem.* **332**, 153-159 (2004).

572. Niesen, F.H., Berglund, H. & Vedadi, M. The use of differential scanning fluorimetry to detect ligand interactions that promote protein stability. *Nat. Protoc.* **2**, 2212-2221 (2007).

573. Jouzi, M., Kerby, M.B., Tripathi, A. & Xu, J. Nanoneedle Method for High-Sensitivity Low-Background Monitoring of Protein Activity. *Langmuir* **24**, 10786-10790 (2008).

574. Choe, W., Durgannavar, T.A. & Chung, S.J. Fc-Binding Ligands of Immunoglobulin G: An Overview of High Affinity Proteins and Peptides. *Materials* **9**, 994 (2016).

575. Saha, K., Bender, F. & Gizeli, E. Comparative Study of IgG Binding to Proteins G and A: Nonequilibrium Kinetic and Binding Constant Determination with the Acoustic Waveguide Device. *Anal. Chem.* **75**, 835-842 (2003).

576. Akerström, B., Brodin, T., Reis, K. & Björck, L. Protein G: a powerful tool for binding and detection of monoclonal and polyclonal antibodies. *J. Immunol.* **135**, 2589-2592 (1985).

577. Djaileb, A. et al. Cross-validation of ELISA and a portable surface plasmon resonance instrument for IgG antibody serology with SARS-CoV-2 positive individuals. *Analyst* **146**, 4905-4917 (2021).

578. Masson, J.-F. Surface Plasmon Resonance Clinical Biosensors for Medical Diagnostics. *ACS Sens.* **2**, 16-30 (2017).

579. Makaraviciute, A., Ramanavicius, A. & Ramanaviciene, A. Development of a reusable protein G based SPR immunosensor for direct human growth hormone detection in real samples. *Anal. Methods* **7**, 9875-9884 (2015).

580. Kamat, V., Rafique, A., Huang, T., Olsen, O. & Olson, W. The impact of different human IgG capture molecules on the kinetics analysis of antibody-antigen interaction. *Anal. Biochem.* **593**, 113580 (2020).

581. Jung, Y., Lee, J.M., Jung, H. & Chung, B.H. Self-Directed and Self-Oriented Immobilization of Antibody by Protein G−DNA Conjugate. *Anal. Chem.* **79**, 6534-6541 (2007).

582. Schwaminger, S.P. et al. Immobilization of PETase enzymes on magnetic iron oxide nanoparticles for the decomposition of microplastic PET. *Nanoscale Adv.* **3**, 4395-4399 (2021).
583. Gordon, S.E., Munari, M. & Zagotta, W.N. Visualizing conformational dynamics of proteins in solution and at the cell membrane. *eLife* **7**, e37248 (2018).
584. Santos, L.H.S., Ferreira, R.S. & Caffarena, E.R. in Docking Screens for Drug Discovery. (ed. W.F. de Azevedo Jr) 13-34 (Springer New York, New York, NY; 2019).
585. Hanwell, M.D. et al. Avogadro: an advanced semantic chemical editor, visualization, and analysis platform. *J. Cheminformatics* **4**, 17 (2012).
586. Molecular Operating Environment (MOE), 2019.01; Chemical Computing Group ULC, 1010 Sherbrooke St. West, Suite #910, Montreal, QC, Canada, H3A 2R7, 2019.
587. D.A. Case, K. Belfon, I.Y. Ben-Shalom, S.R. Brozell, D.S. Cerutti, T.E. Cheatham, III, V.W.D. Cruzeiro, T.A. Darden, R.E. Duke, G. Giambasu, M.K. Gilson, H. Gohlke, A.W. Goetz, R. Harris, S. Izadi, S.A. Izmailov, K. Kasavajhala, A. Kovalenko, R. Krasny, T. Kurtzman, T.S. Lee, S. LeGrand, P. Li, C. Lin, J. Liu, T. Luchko, R. Luo, V. Man, K.M. Merz, Y. Miao, O. Mikhailovskii, G. Monard, H. Nguyen, A. Onufriev, F.Pan, S. Pantano, R. Qi, D.R. Roe, A. Roitberg, C. Sagui, S. Schott-Verdugo, J. Shen, C.L. Simmerling, N.R.Skrynnikov, J. Smith, J. Swails, R.C. Walker, J. Wang, L. Wilson, R.M. Wolf, X. Wu, Y. Xiong, Y. Xue, D.M. York and P.A. Kollman (2020), AMBER 2020, University of California, San Francisco.
588. Di Trani, J.M., PhD Thesis (McGill University, 2018).
589. Snyder, L.R., Peters, J.E., Henkin, T.M. & Champness, W. Molecular Genetics of Bacteria. (Wiley, 2014s).
590. Tanaka, T. & Letsinger, R.L. Syringe method for stepwise chemical synthesis of oligonucleotides. *Nucleic Acids Res.* **10**, 3249-3259 (1982).
591. Pon, R.T. in Protocols for Oligonucleotides and Analogs: Synthesis and Properties. (ed. S. Agrawal) 465-496 (Humana Press, Totowa, NJ; 1993).
592. Ellington, A. & Pollard Jr., J.D. Introduction to the Synthesis and Purification of Oligonucleotides. *Curr. Protoc. Nucleic Acid Chem.* **00**, A.3C.1-A.3C.22 (2000).
593. DNA Oligonucleotide Synthesis, Millipore Sigma, 2022, 13 February 2022, https://www.sigmaaldrich.com/technical-documents/articles/biology/dna-oligonucleotide-synthesis.html
594. McLaughlin, L.W., Piel, N. & Hellmann, T. Preparation of Protected Ribonucleosides Suitable for Chemical Oligoribonucleotide Synthesis. *Synthesis* **1985**, 322-323 (1985).
595. Reddy, M.P., Hanna, N.B. & Farooqui, F. Ultrafast Cleavage and Deprotection of Oligonucleotides Synthesis and Use of CAc Derivatives. *Nucleosides Nucleotides* **16**, 1589-1598 (1997).
596. Sekine, M. DNA Synthesis Without Base Protection. *Curr. Protoc. Nucleic Acid Chem.* **18**, 3.10.11-13.10.15 (2004).
597. Sinha, N.D., Biernat, J., McManus, J. & Köster, H. Polymer support oligonucleotide synthesis XVIII1.2): use of β-cyanoethyi-N,N-dialkylamino-/N-morpholino phosphoramidite of deoxynucleosides for the synthesis of DNA fragments simplifying deprotection and isolation of the final product. *Nucleic Acids Res.* **12**, 4539-4557 (1984).

598. Wright, P., Lloyd, D., Rapp, W. & Andrus, A. Large scale synthesis of oligonucleotides via phosphoramidite nucleosides and a high-loaded polystyrene support. *Tetrahedron Lett.* **34**, 3373-3376 (1993).
599. Sproat, B. et al. An Efficient Method for the Isolation and Purification of Oligoribonucleotides. *Nucleosides Nucleotides* **14**, 255-273 (1995).
600. Berner, S., Mūhlegger, K. & Seliger, H. Studies on the role of tetrazole in the activation of phosphoramidites. *Nucleic Acids Res.* **17**, 853-864 (1989).
601. Wei, X. Coupling activators for the oligonucleotide synthesis via phosphoramidite approach. *Tetrahedron* **69**, 3615-3637 (2013).